5410 - 0005 - RU - 002

PHASE 1A STUDY REPORT

VOYAGER SPACECRAFT

VOLUME 5

ALTERNATE DESIGNS
SUBSYSTEMS CONSIDERATIONS
APPENDICES E-F-G-J-K-L

30 July 1965

Prepared for
California Institute of Technology
Jet Propulsion Laboratory
Pasadena, California

Under Contract Number 951113

NAS-7-100

TRW SYSTEMS GROUP

Redondo Beach, California

CONTENTS

Page

APPENDIX E: STABILIZATION AND CONTROL

1. DISTURBANCE TORQUE ANALYSIS E-1

1.1 Coordinate Systems E-1

1.2 Disturbance Torques E-5

1.3 Fuel Requirements Due to Disturbance Torques . . E-21

2. CONTROL SYSTEM DESIGN ANALYSIS E-26

2.1 Cruise Mode E-29

2.2 Acquisition Mode E-38

2.3 Maneuver and Inertial Attitude Hold Modes E-59

2.4 Thrust Vector Control Mode E-60

3. GYRO REFERENCE ASSEMBLY TRADEOFF CONSIDERATIONS E-70

3.1 General E-75

3.2 Reliability E-76

3.3 Gyros E-77

3.4 Configuration Description E-77

4. SUN SENSORS DESIGN DETAILS E-86

4.1 Coarse Sun Sensors E-86

4.2 Fine Sun Sensors E-87

4.3 Sun Sensor Response E-88

5. Near Earth Detector Design Details E-90

5.1 Design Summary E-90

5.2 Earth Magnitude Calculation E-90

5.3 Near Earth Detector Response E-94

CONTENTS (Continued)

		Page
6.	STAR SENSOR DESIGN DETAILS	E-96
	6.1 Mariner-C Canopus Tracker	E-96
	6.2 Quadrant Photomultiplier Star Tracker	E-100
APPENDIX F: TELECOMMUNICATIONS STUDIES		
1.	RANGE AND RANGE RATE ANALYSIS	F-1
	1.1 Turn-Around Ranging Analysis	F-2
	1.2 DSIF Acquisition	F-10
	1.3 Range and Range Rate Performance	F-15
2.	CAPSULE LINK ANALYSIS	F-18
	2.1 Scope	F-18
	2.2 Mission Description	F-18
	2.3 Systems Synthesis and Analysis	F-21
	2.4 Constraints	F-55
	2.5 Capsule	F-56
3.	PSEUDO-NOISE SYNCHRONIZER PERFORMANCE	F-62
	3.1 Introduction	F-62
	3.2 A Fokker-Planck Solution for First-Order Phase-Lock Loops	F-63
4.	TELEMETRY LINK ANALYSES	F-84
	4.1 Comparison of Synchronization Methods	F-84
	4.2 PN Synchronization Acquisition Performance	F-97
	4.3 Single-Versus Two-Channel Systems	F-100
	4.4 Performance of Two-Channel System	F-107

CONTENTS (Continued)

		Page
5.	TELEMETRY SYNCHRONIZATION AND ACQUISITION ANALYSIS	F-118
	5.1 Frame Synchronization Analysis	F-118
	5.2 Derivation of $F_2(\varepsilon_1 k)$	F-124
	5.3 Derivation of Average Acquisition and Hold Times	F-126
6.	THRESHOLD CRITERIA FOR PHASELOCK RECEIVER	F-129
	6.1 Tracking Loop Dynamic Errors	F-129
	6.2 Carrier Loop Degradation in Two-Way Mode	F-132
	6.3 Data Degradation Caused by Carrier Loop	F-135
7.	TELEMETRY MEASUREMENT LIST	F-140

APPENDIX G: SOLAR ARRAY DESIGN

1.	SOLAR CELL TRADEOFF ANALYSIS	G-1
	1.1 Details of Analysis	G-2
	1.2 Array Characteristics	G-5
	1.3 Solar Cell Damage Curve	G-5
	1.4 Results	G-6
2.	ARRAY MECHANICAL DESIGN	G-12
	2.1 Summary	G-12
	2.2 Substrate	G-14
	2.3 Panel Weight	G-17
	2.4 Adhesive Material	G-17
	2.5 Substrate to Module Interface	G-19
	2.6 Wiring and Layouts	G-21
3.	ARRAY THERMAL DESIGN	G-22
	3.1 Thermal Cycling	G-23

CONTENTS (Continued)

Page

3.2 Thermal Characteristics of the Module-to-Substrate Interface G-25

3.3 Diode Packaging G-30

3.4 Honeycomb Substrate Adhesive G-30

3.5 Cover Glass Adhesive G-31

APPENDIX J: BIPROPELLANT AND MONOPROPELLANT FEED SYSTEM CONFIGURATION STUDIES

1. BIPROPELLANT FEED SUBSYSTEM J-1

1.1 Summary J-1

1.2 Alternate Designs, Description and Tradeoffs . . . J-2

1.3 Bipropellant Feed System Design J-14

2. MONOPROPELLANT ENGINE PROPELLANT SUPPLY J-26

2.1 Summary J-26

2.2 Separately Pressurized Monopropellant Feed . . . J-26

2.3 Blowdown Monopropellant Feed System Design . . J-34

APPENDIX K: PRELIMINARY CALCULATIONS FOR LANDER COVER BASE SEPARATION SPRINGS

1. ASSUMPTIONS K-1

2. EQUATIONS K-1

3. SYMBOLS K-4

APPENDIX L: RADIOMETRIC MODEL OF MARS

1. INFRARED OPTICAL REFERENCES L-1

1.1 The Planetary Surface as an Optical Reference L-2

1.2 The 15μ Band as an Optical Reference L-4

CONTENTS (Continued)

		Page
2.	THE 10-MB, 60 METER ATMOSPHERE	L-5
3.	THE ALTERNATIVES	L-13
4.	CONCLUSION	L-14
5.	REFERENCES	L-14

ILLUSTRATIONS

Figure		Page
E-1	Body Coordinate Sets	E-2
E-2	Orientation of Body 2 Relative to Body 1.	E-2
E-3	Orbital Coordinate Sets	E-3
E-4	Orientation of POP Antenna for Maximum Solar Exposure.	E-6
E-5	Solar Radiation Torque for Spacecraft with C. G. Offset Along Y-Axis	E-8
E-6	Solar Radiation Torque for Spacecraft with C. G. Offset Along Z-Axis	E-8
E-7	Gravity Gradient Torques versus True Anomoly (Sample Orbit - 1971 Mission)	E-10
E-8	Reaction Torque versus True Anomoly (Sample Orbit - 1971 Mission)	E-20
E-9	Voyager Reference Axes	E-28
E-10	Block Diagram of a Single Axis of the Selected Configuration.	E-29
E-11	Typical Limit Cycle Acquisition Prior to Capsule Separation	E-31
E-12	Typical Limit Cycle Acquisition After Capsule Separation.	E-31
E-13	Switching Amplifier and Filter Network Block Diagram	E-34
E-14	Error Signal Time History During Limit Cycle	E-35
E-15	Typical Limit Cycle with Torque Disturbance.	E-36
E-16	Limit Cycle Characteristics for $T_D = 10^{-4}$ ft-lb and I = 5772 slug-ft^2	E-37
E-17	Limit Cycle Characteristics $T_D = 6.4 \times 10^{-5}$ ft-lb and I = 1824 slug-ft^2	E-37

Figure		Page
E-18	Yaw or Pitch Sun Acquisition Mode	E-39
E-19	Roll Canopus Acquisition Mode	E-40
E-20	Switching Lines for a Pitch or Yaw Acquisition Control Channel	E-45
E-21	Initial Sun Acquisition with Initial Rate and 180-Degree Position Error	E-48
E-22	Initial Sun Acquisition with Initial Rate + 3 deg/sec, No Position Error	E-48
E-23	Acquisition After Deboost with Initial Rate and 180-Degree Position Error	E-48
E-24	Acquisition After Deboost with + 3 deg/sec Initial Rate, No Position Error.	E-48
E-25	Initial Acquisition of Baseline Configuration and Derived Rate	E-50
E-26	Block Diagram of Derived Rate Backup Acquisition System	E-51
E-27	Initial Acquisition for Several Backup Configurations - High Inertia	E-54
E-28	Initial Acquisition for Several Backup Configurations - Low Inertia.	E-54
E-29	Initial Acquisition for Backup with Raised Derived Rate Limit and Lowered Gain (K).	E-55
E-30	Block Diagram of Derived Rate and Lead-Lag Compensation Backup Acquisition System	E-55
E-31	Analog Simulation	E-57
E-32	Baseline Switching Logic and Rate Feedback	E-57
E-33	Coarse Sun Sensor	E-58
E-34	Single Axis (Pitch, Roll) Reorientation Block Diagram.	E-60

ILLUSTRATIONS (Continued)

Figure		Page
E-35	50-Degree Reorientation Maneuver, 2 deg/sec Gyro Precession Rate Cruise Mode Configuration.	E-61
E-36	50-Degree Reorientation Maneuver, 2 deg/sec Gyro Precession Rate $2C_{S+1}/2S+1$ Compensation Network	E-62
E-37	50-Degree Reorientation Maneuver, 2 deg/sec Gyro Precession Rate, Gyro Rate Feedback	E-63
E-38	Midcourse Jet Vane TVC Block Diagram	E-65
E-39	Midcourse Jet Vane TVC Root Locus Block Diagram	E-66
E-40	Solid Deboost TVC Block Diagram.	E-67
E-41	Deboost TVC Root Locus Diagram.	E-68
E-42	Thrust Vector Offset Angles versus Spacecraft Spin Rate During Deboost Maneuver	E-69
E-43	Gimballed TVC Block Diagram	E-69
E-44	Gimballed TVC Root Locus Diagram	E-70
E-45	Trim Thrust Vector Angles versus Center of Mass Offset- Bipropellant Configuration	E-71
E-46	Gyro Control Loop (Closed Loop with VCO Integration)	E-73
E-47	Gyro Control Loop (Closed Loop with Capacitor Integration)	E-73
E-48	Gyro Control Loop (Closed Loop with Pulse Torquing	E-74
E-49	Gyro Control Loop (Open Loop).	E-74
E-50	Gyro Reference Assembly Thermal Model.	E-84
E-51	Verification of Theoretical Linearity of Quad Cell Design	E-88

ILLUSTRATIONS (Continued)

Figure		Page
E-52	Geometry of Earthshine Calculation	E-91
E-53	Sun-Earth-Spacecraft Relationship	E-92
E-54	Model of Typical CdS Photocell.	E-96
E-55	Block Diagram for Star Tracker No. - Mariner C	E-100
E-56	Geometric Factor - The Fraction of Circular-Image Area	E-101
E-57	Possible Block Diagram, One-Axis Quadrant Multiplier Phototube Star Tracker.	E-102
E-58	QMP Signals and Filtered Error Signal	E-103
E-59	Collection Efficiency as a Function of Distance from Center Along a Line 45 Degrees to the X-Axis for Various Image Sizes	E-104
E-60	Signal-to-Noise Ratio, QMP Canopus Sensor, 0.25 mm Image, 10 cps Bandwidth	E-108
F-1	Received Spacecraft Signal-to-Noise Power Ratio versus Range.	F-3
F-2	Spacecraft Transponder Turn-Around Ranging Channel.	F-3
F-3	Word Error Probability Orthogonal Codes	F-13
F-4	Entry Geometry.	F-20
F-5	Two Signal Model for Multipath.	F-21
F-6	Vector Representation of Signals.	F-24
F-7	Modulation Envelope Shape.	F-25
F-8	Harmonic Content (Per Cent of Unmodulated).	F-28
F-9	Grazing Angle γ (Degree).	F-29
F-10	Grazing Angle γ (Degree).	F-29

ILLUSTRATIONS (Continued)

Figure		Page
F-11	Noncoherent FSK System	F-41
F-12	Envelope Detector Characteristics	F-43
F-13	Noncoherent FSK-AM System	F-45
F-14	Method of Combining "Ready" and "Phasing" Functions (After Bennett and Davey)	F-47
F-15	Noncoherent FSK System	F-47
F-16	Data Rate versus Frequency Uncertainty for Noncoherent FSK	F-49
F-17	Spacecraft VHF Receiving System	F-52
F-18	VHF Receiver Block Diagram	F-54
F-19	FSK Demodulator Block Diagram	F-55
F-20	Spacecraft Non-Demodulating Repeater Operation	F-57
F-21	S-Band Spectrum	F-58
F-22	Phase-Lock Loop	F-63
F-23	Loop Error Function of PN Code	F-69
F-24	Integral of Loop Error Function-PN Code	F-69
F-25	Probability Density Function of Loop Phase Error	F-70
F-26	Mean Time to Loss of Lock-PN Code	F-72
F-27	Bit Synchronizer Circuit	F-73
F-28	Ideal Loop Error Function	F-73
F-29	Bit Synchronizer Wave Shapes, v(t)	F-75

Figure		Page
F-30	Bit Synchronizer Wave Shapes, Δ_a	F-76
F-31	Decomposition of $\Delta_a = \Delta'_a + \Delta''_a$	F-77
F-32	Calculation of h_{ka}	F-77
F-33	Calculation of (Σ PN + PN' (kT) for a 7-Bit Code	F-80
F-34	Error Function for 7-Bit Code 1110010	F-81
F-35	Error Function for Mariner C Telemetry Code	F-82
F-36	Transmitted Waveform in PN Synchronization	F-85
F-37	Receiver for PN Synchronization	F-86
F-38	Modified PN Receiver	F-87
F-39	I-Q Loop	F-88
F-40	Error Function for Demodulator Loop	F-89
F-41	Error Function for Bit Synchronizer	F-90
F-42	NRZ Spectrum With 4 Cycles per Bit Subcarrier Random Data	F-91
F-43	Tracking Out of Subcarrier by Carrier Loop	F-91
F-44	Different g (ϕ) Functions	F-92
F-45	Range versus Power Levels in Carrier Data and Sync Channels	F-99
F-46	Range versus Acquisition Time for 63-Bit Code	F-101
F-47	Acquisition Time versus Power Level in Sync Channel for 63-Bit Code	F-101
F-48	Single and Two-Channel Modulators	F-102
F-49	Single and Two-Channel Detectors	F-103

Figure		Page
F-50	Signal-to-Noise Density Ratio versus Bit Rate	F-106
F-51	Framelength versus $\frac{n}{N}$	F-120
F-52	P_1 versus Number of Sync Code Bits	F-121
F-53	Syncronization Block Diagram	F-122
G-1	Fraction of Initial Power Remaining versus Total 1 Nev Equivalent Electron Flux	G-1
G-2	Relative Weight versus Glass Thickness	G-9
G-3	Relative Array Area (Weight versus Integrated 1-Mev Electron Flux for Encounter + 6 Months	G-11
G-4	Solar Panel Outlines	G-14
G-5	Aluminum Specific Heat	G-16
G-6	Aluminum + Zinc + X Specific Heat	G-16
G-7	Cross-Section of the Module-to-Substrate Interface	G-25
G-8	Average Coefficients of Linear Thermal Expansion and Contraction for RTV Compounds	G-27
G-9	Typical Load Deflection Recorded by Deflectometer	G-27
G-10	Tensile Modulus versus Temperatures	G-28
G-11	Compression Set (Per Cent of Deformation versus Temperature)	G-28
G-12	Ultimate Elongation versus Temperature	G-29
G-13	Ultimate Tensile Stress versus Temperature	G-29
G-14	Coefficient of Linear of Linear Expansion, Sylgard 182	G-32

ILLUSTRATIONS (Continued)

Figure		Page
J-1	Propellant Baseline Configuration	J-2
J-2	Solid Gas Generator Pressurization Alternate	J-6
J-3	Conventional Explosive Pressurant Control Alternate	J-7
J-4	Redundant Explosive Valve Pressurant Control Alternate	J-8
J-5	Quadrant Solenoid Valve Pressurant Control Alternate	J-8
J-6	Quadrant Pressure Regulator Alternate	J-9
J-7	Series Pneumatic Pressure	J-10
J-8	Parallel Redundant Series Pneumatic Pressure Regulator	J-12
J-9	Quadredundant Check Valve Propulsion Task Isolation Alternate	J-12
J-11	Reliability Improvement as a Function of Weight	J-14
J-12	Bipropellant Fuel System Layout	J-15
J-13	N_2O_4 Tank Cross Section	J-24
J-14	Augmented A2 and C2 Configuration	J-27
J-15	Monopropellant System	J-34
J-16	Augmented Monopropellant System	J-35
L-1	Analysis of Coordinates of 10-mb 60 Meter Atmosphere Case	L-6

TABLES

Table		Page
E-1	Fuel Consumption Estimates Due to Disturbance Torques	E-2
E-2a	Configuration A Parameters	E-27
E-2b	Configuration B Parameters	E-27
E-3	Fuel Consumption for Various Reorientation Configurations	E-64
E-4	Voyager Gyro Reference Assembly Tradeoff Considerations	E-72
E-5	Preliminary Specifications of a Gyro for the Voyager Mission	E-76
E-6	Gyro Units Applicable to Voyager Mission	E-78
E-7	Mariner-C Canopus Characteristics	E-100
F-1	Entry Profile Parameters	F-19
F-2	Postland Parameters	F-19
F-3	System Parameters	F-31
F-4	Capsule-Spacecraft Link Frequency Uncertainties	F-35
F-5	Capsule-Spacecraft Link Frequency Uncertainties	F-35
F-6	Capsule Link Parameters	F-40
F-7	Results of Capsuled Link Parameter Analysis, FKS-AM	F-45
F-8	Performance Summary	F-51
F-9	Basic System Rates, Frequencies and Bandwidths	F-108
F-10	Modulation Losses for Minimum Total Power	F-114
F-11	Acquisition and Hold Time Optimization	F-123
F-12	Preliminary Engineering Measurement List	F-141

TABLES (Continued)

Table		Page
F-13	Summary of Measurement List Sampling Rate	F-150
G-1	Voyager Flux Spectrum	G-3
G-2	Relative Power Remaining at End of Life	G-6
G-3	Relative Areas Required	G-7
G-4	Relative Solar Array Weight	G-8
G-5	10-Ohm-Centimeter Cell Data for Relative Array Weight Normalized to 1 Ohm-Centimeter Cell Data in Table G-4	G-10
J-1	Changes in Weight and Reliability Resulting From Alternations of Baseline Configuration (B-2) . .	J-13
J-2	Monopropellant System Midcourse Correction	J-34
J-3	Propulsion System Configuration A-3 Monopropellant System	J-38

APPENDIX E

STABILIZATION AND CONTROL STUDIES

The details of the analytic and tradeoff work completed during Phase IA in support of the design of the stabilization and control subsystem are assembled in this appendix. After an analysis of the major disturbance torques expected on the Voyager spacecraft, the analyses underlying the choices in the preferred subsystem design are described. Tradeoff studies in the gyro assembly, sun sensor, earth detector, and star sensor are then presented.

1. DISTURBANCE TORQUE ANALYSIS

This section presents a study of the major disturbances expected on the Voyager spacecraft. The investigation is devoted to presenting estimates of the magnitude of the disturbances and their effects on the fuel requirement for the mission.

During the course of the mission, the Voyager spacecraft experiences disturbances from environmental and internal sources. The major environmental sources of disturbances include torques due to solar radiation pressure and gravity force. Internal sources of disturbance are the result of reaction forces from rotating devices such as tape recorders and the planet-oriented package (POP). In time, these disturbances have the effect of adding momentum to the spacecraft.

To maintain three-axis stabilization, the cruise attitude control system is required to remove the above momentum buildup by expending fuel. A breakdown of the fuel requirement due to above disturbances is presented in Table E-1. Based on a year during which the spacecraft is in transit and in orbit, a total of 3.43 pounds of fuel is required to neutralize the effects of disturbances.

1.1 Coordinate Systems

Figure E-1 depicts a nominal orientation of the spacecraft relative to a nonrotating inertial reference ($\bar{s}$, $\bar{u}$, $\bar{v}$) whose origin is

Table E-1. Fuel Consumption Estimates Due to Disturbance Torques (lb)

Period	Disturbance Torques			Total
	Solar Radiation	Gravity Force	Reaction Force	
Cruise (6 months)	0.93	-	-	0.93
Orbit (6 months)	0.57	1.21	0.72	2.50

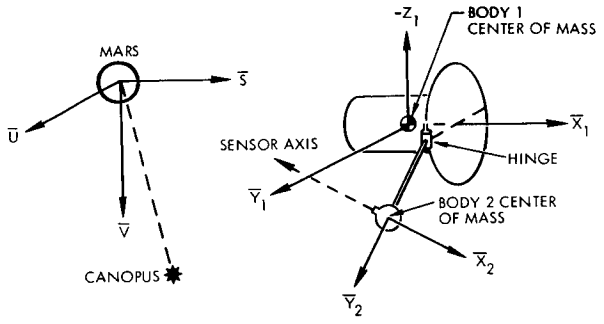


Figure E-1. Body Coordinate Sets

at the center of Mars. The $\bar{s}$ axis is pointed toward the sun, the $\bar{v}$ axis is directed such that a vector to Canopus lies in the $\bar{s}$-$\bar{v}$ plane, and $\bar{u}$ axis is oriented to complete a right hand coordinate set.

The spacecraft's body 1 set ($\bar{x}_1$, $\bar{y}_1$, $\bar{z}_1$) is centered at its center of mass. Figure E-2 shows that the x_1 axis is along the roll axis of the spacecraft and is directed in a positive sense toward the sun; the y_1 axis is parallel to the axis which contains the antenna and POP and is positively directed toward the POP. For perfect attitude control, the orientation of the body 1 set coincides with that of the inertial reference set.

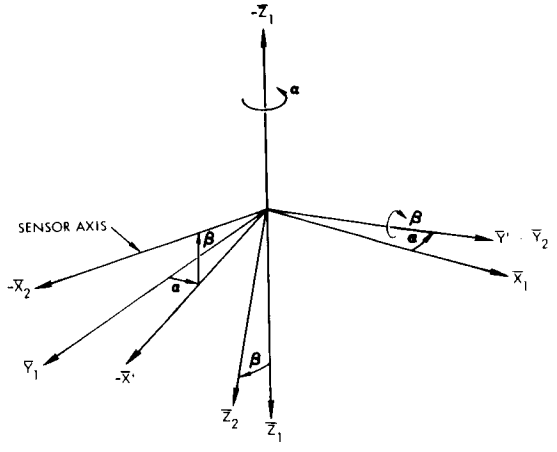


Figure E-2. Orientation of Body 2 Relative to Body 1

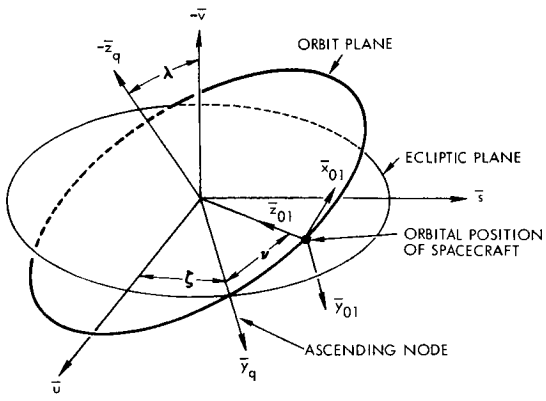


Figure E-3. Orbital Coordinate Systems

The body 2 set ($\bar{x}_2$, $\bar{y}_2$, $\bar{z}_2$) is centered at the center of the mass of the POP. Specifically, the $\bar{y}_2$ axis is directed away from the hinge point along the shaft axis of the POP and the $-\bar{x}_2$ axis, which contains the Mars sensor, is directed toward Mars. As shown in Figure E-3, the body 2 orientation relative to the body 1 set is related by two ordered rotations: first a rotation about the $-\bar{z}_1$ axis through the hinge angle α, yielding

$$\begin{bmatrix} \bar{x}' \\ \bar{y}' \\ \bar{z}' \end{bmatrix} = \begin{bmatrix} -S\alpha & -C\alpha & 0 \\ C\alpha & -S\alpha & 0 \\ 0 & 0 & 1 \end{bmatrix} \begin{bmatrix} \bar{x}_1 \\ \bar{y}_1 \\ \bar{z}_1 \end{bmatrix}$$

and then a rotation about the resulting $-\bar{y}'$ axis through the shaft angle β yielding

$$\begin{bmatrix} \bar{x}_2 \\ \bar{y}_2 \\ \bar{z}_2 \end{bmatrix} = \begin{bmatrix} C\alpha & 0 & S\beta \\ 0 & 1 & 0 \\ -S\beta & 0 & C\beta \end{bmatrix} \begin{bmatrix} \bar{x}' \\ \bar{y}' \\ \bar{z}' \end{bmatrix}$$

where S and C are abbreviations of sine and cosine, respectively.

Combining the above matrices yields

$$\begin{bmatrix} \bar{x}_2 \\ \bar{y}_2 \\ \bar{z}_2 \end{bmatrix} = \begin{bmatrix} -C\beta\, S\alpha & -C\beta\, C\alpha & S\beta \\ C\alpha & -S\alpha & 0 \\ S\alpha\, S\beta & S\beta\, C\alpha & S\beta \end{bmatrix} \begin{bmatrix} \bar{x}_1 \\ \bar{y}_1 \\ \bar{z}_1 \end{bmatrix} \qquad \text{(E. 1)}$$

Thus, for no rotation ($\alpha = \beta = 0$), the Mars sensor is pointed parallel to the $\bar{y}_1$ axis.

To describe the position of the spacecraft in orbit, the study utilizes an orbital reference set ($\bar{x}_{01}$, $\bar{y}_{01}$, $\bar{z}_{01}$) which is related to the inertial reference set. Figure E-3 shows that the $\bar{z}_{01}$ axis is along the local vertical, the $\bar{y}_{01}$ axis is normal to the orbit plane, and the $\bar{x}_{01}$ axis is directed with the same sense as the velocity vector of the spacecraft. The transformation from the inertial reference set to the orbital reference set is given by the matrix Q_{0I}, or

$$Q_{0I} = \begin{bmatrix} 1 & 0 & 0 \\ 0 & 0 & 1 \\ 0 & -1 & 0 \end{bmatrix} \begin{bmatrix} C\nu & -S\nu & 0 \\ S\nu & C\nu & 0 \\ 0 & 0 & 1 \end{bmatrix} \begin{bmatrix} C\lambda & 0 & -S\lambda \\ 0 & 1 & 0 \\ S\lambda & 0 & C\lambda \end{bmatrix} \begin{bmatrix} C\zeta & -S\zeta & 0 \\ S\zeta & C\zeta & 0 \\ 0 & 0 & 1 \end{bmatrix}$$

where

ζ = angle measured from $\bar{u}$ axis to ascenting node

λ = orbital inclination from $\bar{s}$-$\bar{u}$ plane

ν = orbit angle from ascending node.

The above matrix can be expressed as

$$Q_{0I} = \begin{bmatrix} a_{11} & a_{21} & a_{31} \\ a_{12} & a_{22} & a_{32} \\ a_{13} & a_{23} & a_{33} \end{bmatrix} \qquad \text{(E.2)}$$

where

$$a_{11} = C\nu\, C\lambda\, C\zeta - S\nu S\zeta$$

$$a_{12} = S\lambda\, C\zeta$$

$$a_{13} = -S\nu\, C\lambda\, C\zeta - C\nu\, S\zeta$$

$$a_{21} = -C\nu\, C\lambda\, S\zeta - S\nu\, C\zeta$$

$$a_{22} = -S\lambda\, S\zeta$$

$$a_{23} = S\nu\, C\lambda\, S\zeta - C\nu\, C\zeta$$

$$a_{31} = -C\nu\, S\lambda$$

$$a_{32} = C\lambda$$

$$a_{33} = S\nu\, S\lambda$$

Since the orientation of the body 1 set coincides with the inertial reference set for perfect attitude control, the following relation can be written:

$$\begin{bmatrix} \bar{x}_1 \\ \bar{y}_1 \\ \bar{z}_1 \end{bmatrix} = \begin{bmatrix} \bar{s} \\ \bar{u} \\ \bar{v} \end{bmatrix} = Q_{0I}{}^{T} \begin{bmatrix} \bar{x}_{01} \\ \bar{y}_{01} \\ \bar{z}_{01} \end{bmatrix}$$

or

$$\begin{bmatrix} \bar{x}_1 \\ \bar{y}_1 \\ \bar{z}_1 \end{bmatrix} = \begin{bmatrix} a_{11} & a_{12} & a_{13} \\ a_{21} & a_{22} & a_{23} \\ a_{31} & a_{32} & a_{33} \end{bmatrix} \begin{bmatrix} \bar{x}_{01} \\ \bar{y}_{01} \\ \bar{z}_{01} \end{bmatrix} \qquad \text{(E. 3)}$$

1.2 Disturbance Torques

In the following sections, a mathematical description of the disturbance torques is developed and subsequently evaluated for the Voyager spacecraft. The analysis is limited to the investigation of solar radiation torques, gravity gradient torques, and reaction torques from internal rotating components.

1.2.1 Solar Radiation

Based on the derivation presented in Reference E-1, this section develops the equations describing solar radiation torques on the Voyager spacecraft. Perfect attitude control between the main body and the inertial reference axes is assumed in this derivation.

The bombardment of photons transfers a net momentum per unit time to the spacecraft. The momentum per unit time, or force, depends on the amount of surface area affected by the bombardment, the surface reflectivity, and the incidence angle of the sun to the surface. The spacecraft experiences a torque when the force acts at a center of pressure which does not coincide with the spacecraft's center of mass.

The total force $\bar{F}_s$ acting on a surface A due to radiation pressure can be expressed as follows:

$$\bar{F}_s = -V \int_A \left[(1+\nu)(\bar{e}_s \cdot \bar{e}_n)^2 \bar{e}_n + (1-\nu)(\bar{e}_s \cdot \bar{e}_n)(\bar{e}_s \cdot \bar{e}_t) \bar{e}_t \right] dA \qquad \text{(E. 4)}$$

where

V = solar radiation pressure constant

ν = coefficient of reflectivity

$\bar{e}_s$ = unit vector in the direction of the sun

$\bar{e}_n, \bar{e}_t$ = vectors respectively normal and tangent to the surface element dA

While in transit or in orbit about Mars, the Voyager spacecraft is nominally oriented such that the sun line is coincident with the body roll axis. In this orientation, radiation from the sun is always directed toward the end of the spacecraft which includes the POP and antenna as shown in Figure E-4.

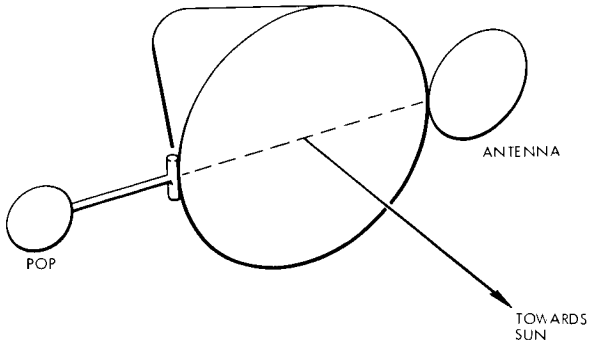


Figure E-4. Orientation of POP and Antenna for Maximum Solar Exposure

Suppose the POP and antenna are deployed such that their major surface areas are in the plane normal to the sun line, as shown in Figure E-4 (α = -90 degrees). Then in terms of body coordinates the following relations can be written:

$$\bar{e}_s \cdot \bar{e}_n = 1$$

$$\bar{e}_s \cdot \bar{e}_t = 0$$

Thus, the force acting on each surface area i facing the sun becomes

$$\bar{F}_{s_i} = -V(1 + \nu_i) A_i \bar{x}_1 \qquad \text{(E. 5)}$$

The above forces are applied at their respective center of pressures. Measured from the nominal center of mass of the spacecraft to the center of pressure of surface i, the vector $\overline{cp_i}$ can be expressed as

$$\overline{cp_i} = d_{x_i}\,\overline{x}_1 + d_{y_i}\,\overline{y}_i + d_{z_i}\,\overline{z}_1 \qquad \text{(E. 6)}$$

where the d's represent distances.

To account for the center of mass offset from the roll axis, a vector $\overline{L}$ is defined as

$$\overline{L} = \ell_y\, y_1 + \ell_z\, z_1 \qquad \text{(E. 7)}$$

where the ℓ's represent offset distances. Hence, the total torque due to solar radiation pressure form surface i can be expressed as

$$\overline{T}_s = \sum_i (\overline{cp_i} - \overline{L}) \times \overline{F}_i \qquad \text{(E. 8)}$$

Substituting Equations (E. 5), (E. 6), (E. 7) into Equation (E. 8) yields the following expression for the solar radiation torque

$$\overline{T}_s = -V \sum_i \left[(1+\nu_i)\, A_i\, (d_{z_i} - \ell_z)\, \overline{y}_1 - (1+\nu_i)\, A_i\, (d_{y_i} - \ell_y)\, \overline{z}_1 \right] \qquad \text{(E. 9)}$$

Equation (E. 9) provides a means for evaluating the solar radiation torque when the antenna and POP are deployed as shown in Figure E-4. Moreover, by setting the respective surface areas to zero, the same equation provides a measure of the solar torques when the antenna and POP are in their stowed positions.

In Figures E-5 and E-6, the magnitude of the solar radiation torques are presented for various deployments of the antenna and POP. (In these figures, the "deployed" positions of the antenna and POP correspond to the orientation of Figure E-4.) To obtain worst-case estimates, the torque calculations were based on a coefficient of reflectivity of unity ($\nu_i = 1$) and a maximum center of mass offset of 3 inches ($|\ell_y| = |\ell_z| =$ 0. 25 foot). It is noted that solar radiation produces the largest torque when the antenna is deployed and the science payload is stowed.

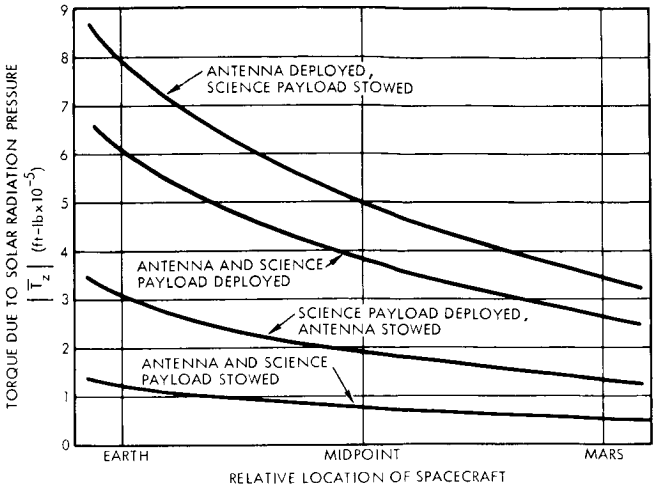


Figure E-5. Solar Radiation Torque for Spacecraft with C. G. Offset Along Y-Axis (ℓ_y = 0.25 ft, ℓ_z = 0, ν_i = 1)

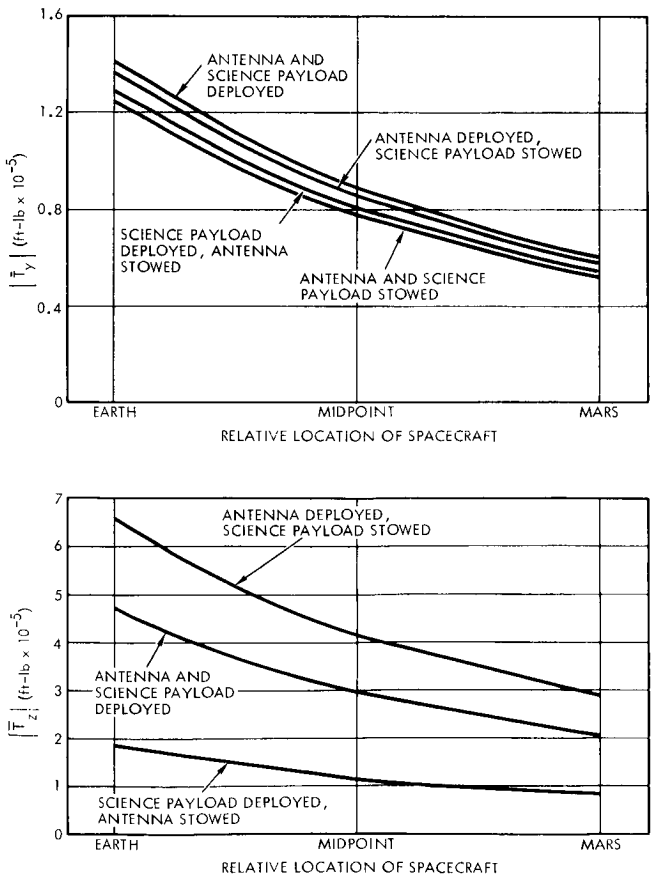


Figure E-6. Solar Radiation Torques for Spacecraft with C. G. Offset Along Z-Axis (ℓ_y = 0, ℓ_z = 0.25 ft, ν_i = 1)

Moreover, it is evident that solar radiation torques are worst when the spacecraft is near the earth. As the spacecraft approaches Mars during transit, the solar torques are reduced since the solar pressure constant V varies inversely as the square of the distance between the sun and the spacecraft.

1.2.2 Gravity Gradient Torques

In this section, torques due to gravity forces are evaluated for the case when the spacecraft orbits Mars. In this case, it is assumed that the main body, POP, and antenna act as a single-rigid body subjected to a gravity force at the center of mass of body 1. Moreover, it is assumed that the body 1 axes corresponds to the principal inertia axes of the spacecraft. When in transit the spacecraft does not experience significant gravitational effects.

Gravity torques depend on the orientation of the spacecraft relative to an orbital reference coordinate system. As indicated in Section 1.1, the body 1 set $(\bar{x}_1, \bar{y}_1, \bar{z}_1)$ is related to the orbital reference set $(\bar{x}_{01}, \bar{y}_{01}, \bar{z}_{01})$ by a direction cosine matrix, i.e.,

$$\begin{bmatrix} \bar{x}_1 \\ \bar{y}_1 \\ \bar{z}_1 \end{bmatrix} = \begin{bmatrix} a_{11} & a_{12} & a_{13} \\ a_{21} & a_{22} & a_{23} \\ a_{31} & a_{32} & a_{33} \end{bmatrix} \begin{bmatrix} \bar{x}_{01} \\ \bar{y}_{01} \\ \bar{z}_{01} \end{bmatrix}$$

where the a_{ij}'s are direction cosines defined in Equation (E. 3).

References E-2 and E-3 present a detailed derivation of the gravity torques on an arbitrary satellite. The results of the derivation provide a means of evaluating gravity gradient torques whose main body components can be expressed as follows:

$$\begin{aligned} T_{gx} &= \frac{3\gamma}{R^3} (I_z - I_y)\, a_{23}\, a_{33} \\ T_{gy} &= \frac{3\gamma}{R^3} (I_x - I_z)\, a_{13}\, a_{33} \\ T_{gz} &= \frac{3\gamma}{R^3} (I_y - I_x)\, a_{13}\, a_{23} \end{aligned} \qquad \text{(E. 10)}$$

where

γ = gravitational constant of Mars (4.29×10^4 km^3/sec^2)

R = distance from center of Mars to spacecraft

I_x, I_y, I_z = principal moments of inertia.

In Figure E-7, the gravity torques are evaluated for the 1971 sample orbit. It is noted that the torques are largest near periapsis (η = 0) and diminish rapidly as the spacecraft approaches its furthest point from Mars.

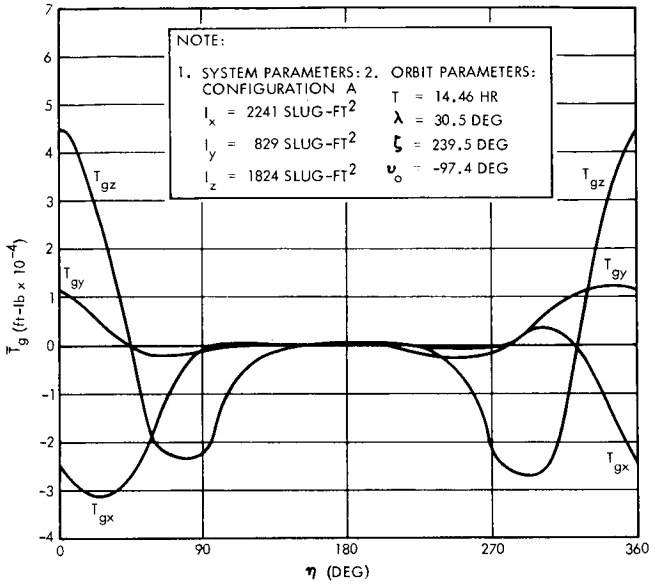


Figure E-7. Gravity Gradient Torques versus True Anomaly (Sample Orbit - 1971 Mission)

1.2.3 Internal Disturbance Torques

The Voyager spacecraft experiences large internal disturbances from two basic sources: 1) tracking motion of the POP; and 2) starting and stopping of the tape recorders, the POP, and the high-gain antenna. The former disturbance is the result of the variable speed at which the POP tracks Mars; the latter disturbance presents impulsive torques to the spacecraft at prescribed intervals during the mission.

a. POP Reaction Torques

As the Voyager spacecraft orbits about Mars, the POP is required to rotate such that its sensor axis points towards Mars. In

this situation, the accelerating motion of the POP results in a net reaction force on the main body of the spacecraft. The expression of the torque due to this reaction force is developed and evaluated for the 1971 sample orbit.

Let $\overline{R}_i$ represent the vector from Mar's center of mass to the center of mass of body i (i = 1, 2). Assuming that only a hinge force $\overline{F}_i$ and a gravity gradient force $\overline{F}_{gi}$ act upon the satellite, Newton's laws can be applied to bodies 1 and 2 to write

$$m_1 \frac{d^2}{dt^2}(\overline{R}_1 - \overline{R}_{01}) + m_1 \frac{d^2}{dt^2}\overline{R}_{01} = \overline{F}_1 + \overline{F}_{g1} \qquad \text{(E. 11)}$$

$$m_2 \frac{d^2}{dt^2}(\overline{R}_2 - \overline{R}_{02}) + m_2 \frac{d^2}{dt^2}\overline{R}_{02} = \overline{F}_2 + \overline{F}_{g2} \qquad \text{(E. 12)}$$

where

$\overline{R}_{0i}$ = vector from Mars' center of mass to body i center of mass when the satellite is in its unforced condition

$\overline{m}_i$ = mass of body i

But

$$\overline{F}_2 = -\overline{F}_1 \qquad \text{(E. 13)}$$

and

$$\overline{R}_2 = \overline{R}_1 + \overline{r}_1 - \overline{r}_2 \qquad \text{(E. 14)}$$

where

$\overline{r}_i$ = vector from body i center of mass to the hinge point.

Substituting relations of Equations (E. 13) and (E. 14) into Equations (E. 11) and (E. 12), and eliminating $d^2\overline{R}_1/dt^2$ between the resulting equations yields

$$F_1\left(\frac{1}{m_1} + \frac{1}{m_2}\right) = -\frac{d^2}{dt^2}(r_1 - r_2) + \left(-\frac{1}{m_1}F_{g1} + \frac{1}{m_2}F_{g2}\right) \qquad \text{(E. 15)}$$

The terms on the right side of Equation (E. 15) will now be evaluated. From Figure E-2, the following vector relations can be written:

$$\bar{r}_1 = \ell_1 \bar{x}_1 + \ell_2 \bar{y}_1 \qquad \text{(E. 16)}$$

$$\bar{r}_2 = -\ell_3 \bar{y}_2 \qquad \text{(E. 17)}$$

where the ℓ's represent distances from the center of mass to the hinge point. The angular velocity of body 1 and body 2 is denoted by ω_1 and ω_2, respectively, and can be written as

$$\bar{\omega}_1 = \omega_{x1} \bar{x}_1 + \omega_{y1} \bar{y}_1 + \omega_{z1} \bar{z}_1 \qquad \text{(E. 18)}$$

$$\bar{\omega}_2 = \omega_{x2} \bar{x}_2 + \omega_{y2} \bar{y}_2 + \omega_{z2} \bar{z}_2 \qquad \text{(E. 19)}$$

Differentiating $\bar{r}_1$ and $\bar{r}_2$ twice with respect to an inertial space yields

$$\frac{d^2 \bar{r}_1}{dt^2} = \frac{d}{dt} (\bar{\omega}_1 \times \bar{r}_1) + \bar{\omega}_1 \times (\bar{\omega}_1 \times \bar{r}_1) \qquad \text{(E. 20)}$$

$$\frac{d^2 \bar{r}_2}{dt^2} = \frac{d}{dt} (\bar{\omega}_2 \times \bar{r}_2) + \bar{\omega}_2 \times (\bar{\omega}_2 \times \bar{r}_2) \qquad \text{(E. 21)}$$

Substituting Equations (E. 16) and (E. 18) into Equation (E. 20) yields $d^2 \bar{r}_1/dt^2$ in body coordinates as

$$\frac{d^2 \bar{r}_1}{dt^2} = \begin{bmatrix} -\dot{\omega}_{z1} \ell_2 + \omega_{y1} \omega_{x1} \ell_2 - \omega_{y1}^2 \ell_1 - \omega_{z1}^2 \ell_1 \\ \dot{\omega}_{z1} \ell_1 - \omega_{x1}^2 \ell_2 + \omega_{x1} \omega_{y1} \ell_1 - \omega_{z1}^2 \ell_2 \\ \dot{\omega}_{x1} \ell_2 - \omega_{y1} \ell_1 + \omega_{x1} \omega_{z1} \ell_1 + \omega_{y1} \omega_{z1} \ell_2 \end{bmatrix} \qquad \text{(E. 22)}$$

A similar expression is derived for $d^2 \bar{r}_2/dt^2$ in body 2 coordinates as

$$\frac{d^2 \bar{r}_2}{dt^2} = \begin{bmatrix} \dot{\omega}_{z2}\, \ell_3 - \omega_{y2}\, \omega_{x2}\, \ell_3 \\ \omega_{x2}^{\ 2}\, \ell_3 + \omega_{z2}^{\ 2}\, \ell_3 \\ -\dot{\omega}_{x2}\, \ell_3 - \omega_{y2}\, \omega_{z2}\, \ell_3 \end{bmatrix}$$

Transforming the above vector in terms of body 1 coordinates through the use of Equation (E. 1) yields

$$\frac{d \bar{r}_2}{dt^2} = \begin{bmatrix} -C\beta\, S\alpha(\dot{\omega}_{z2} - \omega_{y2}\, \omega_{x2})\, \ell_3 + C\alpha(\omega_{x2}^{\ 2} + \omega_{z2}^{\ 2})\, \ell_3 - S\beta\, S\alpha(\dot{\omega}_{x2} + \omega_{y2}\, \omega_{z2})\, \ell_3 \\ -C\beta\, S\alpha(\dot{\omega}_{z2} - \omega_{y2}\, \omega_{x2})\, \ell_3 + C\alpha(\omega_{x2}^{\ 2} + \omega_{z2}^{\ 2})\, \ell_3 - S\beta\, S\alpha(\dot{\omega}_{x2} + \omega_{y2}\, \omega_{z2})\, \ell_3 \\ S\beta\,(\dot{\omega}_{z2} - \omega_{y2}\, \omega_{x2})\, \ell_3 - C\beta\,(\dot{\omega}_{x2} + \omega_{y2}\, \omega_{z2})\, \ell_3 \end{bmatrix} \qquad \text{(E. 23)}$$

The gravitational terms on the right side of Equation (E. 15) are evaluated by making use of Newton's second law and by noting that $\bar{F}_{gi}$ is independent of the body's attitude. Let us define a vector $\bar{V}$ as follows

$$\bar{V} \triangleq \frac{m_1}{\bar{m}} \bar{F}_{g2} - \frac{m_2}{\bar{m}} \bar{F}_{g1} \qquad \text{(E. 24)}$$

where

$$\bar{m} \triangleq \frac{m_1\, m_2}{m_1 + m_2}$$

But the gravity forces on body i can be expressed as

$$\bar{F}_{gi} = \frac{m_i\, \gamma}{R_{oi}^2} \bar{z}_{oi} \qquad (i = 1, 2) \qquad \text{(E. 25)}$$

where γ is the gravitational constant of Mars and $\bar{z}_{oi}$ is a unit vector along the local vertical directed from the center of mass of body i. Substituting Equation (E. 24) into (E. 25) yields

$$\overline{V} = \gamma \overline{m} \left(\frac{1}{R_2^2} \overline{z}_{02} - \frac{1}{R_1^2} \overline{z}_{01} \right)$$

or (E. 26)

$$V = \gamma \overline{m} \left[\left(\frac{1}{R_2} + \frac{1}{R_1} \right) \left(\frac{1}{R_2} - \frac{1}{R_1} \right) \overline{z}_{01} + \frac{1}{R_2^2} (\overline{z}_{02} - \overline{z}_{01}) \right]$$

But forming the dot product of Equation (E. 14) with itself and using the binomial theorem yields

$$\frac{1}{R_2} \cong \frac{1}{R_1} + \frac{1}{R_1^2} \left[\overline{z}_{01} \cdot (\overline{r}_1 - \overline{r}_2) \right]$$

Also from the definition of $\overline{z}_{01}$,

$$\overline{z}_{02} - \overline{z}_{01} = \frac{\overline{R}_1}{R_1} - \frac{\overline{R}_2}{R_2}$$

$$= \frac{-(\overline{r}_1 - \overline{r}_2)}{R_1} + \frac{\left[\overline{z}_{01} \cdot (\overline{r}_1 - \overline{r}_2) \right]}{R_1} \overline{z}_{01}$$

Substituting the above relations into Equation (E. 26), and eliminating higher order terms yields

$$\overline{V} = \frac{\overline{m} \gamma}{R_1^3} \left\{ 3 \left[\overline{z}_{01} \cdot (\overline{r}_1 - \overline{r}_2) \right] \overline{z}_{01} + (\overline{r}_2 - \overline{r}_1) \right\} \qquad \text{(E. 27)}$$

By utilizing the transformation matrix Q_{01} of Equation (E. 2), Equation (E. 27) can be expanded in terms of body 1 coordinates to yield

$$V = \frac{\gamma \overline{m}}{R_1^3} \begin{bmatrix} 3 a_{12}^2 (\ell_1 + \ell_3 C\alpha) + 3 a_{13} a_{23} (\ell_2 - \ell_3 S\alpha) - (\ell_1 + \ell_3 C\alpha) \\ 3 a_{23} a_{13} (\ell_1 + \ell_3 C\alpha) + 3 a_{23}^2 (\ell_2 - \ell_3 S\alpha) - (\ell_2 - \ell_3 S\alpha) \\ 3 a_{33} a_{13} (\ell_1 + \ell_3 C\alpha) + 3 a_{33} a_{23} (\ell_2 - \ell_3 S\alpha) \end{bmatrix} \qquad \text{(E. 28)}$$

From Equations (E. 15) and (E. 24), the reaction force on body 1 can be expressed as

$$\bar{F}_1 = \bar{m}\left[\frac{d^2}{dt^2}\bar{r}_2 - \frac{d^2}{dt^2}\bar{r}_1\right] + \frac{\bar{m}}{m_1 + m_2}\bar{V} \qquad \text{(E. 29)}$$

Substituting Equations (E. 22), (E. 23) and (E. 28) into (E. 29), yields the following components of $\bar{F}_1$ in body 1 coordinates

$$\bar{F}_1 = F_x \bar{x}_1 + F_y \bar{y}_1 + F_z \bar{z}_1 \qquad \text{(E. 30)}$$

where

$$\frac{F_x}{\bar{m}} = -C\beta\, S\alpha(\dot{\omega}_{z2} - \omega_{y2}\omega_{x2})\ell_3 + C\alpha(\omega_{x2}^2 + \omega_{z2}^2)\ell_3 - S\beta\, S\alpha(\dot{\omega}_{x2} + \omega_{y2}\omega_{z2})\ell_3$$

$$+\dot{\omega}_{z1}\ell_2 - \omega_{y1}\omega_{x1}\ell_2 + \omega_{y1}^2\ell_1 + \omega_{z1}^2\ell_1$$

$$+\frac{\gamma}{R_1^3}\cdot\frac{\bar{m}}{m_1+m_2}\left[3\,a_{13}^2(\ell_1 + \ell_3 C\alpha) + 3\,a_{13}a_{23}(\ell_2 - \ell_3 S\alpha) - (\ell_1 + \ell_3 C\alpha)\right]$$

$$\frac{F_y}{\bar{m}} = -C\beta\, C\alpha(\dot{\omega}_{z2} - \omega_{y2}\omega_{x2})\ell_3 - S\alpha(\omega_{x2}^2 + \omega_{z2}^2)\ell_3 - S\beta\, C\alpha(\dot{\omega}_{x2} + \omega_{y2}\omega_{z2})\ell_3$$

$$-\omega_{z1}\ell_1 + \omega_{x1}^2\ell_2 - \omega_{x1}\omega_{y1}\ell_1 + \omega_{z1}^2\ell_2$$

$$+\frac{\gamma}{R_1^3}\cdot\frac{\bar{m}}{m_1+m_2}\left[3\,a_{23}a_{13}(\ell_1 + \ell_3 C\alpha) + 3\,a_{23}^2(\ell_2 - \ell_3 S\alpha) - (\ell_2 - \ell_3 S\alpha)\right]$$

$$\frac{F_z}{\bar{m}} = S\beta(\dot{\omega}_{z2} - \omega_{y2}\omega_{x2})\ell_3 - C\beta(\dot{\omega}_{x2} + \omega_{y2}\omega_{z2})\ell_3$$

$$-\dot{\omega}_{x1}\ell_2 + \dot{\omega}_{y1}\ell_1 - \omega_{x1}\omega_{z1}\ell_1 - \omega_{y1}\omega_{z1}\ell_2$$

$$+\frac{3\gamma}{R_1^3}\cdot\frac{\bar{m}}{m_1+m_2}\left[a_{33}a_{13}(\ell_1 + \ell_3 C\alpha) + a_{33}a_{23}(\ell_2 - \ell_3 S\alpha)\right]$$

Finally, the reaction torque on body 1, $\bar{T}_{r1}$, is given by

$$\bar{T}_r = \bar{r}_1 \times \bar{F}_1$$

which by substitution yields

$$\overline{T}_r = \begin{bmatrix} \ell_2 F_z \\ \ell_1 F_z \\ \ell_1 F_y - \ell_2 F_x \end{bmatrix} \qquad \text{(E. 31)}$$

Equations (E. 30) and (E. 31) describe the body 1 reaction torque in terms of body 1 coordinates. In these equations the angular velocities of the two bodies ($\overline{\omega}_1$, $\overline{\omega}_2$) and the hinge and shaft angles (α, β) are unknown. These kinematic terms will now be specified as a function of orbit position.

The 1971 orbit about Mars is considered to be elliptical with an eccentricity value denoted by e. The location of the spacecraft is an elliptical orbit at a given time t is expressed as follows

$$\left(\frac{2\pi}{T}\right)t = \cos^{-1}\frac{e + C\eta}{1 + eC\eta} - e \sin\left(\cos^{-1}\frac{e + C\eta}{1 + eC\eta}\right) \qquad \text{(E. 32)}$$

where

T = orbital period

η = true anomoly measured from periapsis

The orbit angle ν can be expressed in terms of the true anomoly as

$$\nu = \eta + \nu_o \qquad \text{(E. 33)}$$

where ν_o = angle measured from the ascending node to periapsis.

Differentiating both sides of Equation (E. 32) and noting that $d\nu/dt = d\eta/dt$ yield

$$\frac{d\nu}{dt} = \left(\frac{2\pi}{T}\right)\frac{(1 + eC\eta)^2}{(1 - e^2)^{3/2}} \qquad \text{(E. 34)}$$

Equation (E. 34) provides the magnitude of the angular velocity of the spacecraft as a function of the true anomoly. Thus, the angular velocity of body 1 can be written in Mars centered orbit coordinates (see Figure E-3) as

$$\bar{\omega}_1 = -\frac{d\nu}{dt}\bar{z}_q$$

The above vector can be transformed in terms of body 1 coordinates as

$$\bar{\omega}_1 = \begin{bmatrix} C\zeta & S\zeta & 0 \\ -S\zeta & C\zeta & 0 \\ 0 & 0 & 1 \end{bmatrix} \begin{bmatrix} C\lambda & 0 & S\lambda \\ 0 & 1 & 0 \\ -S\lambda & 0 & C\lambda \end{bmatrix} \begin{bmatrix} 0 \\ 0 \\ -\frac{d\nu}{dt} \end{bmatrix}$$

or (E. 35)

$$\bar{\omega}_1 = \begin{bmatrix} -C\zeta \cdot S\lambda \cdot \frac{d\nu}{dt} \\ S\zeta \cdot S\lambda \cdot \frac{d\nu}{dt} \\ -C\lambda \cdot \frac{d\nu}{dt} \end{bmatrix}$$

Substituting Equation (E. 34) into Equation (E. 35) yields the following components of angular velocity in body 1 coordinates

$$\omega_{x1} = -\frac{\omega_o C\zeta S\lambda}{(1 - e^2)^{3/2}} \cdot (1 + e C\eta)^2$$

$$\omega_{y1} = \frac{\omega_o S\zeta S\lambda}{(1 - e^2)^{3/2}} - (1 + e C\eta)^2 \qquad \text{(E. 36)}$$

$$\omega_{z1} = \frac{-\omega_o C\lambda}{(1 - e^2)^{3/2}} \cdot (1 + e C\eta)^2$$

where

$$\omega_o = \frac{2\pi}{T}$$

The rate of change of $\bar{\omega}_1$ is obtained by differentiating the components of $\bar{\omega}_1$ with respect to ν and noting that

$$\frac{dA}{dt} = \frac{dA}{d\nu} \cdot \frac{d\nu}{dt} \qquad \text{(E. 37)}$$

where A = arbitrary parameter. This results in the following expression

$$\dot{\omega}_{x1} = \frac{2\,\omega_o^2\, e\, C\zeta\, S\lambda}{(1 - e^2)^3} \cdot (1 + e\,C\eta)^3\, S\eta$$

$$\dot{\omega}_{y1} = \frac{-2\,\omega_o^2\, e\, S\zeta\, S\lambda}{(1 - e^2)^3} \cdot (1 + e\,C\eta)^3\, S\eta \qquad \text{(E. 38)}$$

$$\dot{\omega}_{z1} = \frac{2\,\omega_o^2\, e\, C\lambda}{(1 - e^2)^3} \cdot (1 + e\,C\eta)^3\, S\eta$$

The angular velocity of body 2 is simply expressed as

$$\bar{\omega}_2 = \bar{\omega}_1 - \dot{\alpha}\,\bar{z}_1 - \dot{\beta}\,\bar{y}_2$$

Transforming the above vector in terms of body 2 coordinates yields the following components of angular velocity

$$\omega_{x2} = -C\beta\, S\alpha\, \omega_{x1} - C\beta\, C\alpha\, \omega_{y1} + S\beta\,(\omega_{z1} - \dot{\alpha})$$

$$\omega_{y2} = C\alpha\, \omega_{x1} - S\alpha\, \omega_{y1} - \dot{\beta} \qquad \text{(E. 39)}$$

$$\omega_{z2} = S\beta\, S\alpha\, \omega_{x1} + S\beta\, C\alpha\, \omega_{y1} + C\beta\,(\omega_{z1} - \dot{\alpha})$$

Noting that the hinge and shaft angles vary with orbit position, the rate of change of angular velocity of body 2 can be expressed as

$$\dot{\omega}_{x2} = -\dot{\omega}_{x1}\, C\beta\, S\alpha - \omega_{x1}\, \dot{\alpha}\, C\beta\, C\alpha + \omega_{x1}\, \dot{\beta}\, S\beta\, S\alpha - \dot{\omega}_{y1}\, C\beta\, C\alpha + \dot{\alpha}\, \omega_{y1}\, C\beta\, S\alpha$$
$$+ \dot{\beta}\, \omega_{y1}\, S\beta\, C\alpha + S\beta\,(\dot{\omega}_{z1} - \ddot{\alpha}) + \dot{\beta}\, C\beta\,(\omega_{z1} - \dot{\alpha})$$

$$\dot{\omega}_{y2} = \dot{\omega}_{x1}\, C\alpha - \omega_{x1}\, \dot{\alpha}\, S\alpha - \dot{\omega}_{y1}\, S\alpha - \dot{\alpha}\, \omega_{y1}\, C\alpha - \ddot{\beta} \qquad \text{(E. 40)}$$

$$\dot{\omega}_{z2} = \dot{\omega}_{x1}\, S\beta\, S\alpha + \dot{\beta}\, \omega_{x1}\, C\beta\, S\alpha + \dot{\alpha}\, \omega_{x1}\, S\beta\, C\alpha + \dot{\omega}_{y1}\, S\beta\, C\alpha + \dot{\beta}\, \omega_{y1}\, C\beta\, C\alpha$$
$$- \dot{\alpha}\, \omega_{y1}\, S\beta\, S\alpha + C\beta\,(\dot{\omega}_{z1} - \ddot{\alpha}) - \dot{\beta}\, S\beta\,(\omega_{z1} - \dot{\alpha})$$

To determine the hinge and shaft angles as a function of orbit position, it is noted that the local vertical of body 1 and the POP sensor axis are essentially parallel. Thus, in terms of the coordinate sets of Section 2, the following relation can be written

$$\bar{z}_{01} = -\bar{x}_2$$

Transforming the above vectors in terms of body 1 coordinates and equating the components of the two vectors yield

$$S\beta = -S\lambda\, S\nu \tag{E. 41}$$

$$\tan(\alpha - \zeta - \pi) = C\lambda \tan\nu$$

By noting the relationship of Equation (E. 37), the time derivatives of the hinge and shaft angles can be determined

$$\dot{\beta} = -\frac{\omega_o\, S\lambda}{(1 - e^2)^{3/2}} \cdot \frac{(1 + e\, C\eta)^2\, C\nu}{\sqrt{1 - S^2\lambda\, S^2\nu}} \tag{E. 43}$$

$$\ddot{\beta} = \frac{\omega_o^2\, S\lambda}{(1 - e^2)^3} \cdot \frac{(1 + e\, C\eta)^3}{(1 - S^2\lambda\, S^2\nu)^{3/2}} \left[(1 + e\, C\eta)\, S_\nu\, C^2\lambda + 2\, e\, S\eta\, C\nu\, (1 - S^2\lambda\, S^2\nu\right] \tag{E. 44}$$

$$\dot{\alpha} = \frac{\omega_o\, C\lambda}{(1 - e^2)^{3/2}} \cdot \frac{(1 + e\, C\eta)^2}{(C^2\nu + C^2\lambda\, S^2\nu} \tag{E. 45}$$

$$\ddot{\alpha} = \frac{\omega_o^2\, C\lambda}{(1 - e^2)^3} \cdot \frac{(1 + e\, C\eta)^3}{(C^2\nu + C^2\lambda\, S^2\nu)^2} \left[S^2\lambda(1 + e\, C\eta)\, S\, 2\nu - 2\, e\, S\eta (C^2\nu + C^2\lambda\, S^2\nu)\right] \tag{E. 46}$$

For a given orbit, Equations (E. 41) through (E. 46) express the characteristics of the hinge and shaft angle as a function of the orbit abgle, or the true anomoly. These equations along with Equations (E. 36), (E. 38), (E. 39), and (E. 40) provide the necessary relationships to evaluate the reaction torques in Equation (E. 31).

Figure E-8 depicts the reaction torque $\overline{T}_r$ as a function of the true anomoly η. The evaluation of the reaction torque was based on the orbital parameters of the 1971 sample orbit. It is noted that like gravity torques, the reaction torques due to the tracking motion of the POP have peak components near periapsis.

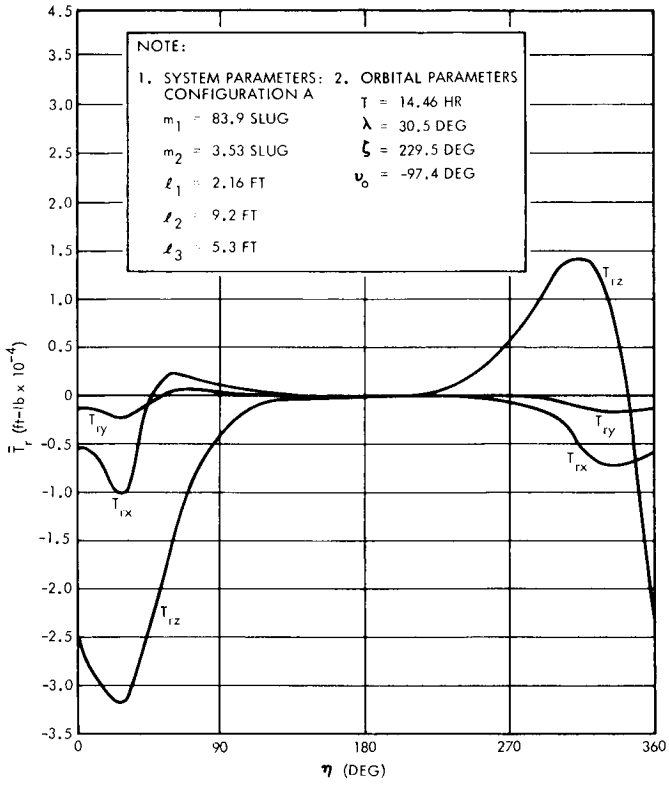


Figure E-8. Reaction Torque versus True Anomoly (Sample Orbit - 1971 Mission)

b. Impulsive Reaction Torques

Impulsive reaction torques are the result of the starting and stopping of the tape recorder, the POP, and the high-gain antenna. The magnitude of the above impulses depend on the load inertia and the characteristics of the motor which drives the rotating component. Based on typical motor characteristics, estimates of the maximum impulse transferred to the spacecraft during the starting or stopping of a rotating component are presented as follows:

POP: $\Delta H_{\text{shaft axis}} = \Delta H_{\text{hinge axis}} \cong 2.6 \times 10^{-5}$ ft-lb-sec

High-Gain Antenna: $\Delta H_{\text{shaft axis}} \cong 2.6 \times 10^{-5}$ ft-lb-sec

$\Delta H_{\text{hinge axis}} \cong 5 \times 10^{-4}$ ft-lb-sec

Tape Recorder: $\Delta H_{\text{spin axis}} = 0.05$ ft-lb-sec

It is evident that the impulses from the tape recorders are more than an order of magnitude larger than those from the POP and antenna.

1.3 Fuel Requirements Due to Disturbance Torques

The purpose of this section is to present calculations which estimate the fuel requirement due to disturbances on the Voyager spacecraft. The results of the calculations are summarized in Table E-1.

During the 6-month transit period, the fuel consumption estimate is based primarily on the effects of solar disturbance torques. In this period, torques due to gravity forces and micrometeorite impacts are relatively small and their effects are neglected. Also, impulses due to the starting and stopping of the tape recorders and antenna are small and do not occur frequently as to affect the fuel requirements.

During the period when the spacecraft is in orbit about Mars, the fuel requirements are based on the effects of solar radiation torques, gravity gradient torques, reaction torques from the POP's tracking motion, and the impulsive torques of the tape recorders over a 6-month period. The orbital parameters of the 1971 sample orbit are assumed to remain constant to provide a conservative estimate of the fuel consumption.

1.3.1 General Considerations

The amount of fuel consumed during a period of time is related to the change in angular momentum by the following relation

$$W_{GC} = \frac{1}{I_{sp}} \left[\frac{\Delta H_x}{\ell_{ex}} + \frac{\Delta H_y}{\ell_{ey}} + \frac{\Delta H_z}{\ell_{ez}} \right] \qquad \text{(E.47)}$$

where

W_{GC} = amount of fuel consumed

I_{sp} = specific impulse of fuel

ℓ_e = effective moment arm of the gas jet system

ΔH = net change in angular momentum

When a disturbance torque $\overline{T}$ acts upon the vehicle for finite time period, there is a buildup of angular momentum $\Delta\overline{H}$ on the spacecraft which can be expressed as

$$\Delta\overline{H} = \int_o^t \left|\overline{T}\right| dt \qquad \text{(E. 48)}$$

where the integration is with respect to inertial space.

Since the orientation of the body axes do not change with respect to the inertial reference set, the net change in angular momentum can be obtained by integrating the body disturbance torques. Thus, the components of $\Delta\overline{H}$ in body coordinates can be determined as

$$\begin{aligned} \Delta H_x &= \int_o^T \left|T_x\right| dt \\ \Delta H_y &= \int_o^T \left|T_y\right| dt \\ \Delta H_z &= \int_o^T \left|T_z\right| dt \end{aligned} \qquad \text{(E. 49)}$$

when T is the period of time the torque acts on the spacecraft. Thus, Equations (E. 46) and (E. 49) provide the necessary relations to estimate the fuel requirements due to disturbance torques.

The remaining sections are devoted to evaluating the fuel requirement for the various sources of disturbances. In estimating the fuel consumed, the following parameters of the cruise control system are assumed

$$\ell_{ex} = \ell_{ey} = \ell_{ez} = 18.4 \text{ ft.}$$

$$I_{sp} = 60 \text{ sec}$$

1.3.2 Solar Radiation Torque

a. Transit Fuel Estimate

A conservative estimate of the torques due to solar radiation pressure was evaluated in Section 1.2.1. For a fixed deployment of the antenna and POP, the solar radiation torque decreases as the spacecraft travels from earth to Mars. Assuming a straight-time variation of the torque with time, the buildup of spacecraft angular momentum during transit can be calculated as follows:

$$\Delta H = \frac{1}{2}\left[(T_s)_{earth} - (T_s)_{Mars}\right]T_p \qquad \text{(E. 50)}$$

where

$\overline{T}_s$ = solar radiation torque

T_p = time period (177 days)

From Section 1.2.1, the worst-case estimates of the solar radiation torque are presented as follows

Earth:

$$\left|\overline{T}_s\right| = \begin{bmatrix} 0 \\ 1.36 \times 10^{-15} \text{ ft-lb} \\ 8.0 \times 10^{-5} \text{ ft-lb} \end{bmatrix}$$

Mars:

$$\left|\overline{T}_s\right| = \begin{bmatrix} 0 \\ 0.58 \times 10^{-5} \text{ ft-lb} \\ 3.5 \times 10^{-5} \text{ ft-lb} \end{bmatrix}$$

The above solar radiation torques were obtained for the worst-case deployment of the antenna and POP and worst-case center of gravity offsets. Substituting the above torque values into Equation (E. 50) yields the following components of angular momentum:

$$\Delta H_x = 0$$

$$\Delta H_y = 148 \text{ ft-lb-sec}$$

$$\Delta H_z = 879 \text{ ft-lb-sec}$$

Thus, solar radiation torques acting upon the spacecraft during the transit period will consume the amount of fuel calculated from Equation (E.47), or

$$W_{GC} = 0.93 \text{ lb}$$

b. Orbital Fuel Estimates

When the spacecraft is orbiting Mars, the magnitude of the solar radiation torque depends on the deployment of the POP and antenna. In general, the solar radiation torque varies with the orbital position of the spacecraft. However, a conservative measure of the fuel requirements can be evaluated by the assuming a constant solar torque during an orbit. Thus, the angular momentum is simply expressed as

$$\Delta \overline{H} = \left| \overline{T}_s \right| \cdot T_p$$

Based on the worst-case solar torques presented in the previous section, the components of the angular momentum buildup for a 6-month orbital period are calculated to be

$$\Delta H_x = 0$$

$$\Delta H_y = 90 \text{ ft-lb-sec}$$

$$\Delta H_z = 544 \text{ ft-lb-sec}$$

The amount of fuel required to neutralize the above momentum buildup is calculated to be

$$W_{GC} = 0.57 \text{ lb}$$

1.3.3 Gravity Gradient Torque

Section 1.2.2 provided a measure of the gravity gradient torques encountered in a sample orbit for the 1971 mission. The gravity gradient

torques were presented as a function of the true anomoly η which is a known function of the time in orbit. The net change in angular momentum per orbit can be estimated by describing absolute magnitude of the gravity gradient torques as a function of time and integrating the torques for a single orbit. The results of these calculations are summarized as follows:

$$\Delta H_x = 1.16 \text{ ft-lb-sec/orbit}$$

$$\Delta H_y = 0.57 \text{ ft-lb-sec/orbit}$$

$$\Delta H_z = 2.71 \text{ ft-lb-sec/orbit}$$

For an orbit period of 6 months ($\sim$300 orbits), the amount of fuel consumed by gravity effects can be calculated from Equation (E. 47) as

$$W_{GC} = 1.21 \text{ lb}$$

1.3.4 Reaction Torques

During the orbit period, the main reaction torques are the result of the tracking motion of the POP and the starting and stopping of the tape recorders. The starting and stopping of the antenna and POP are not considered since their impulsive effects on the spacecraft are much less pronounced and less frequent than that of the tape recorder.

a. POP Motion

The reaction torque due to the POP's motion were presented in Figure E-8. As in the case of gravity torques, the reaction torque can be described as a function of time and integrated to obtain the angular momentum buildup per orbit. The results are summarized as follows

$$\Delta H_x = 0.50 \text{ ft-lb-sec/orbit}$$

$$\Delta H_y = 0.18 \text{ ft-lb-sec/orbit}$$

$$\Delta H_z = 1.56 \text{ ft-lb-sec/orbit}$$

Assuming that the POP tracks Mars during the entire orbit period ($\sim$300 orbits), the gas consumed by the POP's motion can be conservatively estimated as

$$W_{GC} = 0.61 \text{ lb}$$

b. Tape Recorder Impulses

Tape recorders transfer momentum to the spacecraft as it accelerates to or decelerates from a nominal write or playback speed. For every orbit about Mars, one of the two tape recorders on the spacecraft is required to write and to play back. Hence, the spacecraft is subjected to a maximum of four impulses per orbit from each recorder.

Section 1.2.3 specified that each tape recorder will transfer an impulse whose magnitude is less than 0.05 ft-lb-sec. Assuming that the spin axis of the tape recorders are oriented along the $\bar{y}$ and $\bar{z}$ axis, the maximum buildup of momentum per orbit (based on four impulse/orbit) is given by

$$\Delta H_x = 0$$

$$\Delta H_y = 0.2 \text{ ft-lb-sec/orbit}$$

$$\Delta H_z = 0.2 \text{ ft-lb-sec/orbit}$$

where both recorders are assumed to be in operation to obtain worst-case fuel requirements. Thus, for a period of 6 months ($\sim$300 orbits), the gas consumed to neutralize the effects of tape recorder impulses can be calculated from Equation (E.47) to be

$$W_{GC} = 0.11 \text{ lb}$$

The total fuel requirements due to the POP motion and tape recorder impulses is therefore

$$W_{GC} = 0.61 + 0.11$$

$$= 0.72 \text{ lb}$$

2. CONTROL SYSTEM DESIGN ANALYSES

Listed below are the Voyager parameter values utilized for the stabilization and control system (SCS) analyses. Data is given for both Configuration A (Table E-2a) (low-thrust monopropellant midcourse engine,

high-thrust solid rocket deboost engine) and Configuration B (Table E-2b) (liquid bipropellant engine). The reference axes used to define the various system parameters are shown in Figure E-9.

Table E-2a. Configuration A Parameters

Spacecraft Condition	Weight (lb)	Center of Mass Station (in.)	Moment of Inertia, Principal Axis (slug-ft^2) I_x	I_y	I_z	Control Moment Arm, TVC (in.)
Separated Spacecraft	7800	46.6	4778	5772	4058	41.6
Spacecraft Before Capsule Separation	7554	47.5	4697	5699	3989	42.5
Spacecraft After Capsule Separation	5483	26.0	886	1880	2389	14.0
Spacecraft In Orbit	2696	30.2	829	1824	2241	9.8

Table E-2b. Configuration B Parameters

Spacecraft Condition	Weight (lb)	Center of Mass Station (in.)	Moment of Inertia, Principal Axis (slug-ft^2) I_x	I_y	I_z	Control Moment Arm, TVC (in.)
Separated Spacecraft	7800	56.2	4591	4988	4338	30
Spacecraft Before Capsule Separation	7675	56.6	4545	4954	4291	30
Spacecraft After Capsule Separation	5475	35.1	1313	1721	2690	10
Spacecraft In Orbit	2600	35.6	1035	1547	2246	10

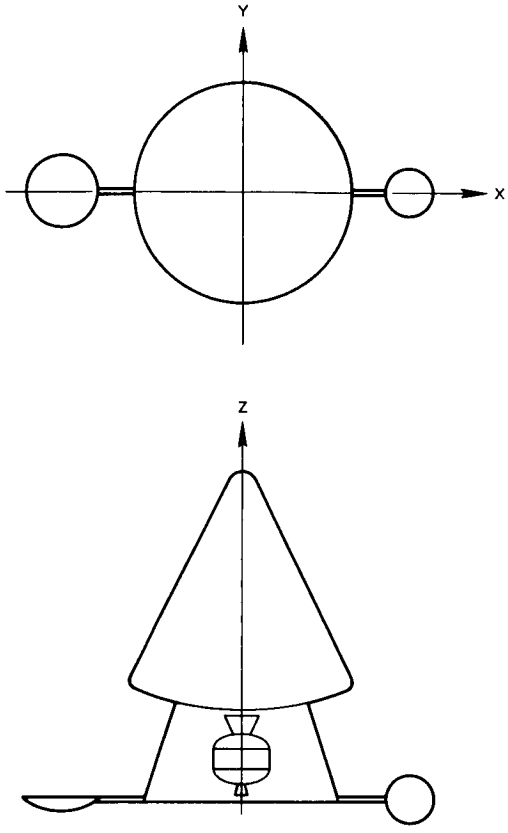


Figure E-9. Voyager Reference Axes

All studies were based on a single axis model of the spacecraft dynamics, consistent with the goals of the preliminary design effort. The analyses are presented for each mode. The vehicle model is defined first, followed by the cruise, acquisition, reorientation and inertial hold, and thrust vector control mode analyses.

The center of gravity data shown in Table E-2a is measured from the field joint (Saturn Station 2048). The thrust level of the monopropellant engine is assumed to be 50 pounds, and the solid rocket engine thrust level varies from 16,000 to 4000 pounds during the first 90 seconds of the 100-second nominal burn time. The bipropellant engine thrust level is assumed to be 1000 pounds. The cold gas jet system used for the cruise mode has a 0.044-pound thrust level.

2.1 Cruise Mode

This section describes an analysis of the SCS cruise mode which is used for attitude stabilization during transit to Mars and while in orbit about Mars. The selected configuration employs cruise sun sensors, a Canopus sensor and derived rate feedback around an on-off electronic switching amplifier.

The on-off electronic switching amplifier is described by a threshold of ±0.5 degree during normal operation and ±0.25 degree during POP imaging and an intentional hysteresis of 0.1 degree. The derived rate feedback filter consists of a 100 second time constant and a gain of 240 deg/ft-lb.

Initial sizing studies and duty cycle calculations (with and without disturbance torques) are presented. Results of the study indicate the following:

- The disturbance free fuel consumption is approximately 6 pounds
- The cruise mode limit cycle rate variation is from 0.7 to 5.2 deg/hr
- Satisfactory limit cycle characteristics are achieved even in the presence of worst-case disturbance torques.

A block diagram of a single-axis of the selected configuration is shown in Figure E-10.

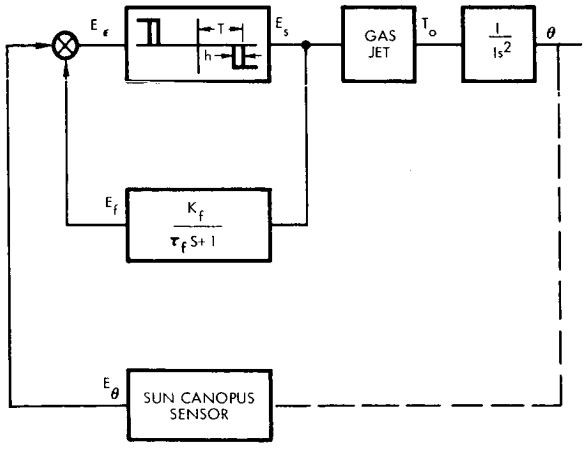


Figure E-10. Block Diagram of a Single Axis of the Selected Configuration

where

E_s = Switching amplifiers output voltage

E_f = High-gain filter output

E_θ = Sun/Canopus sensor output

E_ϵ = Switching amplifier error input

T = Switching amplifier threshold

K_f = Filter gain

τ = Filter time constant

T_o = Gas jet torque output

θ = Spacecraft attitude

h = Switching amplifier hysteresis

The attitude control configuration shown in Figure E-10 has been extensively studied in the past and is commonly called the derived rate system. The design criteria which were employed to define the system parameters are:

- A nominal limit cycle amplitude of ± 0.5 degree
- A nominal limit cycle firing time of 0.05 second
- A nominal limit cycle rate before capsule separation of 1 deg/hr
- A maximum limit cycle rate less than 20.6 deg/hr (based on POP imaging requirements).

The nominal limit cycle characteristics are shown in the phase plane plots of Figures E-11 and E-12. For an initial rate of 18 deg/hr, the cruise mode limit cycle acquisition is illustrated in Figure E-11 for a 5000 slug-ft^2 moment of inertia (representative of the spacecraft prior to capsule separation). Figure E-12 shows the cruise mode acquisition after capsule separation from an initial rate of 22 deg/hr and indicates the higher limit cycle rate due to the reduced moment of inertia.

The maximum transit limit cycle rate (before capsule separation), $\dot{\theta}_{T\,max}$, specified above (1 deg/hr) is given in Equation (E.50) as

$$\dot{\theta}_{T\,max} = \frac{\ddot{\theta}_T \times t_{on}}{2} = 1 \text{ deg/hr} \qquad \text{(E.50)}$$

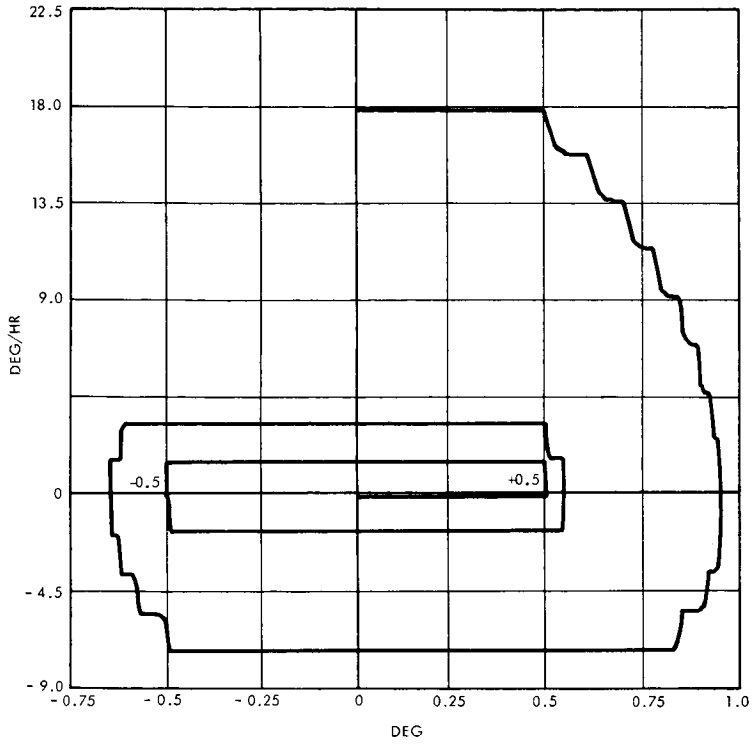


Figure E-11. Typical Limit Cycle Acquisition Prior to Capsule Separation

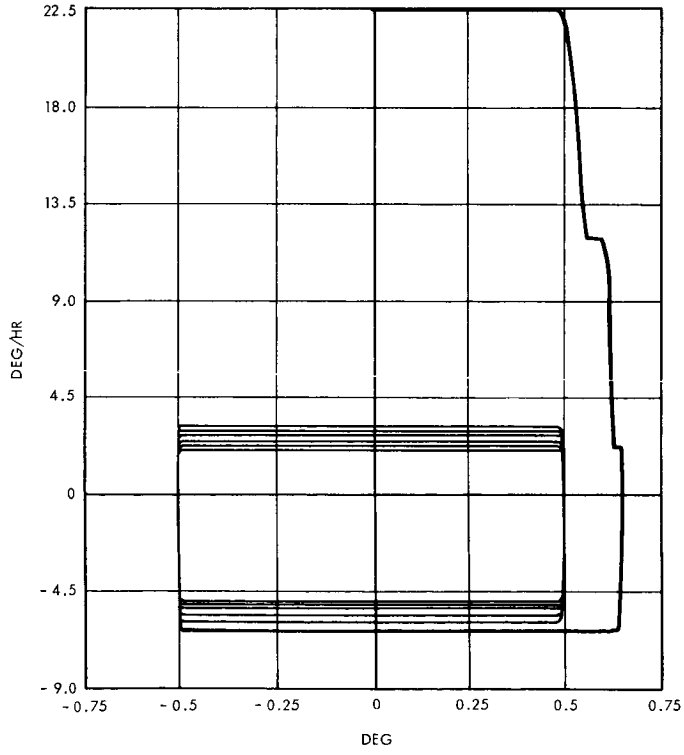


Figure E-12. Typical Limit Cycle Acquisition After Capsule Separation

where $\ddot{\theta}_T$ = spacecraft angular acceleration

t_{on} = limit cycle firing time = 0.05 sec

From Equation (E. 50), the spacecraft angular acceleration can be computed as

$$\ddot{\theta}_T = 0.0111 \text{ deg/sec}^2 = 0.194 \times 10^{-3} \text{ rad/sec}^2 \qquad \text{(E. 51)}$$

The corresponding torque required is given as

$$T = I_{min} \ddot{\theta}_T = 0.83 \text{ lb-ft} \qquad \text{(E. 52)}$$

where I_{min} = minimum transit moment of inertia before capsule separation.

The corresponding jet thrust per nozzle may be computed from the spacecraft geometry. A value of 0.044 pound was computed.

It is considered desirable to maintain a constant thrust level and firing time for all axes of the attitude stabilization system. Consequently, since the moments of inertia vary from transit to orbit due to midcourse and retropropellant firings and capsule separation, the limit cycle rates vary.

Based on in-orbit inertias, the maximum limit cycle rate during orbit, $\dot{\theta}_{max}$, may be computed as

$$\dot{\theta}_{max} = 5.2 \text{ deg/hr} \qquad \text{(E. 53)}$$

which is well below the 20.6 deg/hr maximum angular rate requirement for the planet-oriented science payload.

2.1.1 Duty Cycle Characteristics

In the absence of disturbance torques, etc., the duty cycle characteristics during transit and while in orbit are given on the following page.

a. Transit

For a 1 deg/hr maximum limit cycle rate and a ±0.5 degree threshold, the duty cycle per jet may be computed as

$$1 \frac{\text{pulse}}{\text{hr}} \times \frac{24 \text{ hr}}{\text{day}} \times \frac{177 \text{ days}}{\text{transit}} = 4250 \frac{\text{pulses}}{\text{jet}} \qquad \text{(E. 54)}$$

Since there are three control axes and two jets per axis, the maximum number of pulses is 25,500. For a firing time of 0.05 second per pulse, the total firing time is 1275 seconds. Based on a specific impulse for nitrogen of 60 seconds, the total fuel weight during transit can be computed as

$$\text{Transit fuel weight} = \frac{0.044 \text{ lb thrust} \times 1275 \text{ sec}}{60 \text{ sec}} = 0.935 \text{ lb} \qquad \text{(E. 55)}$$

b. Orbit

An orbit lifetime of 6 months is assumed for the fuel weight computed below. Based on a maximum limit cycle rate of 5.2 deg/hr and a ±0.5 degree threshold, the total firing time is 6630 seconds. The resulting fuel weight is 4.85 pounds.

Combining the results given above, the total fuel weight is approximately 6 pounds. Although the calculations were based on a nominal limit cycle amplitude of ±0.5 degree, which is reduced to ±0.25 degree during POP imaging, the results are considered quite conservative since maximum limit cycle rates were assumed during transit and orbit and POP imaging occurs during a small percentage of the total mission time.

2.1.2 Switching Amplifier and Filter Selection

Figure E-13 shows the switching amplifier and filter network portion of the block diagram of Figure E-10.

From the previous discussion, the following parameter values were given:

T = switching amplifier threshold = 0.5 deg

t_{on} = limit cycle firing time = 0.05 sec

T_o = gas jet torque output = 0.83 lb-ft

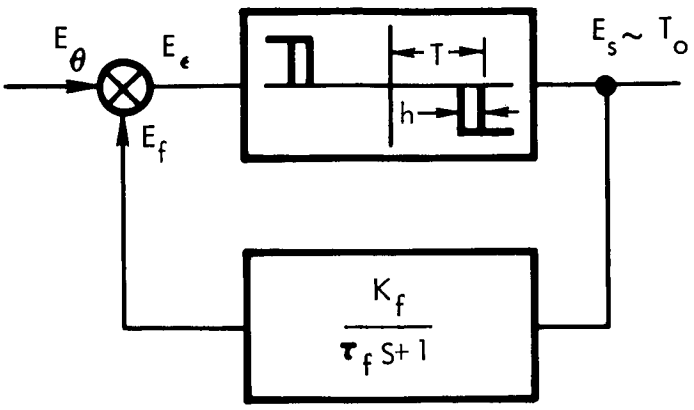


Figure E-13. Switching Amplifier and Filter Network Block Diagram

Selection of the filter time constant τ is based on the following requirements:

a) $\tau \gg 0.05$ sec (t_{on})

b) $\tau \ll t_{off}$ where t_{off} = limit cycle off time = 700 sec minimum

Requirement a) is necessary to generate an accurate "derived rate" signal since the switching amplifier output is proportional to the spacecraft angular acceleration ($\ddot{\theta}$). Requirement b) is necessary to insure that the filter output voltage (E_f) is essentially zero when firing is to occur. The filter time constant selected is $\tau_f = 100$ seconds. Based on a hysteresis (h) of 0.1 degree, the filter gain (K_f) can be computed as

$$h = 0.1 \text{ deg} = (T_o)\left(\frac{K_f}{\tau}\right)(t_{on}) = (0.83 \text{ lb-ft})\left(\frac{K_f}{100}\right)(0.05) \qquad \text{(E.56)}$$

or

$$K_f = 240 \text{ deg/ft-lb}$$

The manner in which the error signal varies during the limit cycle was also investigated to determine the margin which prevents a second firing because of noise disturbances. Since the smallest margin occurs with the lowest limit cycle rate, this situation was studied and a time history of the error signal for part of the limit cycle is shown in Figure E-14 for a hysteresis value of 0.1 degree. As shown in the figure, a minimum firing margin of approximately 0.07 degree exists for a 0.1 degree hysteresis level.

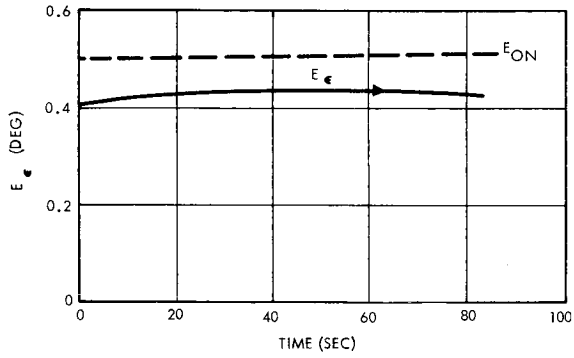


Figure E-14. Error Signal Time History During Limit Cycle

2.1.3 Disturbance Torque Effects

Section 1 of this appendix presents a detailed analysis of the various disturbance torques. Since solar radiation torque was shown to increase fuel consumption greater than any other disturbance torque, its effect on the normal cruise mode limit cycle characteristics was studied. For a constant solar disturbance torque, the spacecraft attitude is given by

$$\theta = \frac{1}{2}\frac{T_D}{I}t^2 - \dot{\theta}_{1c}t + \theta_s \qquad \text{(E.57)}$$

where

t = seconds after limit cycle switching

$\dot{\theta}_{1c}$ = limit cycle rate

θ_s = switching attitude (± 0.5 deg)

T_D = solar disturbance torque.

A typical limit cycle with solar torque is shown in Figure E-15.

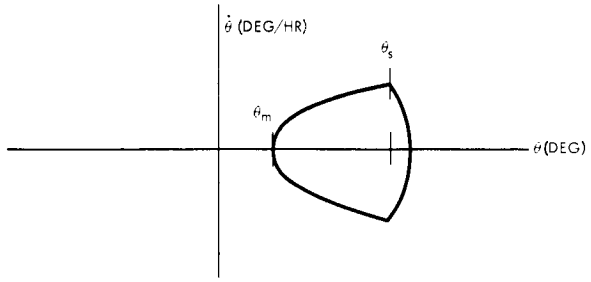


Figure E-15. Typical Limit Cycle with Torque Disturbance

The time to traverse from θ_s to θ_m and back to θ_s can be computed from Equation (E. 58) by setting $\theta = \theta_s$. Based on the maximum effective solar disturbance torque (3.5×10^{-5} ft-lb in orbit), the limit cycle period (t_{1c}) is

$$t_{1c} = \frac{2\,\dot{\theta}_{1c}\, I_{min}}{T_D} = 1200 \text{ sec} \qquad \text{(E. 58)}$$

Since $\theta = \theta_m$ when $t = \frac{t_{1c}}{2}$, the corresponding angular change ($\theta_s - \theta_m$) is

$$\theta_s - \theta_m = \frac{1}{2} \frac{I\,\dot{\theta}_{1c}^{\,2}}{T_D} = 0.42 \text{ deg} \qquad \text{(E. 59)}$$

which indicates a limit cycle which fires on one side only as shown in Figure E-14. Since the undisturbed limit cycle results in a pulse each 720 seconds ($\dot{\theta}_{1c}$ = 5.2 deg/hr, T = 0.5 deg), the total duty cycle and actual fuel consumption are seen to be reduced by this amplitude disturbance torque.

An analog computer simulation of the normal cruise mode configuration was run to verify the analysis presented above and to further investigate the effects of disturbance torques. Figures E-16 and E-17 show the limit cycle characteristics for various disturbance torque levels, moment of inertia values and initial attitude errors and error rates and verifies the above analysis.

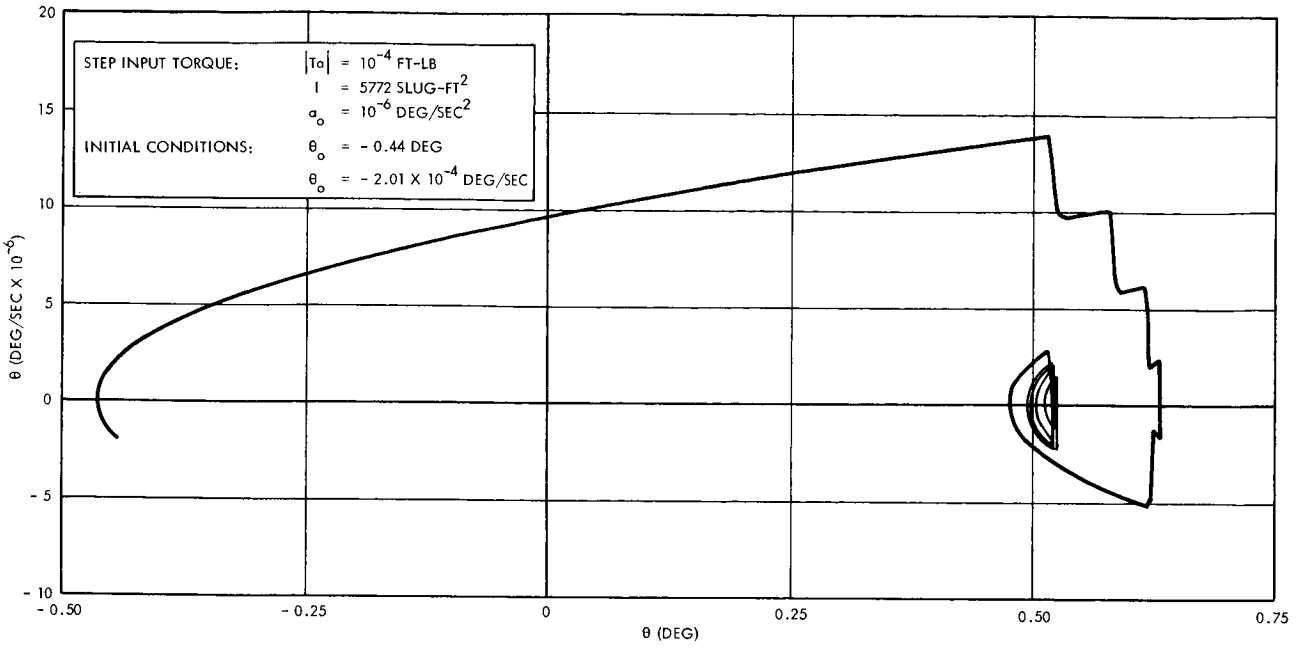


Figure E-16. Limit Cycle Characteristics for $T_D = 10^{-4}$ ft-lb and I = 5772 slug-ft^2

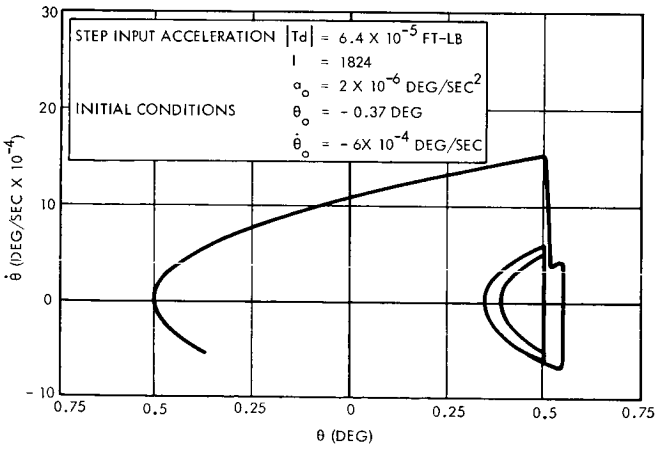


Figure E-17. Limit Cycle Characteristics for $T_D = 6.4 \times 10^{-5}$ ft-lb and I = 1824 slug-ft^2

2.2 Acquisition Mode

This section describes an analysis of the acquisition performance of the stabilization and control system. The results of the analyses have been substantiated by a single axis analog computer simulation which is discussed at the end of this appendix.

The normal operating acquisition configuration employs angular rate signals obtained from rate gyros and position feedback obtained from sun and Canopus sensors. The gas jets, electronic switching amplifiers and derived rate filters are the same devices used in the cruise mode attitude control system. The results of the study show:

- Sun acquisition may take as long as 20 minutes
- Canopus acquisition may take as long as 60 minutes
- Total fuel consumed for an initial acquisition, four midcourse correction acquisitions, acquisition after separation of the flight capsule and an acquisition after deboost is less than 1.343 pounds
- These values can readily be changed by selecting different nominal coasting rates

The results are based on nominal searching rates of 0.2 deg/sec in yaw and pitch and 0.1 deg/sec in roll. Initial rates are assumed as high as 3 deg/sec about each axis for initial acquisition and acquisition after separation of the flight capsule.

The backup configurations present methods for performing sun acquisition without rate gyro information. These modes guard against the possibility of a gyro failure. The acquisition schemes studied proved inferior to the normal operating configuration and cannot be considered alternatives to that design unless the sun sensor characteristics are changed. The results of this study show:

a) The derived rate feedback can provide backup acquisition capability in case of a gyro failure. However, acquisition using the backup mode cannot be assured for all possible combinations of initial rates and attitude errors.

b) The backup acquisition can be considerably improved by extending the derived rate limit from 10 to 50 degrees.

c) Acquisition can be further improved by decreasing the derived rate feedback gain during acquisition.

d) An alternative change to b) and c) is to add a lead-lag network to the output of the sun sensor.

e) Since the coarse sun sensor output saturates for large error signals (see Figure E-18), no rate information is available in the saturated region. Backup acquisition performance could be greatly improved by providing a sun sensor characteristic with a monotonically increasing signal between $\pm$180 degrees. However, since this sun sensor characteristic may degrade the normal sun acquisition performance, detailed tradeoff studies are required to select the optimum sun sensor characteristic.

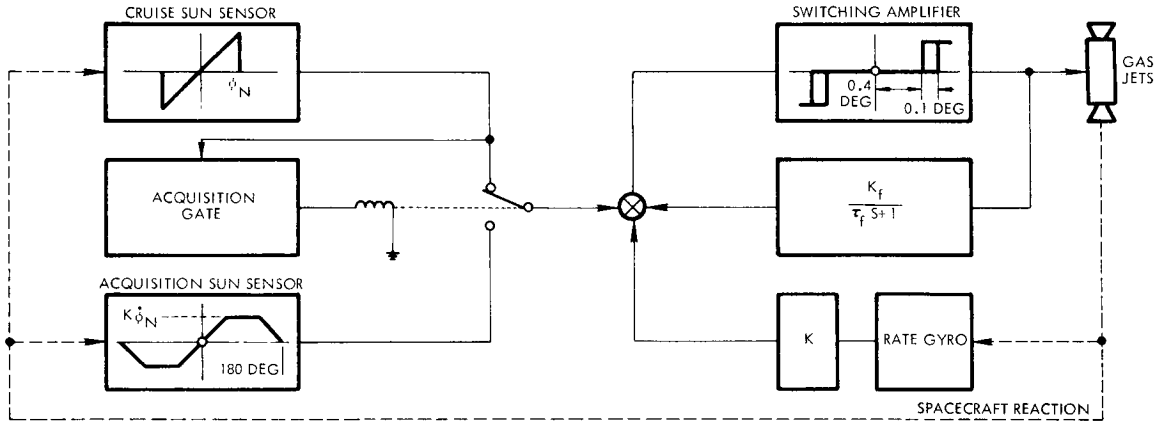


Figure E-18. Yaw or Pitch Sun Acquisition Mode

2.2.1 Normal Acquisition Configuration

The acquisition function is to establish the proper satellite attitude at the beginning of the Mars trajectory, after midcourse maneuvers, capsule separation and deboost. Control is then transferred to the cruise mode for maintenance of this attitude. A saturating output characteristic is provided for the coarse sun sensor to give a controlled slewing rate for large attitude errors. A block diagram for the pitch/yaw channel is shown in Figure E-18 and the roll channel is shown in Figure E-19.

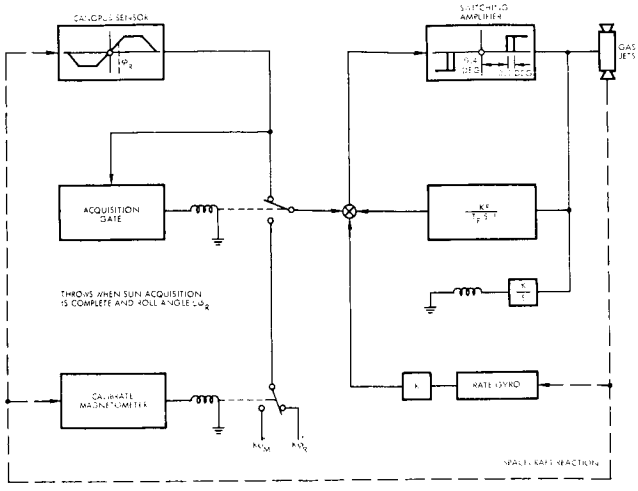


Figure E-19. Roll Canopus Acquisition Mode

2.2.2 Sequence of Operations

The sequence of operations performed for acquisition is enumerated below:

a) If the angular turning rates in pitch and yaw are greater than a nominal rate, $\dot{\phi}_N$ (0.2 deg/sec), the gas jets are turned on to reduce these rates to the desired values. The sign of $\dot{\phi}_N$ is determined by the coarse sun sensor so that the desired attitude will be attained in less than a 180 degree turn about each axis once $\dot{\phi}_N$ has been attained. The roll angular turning rate is driven to zero. These initial angular turning rates may be as large as 3 deg/sec.

b) The pitch and yaw channels continue at this rate ($\dot{\phi}_N$) until the angular pointing error of the individual channel becomes less than a nominal angle ϕ_N (~2 deg).

c) At this point, the coarse sun sensor output is disconnected and the fine sun sensor is switched in for fine pointing control. The rate and position feedback are now linear elements and the yaw and pitch channels are driven so that the pointing errors are within the $\pm$ 0.5 degree deadband of the switching amplifier. $\dot{\phi}_N$ may be selected to approximate a deadbeat response. Sometime during this phase, the roll angular rate error signal is biased to produce a roll rate of 0.22 deg/sec for calibration of the magnetometer.

d) After sun acquisition is completed, the Canopus sensor is turned on and Canopus acquisition begins.

e) The roll rate is reduced to 0.1 deg/sec and this rate is continued until a star within the magnitude range of Canopus comes into the Canopus sensor field of view.

f) When the Canopus sensor indicates lock onto a star, the roll rate bias is removed, and deceleration occurs in the roll channel until the rate approaches zero. The time of this switching may be selected to approximate a deadbeat response.

g) Acquisition of Canopus results in removal of the roll search command and turn off of the gyros by internal command. The system then switches into the cruise mode.

h) Following a midcourse maneuver, the initial rates are approximately zero but the attitude is probably incorrect. The pitch and yaw rates are raised to 0.2 deg/sec and acquisition is accomplished following steps b) through g).

i) After the flight capsule has been separated from the spacecraft, acquisition is again performed to give the proper satellite orientation. The initial angular rates may once again be as high as 3 deg/sec.

j) After spacecraft deboost, acquisition is once again performed following steps a) through g). The initial angular rates are assumed nearly zero.

2.2.3 Design Considerations

The following factors must be considered in the design of the acquisition system.

a. Fuel Consumption

Acquisition should attempt to minimize the fuel consumed. If the loss of efficiency due to initial cross-coupling terms, terminal overshoots and limit cycling is assumed negligible, the amount of fuel consumed can be directly related to the change in satellite momentum by the following relations:

$$\text{fuel} = \int_0^T \frac{|\text{thrust}|}{\text{specific impulse}}\, dt \qquad \text{(E.60)}$$

$$\int_0^T |\text{torque}|\, dt = \int_0^T \left|\frac{d}{dt}\,\text{momentum}\right| dt \qquad \text{(E.61)}$$

$$\text{torque} = 2 \times \text{thrust} \times \text{moment arm} \tag{E.62}$$

$$\text{momentum} = (\text{inertia})\,(\text{angular rate}) \tag{E.63}$$

If we consider the above integration only where thrust $\neq 0$, T is the thrusting time and assume all parameters (thrust level, moment arm, inertia, specific impulse) are constant, the above equations reduce to:

$$\text{fuel} = \frac{\dot{\phi} \times \text{inertia}}{2 \times \text{moment arm} \times \text{specific impulse}} \tag{E.64}$$

where $\dot{\phi}$ is the integral of the absolute value of the changes in angular rate. For the Voyager mission, the following parameter values are assumed:

Thrust = 0.044 lb

Moment arm = 8.55 ft

Specific impulse = 60 sec

Single axis inertia $\sim$5000 slug-ft^2 initially

1800 slug-ft^2 after flight capsule separation

1500 slug-ft^2 after deboost

During the initial and post capsule separation acquisitions, the initial rates may be as high as 3 deg/sec. This rate is reduced to $\dot{\phi}_N$. As $\dot{\phi}_N$ may be of the opposite sign of the initial rate, the rate change may be 3 deg/sec + $\dot{\phi}_N$. This rate must then be brought to zero. During other acquisitions, the initial rate is assumed near zero and the thruster must raise the rate to $\dot{\phi}_N$ and then reduce it to zero. Roll axis acquisition is identical to a pitch or yaw axis acquisition except that the magnetometer is calibrated only during initial acquisition. Define $\dot{\phi}_R$ as the roll search rate and $\dot{\phi}_M$ as the magnetometer calibration rate. The equation for total fuel consumption then is

$$\text{fuel} = 0.9 + (0.5 + 0.3\,N)\dot{\phi}_N + (0.10 + 15N)\dot{\phi}_R + 0.5\,\dot{\phi}_M \tag{E.65}$$

If we assume $\dot{\phi}_N = 0.2$ deg/sec, $\dot{\phi}_R = 0.1$ deg/sec, $\dot{\phi}_M = 0.22$ deg/sec and N = 4, we get

$$\text{fuel} = 1.343 \text{ lb} \tag{E.66}$$

It should be noted that the dominant factor in fuel consumption is the reduction of the initial rates (0.9 lb). The coasting rates have relatively little contribution for values around 0.2 deg/sec.

b. Acquisition Time

A reasonable estimate of acquisition time must be found in order to size the battery. Sun acquisition is the time spent in thrusting to the search rate ($\dot{\phi}_N$) plus the time spent coasting at the rate $\dot{\phi}_N$ and decelerating to zero rate. The longest possible thrusting time for initial acquisition is the time it takes to decelerate from 3 deg/sec to 0 and then to $\dot{\phi}_N$ and then back to 0. The acceleration is the torque (0.83 ft-lb) divided by the inertia (about 5000 slug-ft^2). This gives a thrusting time of $t \sim 300 + 200|\dot{\phi}_N|$ (in seconds).

The maximum possible coasting time occurs when the satellite coasts for 180 degrees (the sign of $\dot{\phi}_N$ is selected so coasting will always be $\leq$ 180 degrees). This gives a maximum coasting time of $180/|\dot{\phi}_N|$. The total initial sun acquisition time is then given as

$$\text{time} = 300 + 200|\dot{\phi}_N| + 180/|\dot{\phi}_N| \tag{E.67}$$

For $|\dot{\phi}_N| = 0.2$ deg/sec, the time is approximately 20 minutes. Note that for this value of $|\dot{\phi}_N|$, the coasting time is the principle factor in sun acquisition time.

The roll acquisition consists of the time it takes to decelerate from $\dot{\phi}_M$ deg/sec to $\dot{\phi}_R$ plus the coasting time to find Canopus plus the time to acquire Canopus (decelerate from $\dot{\phi}_R$). The satellite may be required to coast a full 360 degrees to find Canopus, giving a maximum roll acquisition time of approximately 60 minutes (practically all this time is spent coasting).

The sun acquisition after a midcourse maneuver requires acceleration to $\dot{\phi}_N$ plus the time to coast at most 180 degrees at this rate plus the time to decelerate to 0 deg/sec. The total time is about 15 minutes.

The sun acquisition near the end of flight will require less acceleration time than initial acquisition due to the smaller inertias. The acceleration time will be changed by the ratio of the inertias, giving a time of 91.2 seconds. The coast time will remain constant, giving a total sun acquisition time of about 17 minutes. The Canopus acquisition time will again primarily be used up in coast or about 60 minutes.

c. Sun Acquisition Parameter Study

The sun acquisition scheme should be designed so that fuel consumption, time and the hardware requirements are minimized and an acceptable terminal state is established for transition into the cruise mode. The cruise mode has a nominal limit cycle amplitude of $\pm$ 0.5 degrees and a rate of 1 deg/hr. It is desirable to have a rate feedback gain sufficiently high to reduce rates to values approaching this limit cycle rate when the position error is reduced to an acceptable value. Increasing the rate feedback gain, however, increases the gyro noise sensitivity and increases the acquisition time in the case that the rate is much less than the nominal $\dot{\phi}_N$ (0.2 deg/sec) when the pointing error is $\dot{\phi}_N$ (2 degrees).

One of the schemes that received attention incorporated a coarse sun sensor characteristic with a constant output for commanding slewing and a deadzone which bracketed the fine sun sensor operating range. The phase plane switching lines for this configuration are shown in Figure E-20, for a gain value K of 500 seconds.

With K set at 500 seconds, the following characteristics were found.

a) The biased rate will be followed within the deadzone of the torques or within 0.001 deg/sec.

b) If the angular velocity is $\dot{\phi}_N$ at 2 degrees pointing error, the design shown gives an essentially deadbeat response

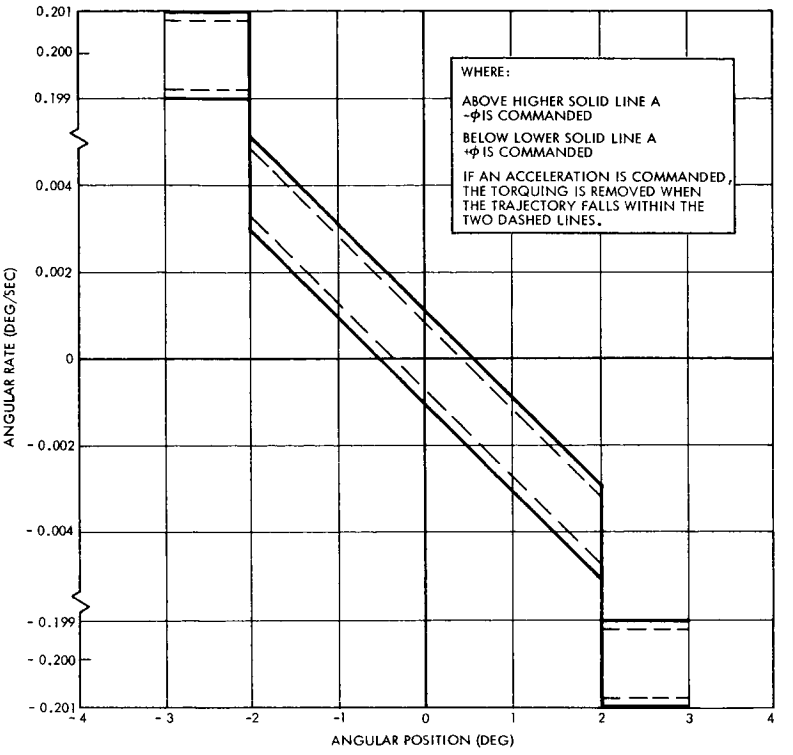


Figure E-20. Switching Lines for a Pitch or Yaw Acquisition Control Channel

with the rate and pointing error going approximately to zero at the same time. The time it takes to decelerate from $\dot{\phi}_N$ is $\sim$100 $\dot{\phi}_N$. If $\dot{\phi}_N$ is 0.2 deg/sec, this becomes 20 seconds. In some unlikely acquisition cases, the rate at 2 degrees will not be $\dot{\phi}_N$ but rather lower. Lower initial rates will give settling times approaching 500 seconds. However, this condition cannot occur during the same acquisition phase that consumed 15 minutes of coasting time as, if the satellite coasts, it will assume the $\dot{\phi}_N$ rate. This additional acquisition time can then be ignored.

c) The deadzone of the torquer will also allow a rate as high as 0.001 deg/sec when cruise is initiated. This is higher than the nominal limit cycle rate of 0.0003 deg/sec and must be damped out in the cruise mode.

d. Canopus Acquisition Parameter Study

The roll channel acquisition is much the same as the pitch and yaw channels except for the changes necessary to accommodate the different characteristics of the Canopus sensor. The Canopus sensor has a roll field of view of just 4 degrees, preventing knowledge of which size

the roll channel rate bias should be to insure no more than a 180 degree rotation (hence the potential 360 degree rotation). Because of the lower nominal torquing rate of 0.1 deg/sec, the Canopus sensor need only have a linear field of view of $\pm$ 0.5 degree and saturation beyond this point (which yields a deadbeat response for a 0.01 deg/sec^2 torquing rate with a response time of 10 seconds). A rate feedback gain of 500 seconds is selected for the same reasons given above.

e. Cross Coupling

In the preceding discussion, the effects of inertia cross-coupling have been neglected. The following is a justification for this assumption. If ω_x, ω_y, and ω_z represent the projections of the body angular rates $\bar{\omega}$ on the spacecraft principal x, y, z axes respectively, and if I_x, I_y, and I_z are the corresponding moments of inertia, the dynamical equations are of the conventional Eulerian form shown below:

$$\begin{aligned} I_x \dot{\omega}_x &= (I_y - I_z)\, \omega_y\, \omega_z + T_x \\ I_y \dot{\omega}_y &= (I_z - I_x)\, \omega_z\, \omega_x + T_y \\ I_z \dot{\omega}_z &= (I_x - I_y)\, \omega_x\, \omega_y + T_z \end{aligned} \qquad \text{(E.68)}$$

where T_x, T_y, and T_z are the control torques along the axis in question. The generalized momentum of the above is:

$$M = \sqrt{\left(I_x \omega_x\right)^2 + \left(I_y \omega_y\right)^2 + \left(I_z \omega_z\right)^2} \qquad \text{(E.69)}$$

and

$$\dot{M} = \left(I_x \omega_x T_x + I_y \omega_y T_y + I_z \omega T_z\right) / M \qquad \text{(E.70)}$$

From Equations (E.69) and (E.70) it can be seen that M is always positive and if T_i is proportional to $-\mathrm{sgn}(\omega_i)$, $\dot{M}$ is always negative. This establishes a Lyapunov function, demonstrating asymptotic stability in the large for such a control system. It can also be seen that the total

momentum is reduced in proportion to the momentum reduction that would be made if the three axes were considered as separate, uncoupled control systems obeying the laws:

$$I_x \dot{\omega}_x = T_x$$

$$I_y \dot{\omega}_y = T_y$$

$$I_z \dot{\omega}_y = T_z \qquad \text{(E.71)}$$

and still considered the total momentum

$$\sqrt{\left(I_x \omega_x\right)^2 + \left(I_y \omega_y\right)^2 + \left(I_z \omega_z\right)^2} \qquad \text{(E.72)}$$

It can then be concluded that the Eulerian coupling can be ignored when making calculations for the effect of control torques on momentum removal if only rate feedback terms are used. If T_x and T_y control laws are biased by a small $\dot{\phi}_N$, the above conclusions still essentially hold until the attitude is within ϕ_N of the correct attitude. The attitude control merely provides a rate bias until then with the rate feedback providing the only actual stabilization. The cross-coupling can then be ignored before the attitude comes to within ϕ_N of the final value and with $\dot{\phi}_N$ sufficiently small, they can certainly be ignored afterwards.

2.2.4 Analog Simulation Results

Sun acquisitions for various initial conditions and inertias were simulated on the analog computer and the results agreed with the analysis to within the noise region of the simulation. The primary differences lay in the switching point. The simulation as scaled could not attain a repeatable switching point with accuracy greater than $\pm$ 20 percent. This has little effect on fuel consumption but does lengthen the acquisition time. Sample acquisitions are shown in Figures E-21 through E-24 showing acquisitions respectively for: 180 degree attitude error, no rate, high inertia; no attitude error, 3 deg/sec, high inertia; 180 degree attitude error, no rate, low inertia no attitude error, 3 deg/sec, low inertia.

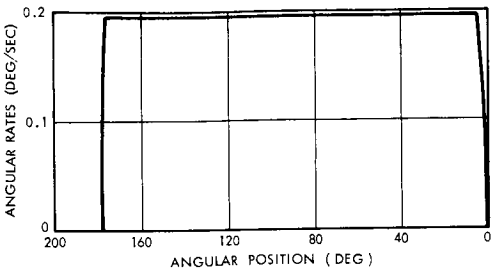


Figure E-21. Initial Sun Acquisition with Initial Rate and 180-degree Position Error

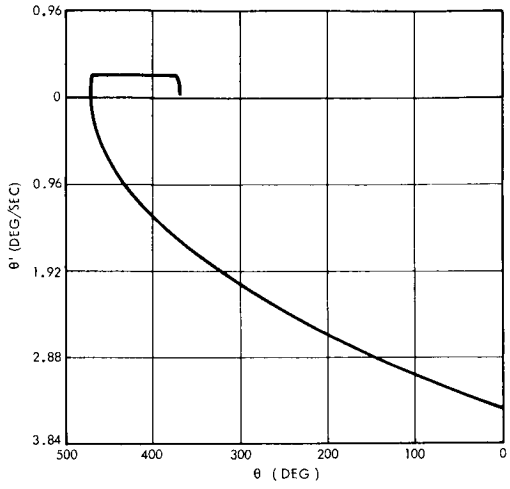


Figure E-22. Initial Sun Acquisition with Initial Rate +3 deg/sec, No Position Error

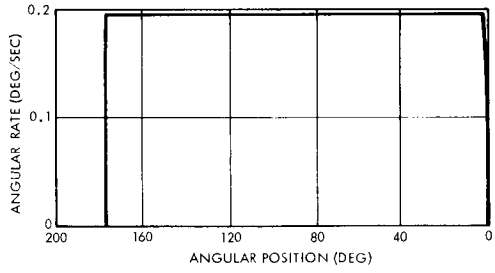


Figure E-23. Acquisition After Deboost with Initial Rate and 180-degree Position Error

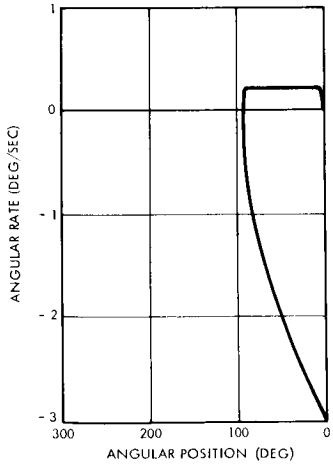


Figure E-24. Acquisition After Deboost with +3 deg/sec Initial Rate, No Position Error

It is noted that for these acquisitions, the derived rate feedback was disconnected from the electronic switching amplifier. Acquisition with the derived rate feedback is discussed in Section 2.2.5. The high inertia cases represent an initial acquisition; and the low inertia cases, acquisition after deboost. The following table compares the fuel consumption calculations with those found in the simulation. This demonstrates the close correlation between the analysis and simulation.

Figure	Calculated Fuel Consumption (lb)	Simulated Fuel Consumption (lb)
E-21	0.034	0.032
E-22	0.272	0.261
E-23	0.010	0.009
E-24	0.082	0.079

2.2.5 Acquisition With Derived Rate Feedback

The previous paragraph discussed acquisition with the derived rate feedback disconnected. It would be functionally simpler if the derived rate were not removed. The effect of derived rate feedback is to change the torques from an essentially on-off switch with a deadband to a modulator. This increases the rate damping but reduces the duty cycle from unit to a value somewhat less. The overall result is to have no effect for large rate or angular errors and slow the settling time when the attitude error is within 2 degrees when the fine sun sensor is switched in. The properties of derived rate feedback are further discussed in Section 2.2.6. A stability problem, however, can exist at the point where sun sensors are switched. A large change in voltage levels as is now scheduled may cause a limit cycle at one of the switching points. Figure E-25 demonstrates this instability. Further detailed studies are requred to insure that inclusion of the derived rate feedback does not significantly degrade the acquisition performance. The motivation for maintaining the derived rate feedback during acquisition is that, in addition to simplifying the switching logic, automatic backup of the rate gyros is achieved.

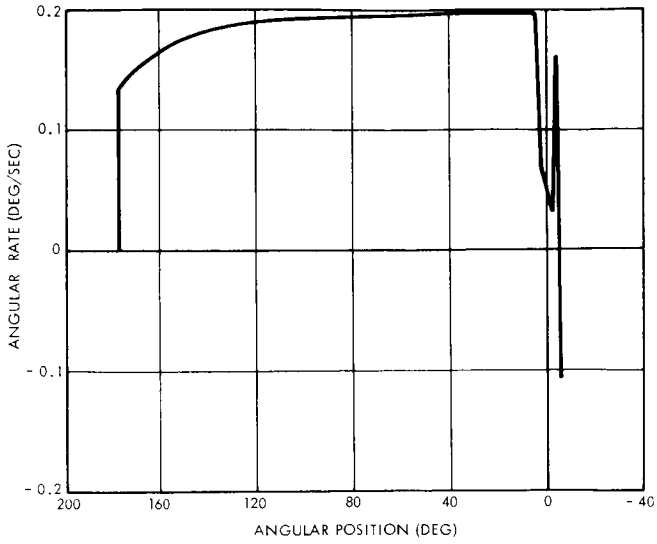


Figure E-25. Initial Acquisition of Baseline Configuration and Derived Rate

2.2.6 Backup Configuration

The purpose of this section is to investigate the performance of various acquisition configurations that do not need gyro information. The dynamic model of the spacecraft for use in single-axis attitude control channel studies is a double integration relating applied torque to attitude displacement. For stability, rate information is necessary. If gyros are not available, the celestial sensors or knowledge of when thrusting occurs must provide the rate information. The two means of extracting rate information that were studied are derived rate feedback and a lead-lag network on the output of the sensor. Both techniques have performances very closely associated with the sensor characteristics. These two designs as well as the effects of redesigning the sensors are discussed in more detail below. In all cases, and single axis — sun oriented channel is studied. Later, a separate discussion for the Canopus channel is presented.

2.2.7 Derived Rate

A block diagram of a derived rate backup acquisition channel is shown in Figure E-26. The coarse sun sensor output characteristic shown here is double valued as discussed in Section 1.5. As the thrusting level is a constant, all the necessary information about system performance can be found from consideration of firing on and off times and those points where the gas jets condition changes. When the gas jets are not firing, the following relations exist:

Angular rate = $\dot{\phi} = \dot{\phi}_o$

Angular position = $\phi = \phi_o + \dot{\phi}_o t$

Derived rate output = $R = R_o e^{-t/\tau}$

Sensor output = $P = P(\phi)$

Error signal = $\epsilon = -P - R$

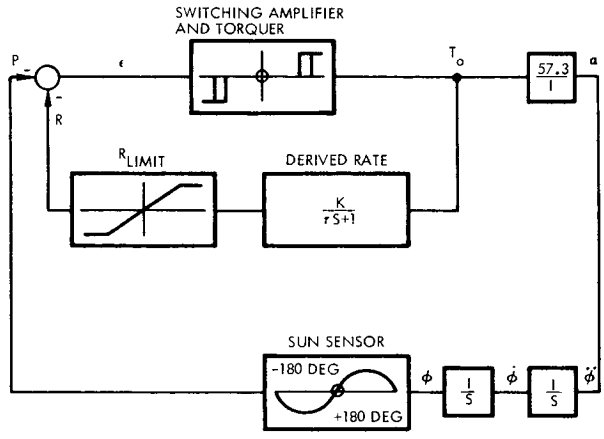


Figure E-26. Block Diagram of Derived Rate Backup Acquisition System

where subzero denotes state at beginning of nonfiring condition. When the gas jets are firing, the following relations exist:

$$\dot{\phi} = \dot{\phi}_o + at$$

$$\phi = \phi_o + \dot{\phi}_o t + \frac{1}{2} at^2$$

$$R = R_o e^{-t/\tau} + T_o K(1 - e^{-t/\tau})$$

$$P = P(\phi)$$

$$\epsilon = -P - R$$

$$T_o = |T_o| \text{ sgn } (\epsilon)$$

where the subzero denotes state at beginning of firing condition.

a = Angular acceleration

T_o = Gas jet torque

The following two observations aid in understanding the operation. First, if, for a large ϕ_o, the gas jets are turned off, $R_o \sim -\phi_o$. As R decays at $e^{-t/\tau}$, this indicates that ϕ is commanded to decay at the same rate. The value for τ determines how rapidly the attitude is commanded to approach zero. Second, if the gas jets are turned on, they will remain on largely dependent on KT_o and τ. The larger KT_o, the smaller the

on-time. In other words, the velocity is commanded to change a smaller increment. It can now be seen that τ determines the magnitude of rate control commanded and K and τ determine the extent of the control exerted if the system does not behave as desired.

As larger initial attitudes are encountered, larger voltages from the derived rate network must be available. The derived rate network must also produce a satisfactory voltage equivalent to the 0.1 deg hysteresis. This places additional demands on the dynamic range of the network. From a design standpoint, it is desired to maintain a dynamic range no greater than 100:1 to 200:1. This indicates that the network will saturate at a level corresponding to between 10 and 20 degrees. If the derived rate output is saturated, only position information is available for attitude control. There will be no rate stabilization or damping for attitude error situations resulting in feedback signals greater than the limit. The result is a conservative system in the saturated region, and a complete spacecraft revolution gives no net change to angular momentum. This situation is wasteful of fuel and may adversely affect acquisition time. The indications are that performance will be improved as the dynamic range of the derived-rate feedback is extended.

As the attitude approaches 180 degrees, the coarse sun sensor gives a decreasing voltage yielding a slope of opposite sign from what it should be ($\dot{P} \sim - \dot{\phi}$). This causes incorrectly signed rate feedback. This behavior may cause torques which increase the angular momentum when it is already excessible for acquisition. Control in this region may then result in excessive fuel consumption and even slower acquisition time. However, as the existing sun sensor can not differentiate between 180 and 0 degrees and position control is desired for any attitude, the following studies will assume this undesirable characteristic. A change in the sensor characteristics to be monotonic between ±180 degrees does greatly improve acquisition performance in the region near 180 degrees where the derived rate signal is not yet saturated.

The above discussion demonstrates that acquisition using derived rate feedback for rate information is improved by:

- Extending the derived rate dynamic range
- Using a monotonic sun sensor characteristic in the interval ±180 degrees
- Choosing a τ properly tuned with T_o and the spacecraft inertias
- Decreasing K until a satisfactory control duty cycle can be achieved.

As the present designs are considered as backup designs, it is desired to achieve a satisfactory acquisition with as little alteration in the selected cruise mode as possible.

The analog computer was used to study quantitatively the use of derived rate as a backup acquisition mode. The nominal cruise mode configuration (τ = 100 sec, K = 240 deg/ft-lb, R_{limit} = 10 deg) was studied to find what initial condition space could be adequately acquired. Adequate acquisition is defined for this study as acquisition within less than three complete rotations of the spacecraft. Due to the characteristics of the sun sensor, the 180 degree attitude error is the most restrictive for allowable initial rates. At 180 degree attitude error, the largest allowable rate was 0.5 deg/sec. A phase plane plot for this acquisition is shown in Figures E-27 and E-28. curve a. Figure E-27 is for the highest expected spacecraft inertia as will be the case for initial acquisition and Figure E-28 is for the lowest expected inertia as will be the case after deboost. The effect of raising the derived rate limit from 10 to 50 degrees is shown by curve b. The effect of lowering the derived rate gain to 100 deg/ft-lb as well as raising the limit is shown in Figure E-29 and Figure E-28, curve d. The fuel consumption for these cases at the high inertia were: curve a = 1.23 pound, curve b = 0.533 pound, Figure E-29 = 0.35 pound versus 0.05 pound for the configuration using rate gyro feedback. The fuel consumptions for these cases at the low inertia were: curve a = 0.930 pound, curve b = 0.140 pound, curve d = 0.141 versus 0.015 pound for the rate gyro configuration.

2.2.8 Lead-lag Compensation

Another means of extracting rate information from the sun sensor output is the use of a lead-lag network. This method has been extensively

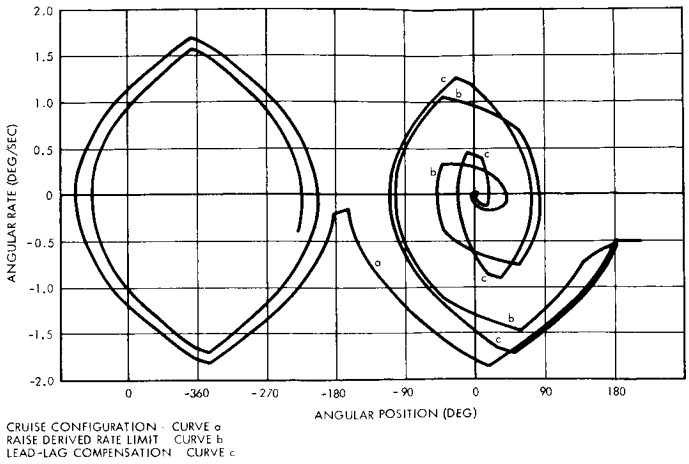


Figure E-27. Initial Acquisition for Several Backup Configurations - High Inertia

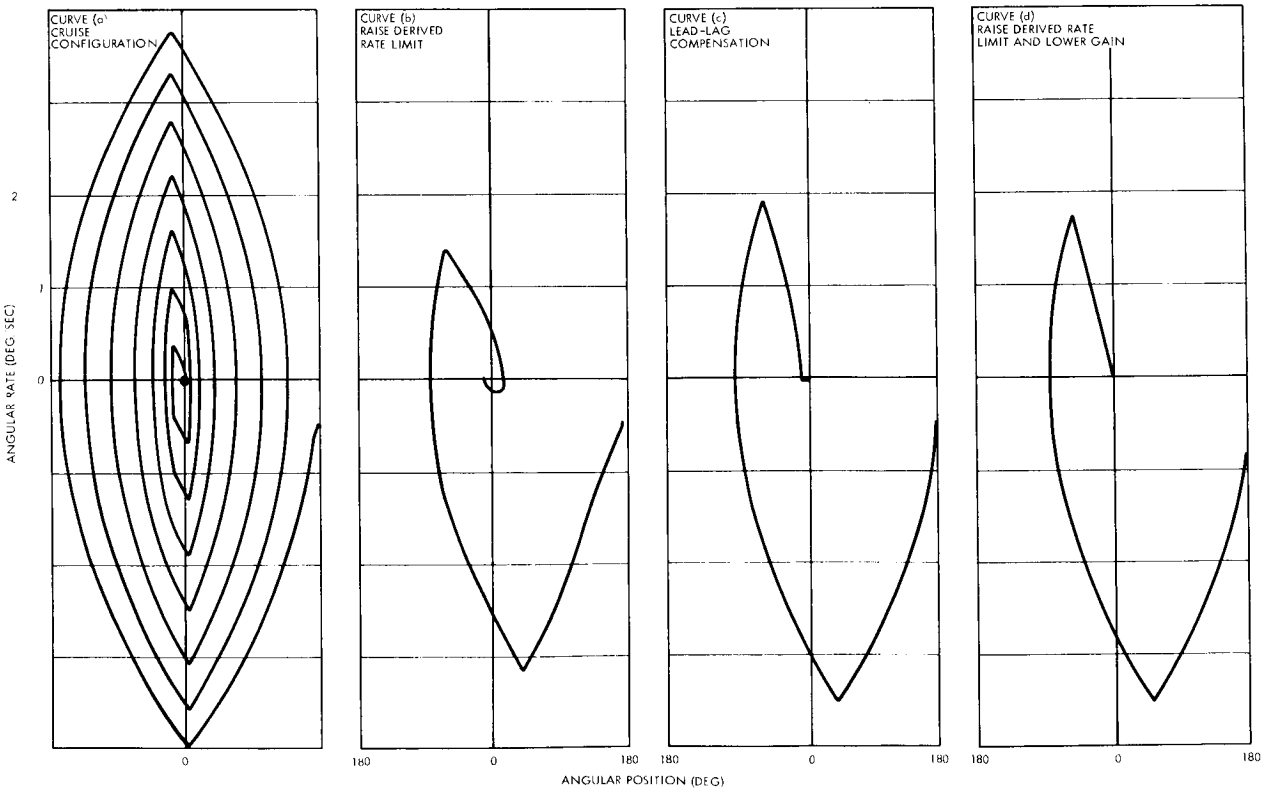


Figure E-28. Initial Acquisition for Several Backup Configurations - Low Inertia

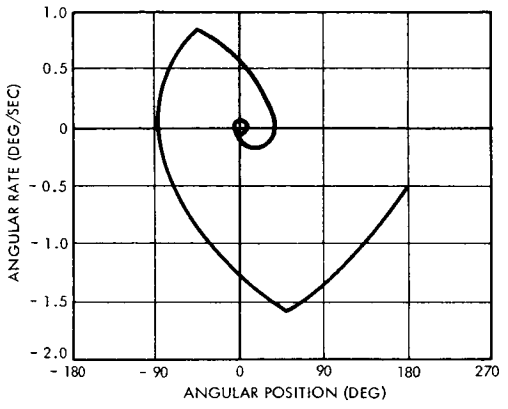


Figure E-29. Initial Acquisition for Backup with Raised Derived Rate Limit and Lowered Gain (K)

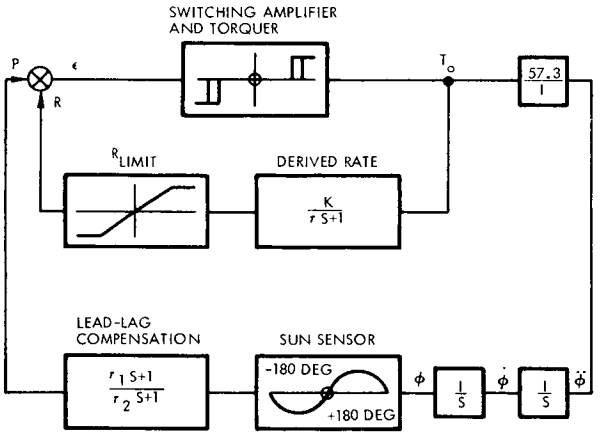


Figure E-30. Block Diagram of Derived Rate and Lead-Lag Compensation Backup Acquisition System

studied and is now used for OGO. The configuration is shown in Figure E-30. The use of a lead-lag network has the advantage over derived rate in that there is no initial rate error. This is because the derived rate network merely integrates changes in angular velocity but does not account for initial attitude rate errors. However, lead-lag networks suffer from the inability to give the effective high ratios of rate to position gain possible with derived rate. Practical design considerations on lead-lag networks typically limit the lead time constant to values such as 20 seconds and the lead to lag ratio to 10. Due to the limitations on the allowable lead, better

results may be obtained if a lead-lag network is used in conjunction with the derived rate feedback. Curve c in Figures E-27 and E-28 show the phase plane trajectories for acquisition from 180 degrees initial position error and 0.5 deg/sec initial rate using a lead-lag network and the derived rate feedback. The curves are for a lead-lag network with a lead-lag ratio of 10 and a 2-second lag time constant, together with the cruise derived rate feedback for the heaviest and lightest expected inertias of the spacecraft. The data shown in curve c in Figures E-27 and E-28 indicate that although the acquisition performance is improved by including the lead-lag compensation, the negative sun sensor slope for attitude errors in excess of 90 degrees significantly degrades the acquisition performance. This performance can be improved considerably by sun sensor characteristic which increase monotonically with attitude error.

2.2.9 Canopus Backup Acquisition

Because of the narrow field of view of the Canopus sensor (±2 deg) and the possible tipoff rates (3 deg/sec), operation of the roll rate sensor may be required for the initial Canopus acquisition. Provision has been made, however, for a ground controlled incremental roll maneuver mode, such as employed on Mariner C. This mode is identical to the roll axis reorientation mode with the exception that the precision torquing current is controlled by fixed timers which results in a fixed incremental roll attitude change. In addition, provision has been made for direct ground control of the roll axis jets. These modes provide backup control for Canopus acquisition and for the high-gain earth pointing antenna.

2.2.10 Analog Computer Simulation

A single axis analog computer simulation was conducted to aid in the acquisition study. The simulation is for the two sun acquisition axes. The characteristics of Canopus acquisition can readily be extrapolated from the results due to the similarity of the control channels. Linearized dynamical equations with no cross-coupling is assumed. The equations simulated are shown below. The computer block diagrams are shown in Figures E-31, E-32, and E-33. Figure E-31 shows all the simulation but the sun sensors. Figure E-32 shows the gyro rate feedback and rate command logic simulated for the baseline configuration. Figure E-33 shows the coarse sun sensor simulation.

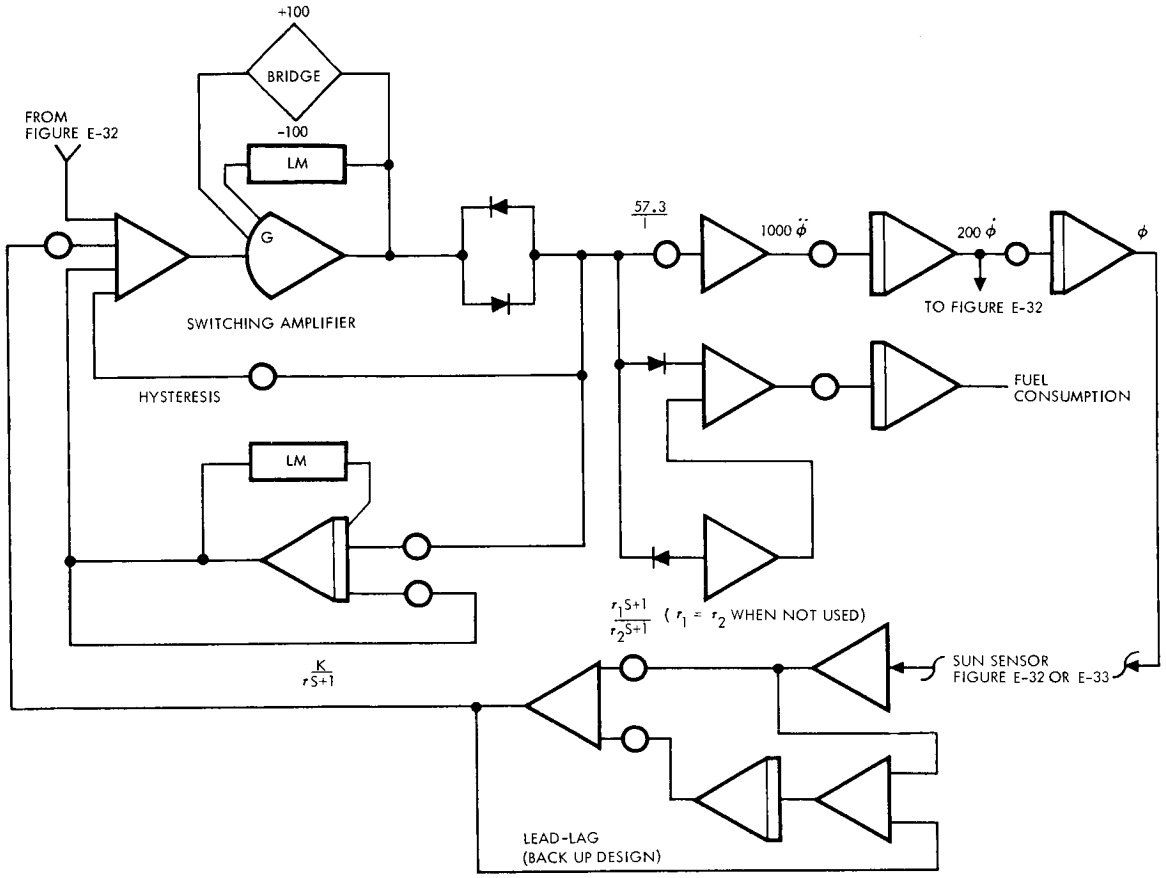


Figure E-31. Analog Simulation

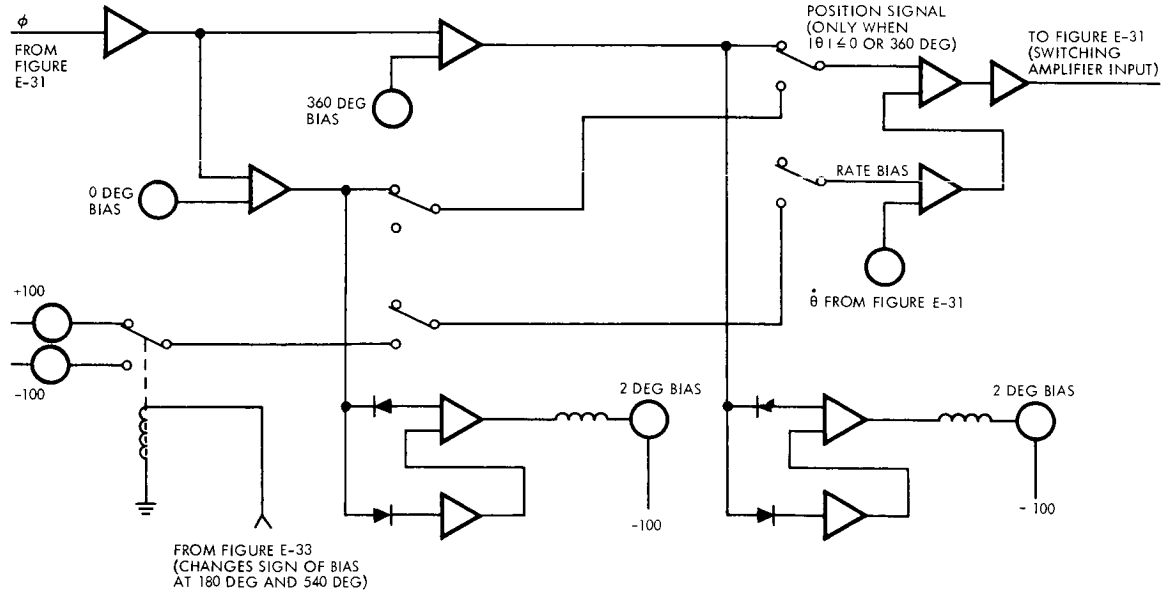


Figure E-32. Baseline Switching Logic and Rate Feedback

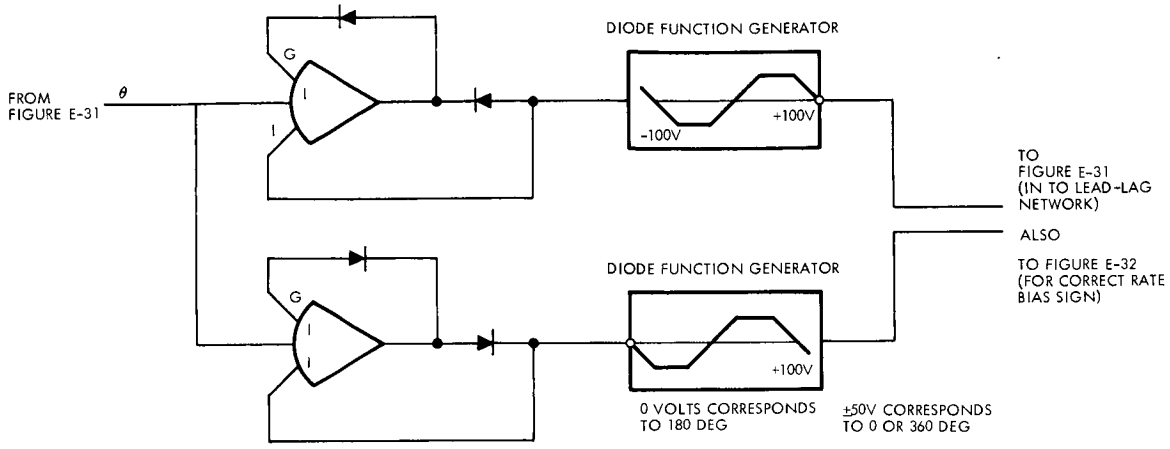


Figure E-33. Coarse Sun Sensor

Equations Simulated:

$$\ddot{\phi} = \frac{57.3}{I} T_o$$

$$\dot{\phi} = \dot{\phi}_o + \int \ddot{\phi}\, dt$$

$$\phi = \phi_o + \int \dot{\phi}\, dt$$

$$\left.\begin{array}{l} P = \phi \text{ if } |\phi| \leq 2 \text{ deg} \\ \\ 0.2\, K \text{ sgn } (\phi) \text{ if } |\phi| \geq 2 \text{ deg} \end{array}\right\} \text{for baseline acquisition}$$

$P = \sin \phi$ for backup studies (this is simulated by a diode function generator)

$$\tau\dot{R} + R = KT_o, \quad |R| \leq R_{limit}$$

$$\epsilon(s) = -P - R - 500\,\dot{\phi} \text{ for baseline acquisition}$$

$$= -P\left(\frac{\tau_1 s + 1}{\tau_2 s + 1}\right) - R \text{ for lead-lag compensation}$$

$$= -P - R \text{ for derived rate backup}$$

$T_o = 0$ if $|\epsilon| \leq 0.4$ deg or if $0.4 \text{ deg} \leq |\epsilon| \leq 0.5$ deg and the jet has not yet fired.

$= |T_o| \text{ sgn } \epsilon$ if $|\epsilon| \geq 0.5$ or if $0.4 \leq |\epsilon| \leq 0.5$ and the jet has already fired.

2.3 Maneuver and Inertial Attitude Hold Modes

Attitude reorientation is required to maneuver the spacecraft for the midcourse velocity correction, capsule separation and deboost phases of the Mars trajectory. Following reorientation, the desired attitude is maintained by the inertial attitude hold mode. The desired spacecraft attitude is determined by ground computation, transmitted to the spacecraft and stored in the CS and C prior to initiating the maneuver. Gyro torquing current generators produce a precision current that will command the desired reorientation attitude. In the maneuver sequence, a roll turn is made followed by a pitch turn. In some cases, a second roll turn may be required to enable the high-gain antenna to point to earth.

It is desired to select an attitude control mode which will satisfactorily accomplish reorientation and attitude hold with a minimum of special switching circuits and design changes from existing control mode configurations. Aided by an analog computer simulation, the following three configurations were studied:

1) Position gyro reference

2) Lead-lag compensation of the position gyro signal

3) Position plus rate gyro control.

To simplify the switching logic, derived rate feedback was maintained around the on-off electronic switching amplifiers. Results of the simulation show that all three configurations give satisfactory reorientation and attitude hold performance. The configuration employing position gyro reference with derived rate feedback (Configuration 1) has been selected as it is the simplest and most reliable design. A block diagram of the selected configuration is shown in Figure E-34.

Comparative single axis reorientations using Configurations 1, 2, and 3 for a 50-degree maneuver and a 0.2 deg/sec gyro torquing rate were studied on an analog computer and are shown in Figures E-35, E-36 and E-37 respectively. Several runs were made for each configuration with various derived rate filter limits. The general conclusions reached from the study are:

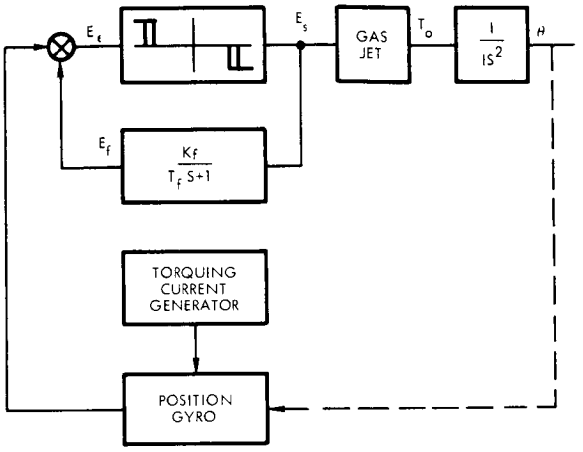


Figure E-34. Single Axis (Pitch, Roll) Reorientation Block Diagram

a) For each configuration, there exists an optimum derived rate limit which is proportional to the torquing rate. Based on a 0.2 deg/sec torquing rate, the optimum limit for the selected configuration appears to be 20 to 23 degrees.

b) Position plus rate gyro control with derived rate feedback (Configuration 3) provided the equivalent of over-critical damping and did not significantly improve performance over Configuration 1.

c) Lead-lag compensation with derived rate feedback (Configuration 2) provides near optimum performance.

Table E-3 lists the fuel consumption for the various acquisitions. Note that all configurations but the lead-lag consume considerably more fuel than the ideal requirement which is determined by the impulse needed to develop the acquisition rate and then remove it after the commanded turn has been completed. Even the inefficient modes, however, consume a small quantity of fuel when compared to the 1.3 pounds that may be consumed during initial acquisition. The additional fuel consumption used by the cruise mode configuration is well worth the simplicity in design achieved.

2.4 Thrust Vector Control Mode

This section presents an analysis of several thrust vector control (TVC) system mechanizations which were considered for the midcourse

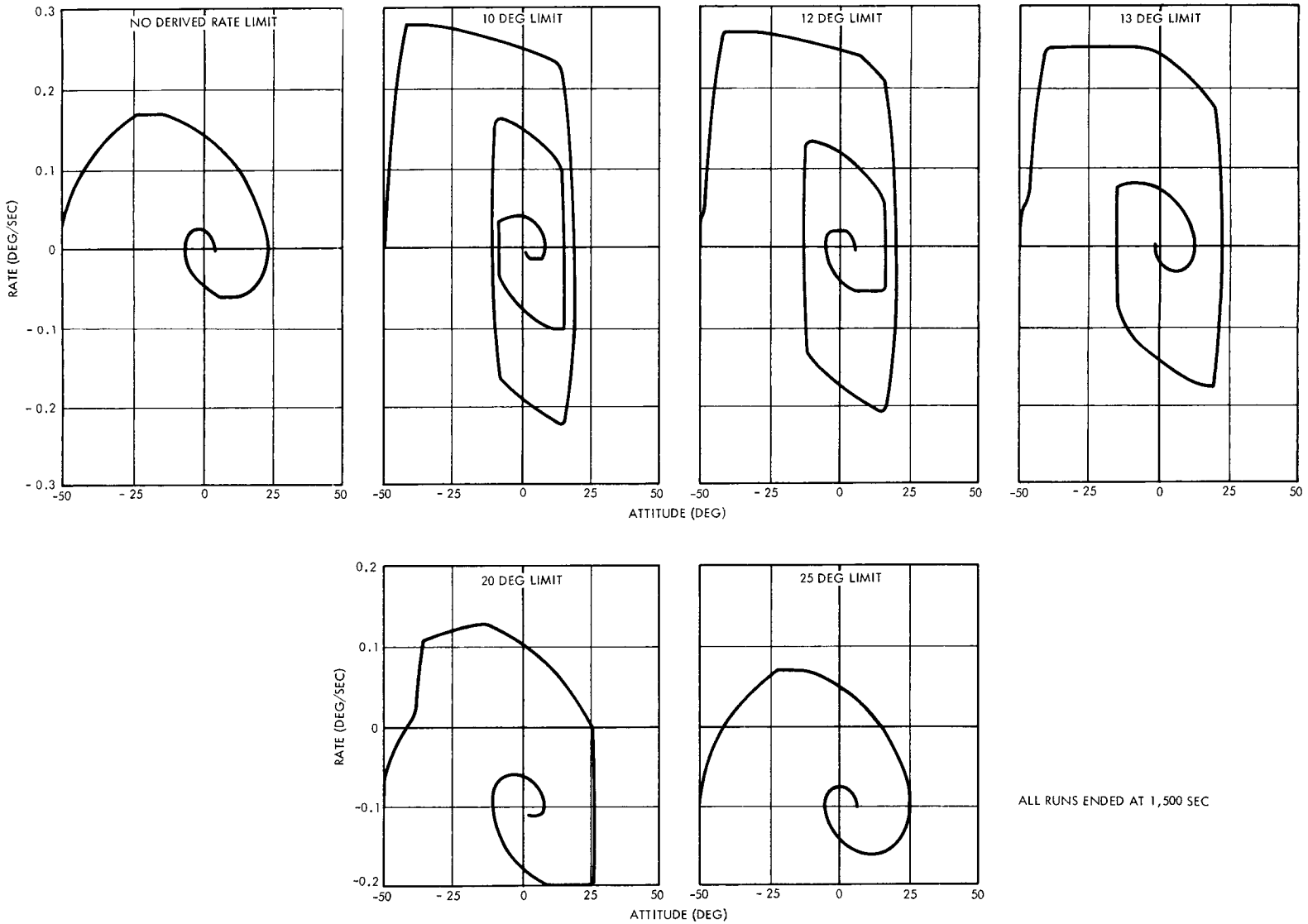


Figure E-35. 50-Degree Reorientation Maneuver, 2 deg/sec Gyro Precession Rate Cruise Mode Configuration

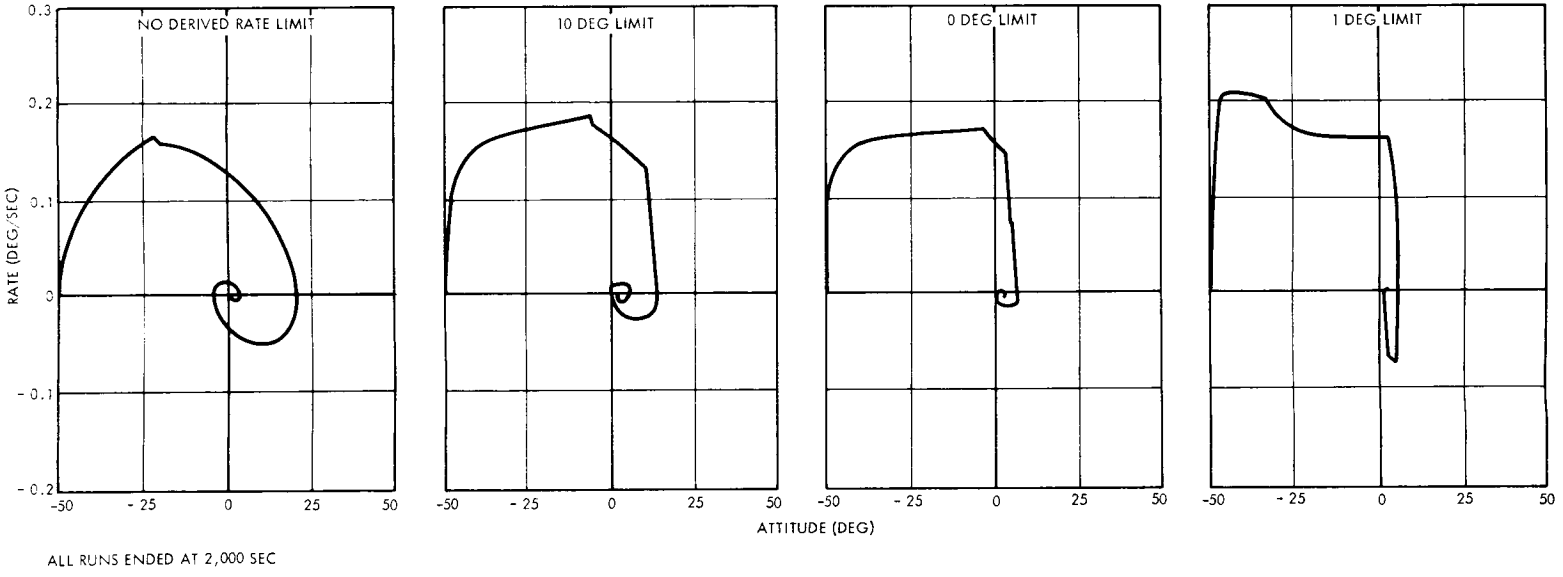


Figure E-36. 50-Degree Reorientation Maneuver, 2 deg/sec Gyro Precession Rate, $\frac{2C_{S+1}}{2S+1}$ Compensation Network

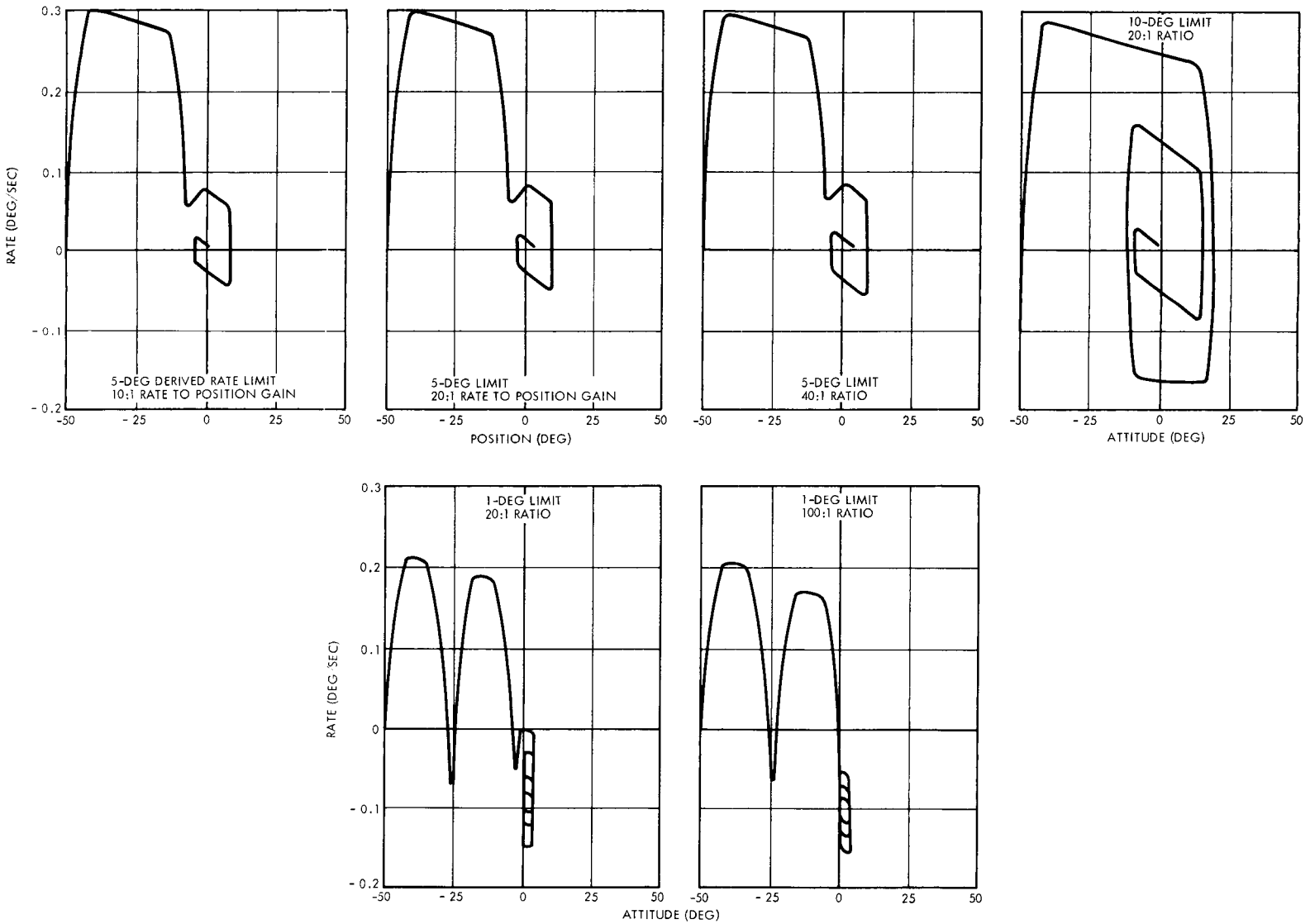


Figure E-37. 50-Degree Reorientation Maneuver, 2 deg/sec Gyro Precession Rate, Gyro Rate Feedback

Table E-3. Fuel Consumption for Various Reorientation Configurations

Figure	Curve	Fuel Consumption (lb)
E-35	No limit in derived rate	0.0485
	10-deg limit	0.156
	12-deg limit	0.132
	15-deg limit	0.103
	20-deg limit	0.071
	23-deg limit	0.0490
E-36	No limit in derived rate	0.0450
	10-deg limit	0.0424
	5-deg limit	0.0363
	1-deg limit	0.0540
E-37	5-deg limit, 10:1 rate/position ratio	0.0730
	5-deg limit, 20:1 ratio	0.0728
	5-deg limit, 40:1 ratio	0.0737
	10-deg limit, 20:1 ratio	0.1460
	1-deg limit, 20:1 ratio	0.1758
	1-deg limit, 100:1 ratio	0.1420
	Ideal	0.0340

velocity correction and deboost phases of the Voyager mission. Two spacecraft propulsion configurations were studied which consisted of: 1) a low thrust monopropellant engine for the midcourse velocity correction and a high thrust solid rocket engine for deboost (Configuration A or C) and 2) a bipropellant engine configuration which is used for both the midcourse velocity correction and deboost maneuvers (Configuration B). For both of these configurations, the TVC system maintains stability about the spacecraft pitch and yaw axes. Roll stability is obtained through the roll axis inertial attitude hold mode.

2.4.1 Configuration A or C

a. Midcourse Correction

Pitch and yaw axis control during the midcourse velocity correction is accomplished by jet vanes. A block diagram of a single axis jet vane control system is shown below in Figure E-38.

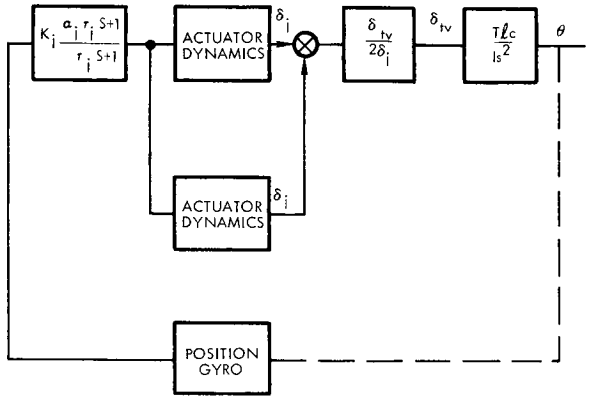


Figure E-38. Midcourse Jet Vane TVC Block Diagram

where

δ_j = Jet vane position

δ_{tv} = Thrust vector deflection

T = Engine thrust = 50 pounds

ℓ_c = Moment arm from thrust chamber to c.g.

I = Principal axis moment of inertia

K_j = Attitude error gain

θ = Spacecraft attitude

$\alpha_j \tau_j$ = Lead time constant

Based on a criterion of one-half the maximum jet vane deflection for a 1/2 degree pointing error, an attitude error gain of 25 was selected. The maximum jet vane deflection and the ratio of jet vane deflection to thrust vector deflection were taken from Mariner C data

and are 25 to 5 degrees, respectively. This lead-lag time constant (τ_j) is 0.2 second and the lead ratio (α_j) is 10. The lead-lag compensation parameter values listed above were selected on the basis of providing satisfactory closed loop response characteristics with reliable hardware components. Figure E-39 shows a root locus plot of the rigid body control mode, neglecting actuator dynamics, and illustrates the variation in closed-loop roots over the extreme range of system parameters ($T\ell_c/I$) during the midcourse velocity correction.

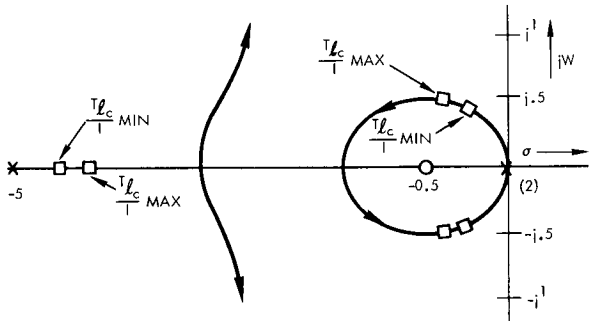


Figure E-39. Midcourse Jet Vane TVC Root Locus Diagram

As shown in Figure E-39, essentially constant closed loop response characteristics are maintained for the pitch and yaw axes during the midcourse maneuvers.

Due to the proximity of the effective gimbal point to the center of mass (c.m.) and the lateral c.m. uncertainties, thrust vector offset angles are generated. Based on current data for Configuration A or C, the 3σ thrust offset angle is approximately 0.4 degree. The resulting attitude error is 0.08 degree. The net result is, however, an effective 0.48 degree thrust offset angle since the attitude error and thrust offset are additive.

Roll attitude stabilization during the midcourse maneuver is maintained by the roll axis inertial attitude hold mode which is discussed in Section 2.3.

b. Solid Rocket Deboost

Pitch and yaw axis control during the solid rocket deboost maneuver is obtained by liquid injection thrust vector control. A block diagram of a single axis TVC system is shown in Figure E-40.

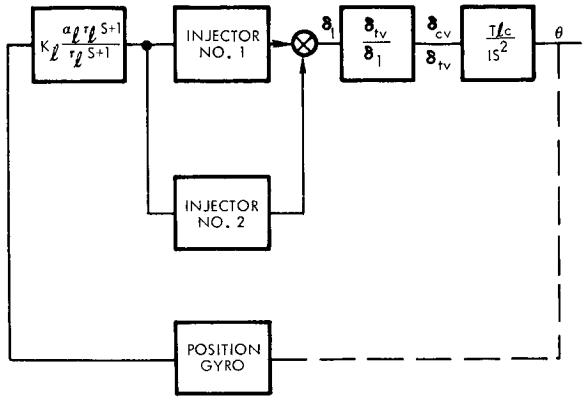


Figure E-40. Solid Deboost TVC Block Diagram

The moment of inertia (I) and the control moment arm (ℓ_c) remain essentially constant during deboost (solid tank located close to center of gravity); therefore, the loop gain parameter ($T\ell_c/I$) is seen to vary in direct proportion to the thrust level. Representative curves showing thrust time histories for various solid motors indicate a thrust variation by approximately a factor of four (16000 to 4000 pounds) up to the last 10 seconds of burning (based on a total burning time of approximately 100 seconds). Due to the relatively high thrust levels at deboost compared to midcourse (16,000 lb max/50 lb max), the loop gain parameter ($T\ell_c/I$) is correspondingly higher which permits a lower attitude error gain (K_ℓ). The lead-lag time constant selected is 0.05 second and the lead ratio (α_ℓ) is 10. Figure E-41 shows a root locus plot of the rigid body control mode for an attitude error gain (K_ℓ) of two and indicates the maximum variation in closed loop roots during 90 percent of the burning time.

A possible problem with the solid rocket TVC system is the thrust vector offset angle resulting from lateral c.m. uncertainties and the relatively short control moment arm (~15 inches). Based on a

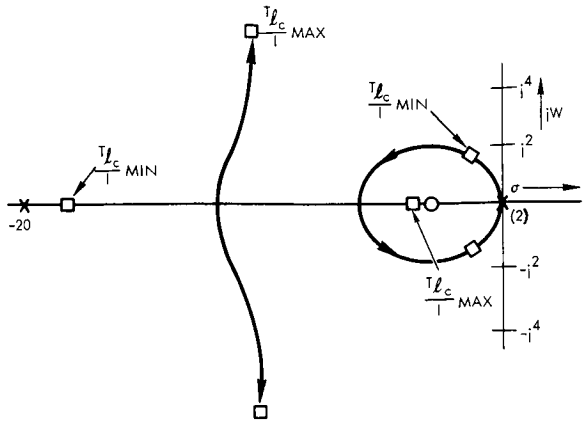


Figure E-41. Deboost TVC Root Locus Diagram

lateral c.m. uncertainty of 0.2 inch, the maximum thrust vector deflection is approximately 0.75 degree. Due to the injection fluid required to maintain this thrust vector deflection, tight control of the lateral c.m. uncertainty is indicated. Estimates of the lateral c.m. control achievable by proper appendage location and standard balancing techniques indicate that a 0.1-inch uncertainty is possible.

Due to the high thrust levels obtained with the solid rocket and the present center of gravity uncertainties, the roll disturbance torque level may exceed the normal inertial attitude hold control torque. As a result, a requirement may exist to increase the roll axis jet thrust level during the deboost maneuver. Based on data available from solid propelled vehicles, the disturbance torque may be as large as 3 ft-lb. Since the effective moment arm due to the two roll jets is 19 feet, a thrust level of approximately 0.5 pound may be required. Roll attitude stabilization during deboost may, therfore, require a separate pair of high thrust jets which could operate through the normal roll attitude inertial hold mode. The requirement for separate gas jets for roll stabilization will be re-evaluated when the spacecraft goemetry, c.m., and propulsion uncertainties are better defined.

In addition to the thrust vector control system, a spin stabilization scheme was considered for the deboost attitude stabilization. Results of this study indicate the following:

- A minimum rate of 2.6 rad/sec is required to maintain the thrust vector angle within ±1 degree
- The resulting centrifugal acceleration (2.1 g) increases the required lateral structural loading and imposes additional requirements on the appendages.

Figure E-42 shows a curve of the thrust vector offset angle as a function of spin rate and indicates an optimum spin rate of 3.6 rad/sec for a 1-second spinup time.

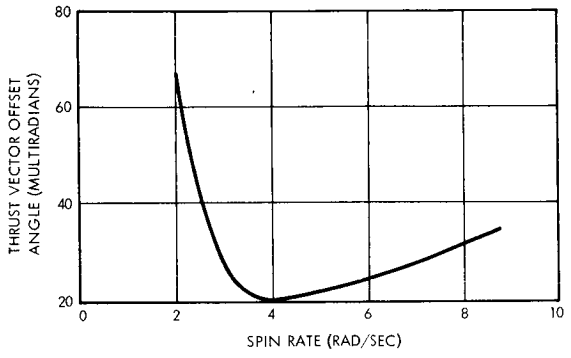


Figure E-42. Thrust Vector Offset Angles versus Spacecraft Spin Rate During Deboost Maneuver

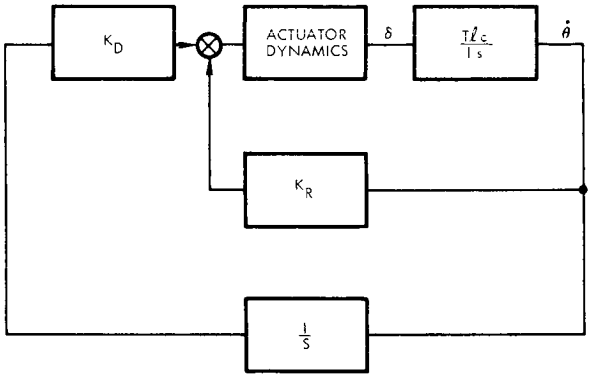


Figure E-43. Gimballed TVC Block Diagram

2.4.2 Configuration B TVC Studies

Unlike Configurations A or C which employ separate engines for midcourse and deboost, Configuration B utilizes one thrusting engine for all velocity corrections. Consideration was given to two bipropellant TVC system configurations. Initial studies were made of a conventional gimballed thrust chamber system and later efforts were directed to a lateral displacement configuration.

Figure E-43 shows a block diagram of a single-axis (pitch or yaw) gimballed engine TVC system.

Root locus studies were made to determine control system gains which would yield satisfactory attitude response characteristics during the midcourse correction and deboost phases of the Mars trajectory.

Based on a criterion of one-half the maximum thrust vector deflection for a 1/2 degree pointing error and an assumed maximum thrust vector deflection of $\pm$ 15 degrees, the attitude error gain was computed as 15. Figure E-44 shows a root locus plot of the rigid body control mode neglecting actuator dynamics and illustrates the variation in closed-loop roots for the extreme range of system parameters $(\frac{T \ell_c}{I})$ from midcourse correction to deboost.

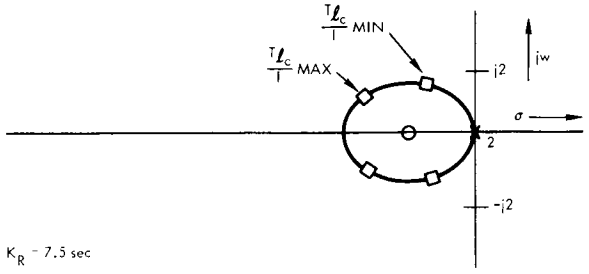


Figure E-44. Gimballed TVC Root Locus Diagram

As shown in Figure E-44, satisfactory closed-loop response characteristics are achieved for both the pitch and yaw axes from midcourse correction through deboost with constant attitude error and attitude rate gains.

For the configuration studied, the thrust vector control moment arms (ℓ_c) were approximately 30 inches and 10 inches for the midcourse correction and deboost phases of the Mars trajectory, respectively. Figure E-45 shows a plot of the trim thrust vector angle (δ_{trim}) for the two thrust vector moment arms (ℓ_c) given above versus center of gravity offset. Based on a maximum c.m. offset of 0.5 inches, a trim thrust vector angle of approximately 3 degrees is required for deboost. Due to the magnitude of these trim thrust vector deflections, consideration was given to a lateral displacement control actuator scheme.

3. GYRO REFERENCE ASSEMBLY TRADEOFF CONSIDERATIONS

The purpose of this section is to describe in some detail the various gyro reference assembly (GRA) configurations which were considered for the Voyager mission. These configurations were originally selected on

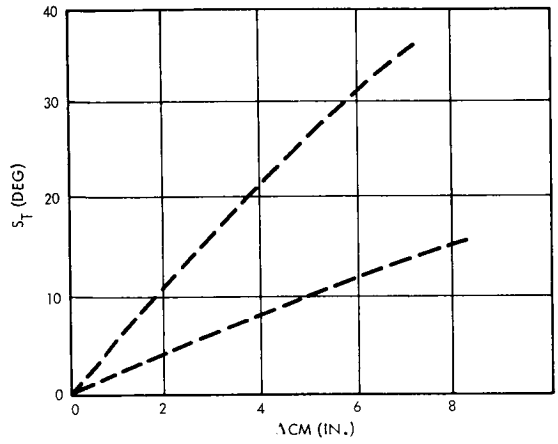


Figure E-45. Trim Thrust Vector Angles Versus Center of Mass Offset - Bipropellant Configuration

the basis of meeting the system operational requirements with high reliability. A preliminary study was then made of each of these configurations in order to arrive at what is presently considered to be an optimum choice.

In addition to the configuration tradeoff studies, the major gyro manufacturers were contacted for information concerning the status and performance of their instruments which appeared to be suitable for the Voyager application. These results are discussed below.

The major results of this initial configuration tradeoff study are summarized in Table E-4. Note that the quantities tabulated represent estimates of the performances of a final design. The present configuration choice is No. 4 which consists of three heated single-degree-of-freedom gyros and associated electronics. The three gyros can be electrically caged with a feedback loop which then provides three axes of spacecraft angular rate information. By means of switching, the loops can be opened, in which case the gyro output signals are proportional to spacecraft angular position. A constant current source and polarity switching device are provided to torque the pitch and roll gyros to achieve spacecraft reorientation. This configuration is one of the simplest in terms of required circuitry, and represents a conservative solution of the design problem. Gas bearing gyros are utilized in order to increase reliability and heater power is provided to stabilize the gyro temperature

Table E-4. Voyager Gyro Reference Assembly Tradeoff Considerations

Configuration No.	Description	Reference	Probability of Successful Mission Completion	Electronic Parts Count	Weight (lb)	Power (watts)	Remarks
1	Closed-loop with VCO integration	Figure E-46	0.9816	737	11.1	10.2	More sophisticated system than required.
2	Closed-loop with capacitor integration	Figure E-47	0.9915	365	13.0	8.7	Performance is dependent on the reliability of three large (4000 μf) capacitors.
3	Closed-loop with pulse torquing	Figure E-48	0.9840	621	10.8	11.7	The complexity of pulse torquing is not justifiable.
4	Open-loop with heater	Figure E-49	0.9915	333	10.0	18.1	Second in simplicity to Configuration 5, but does not have large gain and drift variations.
5	Open-loop without heater	Figure E-49	0.9929	279	9.9	8.5	Simplest system but large gain variation must be compensated in the system electronics.
6	Two-degree-of-freedom gyros with VCO integration	Figure E-46	0.9806	810	10.2	9.1	Two-degree-of-freedom gyros have not previously been used in this application.
7	Two-degree-of-freedom gyros with capacitor integration	Figure E-47	0.9905	438	12.2	7.6	Gyro characteristics relatively unknown.

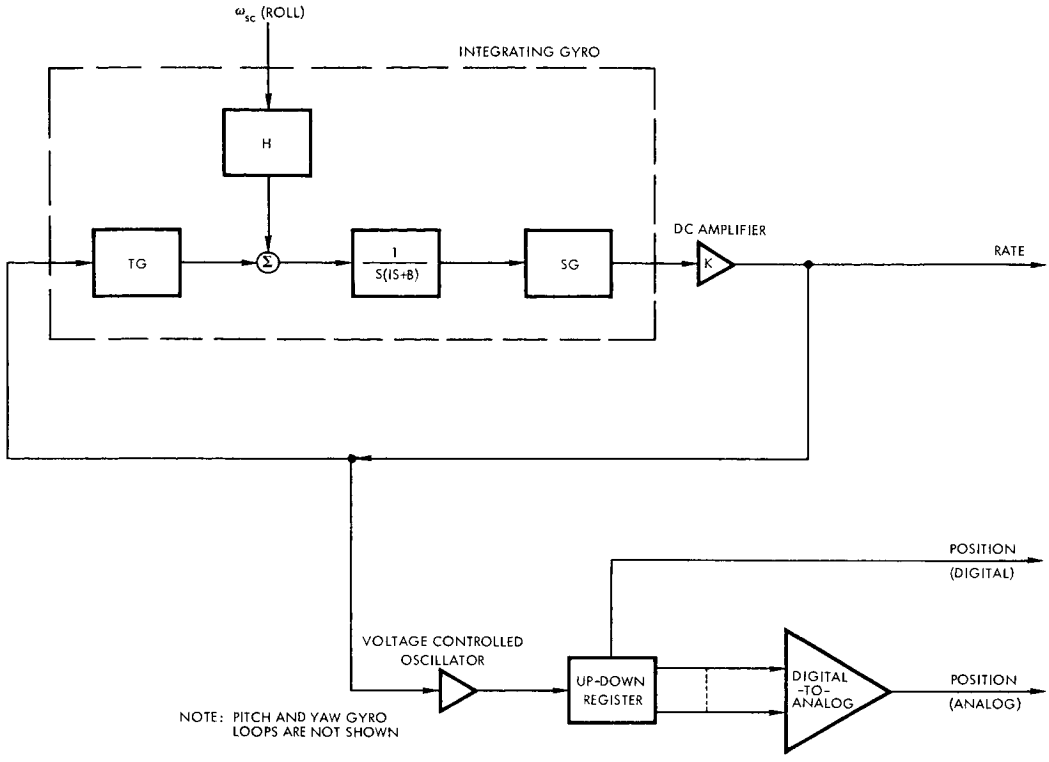


Figure E-46. Gyro Control Loop (Closed Loop With VCO Integration)

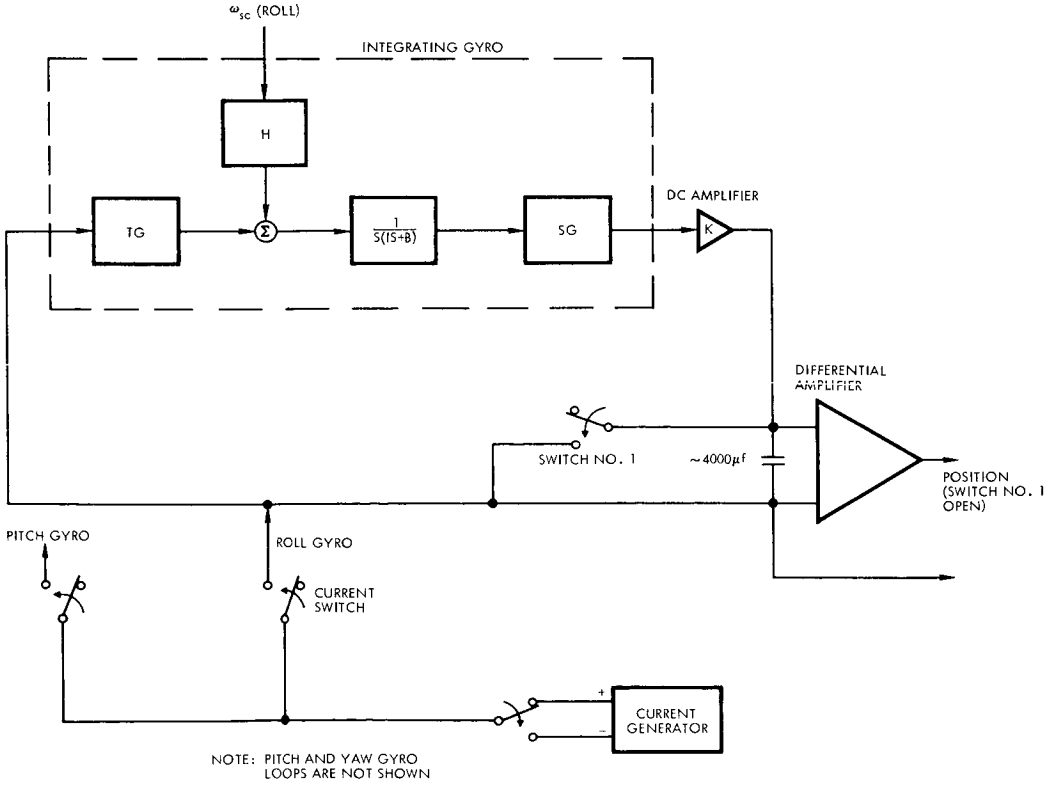


Figure E-47. Gyro Control Loop (Closed Loop with Capacitor Integration)

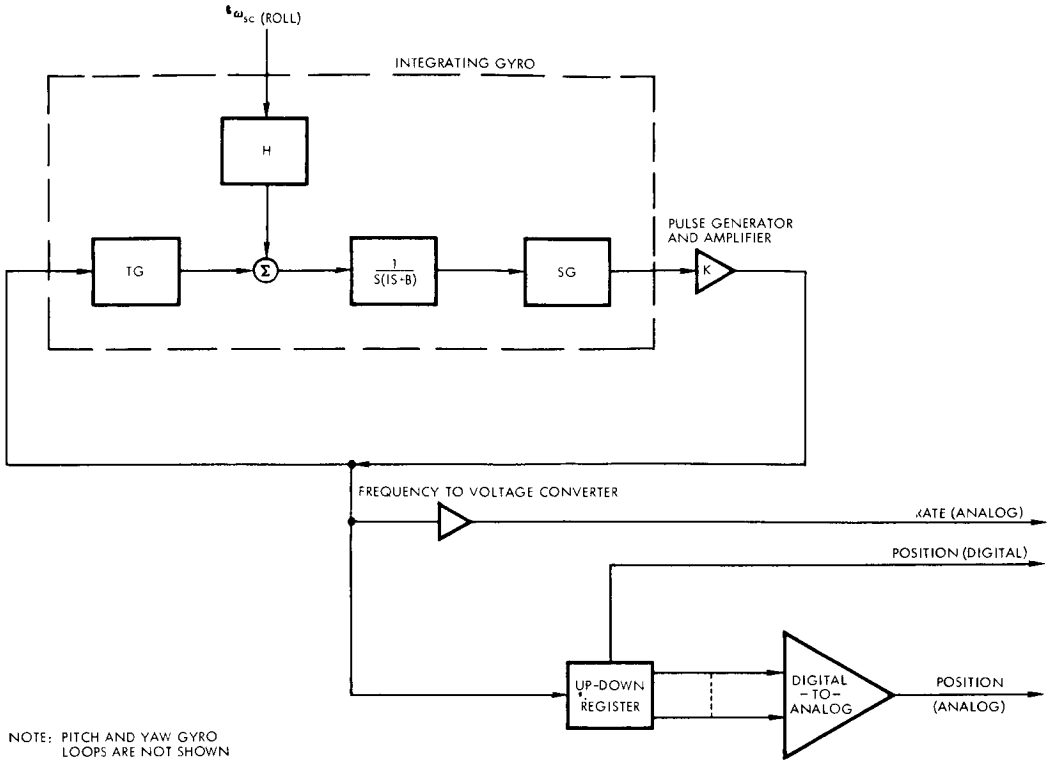


Figure E-48. Gyro Control Loop (Closed Loop With Pulse Torquing)

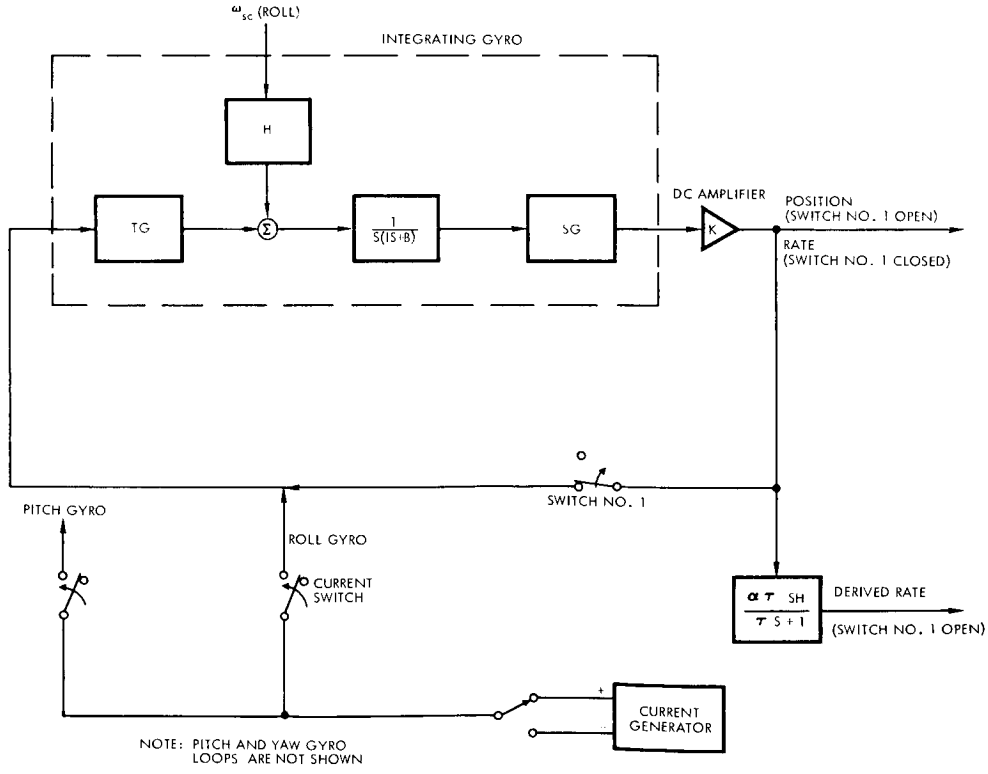


Figure E-49. Gyro Control Loop (Open Loop)

and thus avoid large variations in gain and eliminate the presently undefined changes in fixed drift. The disadvantage of this configuration is the heater power required and also the associated requirement for temperature control electronics. Currently in the Voyager design, the requirement for heater power does not appear to be unreasonable relative to available spacecraft power. However, should this become a problem after further study, a modification of the gyro reference assembly is possible. In this case, a study of eliminating the requirement for heater power would be undertaken and the possibility of compensating for the gyro temperature sensitivities would be investigated.

The gyro characteristics suitable for this application are listed in Table E-5. These characteristics are considered to be conservative relative to instruments that are presently available from gyro manufacturers.

3.1 General

The purpose of collecting the data for presentation in Table E-4 was to quantitatively assess the relative merits of reliability, weight, and power among the various configurations studied. It should be obvious that each number is a preliminary estimate based on an accounting procedure and a number of assumptions. For instance, the reliability numbers are based on estimates of the electronics part counts and estimates of the various component failure rates which in some cases are not well established.

In spite of the estimations, Table E-4 is useful to detect relative shortcomings between the various configurations and to establish preliminary performance estimates. The final configuration choice was based on this table plus some other considerations. Circuit complexity was minimized and the configuration avoids some potential design problems (gyro temperature sensitivity) which are presently not well understood. As a result, this choice is considered conservative and well within the present state of the art. Further study may result in a revision of this choice at a later date in order to improve reliability and/or reduce power and circuit complexity.

Table E-5. Preliminary Specifications of a Gyro for the Voyager Mission

Weight	1 lb (max)
Size	2 in. diameter x 3 in. long
Gimbal gain	$0.6 = \frac{\text{Output Angle}}{\text{Input Angle}}$ at 140°F
Input axis angular freedom	±5 deg (min)
Gimbal freedom	±3 deg (output axis)
Gimbal bearing	Pivot and jewel or flexure
Motor	
Type	Synchronous hysteresis, 4 pole
Excitation	Two-phase square-wave 800 cps
Starting power	10 watts peak for less than 45 sec
Running power	2 watts (max)
Signal generator power	4100 cps, 0.5 watts (max)
Spin bearing	Hydrodynamic with notches added to the journal portion
Long term drift	
G-Insensitive	Initial value ±0.3 deg/hr (max) Stability 0.4 deg/hr, 3σ, 1 yr
G-Sensitive	Initial value ±1.0 deg/hr-g (max) Stability 0.7 deg/hr-g, 3σ, 1 yr
MTBF	10^6 hr

3.2 Reliability

The reliability estimates were based on the following mission time intervals and component failure rates:

a) Cruise Phase - 101 hr of GRA operation

b) Thrust Phase - 0.38 hr of GRA operation during velocity correction maneuvers.

Assumed Failure Rates

Component	Failures per 10^9 hr of operation*
Analog integrated circuit	80
Digital integrated circuit	35
Transistors	50
Power transistors	130
Resistors	8
Diodes	40
Tantalum capacitors	20
Mylar capacitors	30
Transformers	120
Gyros (gas bearing)	1000

*This is failure rate during the cruise phase, to obtain failure rate during the thrust phase multiply by 1000.

Failure rates for those time intervals during which the system is not operated were, for the purpose of this study, assumed to be zero. While this assumption is probably not valid, realistic failure rates under storage (or cruise) conditions are not available. It is thought that including this effect in the analysis would not materially affect the relative standings of the various configurations.

3.3 Gyros

Seven gyro manufacturers provided information on units applicable to the Voyager mission. Those units most closely suited to Voyager are listed in Table E-6. Based on presently available information, each of these gyros is considered capable of meeting the required applicable performance criteria with the exception listed in Table E-5.

3.4 Configuration Descriptions

3.4.1 Configurations 1 and 2: Closed-Loop with VCO and Capacitor Integration

Configurations 1 and 2 are to some extent functionally similar and, where appropriate, the basic descriptions will be combined. Referring to Figures E-46 and E-47, these configurations consist of unheated single-degree-of-freedom gyros each with analog caging between the gyro pick-off and torquer. An electrical voltage proportional to torquer current is obtained and used as a spacecraft angular rate signal during the acquisition maneuver. Angular position information is obtained by integration of the

Table E-6. Gyro Units Applicable to Voyager Mission

No.	Manufacturer	Model No.	Spin Motor Power (watts)	Size (in.)	Weight (lb)	Remarks
1	Nortronics	GI-M1	< 2.0	2 dia 3 long	0.9	Gas spin bearing ceramic case
2	Sperry	SYG-4200	< 2.0	2 dia 3.86 long	1.4	Gas spin bearing
3	Kearfott	Alpha 2564	<3.5	2 dia 2.8 long	0.9	Ball spin bearing; gas bearing is in design. This is a production and performance proven gyro.
4	Autonetics	G 40	<2.0	2.4 dia 2.4 long	0.8	Two-degree-of-freedom, gas spin bearing. This gyro would have to be operated closed loop. It has potentially high reliability and low power.
5	Litton	G300-G2	< 3.5	3.1 dia 2.375 long	0.8	Floated, two-degree-of-freedom, gas spin bearing.
6	Honeywell	GG159	5.0	2.24 dia 3 long	1.0	Gas spin bearing. Fluid suspension requiring operation of a pump.
7	Norden	RI-203	3.0	2 dia 3.1 long	0.8	Ball spin bearing.

angular rate signal and the implementation of this capability results in the difference between the two configurations.

Configuration 1 uses an analog to digital converter and digital register to perform the required integration. The previously mentioned rate signal is applied to the input of a voltage controlled oscillator which in turn provides an output signal with a frequency proportional to the input voltage. This output signal is counted by an up-down register and the change in total count is proportional to the time integral of the VCO input voltage. Thus the count is proportional to spacecraft angular position. Reorientation of the spacecraft would be accomplished by inserting a number representing the desired angular change into the register and then command the spacecraft attitude in such a direction as to drive the subsequent register count to zero. At any time during the maneuver the number in the register represents the remaining angle to be turned. Note that in this case the gyro/VCO/register combination acts as an instrument which measures the change in angle through which the spacecraft has rotated over the interval of interest. In order to facilitate control of the spacecraft attitude during holding portions of the velocity correction maneuvers, the register count will be converted to an analog signal by means of a digital-to-analog converter.

This configuration is attractive relative to an unheated open loop configuration because the temperature induced gyro gain variations only affect the performance of the gyro rate loop and therefore do not influence the rest of the attitude control system. The rate loop can readily be designed to operate satisfactorily in the presence of the anticipated 2.8:1 gain change. Another advantage of this configuration is that rate and position signals are simultaneously available at all times and hence derived rate signals are not required during reorientation maneuvers. The disadvantages of this configuration are that the attitude control system is subject to the fixed drift and mass unbalance changes which are induced by the expected heat sink temperature variation estimated to be 60 degrees (total). Presently, little is known about the stability versus repeatability of gyro drift coefficients and coefficient sensitivities when subjected to

this environment. Another problem is the circuit complexity caused by the requirements for a VCO and digital-to-analog electronics.

The second configuration differs from the first only by the manner in which the spacecraft angular rate integration is accomplished. During acquisition maneuvers Switch No. 1 is closed and the gyro and its loop operate as an angular rate sensor. During those modes requiring spacecraft angular information, Switch No. 1 is opened and rate integration is accomplished by inserting a capacitor in series with the gyro torquer. In this case the electric charge on the capacitor equals the time integral of the torquing current. Hence the voltage across the capacitor is proportional to the angle through which the gyro has turned from its null position. During inertially referenced attitude hold maneuvers the position signal is servoed to null by means of the spacecraft attitude control system. To reorient the spacecraft the position signal is servoed to null as above but a precise current of appropriate sign is applied to the gyro torquer for a predetermined time interval. This causes the spacecraft attitude control system to turn through a desired angle along the axis in question. Note that in this configuration the gyro/capacitor combination serves as an angular null detector which is being continuously servoed to null by the spacecraft pneumatic system. Therefore the capacitor integration system is not required to measure the total angle through which the spacecraft moves but simply measures the servo angular error. Furthermore variations in the value of capacitance affect only the null detector scale factor and because of the configuration do not affect the magnitude of the steady state or final turn angle.

This configuration was successfully utilized in the Mariner 4 spacecraft and has the advantage that heater power is not required in order to avoid gyro gain variations. However, the design is considered more complex than necessary and is directly dependent on successful operation of the integrating capacitors. This component has a relatively large capacitor (~4000 μf) and hence is quite heavy, weighing approximately 1 pound per axis. The reliability of these capacitors is relatively unknown and would need substantiation.

3.4.2 Configuration 3: Closed-Loop with Pulsed Torquing

The use of pulsed torquing to cage an unheated single-degree-of-freedom gyro and to facilitate angular rate integration was considered for Configuration 3. The block diagram of a typical system is shown in Figure E-48. In this case the gyro rebalance current would be held constant and it would be applied to the torquer coil as a series of precisely timed constant intervals and each pulse would be applied in the proper direction to hold the instantaneous pickoff signal approximately at zero. The resulting train applied to the torquer is monitored by an up down counter which tallies the sign and magnitude of the net number of torque pulses (positive minus negative). In this case each pulse represents an increment of angle and the net angle that the spacecraft/gyro turned through is equal to the number of net pulses recorded at the end of the interval of interest.

The spacecraft angular rate is proportional to the net pulse frequency. In order to utilize this information for attitude control an analog signal is required, and is obtained by means of a frequency to analog converter. Also, to facilitate attitude control, analog position information is obtained near the register zero by means of a digital-to-analog converter. This converter operates only on the least significant digits over a wide enough angle to handle twice the largest anticipated error signal. Attitude hold maneuvers are performed by commanding the SCS to hold each of the gyro registers at zero.

Reorientation is obtained by inserting a number associated with the desired magnitude and direction of turn in the register and then commanding the ACS to move so as to drive that number to zero. As before, the number contained in the register at any time during the maneuver represents the remaining angle to be turned through.

Pulsed torquing is a relatively new technique and is currently in vogue for many inertial guidance applications. Basically the technique offers three advantages:

a) Improved effective torquer linearity

b) Constant torquer (and hence gyro) power dissipation

c) An output which is readily integrated (counted).

After a little consideration it is readily apparent that the above advantages are not required for the Voyager mission especially when compared with the circuit complexity required for the pulsed torque servo. Torquer linearity is not a requirement since only one precise command rate is needed, and the GRA can readily be calibrated at the desired rate (0.2 deg/sec). At the command rate the power dissipated in the gyro torquer was estimated at only 5 mw and is expected to have negligible effect on the gyro drift coefficients. Therefore, the desirability of having constant torquer power dissipation is not applicable. The output integration capability can more easily be obtained by the techniques described in the other configurations. Also, the circuit complexity required with pulsed torquing is formidable. The constant current source and the switches are quite complex, and this configuration also requires a frequency to voltage converter and a digital-to-analog converter.

3.4.3 Configurations 4 and 5: Open-Loop With and Without Heaters

These configurations are identical except that Configuration 4 utilizes temperature controlled gyros while Configuration 3 does not. The equipment for each axis is essentially identical; a typical axis (roll) will be described by referring to Figure E-49. In the acquisition mode Switch No. 1 is closed and the gyro is caged with an analog torquing signal. The electrical output is the voltage across the gyro torquer, and is proportional to the input roll rate from the spacecraft.

Reorientation of the spacecraft is achieved by opening Switch No. 1 in the roll gyro loop and closing the roll gyro current switch. The precise torquing current of the desired polarity is applied to the gyro torquer. The current is applied by command for a predetermined length of time and then the current switch is opened. The gyro then serves as the inertial reference during the reorientation of th other axis and the velocity correction maneuver. The same turning procedure is then

performed using the pitch gyro loop. When current is applied to the gyro torquer the float will move from pickoff null causing the gas jets to fire, resulting in spacecraft motion about the selected axis. This motion has an average rate equal to the angular rate associated with the torquer current, which is nominally 0.2 deg/sec. The angle through which the spacecraft is turned is controlled by commanding the polarity and length of time the current is applied to the torquer. The output voltage signal is proportional to spacecraft position and the gas jets act to move the spacecraft and drive this position signal to zero. The spacecraft rate (derived rate) information is obtained by passing this position signal through a lead network.

The switching sequence will be designed in such a manner that the gyros will always be caged by means of the rate loop (Switch No. 1 closed) prior to operating open loop (Switch No. 1 open). This will insure that the gyro floats will be at pickoff null prior to being utilized as an inertial reference in the attitude hold and reorientation modes.

During the attitude hold mode Switch No. 1 is opened and position and derived rate signals are obtained in the same manner as during the reorientation maneuver. The position signal is proportional to the angle through which the gyro input axis has turned and this signal is servoed to null by utilizing the gas jets to torque the spacecraft about the three axes.

The three gyros and their associated electronics will be mounted in a temperature controlled block. The temperature will be maintained by a proportional servo which applies DC power to an appropriate combination of gyro and block heaters. The gyro temperature sensors will be used as the temperature reference for the control electronics. Present spacecraft temperature design indicates a heat sink temperature range of 30 to 90°F, and in the worst case (30°F) approximately 9.6 watts of heater power will be required. These considerations are outlined in Figure E-50. Gyro and heater power are not required when the instruments are not being utilized. The gyro reference assembly specifications are given in Table E-5.

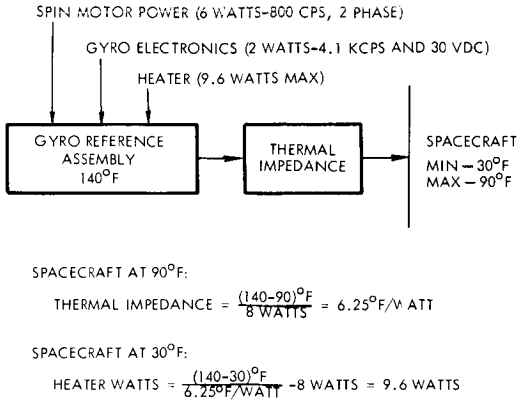


Figure E-50. Gyro Reference Assembly Thermal Model

Note that the heater power requirement in the worst case (30°F) is directly related to the amount of power dissipated in the reference assembly. The largest power sources are the gyro spin motors, which are currently undergoing considerable improvement. Manufacturers are quoting power requirements of 2 watts which is considered to be conservative. Should the actual gyros selected for Voyager dissipate less power than this, the required heater power would also be reduced. Loss of heater power would result in degraded SCS performance but would not be catastrophic. The gyros would continue to operate at reduced gain which would result in a larger SCS deadzone. The fixed drift coefficient would also be different from its value at the normal operating temperature.

Configuration 5 utilizes unheated gyros and was considered attractive because of the savings in heater power. However, the 60°F variation in heat sink temperature would result in a 2.8:1 change in gyro gain. In addition, the fixed drift coefficient would be subject to change as the temperature varied. Compensation for both of these effects might be utilized in the circuit electronics, however, at this time little information exists on the performance of inertial quality gyros when operated in this manner. Since heater power is available the more conservative design was chosen. Should spacecraft power requirements increase in the future, this area could be reinvestigated.

3.4.4 Configurations 6 and 7: Two-Degree-of-Freedom Gyros with VCO and Capacitor Integration

These configurations are identical to Configurations 1 and 2 except that two-degree-of-freedom gyros are utilized. At this time two-degree-of-freedom gyros are considered less desirable for this application since they have not been used previously in this manner and much less is known about their characteristics. Most two-degree-of-freedom units were designed for use on stable platforms and to date none have been utilized in the strapped down mode. Because of this situation their characteristics when operated in this manner are not wellknown and further detailed investigation would be required. One possible advantage of a system utilizing three of these gyros would be the axis redundancy obtainable. Circuits and commands would have to be provided to switch each control axis to the appropriate axes of either of two gyros. With this configuration, the system would operate normally in the presence of one gyro failure. However, the preliminary data available on gas bearing gyro failure rates is such that the impact of a gyro failure on the probability of mission success is small. Therefore the extra complexity required by the redundancy is probably not justified.

Note that the failure of a two-degree-of-freedom gyro is no worse than failure of a single-degree-of-freedom unit even though two spacecraft axes may be disabled. The reason for this is that failure of any one axis is catastrophic to the Voyager mission.

The two-degree-of-freedom gyros are not utilized in the open loop mode because it is not possible to obtain a unit with an input angular freedom of ±5 degrees.

There is one two-degree-of-freedom gyro that may merit further study before a final configuration is selected. The Autonetics G10 or G40 are small two-degree-of-freedom gyros which appear to have many desirable characteristics. They do not require heating, utilize a gas spin bearing, are not floated, and have no flex leads or gimbal bearings. They are a miniaturization of the Autonetics G6 gyro which has demonstrated a fantastically low failure rate in the Minuteman guidance system. The

spin motor power required in space would be less than 1 watt per gyro. A configuration based on this gyro would presumably have the desirable characteristics of high reliability low power and small size. However, not enough is known about the instruments to verify that they would meet the other design constraints required of the SCS. Further investigation in this area is intended.

4. SUN SENSORS DESIGN DETAILS

This section contains details of the sun sensor design including summaries of the specifications and a parts count. In addition, the calculations of sun sensor response are presented.

4.1 Coarse Sun Sensors

4.1.1 Pitch Coarse Sun Sensor Assembly (signal amplifier not included)

Type	Immersed solar cells back-to-back
Size	1 in. diameter x 0.5 in. thick
Weight	0.15 lb
Power	None required
Components	1/2 in. diameter solar cells (2)
	1/8 watt metal film resistor (1)

4.1.2 Yaw Coarse Sun Sensor

Same as pitch coarse sun sensor.

4.1.3 Coarse Sun Sensor Preamplifier for both Pitch and Yaw Axes

Size	1 x 1 by 1.5 inches
Weight	0.15 lb
Power	150 mw
Components	1/8-watt metal film resistors (8) ua 702A integrated circuit amplifiers (2) ceramic capacitors (2)

4.1.4 Coarse Sun Sensor Performance Data

Field of view	4 πsteradians
Linearity	$\pm$ 10 per cent for $\pm$20 deg about null plane (each axis)

Null accuracy	Between 0.5 and 1 deg
Temperature range	-50 to +140°F

4.2 Fine Sun Sensor

4.2.1 Fine Sun Sensor Assembly (signal amplifier not included)

Type	Silicon solar cell - shaded quad
Size	1.5 x 1.5 x 2 in.
Weight	0.2 lb
Power	None required
Components	silicon solar cells (4) 1/8-watt metal film resistors (2)

4.2.2 Fine Sun Sensor Preamplifier (dual channel, handles two-axis signals)

Same as coarse sun sensor preamplifier.

4.2.3 Switching Sensor

Type	Silicon solar cell with pinhole optics
Size	0.5 in. diameter x 0.75 in. long
Weight	0.06 lb
Field of view	10 deg half-angle cone
Power	None required
Components	silicon solar cell, 1 x 1 cm (1)

4.2.4 Fine Sun Sensor AGC Amplifier (Optional)

Type	Pulsewidth modulation
Size	1.5 x 1.5 x 1 in.
Power	200 mw
Weight	0.2 lb
Components	transistors (2) 1/8-watt metal film resistors (10) diodes (2) tantalum capacitor (1) ua 702A integrated circuit amplifiers (2) ceramic capacitors (2)

4.2.5 Fine Sun Sensor Performance

Field of view	10 deg half-angle cone
Null accuracy	0.1 deg in each axis

Linearity	Better than 10 per cent within field of view
Scale factor	Changes less than 10 per cent with 300 per cent change in illumination if optional AGC amplifier is used; if AGC amplifier is not used, scale factor varies in direct proportion to solar energy.
Temperature range	0 to 110°F

4.2.6 Solid-State Switch and Pitch Output Amplifier

Components	ua 702A integrated circuit amplifier (1) chopper transistors (2) 1/8-watt metal film resistors (8) ceramic capacitor (1)
Power	200 mw
Size	1 cu in.
Weight	0.10 lb

4.2.7 Solid State Switch and Yaw Output Amplifier

Same as for pitch.

4.3 Sun Sensor Response

The output signal levels for the sun sensor designs considered in the text were determined from test data and published specifications of the detector manufacturers. Verification of the theoretical linearity of the quad cell design is presented in Figure E-51.

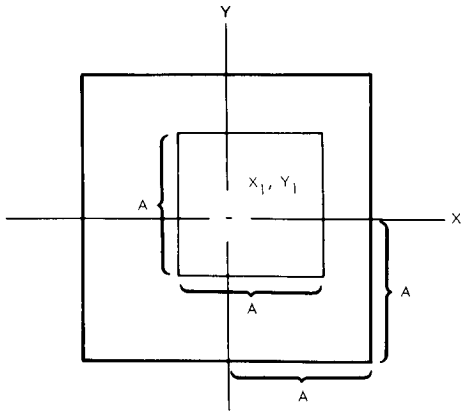


Figure E-51. Verification of Theoretical Linearity of Quad Cell Design

Let

A_1 = illuminated area of quad cell No. 1

A_2 = illuminated area of quad cell No. 2

A_3 = illuminated area of quad cell No. 3

A_4 = illuminated area of quad cell No. 4

V_{13} = difference in voltage of cells 1 and 3 assuming identical load resistance

V_{24} = difference in voltage of cells 2 and 4 assuming identical load resistance

where

$$A_1 = (a/2 + x_1)(a/2 + y_1) \qquad -a/2 \le x_1, y_1 \le a/2$$
$$= a^2/4 + a/2\,(x_1 + y_1) + x_1 y_1$$

$$A_2 = (a/2 - x_1)(a/2 + y_1)$$
$$= a^2/4 + a/2(y_1 - x_1) - x_1 y_1$$

$$A_3 = (a/2 - x_1)(a/2 - y_1)$$
$$= a^2/4 - a/2(x_1 + y_1) + x_1 y_1$$

$$A_4 = (A/2 + x_1)(a/2 - y_1)$$
$$= a^2/4 + a/2(x_1 - y_1) - x_1 y_1$$

If the cells are operated in the "short circuit current" mode, the signal will be directly proportional to the area illuminated for each cell. Thus, $V_{13} = K(A_1 - A_3)$, and $V_{24} = K(A_2 - A_4)$. Substituting the expressions for A_1, A_2, A_3, and A_4 produces the following result:

$$V_{13} = Ka(x_1 + y_1)$$

$$V_{24} = Ka(y_1 - x_1)$$

It may be noted that the displacement of the light spot from the center of the quad may be related to the pitch and yaw angles of the sun in the following fashion

$$x_1 = d \tan \theta \quad \text{where } \theta = \text{yaw angle}$$
$$y_1 = d \tan \psi \quad \text{where } \psi = \text{pitch angle}$$
$$\text{and } d = \text{distance from mask to detector plane}$$

Since the fine sun sensor is to be used only for angles less than 10 degrees, the tangent function is very nearly linear. Thus V_{13} and V_{24} may be combined by means of a linear summing network to provide signals which vary

linearly with the pitch and yaw angles. The nonlinearity of the tangent function may be canceled to some extent by increasing the load resistance of the cells to such a point that voltage saturation is approached, introducing nonlinearity in the opposite direction.

5. NEAR EARTH DETECTOR DESIGN DETAILS

This section contains details of the near earth detector design. A design summary is presented. The details of the calculation of earthshine magnitude are given together with the response available with various detectors.

5.1 Design Summary

5.1.1 Assembly

Type	CdS photocell
Size	1.75 in. diameter x 3 in. long
Weight	0.25 lb
Power	150 mw
Components	CdS photocells (NSL-54 or equivalent) (2) 1/8-watt metal film resistors (6) 1/4-watt carbon composition resistors (2) ua702A integrated circuit amplifiers (2) Transistors, silicon, low power (2) Ceramic capacitor (1) Tantalum capacitor (1) Miniature transformer (1)

5.1.2 Performance

Detects earth presence within 10 degree half-angle cone during first 10 days of Voyager mission.

5.2 Earthshine Magnitude Calculation

The illuminance from a diffusely reflecting element of area will be derived to compute the earthshine magnitude (Figure E-52). Assume that a reflecting surface dA is illuminated from an angle β away from normal with an irradiance I_s. Assume that dA diffusely reflects a fraction K_r of the energy reaching it in a lambertian fashion, so that

the reflected illuminance I varies as the cosine of the angle Γ from the normal to dA:

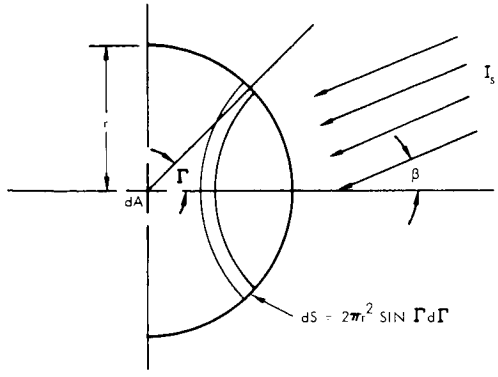


Figure E-52. Geometry of Earthshine Calculation

If the illuminance along the normal to dA is I_o, then

$$I = I_o \cos \Gamma \tag{E.74}$$

The amount of energy received by dA is $dAI_s \cos\beta$. Thus the total reflected energy is $K_r dAI_s \cos\beta$, so that we may write

$$\int_S Ids = K_r I_s \cos\beta \, dA \tag{E.75}$$

where S is the surface of a hemisphere

Hence π_2

$$\int_o I_o \cos\Gamma \, 2\pi\Gamma^2 \sin\Gamma \, d\Gamma = K_r I_s \cos\beta \, dA \tag{E.76}$$

$$I = I_o \cos\Gamma = \frac{K_r I_s}{\pi r^s} \cos\Gamma \cos\beta \, dA \tag{E.77}$$

Equation (E.77) may now be applied to the earthshine calculation problem. Consider the geometry in Figure E-53.

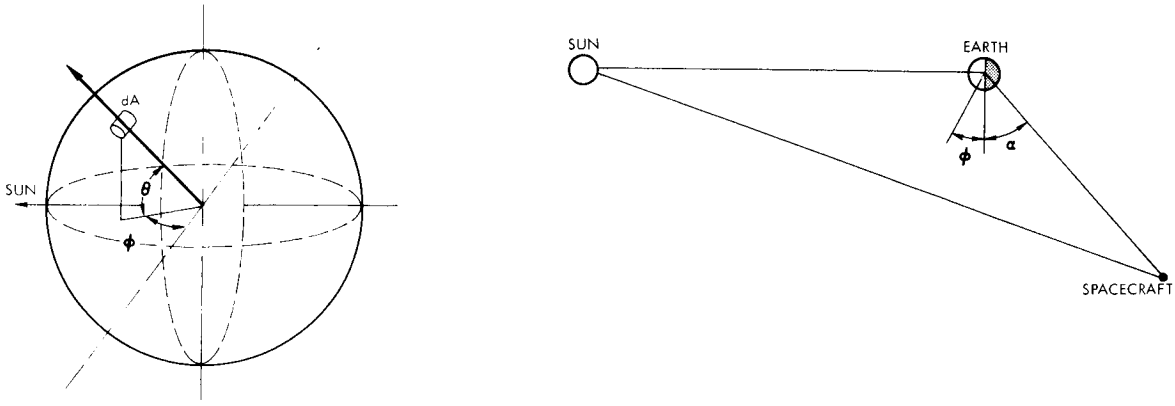


Figure E-53. Sun-Earth-Spacecraft Relationship

The light from dA at the spacecraft, dI, is given by Equation (E.77) to be

$$dI = \frac{K_r Is}{\pi r^2} \cos \Gamma \cos\beta \, dA$$

where

β = angle between sunlight and dA normal

Γ = angle between spacecraft and dA normal

r = distance from spacecraft to earth

Since for the case being considered the angle subtended by the earth at the spacecraft is less than 1 degree, the line from the spacecraft to any area dA on the earth may be considered parallel to the line from the spacecraft to the earth's center. With this approximation,

$$\cos\beta = \cos\theta \cos\phi \qquad \text{(E.78)}$$

$$\cos\Gamma = \cos\theta \cos(\phi + \alpha) \qquad \text{(E.79)}$$

$$dA = r_e^2 \cos\theta \, d\theta \, d\phi \qquad \text{(E.80)}$$

where

r_e = radius of earth

θ, ϕ and are as shown in Figure E-53.

Let θ_e = angle subtended by earth's diameter. Within a very good approximation,

$$\theta_e = 2\frac{r_e}{r} \tag{E.81}$$

Integrating over proper limits to find the illuminance from the visible sunlit portion of the earth,

$$I = \frac{K_r I_s \theta_e^2}{\pi 2} \int_{0=0}^{\frac{\pi}{2}} \int_{0=0}^{\frac{\pi}{2} - a} \cos^3\theta \left[\sin\phi \cos\phi \cos a - \sin^2\phi \sin a\right] d\phi d\theta$$

$$= \frac{K_r I_s \theta_e^2}{2\pi} \int_0^{90^\circ} \cos^3\theta \left[\frac{1}{2} \sin^2\left(\frac{\pi}{2} - a\right) \cos a - \sin a \left(\frac{\frac{\pi}{2} - a}{2} - \frac{\sin(\pi - 2a)}{4}\right)\right] d\theta \tag{E.82}$$

$$= \frac{K_r I_s \theta_e^2}{6\pi} \left[\cos^3 a - \left(\frac{\pi}{2} \sin 2a - a\right) \sin a\right] \tag{E.83}$$

After 10 days of the Voyager mission,

$$\theta_e = 0.0058 \text{ rad}$$

$$\text{and } a = 20 \text{ deg or } 0.35 \text{ rad}$$

These conditions provide less energy than at any previous time in the mission. For a conservative result, take $K_r = 0.2$. The sunlight at the earth is known to be very nearly 140 mw/cm^2.

Evaluating Equation (E. 83) for the conditions 10 days after launch,

$$I = \frac{(0.2)(140)(5.8 \times 10^{-3})^2}{(6)(3.14)} [0.833 - .342(1.57 - 0.32 - 0.35)]$$

$$= 2.63 \times 10^{-5} \text{ mw/cm}^2 \tag{E.84}$$

5.3 Near Earth Detector Response

5.3.1 Solar Cell Detector

Assume that a 2-inch diameter lens is used to focus earthshine onto a solar cell 0.2 inches square. The short circuit current response of a solar cell of this size is,

$$I_{sc} = .05 \text{ ma per mw/cm}^2 \text{ solar irradiance}$$

The irradiance is given by the result found in Section 5.3.3 times the ratio of lens area to cell area, neglecting losses:

$$\text{Irradiance} = (2.63 \times 10^{-5})\,(\quad/.04) \quad = 2.1 \times 10^{-3} \text{ mw/cm}^2$$

The calculated short circuit current is,

$$I_{sc} = 0.105 \text{ μa}$$

For such low light levels, the short circuit current of the cell will flow through a relatively high impedance since the voltage remains quite low. A reasonable load resistance for the solar cell would be 10 kphms. The voltage across this load resistance would be approximately:

$$V = (10^4)\,(.105 \times 10^{-6}) \cong 1 \text{ millivolt}$$

5.3.2 Photo Transistor

The following characteristics are published for the GS-600 photo transistor:

Active area ≅ 0.010 x 0.010 in.

Sensitivity ≅ 1 ua with 0.01 mw/cm^2 irradiance from a 2870°K source

Maximum dark current = 25 nanoamperes at 25°C

The spectral response of the photo transistor (a silicon device) is essentially the same as that of the silicon solar cell. For the solar cell response characteristic, 1 milliwatt of solar energy produces the same output

as 1.7 milliwatts of 2870°K blackbody energy. Thus, the effective sensitivity would be:

I_c = 1.7 μa for 0.01 mw/cm^2 of solar energy, where

I_c = collector current of photo transistor

To obtain a sufficiently large field of view for the detector, the illuminated spot must be 0.1 inch in diameter as a minimum. The lens diameter required to produce 0.01 mw/cm^2 at the detector plane, using the result of Section 5.3.3 is determined by the equation:

$$(2.63 \times 10^{-5})\left(\frac{D_{lens}}{0.1}\right)^2 = 10^{-2}$$

$$D_{lens} = 1.95 \text{ in.}$$

Assuming a collector resistance of 5000 ohms, the 1.7 μa current would produce a signal voltage of 8.5 millivolts. If a 1-inch focal length lens were used, the field of view would be approximately a cone with a half angle equal to the arc tangent of the spot radius divided by the focal length, or $\tan^{-1}\left(\frac{.050}{1.0}\right) = 2.65$ degrees.

5.3.3 Cadmium Sulfide Photocell

Assuming the same lens and spot size that was used for the photo transistor, the illuminance on the detector would be:

I = 0.01 mw/cm^2 within the spot, solar spectrum

This illuminance is equivalent to approximately 0.93 footcandle, in terms of photometric units which are used by the manufacturer. For a CdS cell, 0.93 footcandle of solar energy is equivalent to only about 0.56 footcandle of energy from a 2870°K color temperature source.

A typical CdS photocell is the NSL-54. For this cell, the 0.10 inch diameter light spot covers about 1/10 of the photosensitive area. Since

all of the photoresistive material acts like resistors in parallel, the call may be treated by means of the model in Figure E-54.

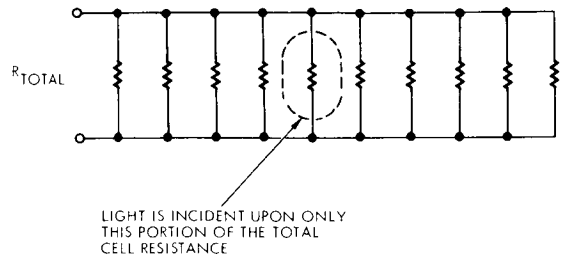


Figure E-54. Model of Typical CdS Photocell

In the dark, the total resistance of the CdS cell is 0.1 megohm. Thus, each of the 10 parallel resistors of the model has a dark resistance of approximately 1 megohm.

From the manufacturer's data, with 0.56 footcandle illumination from a 2870°K source the total resistance of the cell is 1 kohm if the cell is uniformly illuminated. Therefore, each of the 10 parallel resistors would have a resistance of 10 kohms when exposed to 0.56 footcandle of 2870°K energy. Hence the resistance with only one of the 10 elements illuminated, as in the near earth detector application, the resistance of the cell would be

$$R = \left(\frac{1 \text{ megohm}}{9}\right) \Big\| \text{ 10 kohms}$$

$$\cong \text{ 10 kohms}$$

6. STAR SENSOR DESIGN DETAILS

This section contains details of the Mariner C Canopus tracker and the quadrant photomultiplier star sensor discussed in Section 1.5.

6.1 Mariner-C Canopus Tracker

6.1.1 General Sensor Features

The sensor consists of a wide field of view, corrected lens, a diaphragm, filters, image dissector tube and deflection yoke plus electronics for processing signals. A simple sun sensor shutters the star sensor to protect it from solar radiation above a thresholded value of 1000 ±100 foot candles.

An image dissector has the following advantages over other electronically scanned tubes like vidicon or image orthicon for the following reasons:

a) Image dissectors with resolution of up to 1000 TV lines per inch are presently available with up to 2-2/4 inch diameter screens.

b) The photocathode screen is not damaged if one small elemental area is scanned for long periods of time. This is not true of vidicons, to the same degree, and orthicon tubes are notoriously poor in this respect.

c) The image dissector does not employ a thermionic electron gun, therefore power consumption is low, the tube less complex, and more reliable.

d) Signal-to-noise levels are adequate for tracking and image display. The tube employed in the tracker has the following characteristics:

Spectral response	S-11 (λpeak = 4500 Å)
Quantum efficiency	10.5 percent
Sensitivity	05 amps-watt^{-1}
Diameter of photocathode	1.5 in.
Resolution	up to 1000 lines/in.
Aperture	slit configuration 0.010 x 0.138 in.
Total tube length	7.5 in.

6.1.2 Operational Procedure

The sun sensor acquires and tracks the sun, and the vehicle roll axis is directed along the sun line. Rotation about the roll axis is commanded. The instantaneous field-of-view is 0.86 in. in roll, 11 degrees in pitch. Total pitch coverage of 30 degrees is provided by the commanded step function. The instantaneous FOV is scanned ±2 degrees about the sensor roll axis. The entire cone angle can be stepped digitally by command from earth in order to encompass greater pitch coverage to handle all trajectory geometries. Six distinct cone angle

positions, each 4.6 degrees form the preceding step, are incorporated. The initial step is set at prelaunch.

The performance requirements include reliable performance in environments with temperature variations from 0 to +100°F. A ±3 per cent power voltage variation is permissible, with a frequency variation of ±1 per cent.

Null offset (angle accuracy) between electronic null and mechanical axis pointing does not exceed ±0.1 degree arc. At null, total noise output is less than 100 mvolts peak-to-peak, which corresponds to a 0.013 degree error or 45 arc seconds.

A maximum roll signal level of 14.0 VDC is allowed. The roll time constant does not exceed 0.5 seconds. Radio command switching of cone angle steps, triggered by a 100 milliseconds pulse at 25 volts amplitude, must have a response time of 1 second or less.

A low gate raises the signal output voltage from 0 VDC to 12 VDC when the 0.25 Canopus threshold is surpassed. If signal fluxes indicate four x Canopus flux, the voltage will drop from +12.0 VDC to 0.0 VDC in 0.5 second, or less.

Power requirements are limited to 100 volts peak-to-peak with a 2400 cps square-wave. Power dissipation allowed is 3 volts maximum in the track mode and 6 volt maximum in the safety mode with the sun shutter operational.

6.1.3 Design Considerations

Because the magnitude of the pitch angle varies from 74 to 106 degrees elevation with respect to the roll axis, or ±16 degrees about yaw axis, pitch gimbaling is required and is performed electronically.

A list of major components and subsystems are given below with a brief description of their operation.

a) Optics - Semisolid Schmidt-Cassegrain. Consists of an aspheric corrector and a fuzed quartz meniscus lens. The FOV = 32 x 4 degrees; a 0.8 in. focal length at F/1.

b) Image Dissector Tube - CL-1147 by CBS Laboratories. Uses fiber optics corrector in front of tube to match flat image plane with curved surface of photocathode. The tube is 1-1/2 in. diameter and 7-1/2 in. over-all length. Nominal power is 27 milliwatts. It is ruggedized by heliarc welding - glass to metal construction. Instantaneous field if 0.86 degrees in roll, 12 degrees in pitch. Actual anode slit 0.010 roll x 0.128 in. pitch.

c) Pitch Digital-to-Analog Converter. Develops the six-step angle gimbaling deflection voltages in accord with preprogrammed register drive.

d) Up-Down Shift Register Counter. Combines a 5-bit ring counter with incremental control logic and a clock oscillator to cycle the ring.

e) Roll Sweep Generator. The horizontal (roll) sweep is generated by amplitude-controlled 1000 cps sinusoidal oscillator-buffer and balanced output circuits to provide reference to demodulator.

f) Preamplifier. Augments gain of electron multiplier and provides needed impedance transformation to following circuitry.

g) Narrowband Filter for Nulling.

h) Phase Sensitive Demodulator. To detect phase of the sensed error and outputs bipolar DC roll error signal.

i) Wideband Filter. Extracts fundamental and harmonic components of star signal (proportional to star intensity) and drives high voltage dynamic gain control of the image dissector.

j) High Voltage Power Supply.

k) Acquisition Gates.

l) Pitch-to-Roll Coupling Network.

m) Sun Shutter.

n) Power Supplies.

These components are indicated in Figure E-55. The sensor characteristics are shown in Table E-7.

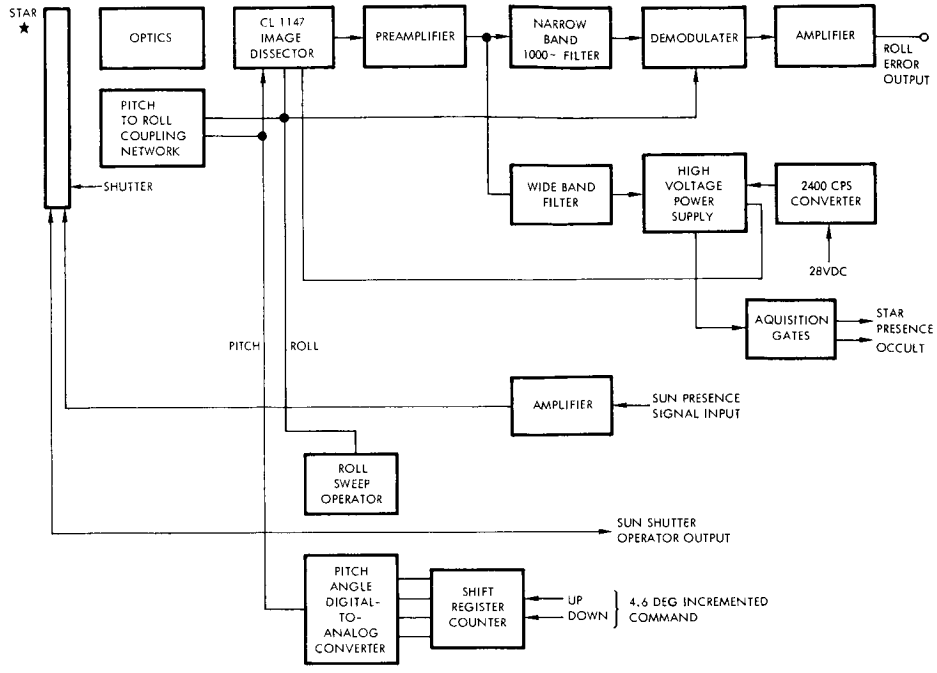


Figure E-55. Block Diagram for Star Tracker No. 1 - Mariner C

Table E-7. Mariner-C Canopus Tracker Characteristics

Total field of view	4 deg (roll) x 30 deg (pitch)
Instantaneous field of view	0.86 deg (roll) x 11 deg (pitch)
Gimballing	all electronic
Roll	continuous sinusoidal sweep
Pitch	six positions - 4.6 deg/position
Sensitivity (threshold set)	+0.6M to -2.4M
Null offset	±0.1 deg
Error gradient (at null)	8 volts/deg
Equivalent noise	0.013 deg peak-to-peak
Time constant (roll axis)	0.5 sec
Optics	0.8 in. F/1.0 semi-solad Cassegrain Schmidt
Size	4 x 5 x 11 in.
Weight	6 lb
Power	1.8 watts (average)

6.2 Quadrant Photomultiplier Star Tracker

6.2.1 Operation and Design Features

The quadrants of the phototube are biased in the following sequence: 1 and 4, 2 and 3, as shown in Figure E-56. Each pair is switched on for 625 microseconds and the switching system must be capable of

switching 170 volts between each photocathode quadrant and the first dynode at this rate. Four high voltage switching transistors are utilized. The processing of signals by pairing provides the one-axis operation without altering the tube electronic or structural configuration.

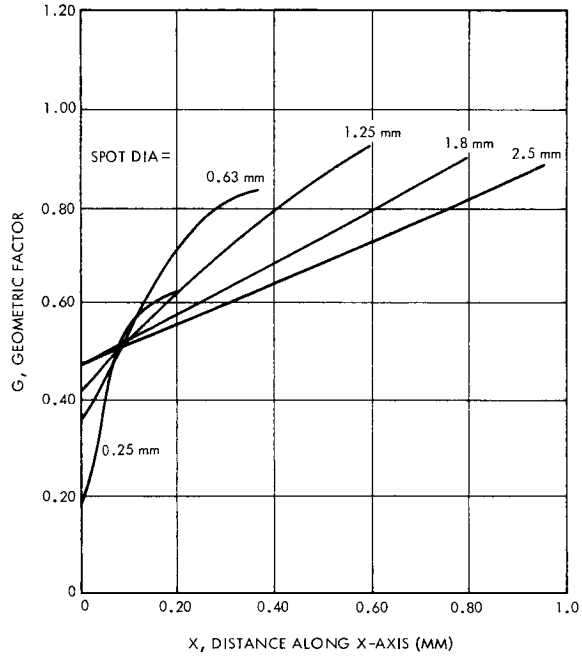


Figure E-56. Geometric Factor - The Fraction of Circular-Image Area

The switching network (see Figure E-57) is driven by a 1.6 kc clock generator which is synthesized by half save rectifying the 400 cps signal supplied by the power supply, then filtered and amplified at the 4th harmonic. This 4th harmonic of the 28 volts, 400 cps voltage is 1.2 volts. When the star is centered between quadrants 1 and 4, and 2 and 3 of the phototube, pulses of quadrants 1 plus 4 will equal pulses of quadrants 2 plus 3, and no 800 cps roll error component will be present. If these pulses are not equal, the roll channel produces a 800 cps error signal which is fed to a filter, amplifier and emitter follower, whose output is proportional to roll errors. If desired a slightly different switching mode may be used resulting in a 1600 cps star presence signal not vanishing at null in addition to the roll error signal.

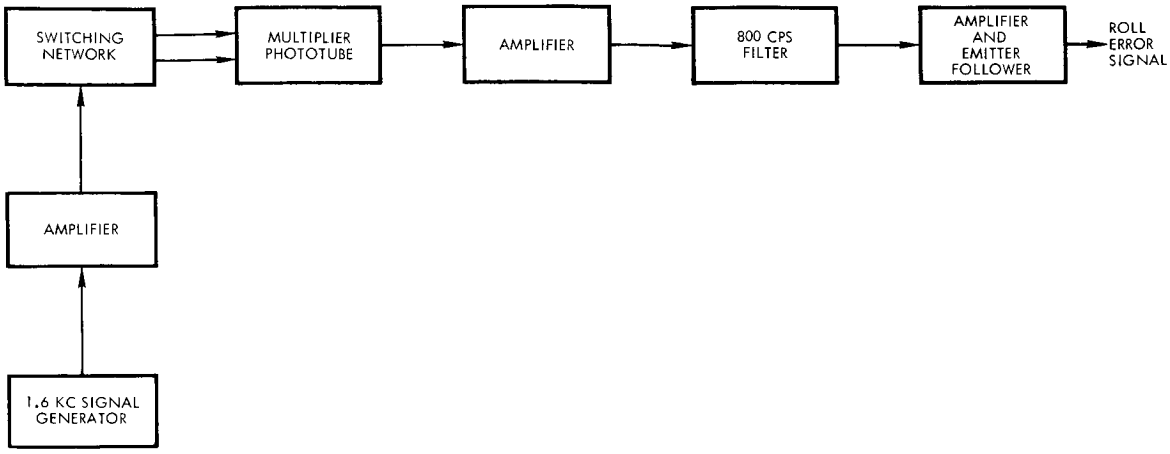


Figure E-57. Possible Block Diagram, One Axis Quadrant Multiplier Phototube Star Tracker

a) Power, Weight, and Volume Estimates

	Input Power	Weight (lb)	Volume (in^3)
Star Tracker	3.91 watts	3.10	100
Converter	(80 percent efficiency)	0.40	15
Optics			
Phototube		0.80	7
Lens		0.20	2
Housing		1.50	80
	5.35 watts (28 VDC)	6.00	204

b) Estimated Parts Count Considering Discrete Components

	Star Tracker Electronic	Converter Electronics
Transistor	16	8
Diode	5	7
Resistor	73	22
Capacitor	44	8
Coil	4	2
Transformer	-	4
Integrated Circuits	8	-

6.2.2 Quadrant Multiplier Phototube (QMP)

This tube contains four independent and adjacent semi-transparent photocathode quadrants in a common image plane. For single axis

tracking two of the four photocathode segments are biased off by means of a retarding field, while emission from the other pair is collected by the electron multiplier. With a sequential operation, the photocathode quadrants perform the function of multiple phototubes in an all-electronic nulling type tracker. No rotating reticles or mechanical modulators are required in the optics. Because the photosurfaces are process in common, and represent portions of a single layer, the quadrants possess identical sensitivity and spectral response.

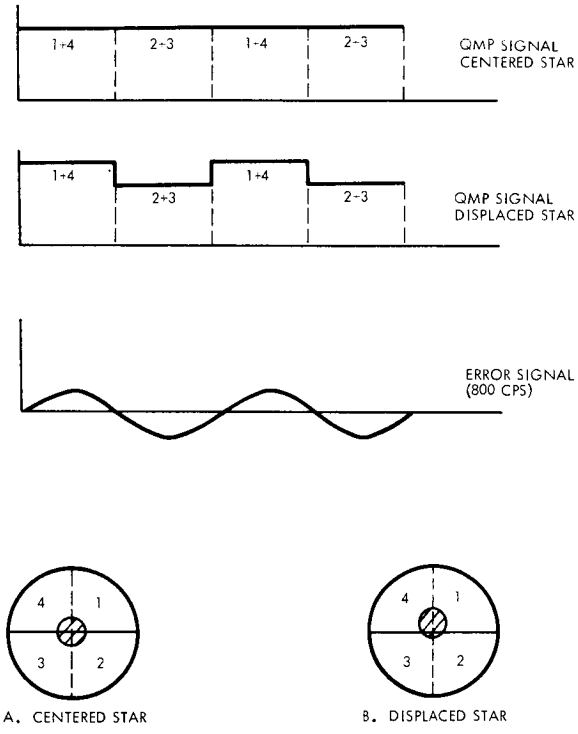


Figure E-58. QMP Signals and Filtered Error Signal

The image of a small source like a star is blurred deliberately by the optics to an optimum spot diameter. On-center imaging produces equal signals (null) from each quadrant pair. Figure E-58 indicates a centered and noncentered star position with the appropriate QMP output and error signal waveforms. For any position of the star image center on the photocathode, the anode output current due to emission from quadrants 1 and 4 is

$$I_{1+4}(x) = \frac{K}{2.51} m S L g(x) \gamma(x)$$

where

$K = 2.65 \times 10^{-10}$ lumens/cm^2 *

m = The visual magnitude of Canopus, -0.9

*Allen, C. W. Astrophysical Quantities, p. 191; London the Athlone Press, 1963.

S = Anode luminous sensitivity to the flux of Canopus = 175 amps/lumen with gain of 10^6 *

L = Lens collecting area = 3.2 cm^2

g(x) = Geometric factor which is dependent on size of image and displacement from the null center (see Figure E-56)

$\gamma(x)$ = Col ection efficiency dependent upon the same parameters due to the incomplete collection of photoelectrons from an on cathode (see Figure E-59)

x = Displacement from null of image center

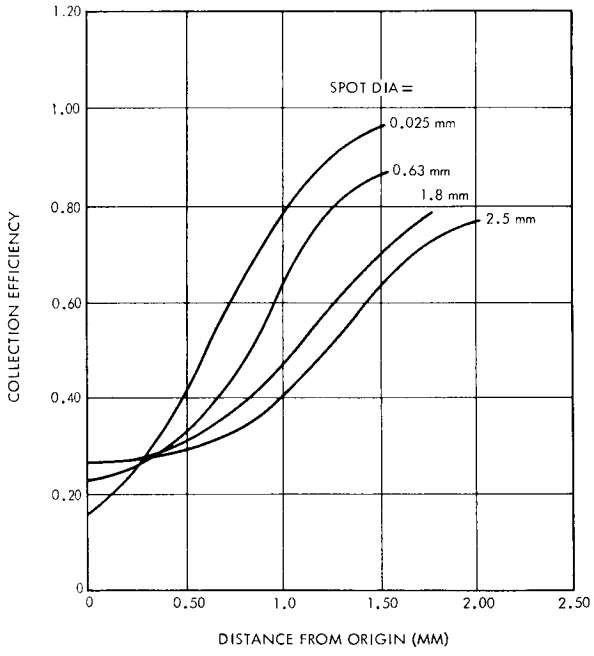


Figure E-59. Collection Efficiency as a Function of Distance from Center Along a Line 45 Degrees to the X-Axis for Various Image Sizes

---

*Computed from Canopus spectral irradiance $H_\gamma\left(\frac{\text{watts}}{\text{cm}^2}\right)$, detector spectral responsivity R $\frac{\text{amps}}{\text{watt}}$ and the visibility curve $V_\gamma\left(\frac{\text{lumens}}{\text{watt}}\right)$:

$$S = \frac{\int_0^\infty R_2 H_\lambda d}{\int_0^\infty V_\lambda H_\lambda d}$$

The quantity of interest is the difference signal between the two quadrant pairs corresponding to a certain star image displacement in the pitch direction. For displacements greater than the star image radius this difference is given simply by Equation (E. 85), since no flux is incident upon pair 2 and 3. For displacements less than this, however, the contribution from the opposing pair must be considered. For these displacements the analysis is simplified by assuming a constant collection efficiency and a geometric factor with constant slope. The data presented in Figures E-56 and E-59 verify this assumption with the spot diameter fixed at 0. 25 mm. If the image center is displaced a small amount x in the direction of quadrants 1 and 4:

$$I_{1+4}(x) = I_{1+4}(0) + \left(\frac{dI_{1+4}}{dx}\right)_{x=0} x$$

and

$$I_{2+3}(x) = I_{2+3}(0) - \left(\frac{dI_{2+3}}{dx}\right)_{x=0} x$$

The difference signal resulting, from which the error signal may be derived is:

$$I_e(x) = I_{1+4}(x) - I_{2+3}(x)$$

$$I_e(x) = 2\left(\frac{dI_{1+4}}{dx}\right)_{x=0} x$$

Since $I_{2+3}(x)$ and $I_{4+1}(x)$ are the same function. Under the previously stated assumptions:

$$\left(\frac{dI_{1+4}}{dx}\right)_{x=0} = \frac{K}{2.51^m} SL\ \gamma(0)\left(\frac{dg}{dx}\right)_{x=0} x$$

so

$$I_e = \frac{2K}{2.51^m} S L \gamma(0) \left(\frac{dg}{dx}\right)_{x=0} x \qquad \text{(E-86)}$$

The peak-to-peak amplitude of the 800 cps roll error signal is given directly by I_e. For large displacements of the star center, greater than the image radius, the error signal is given by $I_{1+4}(x)$. The peak amplitude of the filtered 800 cps sine wave output from the processing circuitry will be designated as the output error signal $I_{oe}(x)$:

$$I_{oe}(x) = \begin{cases} \frac{2}{\pi} I_e\ (x), & x < \text{image radius} \\ \frac{2}{\pi} I_{1+4}(x), & x > \text{image radius} \end{cases} \qquad \text{(E.87)}$$

The performance of the sensor will be determined by the signal-to-noise ratio as a function of star displacement. To evaluate this parameter it is necessary to know the sensor noise level. Although several noise sources are present, only that noise originating at the photomultiplier cathode and first dynode is significant. Noise sources further down the processing chain are effectively suppressed by the high gain of the multipliers. The noise current output referred to the dector anode is given by the well known expression:*

$$i_n = \left[2e\, I_c \left(\frac{g}{g-1}\right) F\right]^{1/2} G \text{ amps, rms} \qquad \text{(E-88)}$$

where:

e = charge on the electron, 1.6×10^{-19} coulombs

I_c = total cathode current, light + dark

g = multiplier gain per stage $\cong 2.7$

*V. K. Zworykin and E. G. Ramberg, "Photo electricity and its Application," John Wiley and Sons, Inc., 1949, pp. 148-150, 258.

F = output bandwidth, 10 cps

G = total multiplier gain, $2.7^{14} = 10^6$

Since the luminous input from Canopus is $\sim 10^{-9}$ lumens and the equivalent dark current input of the photomultiplier is $\sim 10^{-11}$ lumens the dark current component may be ignored in I_c. For displacements less than an image radius the cathode light current for a given quadrant pair is essentially:

$$I_c = \frac{1}{G} I_{1+4} \quad (0)$$

Inserting the parametric values in Equations (E. 85), (E. 86) and (E. 88) above:

$$I_{1+4}(0) = 0.0104 \text{ microamps}$$

$$I_e(x) = 0.324x \text{ microamps}$$

$$i_n = 0.000227 \text{ microamps}$$

From Equation (E. 87) then, for displacement less than an image radius:

$$S/N = 907\ X \qquad \text{(E. 89)}$$

Equation (E. 89) expresses the ratio of the peak value of the roll error signal to the rms sensor noise. Figure E-60 is a plot of signal-to-noise ratio vs displacement. This curve has been extended and includes displacements in excess of the image radius.

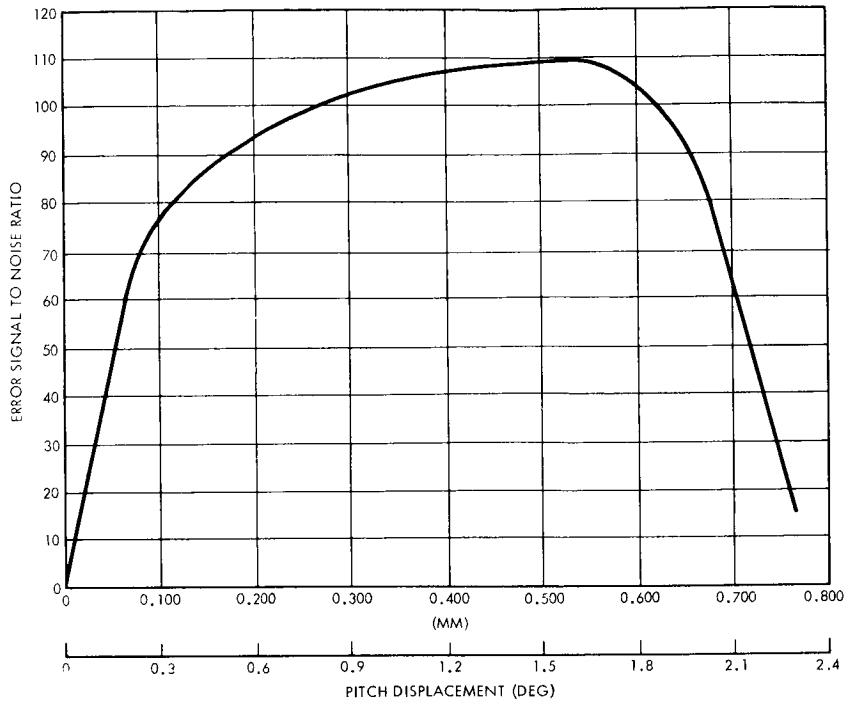


Figure E-60. Signal-to-Noise Ratio, QMP Canopus Sensor, 0.25 mm Image, 10 cps Bandwidth

REFERENCES

E-1. McElvain, R. J., "Effects of Solar Radiation Pressure Upon Satellite Attitude Control," Progress in Astronautics and Rocketing, Edited by R. E. Roberson and J. S. Farrior, Academic Press, New York, 1962.

E-2. Sabroff, A. E., "A Summary of Gravity Gradient Stabilization of Earth Satellites," STL Report No. 9990-6715-RU000, July 1964, pp. 1.2 to 1.6.

E-3. Nidley, R. A., "Gravitational Torque on a Satellite of Arbitrary Shape," ARS Journal, Volume 30, February 1960, pp. 203-204.

APPENDIX F

TELECOMMUNICATIONS STUDIES

Seven studies bearing on the conclusions concerning the communications and data handling problems of the Voyager spacecraft are incorporated in this appendix. The first section evluates the turn around ranging system performance. The capsule-to-spacecraft link is then analyzed in detail in Section 2, leading to conclusions concerning the design of this element of the communication subsystem. In the third section, the performance of the pseudonoise synchronizer is examined analytically. PN synchronization is then compared with NRZ synchronization in Section 4, and conclusions are reached on that basis concerning the relative capabilities of one-channel and two-channel telemetry links with respect to the Voyager goals. Telemetry acquisition and recognition is discussed in Section 5, followed in Section 6 by an analysis of the threshold criteria for the phase-lock receivers in the spacecraft and at the ground station. Finally, the telemetry measurements list as now conceived for the Voyager spacecraft telemetry is given at the end of the appendix.

1. RANGE AND RANGE RATE ANALYSIS

The Voyager mission will utilize a coherent, two-way range and range rate tracking system. Since the PN ranging code is simply turned around in the spacecraft transponder, the critical question is the effect of the up-link or turn-around noise on the over-all tracking performance. A similar analysis is required for the reconstructed carrier; this is performed in Section 4.

The signal-to-noise ratio as received at the spacecraft in 3.3 Mc is shown versus range in Figure F-1. As the S/N becomes negative, the noise power suppresses the signal in the limiter. Since the scale factor of the phase detector depends on the incident signal level, the recovered up-link code modulation is also suppressed. Eventually the turn-around noise in the video baseband will dominate the down-link phase modulation of the carrier resulting in power lost to the useful signals, the PN range

code and the carrier. Thus, the up-link S/N into the limiter must be kept above some threshold.

In addition to the turn-around ranging analysis (Section 1.1), DSIF acquisition procedures and carrier and ranging acquisition times are given in Section 1.2. Finally, the range and range rate accuracies are evaluated in Section 1.3.

1.1 Turn-Around Ranging Analysis

1.1.1 General Analysis

A block diagram of the turn-around ranging channel in the spacecraft transponder is shown in Figure F-2. The uplink signal is hard limited in the receiver IF and then demodulated by the phase detector. The uplink spectrum at baseband is then filtered and amplified to the proper level for the desired downlink PRN modulation index by the turn-around ranging channel amplifier. The output of the amplifier then modulates the downlink phase modulator along with the downlink communications.

The output of a bandpass limiter with input signal plus gaussian noise has been analyzed by Davenport.* Although Davenport's results are for an unmodulated sinewave signal, they will be used here for the modulated sinewave signal present at the limiter input. Davenport's complex expressions for the limiter output signal and noise terms can be approximated by the following expressions

$$P_s = \frac{1}{2}\left(\frac{4L}{\pi}\right)^2 a_s^2 \qquad (F.1)$$

$$P_n = \frac{1}{2}\left(\frac{4L}{\pi}\right)^2 a_n^2 \qquad (F.2)$$

*W.B. Davenport, Jr., "Signal-to-Noise Ratios in Bandpass Limiters," J. Appl. Phys., Vol. 24, June 1953.

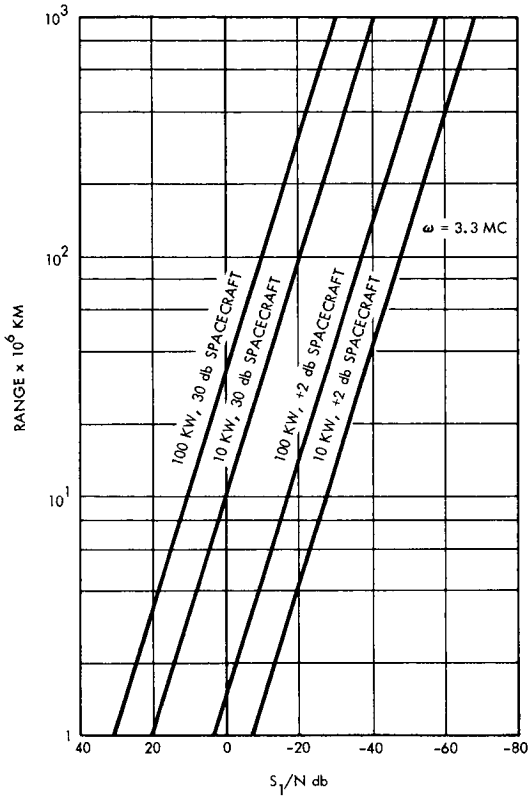


Figure F-1. Received S/C Signal-to-Noise Power Ratio vs. Range

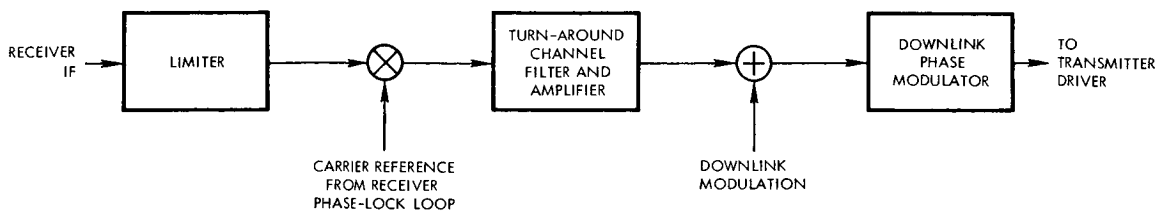


Figure F-2. Spacecraft Transponder Turn-Around Ranging Channel

where P_s is the limiter output signal power, P_n is the output noise power, L is the limiter output voltage level before filtering, a_s is the limiter signal suppression factor, and a_n is the noise suppression factor. Since the limiter is a constant output device, the sum $P_s + P_n$ should be constant. With a_s and a_n as given below, the sum is constant within about 1.0 db over the full range of limiter input signal-to-noise ratio—$(SNR)_i \equiv 1/\beta$.

$$a_s^2 = \frac{(SNR)_i}{\frac{4}{\pi} + (SNR)_i} = \frac{1}{1 + \frac{4}{\pi}\beta} \qquad (F.3)$$

$$a_n^2 = \frac{1}{1 + 2(SNR)_i} = \frac{\beta}{\beta + 2} \qquad (F.4)$$

The noise spectral density at the input to the phase detector is equal to

$$\Phi = \frac{P_n}{B_L} = \frac{\frac{8L^2}{\pi^2} a_n^2}{B_L} \qquad (F.5)$$

where B_L is the limiter output noise bandwidth. The input signal to the phase detector is equal to

$$S(T) = \sqrt{2P_s} \sin\left\{\omega_{IF}t + \sum_{i=1}^{N} \theta_i \cos\left[\omega_i t + \gamma_i(t)\right] + \theta_U m(t)\right\} \qquad (F.6)$$

where

ω_{IF} = Reciver IF frequency

ω_i = i^{th} uplink subcarrier frequency

θ_i = i^{th} uplink subcarrier modulation index

$\gamma_i(t)$ = i^{th} uplink subcarrier modulation waveform

N = Number of uplink sinusoidal subcarriers

m(t) = PRN ranging waveform (±1)

θ_U = PRN ranging uplink modulation index

The output of the phase detector (product demodulator) is given by

$$S_o = S(t)\left(\sqrt{2}\cos\omega_{IF}t\right) \quad \text{(less } 2\omega_{IF} \text{ terms filtered out)}$$

$$= \sqrt{P_s}\sin\left\{\sum_{i=1}^{N}\theta_i\cos\left[\omega_i t + \gamma_i(t)\right] + \theta_U m(t)\right\} \qquad \text{(F.7)}$$

Equation (F.7) reduces to the following form after expansion into a Bessel function series.

$$S_o = \sqrt{P_s}\left\{\sum_{i=1}^{N} 2J_1(\theta_i)\prod_{\substack{j=1\\ j\neq i}}^{N} J_o^2(\theta_i)\cos\theta_U\cos\left[\omega_i t + \gamma_i(t)\right] + \left[\prod_{i=1}^{N} J_o(\theta_i)\sin\theta_U\right]m(t) + \text{higher order sidebands}\right\} \qquad \text{(F.8)}$$

The gain of the amplifier is set such that under strong signal conditions the PRN modulation index on the downlink carrier is equal to some desired value θ_D. Under strong signal conditions $a_s = 1$. Therefore, the voltage gain of the amplifier is equal to

$$G_V = \frac{\theta_D}{\frac{1}{\sqrt{2}}\left(\frac{4L}{\pi}\right)\prod_{i=1}^{N} J_o(\theta_i)\sin\theta_U} \qquad \text{(F.9)}$$

With unity phase modulator gain, the downlink modulation indices of the uplink subcarriers and the PRN ranging code are obtained from Equations (F.8) and (F.9). Higher order products of the uplink subcarriers are also present in the turn-around channel but will be small so their effect on the downlink will be ignored.

$$\theta_i' = \left[2\frac{J_1(\theta_i')}{J_o(\theta_i')}\right]\frac{a_s\theta_D}{\tan\theta_D} \qquad \text{(F.10)}$$

$$\theta_D' = a_s\theta_D \qquad \text{(F.11)}$$

where

θ_i' = Effective downlink modulation index of ith uplink subcarrier

θ_D' = Effective downlink PRN modulation index

The noise spectral density at the amplifier input is equal to the IF noise spectral density given in Equation (F.5). therefore, the noise power at the amplifier output is given by

$$\sigma_n^2 = \frac{8L^2}{\pi^2}\left(\frac{a_n^2 B_V}{B_L}\right)G_V^2 \qquad (F.12)$$

where B_V is the noise bandwidth of turn-around ranging video amplifier. The rms noise level into the phase modulator is therefore

$$\sigma_n = \left[\frac{\sqrt{\frac{B_V}{B_L}}}{\prod_{i=1}^{N} J_o(\theta_i)}\right]\frac{a_n \theta_D}{\sin \theta_U} \qquad (F.13)$$

Phase modulation of a carrier by gaussian noise* results in a spectrum about the carrier of about the same shape as the input noise spectrum. The power in the carrier after modulation by the noise is reduced by the factor $\exp(-\sigma_n^2)$. Consequently, since a PM spectrum is a convolution of the modulating waveform spectra, the downlink carrier is reduced in power by the turn-around noise and uplink subcarriers in the following amount.

$$\text{downlink power reduction} = e^{-\sigma_n^2\left[\prod_{i=1}^{N} J_o^2(\theta_i')\right]} \qquad (F.14)$$

This power loss represents unwanted modulation of the downlink carrier. Additionally, the uplink noise appears in the sidebands of the downlink carrier. The uplink noise power receiver at the ground station is equal to

*J.L. Stewart, "The Power Spectrum of a Carrier Frequency Modulated by Gaussian Noise," Proc. IRE, October 1954.

$$\text{received uplink noise power} = \left(1 - e^{-\sigma_n^2}\right) S_g M_c \left[\prod_{i=1}^{N} J_o^2(\theta_i')\right] \cos^2 \theta_D' \qquad \text{(F.15)}$$

where

S_g = Received signal power at ground receiver

M_c = Carrier reduction or modulation loss due to downlink communications

This noise is detected and will add to the ground receiver system noise. It is assumed that the detected uplink noise occupies the same bandwidth as the bandwidth of the turn-around ranging channel in the spacecraft. This bandwidth in most cases should be wide enough to occupy at least as large a bandwidth as the ground receiver noise. Therefore, the receiver effective noise spectral density becomes

$$\text{effective noise spectral density} = \Phi_g + \frac{\left(1 - e^{-\sigma_n^2}\right) S_g}{B_V} M_c \left[\prod_{i=1}^{N} J_o^2(\theta_i')\right] \cos^2 \theta_D' \qquad \text{(F.16)}$$

where

Φ_g = Ground station spectral noise density in absence of turn-around noise

1.1.2 Applications to Voyager

Equations (F.11), (F.14) and (F.16) summarize the effects of uplink noise and subcarriers in the PRN ranging channel. The downlink PRN deviation θ_D' is reduced from its strong signal value θ_D

$$\theta_D' = \frac{\theta_D}{\sqrt{1 + \frac{4}{\pi}\beta}} \qquad \text{(F.11)}$$

where β is the uplink SNR at the input to the transponder limiter. The turn-around noise extracts power from the carrier and ranging channels

$$\text{Modulation loss due to uplink noise} = e^{-\sigma_n^2} \qquad \text{(F.14a)}$$

where σ_n is the downlink phase deviation caused by noise and is defined in Equation (F. 13). Finally, the downlink noise spectral density is effectively increased by the uplink noise density as follows:

$$\text{Effective noise spectral density} = \Phi_g \left[1 + \left(1 - e^{-\sigma_n^2} \right) \cos^2 \theta_D' \left(\frac{S}{N} \right)_{g, B_V} \right] \tag{F. 16a}$$

where only the ranging signal and turn-around noise are assumed present.

For Voyager it is desired to have ranging information up to Mars encounter plus 1 month. Since this will also constitute the worst case insofar as uplink noise effects are concerned, we will determine the ranging channel requirements at this range (250 million kilometers). Reference to the design control table for ranging (Volume 2, Section 5. 3. 3) shows that at this range, employing the 100 kw DSIF transmitter and the spacecraft high-gain antenna, the received SNR in 3. 3 Mc is -9. 5 db ($\beta = 9$). This means the signal suppression factor is

$$\alpha_s \cong \pi/4\beta$$

and the noise suppression factor is

$$\alpha_n \cong 1$$

Therefore, the downlink noise phase modulation is

$$\sigma_n^2 \cong \frac{1}{2} \frac{\theta_D^2}{\sin^2 \theta_U^2} , \quad B_V = \frac{1}{2} B_L$$

which indicates that the downlink PRN deviation should be minimized and uplink deviation maximized (consistent with carrier tracking requirements) in order to minimize the modulation loss caused by uplink noise as well as its contribution to the overall noise spectral density at the DSIF receiver. The latter effect is small in any case, less than 0. 1 db in the control table (Item 29).

1.1.3 Link Optimization

For a carrier phase modulated by a turn-around PN code and uplink noise, the total power P_T is distributed as follows:

$$\text{Carrier power, } P_C = P_T \cos^2 \theta_D' \, e^{-\sigma_n^2}$$

$$\text{Ranging power, } P_R = P_T \sin^2 \theta_D' \, e^{-\sigma_n^2} \qquad (16)$$

Given the relative power requirements of the carrier and ranging channels, the optimum PN code deviation can be found. The carrier requires 6 db in $2B_{LO} = 12$ cps (Appendix 4) or 16.8 db in 1 cps. The ranging threshold is taken as 21 db/cps (Section 4.2). Assuming the total noise spectral density at the ground receiver is the same for both channels, we have

$$\frac{P_R}{P_C} = \tan^2 \theta_D' = 2.61 (+4.2 \text{ db})$$

and

$$\theta_D' = 1.02 \text{ rad}$$

If we take $\theta_U = 1.25$ rad as the maximum practical uplink deviation (resulting in a carrier modulation loss of 10 db), then

$$\theta_D = K\theta_U = 1.25 \, K = \sqrt{\frac{4\beta}{\pi}} \, (1.02) \text{ rad}$$

Since θ_D is the strong signal downlink deviation in the absence of noise, the turn-around factor K must be unity or less unless the uplink index is changed during the flight. This limits the allowable $\beta = N_1/S_1$ at the transponder input under high noise conditions. Namely, taking K = 1 as an upper limit

$$\beta \leq \frac{\pi}{4}\left(\frac{1.25}{1.02}\right)^2 = 1.18 \, (0.7 \text{ db})$$

The high gain antenna (30 db) and 100 kw transmitter will give a predetection ranging SNR of -9.5 db as mentioned above. The optimum downlink index (1.02 rad) cannot be achieved; instead, the nominal index will be $\theta_D' = 0.356$ rad.

Setting the turn-around gain K at unity, therefore, the phase noise deviation is

$$\sigma_n^2 = 0.772 \text{ rad}^2$$

and the modulation loss due to uplink noise is

$$10 \log e^{-\sigma_n^2} = -4.34\sigma_n^2 = -3.35 \text{ db}$$

The modulation losses due to the PN code are

$$10 \log \sin^2 \theta_D' = -9.17 \text{ db}$$

$$10 \log \cos^2 \theta_D' = -0.57 \text{ db}$$

The total carrier loss is 3.35 + 0.57 = 3.92 db and the ranging channel loss is 12.52 db. Thus, the total ratio of signal-to-noise density required is

Carrier: 16.8 + 3.92 = 20.7 db in 1 cps

Ranging: 21.0 + 12.52 = 33.5 db in 1 cps

To the ranging threshold must be added the effect of the uplink noise density. For the present case the effect is less than 0.1 db.

1.2 DSIF Acquisition Procedures

JPL technical memorandum 33-83, pages 43-45, discusses the DSIF acquisition procedures. There are four different functions for the tracking mode acquisition. These are: (1) pointing the antenna in the direction of the spacecraft, (2) tuning and locking the receiver to the spacecraft transmitted frequency, (3) locking the spacecraft receiver to the earth transmitted frequency, and then (4) establishing range lock.

1.2.1 Frequency Acquisition

Frequency standards for the earth stations will be atomic clocks whose drift errors will be less than 2 parts in 10^{11}. If the spacecraft oscillators have a stability accuracy of 1 part in 10^{7}, then the frequency uncertainty on the uplink is ± 212 cps and the uncertainty on the downlink is ± 230 cps.

When a priori information on the spacecraft velocity and receiver frequency is known, the earth receiver must search the frequency uncertainty region until the earth receiver is locked onto the received signal from the spacecraft. For a threshold PLL bandwidth of 12 cps, a SNR of 6 db is required or 16.8 db in 1 cps. A sweep speed of 6 cps/sec is used. Therefore, the time to determine acquisition on the downlink is

$$T_{AD} = \frac{460}{6} = 92 \text{ seconds} = 1.5 \text{ minutes}$$

The second step is to vary the frequency of the earth transmitter until it locks into the frequency of the spacecraft. Here it is necessary to account for the large time delays between the earth and spacecraft. At each frequency setting, it is necessary to wait for lock verification from the spacecraft.

Thus, the time per setting is

$$(T + \text{total delay time}) \doteq 27 \text{ minutes}$$

With a sweep speed of 6 cps/sec the time for 420 cycles uncertainty is 424/6 = 70 seconds = 1.2 minutes.

The delay time is 27 minutes at 2.5×10^{8} km. Thus, the total time for acquisition of frequency on the uplink is 1.2 + 27 = 28.2 minutes.

After the spacecraft oscillators are locked to the received signal, it may be necessary to retune the earth receiver to lock to the received signal from the spacecraft.

The total time for acquiring the up and downlink lockup is

$$T_{total} = \underbrace{28.2 \text{ minutes}}_{\text{up}} + \underbrace{1.5 \text{ minutes}}_{\text{down}} = 29.7 \text{ minutes}$$

1.2.2 Ranging Acquisition

After two-way lock has been obtained, range measurements may be made. This measurement is realized by modulating the carrier with a PN coded signal. At the earth receiver the phase of this received signal is compared with a similar reference signal. After synchronization is obtained, this phase difference is a measure of the transmission range. Tracking circuits will then keep the received and reference signals in synchronization.

The multiple-component lunar code for the DSIF Mark 1 ranging system is composed of four PN sequences of periods of 11, 31, 63, and 127 bits. It is possible to determine the phase of the composite sequence by separately determining the phases of the component sequences. This requires at most 11 + 31 + 63 + 127 or 232 total correlations. The length of this composite sequence is (11)(31)(63)(127) or 2.73×10^6 bits. Since the clock frequency is 500 kc the length of this code is 5.5 seconds after the clock is modulo 2 summed with the PN code. The acquisition technique is discussed by Easterling.* Since the PN components in the ranging code are nearly orthogonal, very close results may be obtained by using the performance characteristics of orthogonal codes. In order to use these results it is important to specify what is meant by a bit of information for the ranging situation.

It is usually assumed that there is no a priori information available about the range. Thus, for a component of the composite code with a period p_1, there are p_1 equally probable phases of the received code. The amount of information is then $\log_2 p_1$ bits. Figure F-3** shows the word error probability $P_W(n)$ versus the received signal energy per bit divided by the noise power spectral density or ST_B/N_o for orthogonal codes.

*S. Golomb, Digital Communications, Prentice Hall, Chapters 6 and 7.

**A. J. Viterbi, "On Coded Phase-Coherent Communications," JPL Report 32-35, Section IV, August 1960.

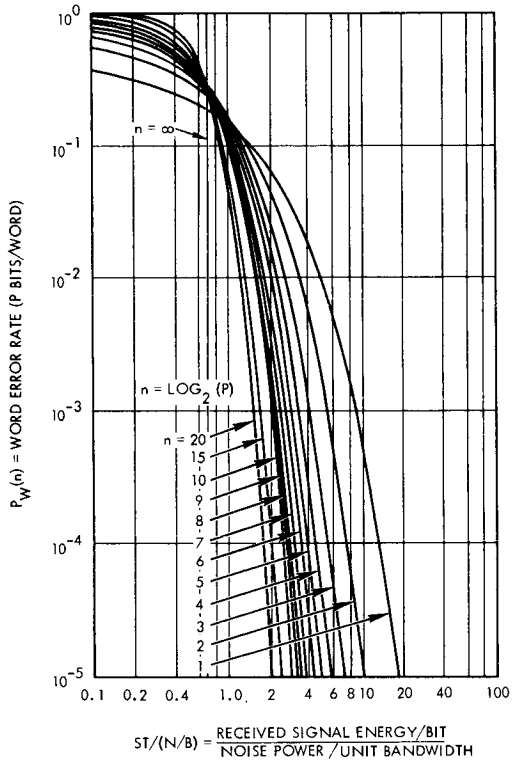


Figure F-3. Word Error Probability Orthogonal Codes

The amount of information in the code is $\log_2 p = n$ bits. Since the duration of the coded word is T seconds, the transmitted information rate is

$$R = \frac{n}{T} \text{ bits/second}$$

Or, equivalently, the time required to transmit one bit is

$$T_B = \frac{T}{n} \text{ seconds/bit}$$

The error probability is determined by the basic system parameter ST_B/N_o. The numerator is controlled by the communicator whereas the denominator is determined by the channel. The error probability $P_W(n)$ as a function of ST_B/N_o is a measure of a comparison for signal sets of different size p. In our problem T is the required integration time for a given $P_W(n)$.

To illustrate the technique, consider the component code of length 127.

$$p = 127 \text{ bits}$$

$$n = \log_2 p = 6.98$$

Let $X = ST_B/N_o$, then for $P_W(n) = 10^{-3}$

$$X = 2.5$$

$$T_B = \frac{2.5}{\frac{S}{N_o}}$$

From Figure F-3, consider the threshold case for which the signal-to-noise density ratio $(S/N_o) = 21$ db/cps (Section 4.2). Therefore,

$$T_B = \frac{2.5}{1.26 \times 10^2} = 1.98 \times 10^{-2}$$

The required integration time

$$T = nT_B = 6.98 \times 1.98 \times 10^{-2}$$

$$T = 140 \text{ ms}$$

Note that T = 1100 periods of the 127 microsecond code.

The change in correlation level during acquisition of any of the codes is 25 per cent or 1/4. This is the same as saying 1/16 of the total power in the signal affects the indicated correlation level for any one code. Thus, the total integration time must be increased by 16 to obtain the required period.

In addition, since the set integration cannot be varied from component to component, the worst case component must be selected. Finally, the integration times are available only in binary multiples of a major machine cycle (124 μsec). From the ranging system specification DFN-1003-FNC,

the integration time nearest 140 ms is 2^{10} x 124 μsec = 127 ms. The resulting acquisition time for the above conditions is

$$T_A = 16 \times 0.127 \times 232$$

$$= 471 \text{ seconds or } 7.9 \text{ minutes}$$

To this time must be added the time to acquire the 500 Kc range clock and about 1 second for other system delays.

1.3 Range and Range Rate Performance

1.3.1 Range Rate Accuracy

It has been shown* that for a two-way coherent doppler measuring system, the rms error in measuring frequency is

$$\sigma_n(\delta f) = \frac{1}{\pi\sqrt{2}\,T}\,\sigma_n(\phi) \qquad \text{(F. 17)}$$

where

T = Smoothing time, seconds

$\sigma_n(\phi)$ = Rms phase jitter in loop noise bandwidth

The specified DSIF frequency measurement accuracy is 0.003 meters/sec. A reasonable allowance for the error in range rate because of noise is 0.001 meters/sec or 3 parts in 10^{12}. The S/N is determined from the power budgets. In particular, at doppler tracking threshold, the effective loop jitter is 1 radian. The integration time T is

$$T = \frac{1}{\pi\sqrt{2}\,\sigma_n(\delta f)} = 70 \text{ sec}$$

since

$$\sigma_n(\delta f) = \frac{1}{2}(3 \times 10^{-12})(2 \times 10^{9}) = 0.003 \text{ cps}$$

---

[5] J.A. Develet, Jr., "Fundamental Accuracy Limitations in a Two-Way Coherent Doppler Measurement," IRE Trans. on Space Electronics and Telemetry, September 1961.

Of course, a complete analysis of the doppler measurement would consider other sources of error: oscillator stability, quantization, uncertainty in the velocity of light, propagation anomalies.

1.3.2 Ranging Accuracy

The ranging noise error results from phase jitter on the VCO output of the range clock PLL. The rms range error $\sigma_n(R)$ in terms of the phase jitter $\sigma_n(\phi)$ is

$$\sigma_n(R) = \frac{c}{2\omega_{cl}} \sigma_n(\phi)$$

$$= \frac{3 \times 10^2}{2\pi} \sigma_n(\phi)$$

for a 500 Kc clock. The phase jitter as a function of loop SNR is (for SNR >10)

$$\sigma_n(\phi) = (2S/N)^{-1/2}$$

Besides the tracking performance threshold there is an absolute ranging threshold set by the probability of losing range clock lock during the acquisition procedure. With the Mark I ranging system, for example, during acquisition of the X component of the code, the recovered clock is 1/4 (-12 db) of the fully-correlated level. Following Springett,* we take as an absolute threshold 9 db SNR in the minimum Mark I bandwidth of $2B_{LO}$ = 0.8 cps, requiring a ranging signal-to-noise ratio of 9 + 12 + 1 = 22 db in $2B_{LO}$ or 21 db in 1 cps. The additional one decibel accounts for the $8/\pi^2$ loss caused by tracking only the clock fundamental.

*J. C. Springett, "Telemetry and Command Techniques for Planetary Spacecraft," Technical Report No. 32-495, Jet Propulsion Laboratory, January 15, 1965.

For a signal 12 db above absolute threshold, the loop bandwidth will have expanded to about 5.5 cps. The loop S/N will then be 13.6 db and

$$\sigma_n(R) = \frac{3 \times 10^2}{2\pi} (45.7)^{-1/2}$$

$$= 7 \text{ meters rms}$$

It must be remembered that several other sources of error—loop dynamics, oscillator noise, phase instability in spacecraft and ground equipment, quantization and time measurement—have been ignored in this analysis. However, the noise error computed above is not inconsistent with the specified accuracy of ±15 meters given in Specification No. DFN-1003-FNC.

2. CAPSULE LINK ANALYSIS

2.1 Scope

The capsule link mission requirements and the normal mission profile are defined. Analysis of propagation effects, frequency uncertainties, and operating frequency optimization is performed. A noncoherence FSK communication link is selected, and performance parameters and constraints defined for the spacecraft and capsule equipment.

2.2 Mission Description

2.2.1 Mission Profile

The over-all mission for the link between the capsule and the spacecraft is divided into three basic phases: during the first (separation) phase, the capsule transmits back to the spacecraft at short range for checkout purposes. This phase will receive minimal emphasis here since, because of the short range, the only problem is to avoid deleterious effects due to spacecraft receiver overload. The second (entry) phase involves transmission during the pre and postblackout phases until the landing has been achieved. This is the most important phase of the mission. The third (postland) phase involves transmission to the orbiting spacecraft following capsule impact. This is of secondary importance to the mission and is not a firm requirement.

The communication requirements are an information rate of 10 bits per second minimum at a bit error probability rate of 10^{-3} for this link by itself.

2.2.2 Mission Parameters

A number of physical parameters are associated with the entry and postlanding phases of the mission. These are tabulated in Tables F-1 and F-2 and are discussed below. The values used in these tables are drawn from the discussions presented in other sections of the appendix.

For a number of the parameters, high and low limit values are shown which show the range of variation as the entry angles and atmospheric models used are varied. In the subsequent analyses the worst case parameters will be used.

Table F-1. Entry Profile Parameters

Spacecraft to Capsule Range	40,000 km maximum
Capsule Entry Geometry	See Figure F-4
Capsule Entry Angles (γ_e)	45 to 90 degrees
Descent Time	
Entry to impact	5 to 20 min
Postblackout to impact	4 to 19 min
Maximum Deceleration During communications	14 g (earth G)
(Supersonic Chute deployment)	
Descent Velocity[1] During Communications	
Immediately postblackout	10,000 ft/sec (approx)
During chute descent	40 to 230 ft/sec
Capsule to Mars Vertical Range	
Start of entry	800,000 feet (approx)
End of blackout	70,000 to 300,000 feet (approx)
Parachute Swing	$\pm 6^{\circ}$ max
Spacecraft Velocity [1]	15,000 ft/sec

Table F-2. Postland Parameters

Spacecraft to Capsule Range	
Immediately post-impact	40,000 km (approx)
Orbital phase	5,000 to 21,000 km

[1] Velocity with respect to Martian surface

Figures F-4 and F-5 illustrate the entry geometry as it relates to the communication problem.

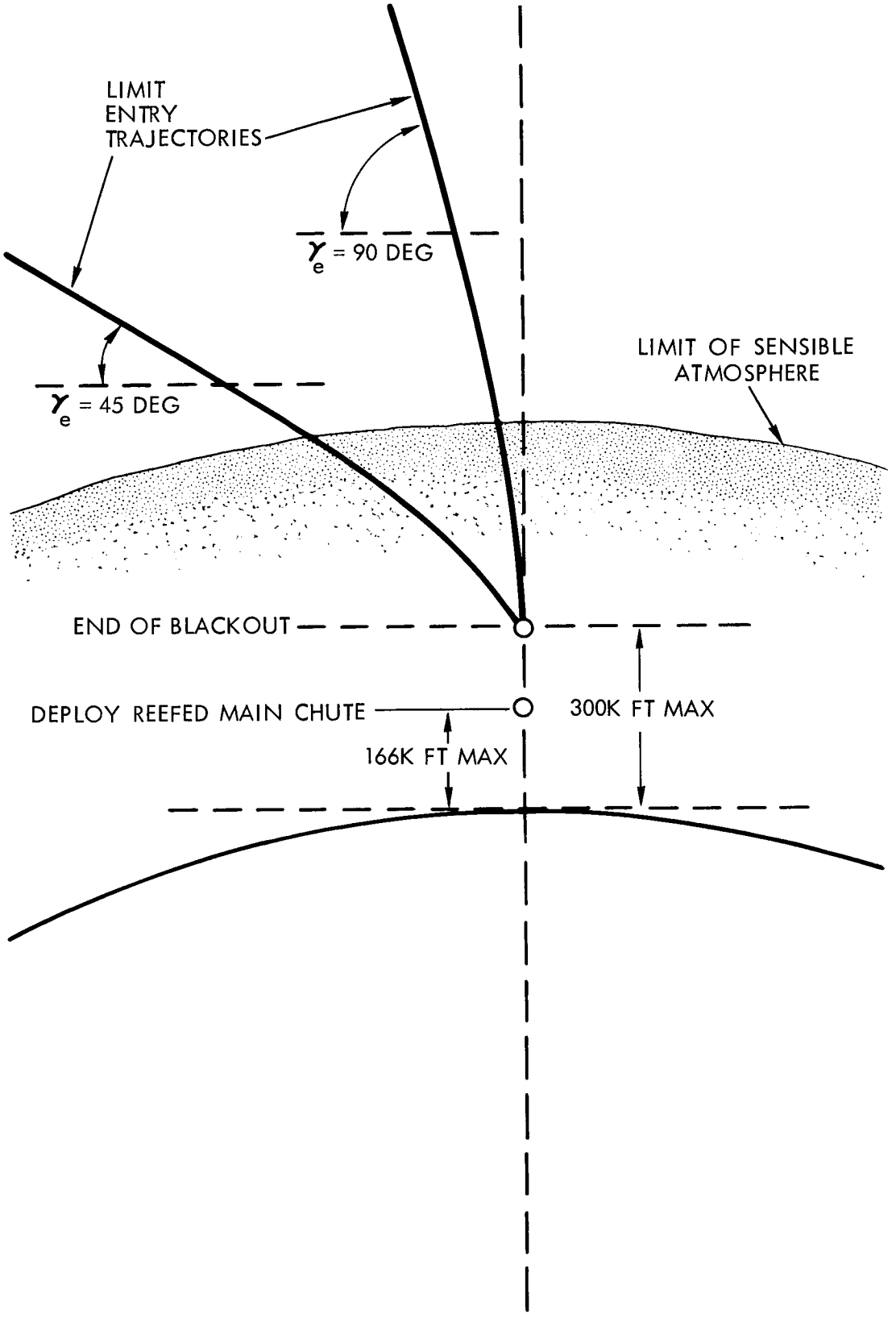


Figure F-4. Entry Geometry

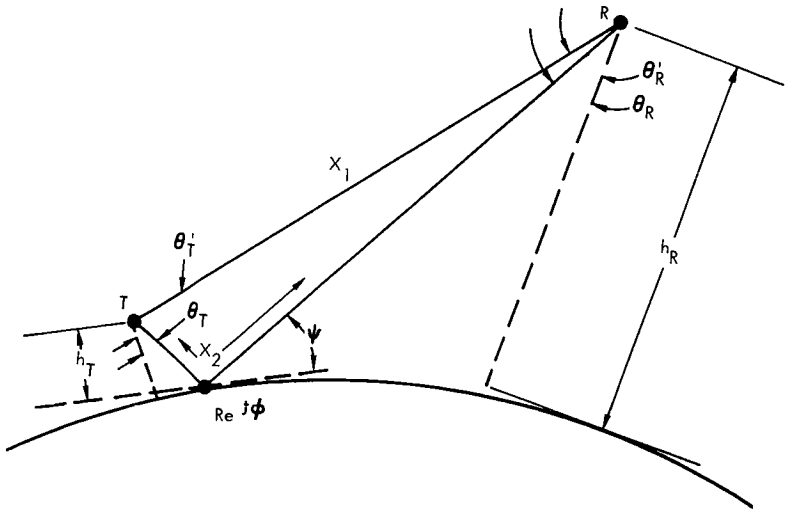


Figure F-5. Two Signal Model for Multipath

2.3 Systems Synthesis and Analysis

2.3.1 Radio Propagation

a. Introduction

To a first approximation, the Mars atmosphere may be considered to be transparent for radio signals in the VHF region and above, and at grazing angles close to 90 degrees. Present information about the surface of Mars is that it approximates the desert regions on Earth. As the capsule leaves the blackout region, the effect of the reflected signals from the surface of Mars on the resultant received signal starts to become important. It is in this region of increasing signal fading that the scientific measurements are most important. During entry the grazing angle increases and the effect of fading due to multipath increases. It is desired to keep this angle at least 45 degrees. A large angle is also desired for a large visibility region between the capsule and spacecraft. Also, the larger this angle, the larger the discrimination between the direct and reflected rays due to the directivity pattern of the capsule antenna.

b. Derivation of Equation of Carrier Signal

A rigorous analysis of the multipath effect may be made by considering the vector relationship of the direct and indirect signals at the receiving antenna terminals. Since the reflecting surface will vary with distance because of its physical nature and topography, and the path of each reflected signal will be different, the resultant signal at the receiver antenna will be random. In addition, the spacing between the capsule and spacecraft will be changing in time. The solution of this problem is quite complex and time does not permit a rigorous solution. However, a simple two signal model shown in Figure F-5 will permit an understanding of the basic problem. The justification of this simple model requires further investigation.

The following analysis closely follows Reed and Russell.*

$R = Re^{j\phi}$ reflection coefficient

x_1 = Direct path length

x_2 = Indirect path length

$\Delta X = (x_2 - x_1)$

h_T = Height above surface for T

h_R = Height above surface for R

Φ = Grazing angle

$G_R(\theta_R)$ = Receiving antenna gain times directivity

$G_T(\theta_T)$ = Transmitting antenna gain times directivity

D = Divergence factor

c = Velocity of light

Signal received over direct path

$$E_1 = \frac{E_K G_T(\theta_T') G_R(\theta_R')}{x_1} e^{j(\omega t - \beta x_1)}$$

* H. R. Reed and C. M. Russell, VHF Propagation, Boston Technical Publishers, Chapters 4 and 10, 1964.

β = Phase constant = $\frac{\omega}{c}$

ω = $2\pi f$

E_K = Field intensity with a magnitude which depends on transmitter power output, has a zero phase angle and a constant angular velocity

The signal received over the indirect path is given by

$$E_2 = \frac{E_K G_\tau(\theta_\tau) G_R(\theta_R)}{x_2} DR e^{j(\omega t - \beta x_2 + \phi)}$$

The resultant signal at the receiving antenna

$$E_R = E_1 + E_2$$

$$= \frac{E_K G_\tau(\theta_\tau') G_R(\theta_R')}{x_1} e^{j(\omega t - \beta x_1)} + \frac{E_K G_T(\theta_\tau) G_R(\theta_R)}{x_2} DR e^{j(\omega t - \beta x_2 + \phi)}$$

Define:

$$\text{Modulation Factor} = \frac{\text{indirect received voltage amplitude}}{\text{direct received voltage amplitude}}$$

$$= \frac{x_1}{x_2} \frac{G_T(\theta_T)}{G_T(\theta_T')} \frac{G_R(\theta_R)}{G_R(\theta_R')} DR$$

and

$$\gamma = \beta \Delta x - \phi$$

therefore,

$$E_R = E_1 \left(1 + m\, e^{-j\gamma}\right) e^{j(\omega t - \beta x_1)}$$

$$E_R = E_R'\, e^{j\alpha R}$$

where

$$E_R' = E_1 \left(1 + m^2 + 2m \cos \gamma\right)^{1/2}$$

$$\alpha_R = \omega t - \beta x_1 - \tan^{-1}\left(\frac{m \sin \gamma}{1 + m \cos \gamma}\right)$$

Since x_1 and x_2 are functions of time, m will be a function of time.

The angular frequency of the resultant carrier is the time rate of change of the phase a_R or

$$\omega_c = \frac{da_R}{dt} = \omega - \beta \frac{dx_1}{dt} - \left(\frac{m^2 + m \cos \gamma}{1 + m^2 + 2m \cos \gamma} \right) \frac{d\gamma}{dt}$$

The angular frequency of the modulated components of the carrier is

$$\frac{d\gamma}{dt} = \omega_m = \frac{d\Delta x}{dt} - \frac{d\phi}{dt} = \frac{\omega}{c} \left(\frac{dx_2}{dt} - \frac{dx_1}{dt} \right) - \frac{d\phi}{dt}$$

If $d\phi/dt$ is negligible compared to $\beta(d\Delta x/dt)$, then ω_m is directly proportional to the carrier frequency and the difference of the time rates of change of the direct and indirect transmission paths. As the positions of the transmitter and receiver vary in time, the region of reflection will vary and therefore ϕ will vary with time.

The Figure F-6 vector representation of the resultant carrier signal shows that E_1 rotates at an angular frequency equal to the transmitted carrier angular frequency minus the Doppler shift. The indirect signal ME_1 rotates at an angular frequency relative to the vector E_1 equal to $d\tau/dt \equiv \omega_m$. The resultant vector E_R is the vector sum of E_1 and mE_1 and it rotates at an angular frequency ω_c. It is seen that as the vector mE_1 rotates about E_1 the amplitude of E_R varies as $E_1\left(1 + m^2 + 2m \cos \gamma\right)^{1/2}$ and its angular frequency varies as $\left[(m^2 + m \cos \gamma)/(1 + m^2 + 2m \cos \gamma)\right](d\gamma/dt)$.

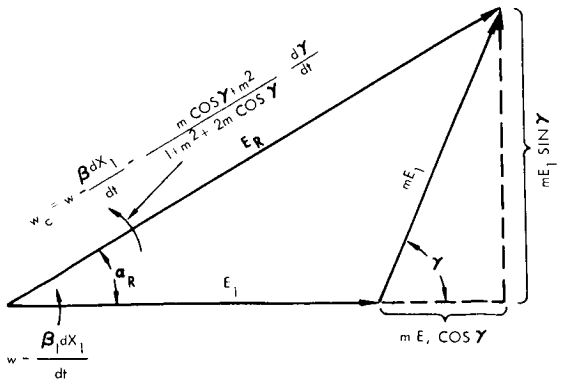


Figure F-6. Vector Representation of Signals

In a comparison of an amplitude modulated system and a frequency modulated system primary interest is in (1) the amplitude envelope of the carrier, (2) the instantaneous angular frequency ω_c, and (3) the instantaneous angular frequency at which E_R and ω_c are modulated, represented by ω_m. The general shape of the modulation envelope is shown in Figure F-7 for two values of m. For m relatively small

$$E_K \cong E_1(1 + m \cos \omega_m t)$$

and

$$\omega_c \cong \omega - \frac{\omega}{c} \frac{dx_1}{dt} - \omega_m m \cos \omega_m t$$

The resultant carrier then appears as a cosinusoidal frequency modulated signal shifted in frequency by the direct path Doppler shift $-(\omega/c)(dX_1/dt)$. If the separation between R and T is increasing the resultant angular frequency will be decreasing and vice versa. The maximum lobe modulation frequency is

$$f_m(\max) = \frac{fv}{c}$$

where

f = Carrier frequency

v = Relative velocity of the capsule and spacecraft = dx_1/dt

c = Velocity of light

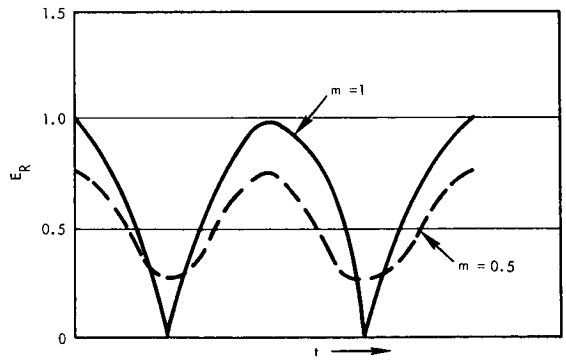


Figure F-7. Modulation Envelope Shape

The resultant carrier signal amplitude in the frequency analysis of the modulation envelope is

$$E_R = E_1\sqrt{1 + m^2 + 2m\cos\gamma}$$

and since

$$\omega_m = d\gamma/dt \quad \text{or} \quad \gamma = \omega_m t$$

then

$$E_R = E_1\sqrt{1 + m^2 + 2m\cos\omega_m t}$$

The Fourier series for the lobe modulation envelope is given by

$$E_R = \frac{A_n}{2} + \sum_{n=1}^{\infty} A_n \cos n\omega_m t + \sum_{n=1}^{n} B_n \sin\omega_m t$$

where

$$A_n = \frac{2}{T}\int_o^T \sqrt{1 + m^2 + 2m\cos\omega_m t}\ \cos n\omega_m t\, dt$$

$$B_n = \frac{2}{T}\int_o^T \sqrt{1 + m^2 + 2m\cos\omega_m t}\ \sin n\omega_m t\, dt$$

where n is the order of the harmonic.

Solution gives

$$B_n = 0$$

$$A_n = \frac{2\Gamma(3/2)\sqrt{1 - m^2}}{\Gamma(n + 3/2)\cos n\pi} P^n_{1/2}\left(\frac{1 + m^2}{1 - m^2}\right)$$

where

$\Gamma(3/2) = 0.8862$ and $\Gamma(a + 1) = a\Gamma(a)$

$P^n_{1/2}(X)$ is the associated Legendre function.

Therefore, the modulation envelope consists of the d-c component plus the sum of a series of cosine terms which takes the form

$$E_R = \frac{A_o}{2} + \sum_{n=1}^{\infty} A_n \cos n(\omega_m t - \pi)$$

Figure F-8 shows the harmonic content of E_R versus m.

The magnitude R and phase ϕ of the reflection coefficient versus grazing angle ψ for smooth land and for a transmitting frequency of 100 Mc/sec are shown in Figures F-9 and F-10.

These curves are given for both vertical and horizontal polarization. Since circularly polarized antennas will be used, the reflected signal will be composed of the vector sum of the horizontally and vertically polarized signals with an additional 90 degree phase shift on the signal which was shifted at the transmitter. As indicated in Figure F-9, the phase shift for horizontally polarized signals is about 180 degrees whereas the phase shift for the vertically polarized signals is about 25 degrees for a grazing angle greater than 45 degrees. This means that the reflected circularly polarized wave will be approximately 180 degrees reversed in polarity. Or, if the incident wave is right hand circularly polarized the reflected wave will be approximately left hand circularly polarized.

In addition, the amplitudes of the reflected waves for the vertical and horizontal signals will be about the same at a grazing angle of 90 degrees which will result in circular polarization. But there will be about a two to one difference in amplitudes of the signals for a grazing angle of 45 degrees, thereby resulting in an elliptically polarized wave. Since the direct wave and the reflected wave may be oppositely polarized, the receiving antenna which is designed to accept the direct wave will discriminate against the reflected wave. This will decrease the effect of fading. This problem requires further investigation. The following example assumes that the receiving antenna has a 3 db discrimination between the reflected and direct signals.

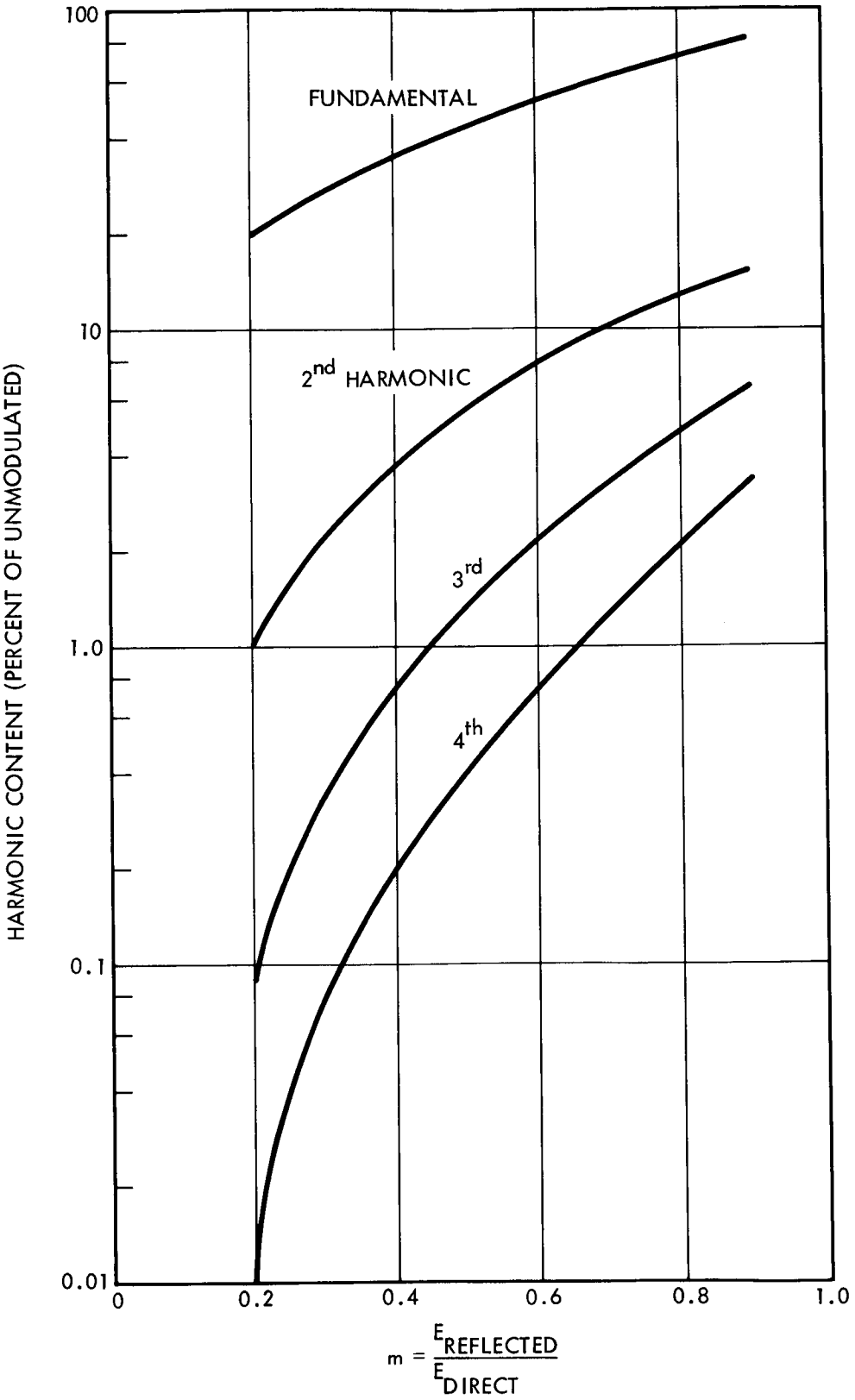


Figure F-8. Harmonic Content (Percent of Unmodulated)

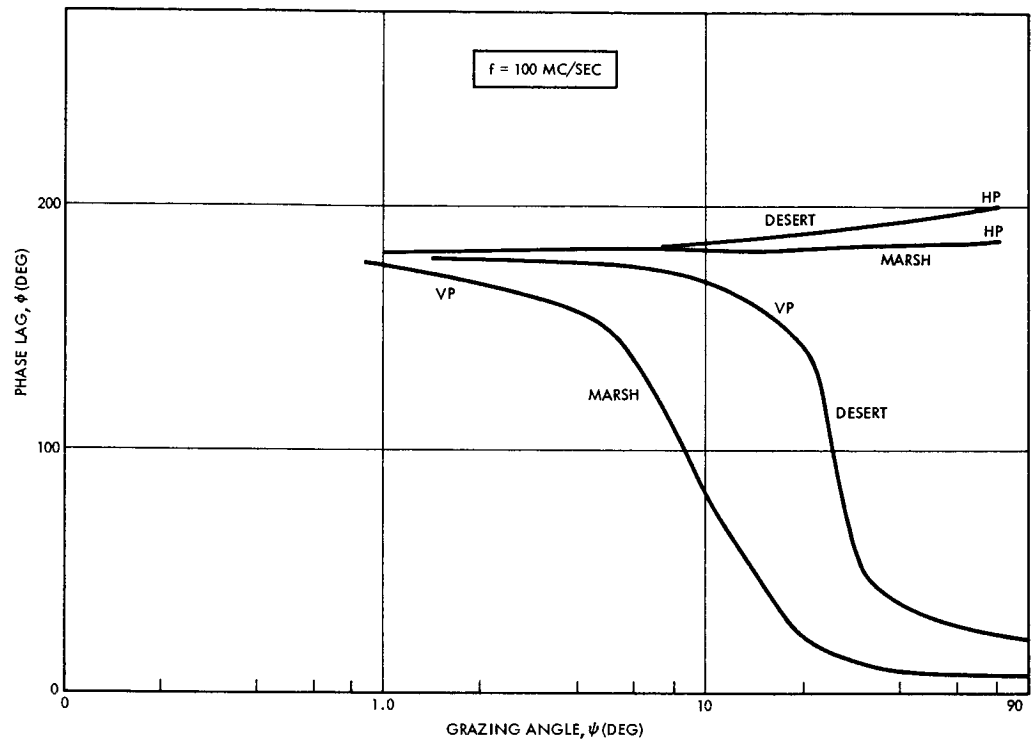


Figure F-9. Grazing Angle γ (Deg)

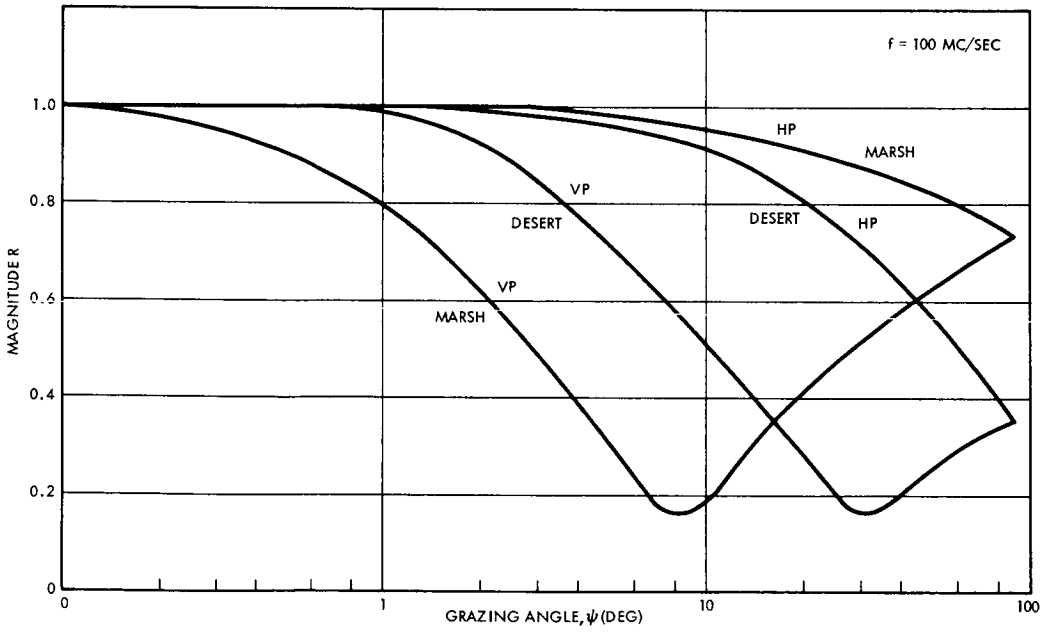


Figure F-10. Grazing Angle γ (Deg)

c. Typical Example

The system parameters are given in Table F-3. The modulation angular frequency is

$$\omega_m = \frac{\omega}{c}\left[\frac{dx_2}{dt} - \frac{dx_1}{dt}\right] - \frac{d\phi}{dt}$$

Assume that $d\phi/dt$ = is negligible, therefore:

1) Between blackout and before chute opening

$$f_m = \frac{1.36 \times 10^8}{9.6 \times 10^8}\left(10,000\right) = 1420 \text{ cps}$$

2) Maximum after chute opening

$$f_m = \frac{1.36 \times 10^8}{9.6 \times 10^8}\left(460\right) = 65 \text{ cps}$$

3) Minimum after chute opening

$$f_m = \frac{1.36 \times 10^8}{9.6 \times 10^8}\left(80\right) = 11 \text{ cps}$$

The maximum doppler frequency is

$$f_D = \frac{f}{c}\frac{dx_1}{dt}$$

$$= \frac{1.36 \times 10^8}{9.6 \times 10^8}\left(14.7 \times 10^3\right) = 2080 \text{ cps}$$

The modulation factor is

$$m = \frac{x_1}{x_2}\frac{G_T(\theta_T)}{G_T(\theta_T')}\frac{G_R(\theta_R)}{G_R(\theta_R')}DR$$

let

$$x_1 \doteq x_2 \quad , \quad D = 1$$

therefore,

$$m = \frac{0.5}{1.0} \cdot \frac{1.1}{1.6} \cdot (0.51)$$

$$= 0.27$$

Table F-3. System Parameters

$f = 100$ Mc

$\psi = 45$ deg to 90 deg

Desert land $\psi = 90$ deg $\psi = 45$ deg

$R_H = 0.35$ 0.6

$R_V = 0.35$ 0.26

$\phi_H = 200$ deg 194 deg

$\phi_V = 24$ deg 32 deg

Resultant for circular polarization

$R_c = 0.51$

$\phi_c = -23$ deg

$x_1 = 10,000$ to $40,000$ km

$x_2' = 85 + 10,000$ to $85 + 40,000$

$x_1 \doteq x_2$ after blackout

$\frac{dx_2}{dt} = 14,700$ ft/sec to 460 ft/sec after chute opening

= 14,700 ft/sec to 10,000 ft/sec = 4700 ft/sec immediately after blackout and before chute opening

$G_T(\theta_\tau) = -6$ db

$G_T(\theta_\tau') = 0$ db

$G_R(\theta_R) = 1$ db

$G_R(\theta_R') = 4$ db

d. Conclusions

The derivation of the equation of the carrier signal was determined for a simple two signal reflection model. This was done to get first order magnitudes of the fading rate, doppler frequency, and magnitude of modulation envelope. Further investigation is required to justify this very simple model.

Some typical results are:

1) Fading Rate

Between blackout and before chute opening = 1420 cps

Maximum after chute opening = 65 cps

2) Maximum Doppler Frequency

f_D = 2080 cps

3) Reflection Coefficient

There is approximately a 180 degree reversal of the circular polarization for grazing angles above 45 degrees. The reflection coefficient is calculated for desert type land. This reflection coefficient at a grazing angle of 45 degrees is approximately

$$R = 0.51\, e^{-j0.4}$$

4) Modulation Factor

The amplitude modulation factor for the received carrier is 27 per cent.

2.3.2 Frequency Uncertainties

a. General Discussion

For data rates of 10 bits/sec the problem of dealing with the frequency uncertainties in the capsule-to-spacecraft link dominates the link design. These uncertainties are primarily because of oscillator crystal tolerances and doppler shift of the carrier frequencies. These uncertainties have, of course, certain long-term nominal values. They also have rates of change; for example, the doppler shift has a rate of change which

would have to be considered in the design of the carrier tracking loop bandwidth for a coherent phase modulation system. To give a feel for the magnitude of the problem at this point, it will be found in the following section that the total range of frequency uncertainty, ΔF_F will be approximately three orders of magnitude larger than the bandwidth required for the data.

There are a number of ways of approaching the frequency uncertainty problem. Certain significant options are as follows:

1) Total ΔF_F System

The link modulation technique could be chosen such that a nonfrequency-tracking spacecraft VHF receiver is used. Its predetection bandwidth would be chosen to be large enough to encompass the total range of frequency uncertainties. Two such modulation techniques are PCM-FSK and PCM-FSK-AM. This is the simplest approach.

2) Partially Compensated ΔF_F System

A close relative to the above system would again use a nonfrequency tracking VHF receiver with a broad predetection bandwidth. It would, however, provide a number of choices for the nominal center frequency of this bandwidth. Many of the sources of frequency uncertainty to be listed can be divided into a predictable component and a nonpredictable component.

For example, the frequency of the spacecraft receiver crystal is determined by its nominal center frequency, adjustment drift due to aging, drift due to temperature and offset due to the vibration of launch. Once the spacecraft is in flight many of these variables then become fixed (at least for periods of hours). Thus, given the ability to measure the value of the frequencies involved and given the ability to vary the band center of the spacecraft receiver, the total ΔF_F to be accommodated can be reduced.

3) Frequency Tracking System

It is possible to design systems using a frequency or phase tracking spacecraft receiver in which the bandwidth of the tracking loops are made large enough so that the acquisition time and rate tracking errors are made satisfactorily low. For these types of systems the total noise bandwidth of the system would be substantially less than the total ΔF_F to be tolerated but would be much larger than the data rate (10 cps). These types of systems increase the spacecraft complexity and are critically dependent upon the detailed nature of the received VHF radio frequency signals.

4) Spacecraft Repeater Systems

The last type of system is one in which the IF output of the spacecraft VHF receiver is transmitted to the DSIF as a subcarrier on the S-band link. Here the data detection process is done on earth, possibly using both real time detection plus predetection recording with subsequent delayed detection. This system places minimal complexity in the spacecraft and preserves doppler and fading rate information for analysis on earth.

b. Numerical Evaluation of Uncertainties

To supply a numerical basis for the following discussion, this section will evaluate the range of the total frequency uncertainty, ΔF_F, which will be experienced. A list of these uncertainties is shown in Tables F-4 and F-5.

Table F-4 is a conservative estimate of the total frequency uncertainty assuming a carrier frequency of 136 Mc. The doppler shift of +2.0 Kc is a worst case value with the spacecraft velocity vector considered normal to the Martian surface and the capsule descending slowly on a parachute. The lander crystal nominal value ($\pm 3 \times 10^{-5}$) is a value quoted by Aeronutronics for its solid state transmitter designed for lunar hard landing. The capsule high G value of 2×10^{-5} is twice the experimental value measured by JPL for the permanent offset of crystal frequency due to high G impact.* The resultant ΔF_F of about 21 Kc is conservative and would, in the course of a development program, be refined by a large number of measurements. It should be borne in mind that a statistical approach would be required to choose the design ΔF_F so that a very high probability of never exceeding this value would be assured.

In Table F-5 it is assumed that a receiver is used which partially compensates for the frequency uncertainty. Here, the expected values of the spacecraft and capsule crystals would be computed using temperature measurements or measured on earth (before entry). Then the spacecraft receiver center frequency would be adjusted to place the actual carrier in the center of the chosen band. It is assumed that programming out the doppler shift of 2.0 Kc would be extremely unwise because of the uncertainty

*J.O. Lonborg, "High Impact Survival," JPL TR 32-647, page 20, 30 September 1964.

Table F-4. Capsule-Spacecraft Link Frequency Uncertainties

F = 136 Mc, Noncompensated Values

Item No.	Source	Assumed Parameter	ΔF_F(Kc)
1	Doppler Shift	15,000 ft/sec, γ_e = 90 deg	+2.0 -0.0
2	Spacecraft Receiver		±2.7
3	Capsule Crystal - Nominal		±4.1
4	Capsule Crystal - High G		±2.7
5	Total		+11.5 -9.5
6	ΔF_F		21.0*

*A noise bandwidth of 22 Kc will be used in other parts of the analysis contained in this appendix to accommodate the 21 Kc frequency uncertainty.

Table F-5. Capsule-Spacecraft Link Frequency Uncertainties

F = 136 Mc, Partially Compensated Values

Item No.	Source	Assumed Parameter	ΔF_F(Kc)
1	Doppler Shift	15,000 ft/sec, γ_e = 90 deg	+2.0 -0.0
2	Spacecraft Receiver	$\pm 5 \times 10^{-6}$	±0.7
3	Capsule Crystal - Nominal	$\pm 5 \times 10^{-6}$	±0.7
4	Capsule Crystal - High G	$\pm 1 \times 10^{-5}$	±1.4
5	Total		+4.9 -2.8
6	ΔF_F		7.7

in its time of occurrence. By this technique the total ΔF_F could be reduced to say 8 Kc. This would improve the predetection C/N value by about 4.4 db. Although this is a significant number, it comes at the expense of a considerable increase in system complexity.

c. Conclusions

In summary, pending a more detailed analysis, the most conservative approach is represented by a Type 1 total ΔF_T system with a frequency uncertainty of approximately 21 Kc. Type 2 and 3 systems should be studied further but could not be recommended at this time. A Type 4 spacecraft repeater system also represents a very conservative approach and will be discussed in more detail in a later section. During Phase 1B effort will be devoted to more accurately determining the actual value of frequency uncertainty to be accommodated. This will be done by a thorough investigation of all causes of crystal frequency change, a more detailed comparison of the above approaches, and by coupling these to a statistical approach. This will then result in a final ΔF_F to be accommodated which will be coupled to a probability of mission success.

2.3.3 Frequency Choice

a. General Discussion

The following factors must be considered in choosing the frequency of the link between the capsule and the spacecraft:

- The frequency uncertainty problem
- Propagation efficiency
- Receiving system noise temperature
- Efficiency of the solid state capsule transmitters
- Spacecraft and capsule antenna design problems

The following discussion will treat these considerations under the assumption that the general frequency range of interest is 100 to 400 Mc.

b. Frequency Uncertainty

The discussion in Section 2.3.2 indicated that the frequency uncertainty problem was a major factor in system design. Since the arithmetic value of ΔF_F to be accommodated is directly proportional to the carrier frequency, it is obvious that this consideration requires the use of as low a frequency as possible.

c. Propagation Efficiency

Another major factor is the propagation efficiency—the transmitter power output required to provide sufficient spacecraft receiver input power. In the case of this link the transmission is between a capsule antenna system which can be considered as a near isotropic radiator and a fixed beamwidth, fixed gain spacecraft antenna. So that the geometry of the entry and postland orbital portions of the mission be satisfied, it is required that the spacecraft antenna have a beamwidth of the order of 100 degrees. For this case the form of the free space equation which applies is

$$\frac{P_R}{P_T} = \left(\frac{\lambda}{4\pi d}\right)^2 G_T G_R$$

and the loss between transmitter and receiver increases 6 db per octave of frequency increase. Thus, this factor also favors operation at as low a frequency as possible.

d. Receiving System Noise Temperature

The three contributors to the receiving system noise temperature are planetary noise temperature, cosmic noise, and spacecraft receiver noise. The planetary noise, if it totally filled the spacecraft antenna beam would contribute approximately 300°K to the system noise temperature. For the actual geometry, however, only a small portion of the beam is filled with the planet. Thus cosmic noise has a significant contribution to the system noise temperature. In the 100 to 400 Mc frequency range low noise transistor preamplifiers are available which can conservatively provide a 3 to 5 db noise figure.

In summary the total noise temperature of the system varies as follows (estimated):

Frequency (Mc)	Noise Temperature (^{o}K) Cosmic	Receiver	Total
100	1200	300	1500
136	600	420	1020
200	200	420	620
400	50	600	650

Thus, it can be seen that in the range of 136 to 400 Mc only a 2-db change is in system noise temperature. This factor alone favors the mid-portion of this frequency range.

e. Solid State Transmitter Efficiencies

In general, the efficiency of solid state transmitters will decrease with increasing frequency. This factor will at least offset the system noise temperature variation. So, in summary, the equipment factors of receiving system noise temperature and transmitter efficiency vary in a very broad manner such that they do not control or heavily influence the frequency choice.

f. Spacecraft and Capsule VHF Antenna Design

Thus far all considerations have pointed toward the use of low frequencies in the vicinity of 100 to 200 Mc with the frequency uncertainty problem and propagation efficiency heavily favoring the lowest possible frequency and cosmic noise becoming quite influential at 100 Mc. Thus, aside from the design of the two antennas, the use of 136 Mc is indicated. Regarding the antenna designs, it would be desirable to work at the higher frequencies for a number of reasons:

1) The spacecraft antenna size for a given required beamwidth is smaller at higher frequencies.

2) Achieving a high capsule antenna front-to-back ratio would be easier at high frequencies. (This is desirable to minimize multipath reflections.)

3) Due to the restricted size of the capsule, a lower bound in frequency exists for which the antenna can be designed. It will be assumed that these constraints can be satisfied at 136 Mc.

g. Conclusions

In conclusion, then, it is found that 136 Mc represents a sensible compromise favoring the very influential frequency uncertainty and propagation efficiency factors, and providing a satisfactory compromise in the other areas.

2.3.4 Modulation, Demodulation, and Synchronization

As a first approximation, there is a high probability that the fading rate will be comparable to the information rate. It has been shown* that for a differential PSK (DPSK) system or DPSK-AM system when the fading rate is only about 20 per cent of the information rate, this type of system is useless. The FSK system has a very gradual degradation with fading rate.

The next decision is to determine whether the system should be coherent or noncoherent. A coherent system requires phaselocking the reference oscillator and the received signal. It has been shown** that the acquisition time T_A is related to the frequency uncertainty ΔF and the noise bandwidth B_{no} of the phaselock loop by

$$T_A = \frac{10\Delta F}{(B_{no})^2}$$

This is the acquisition time for a 95 per cent probability of success and a signal-to-noise power ratio equal to 9 db. The rms phase jitter is 0.15 radians or 9 degrees. Since the time at the end of blackout to impact may be as low as 4 minutes, the acquisition time should be about 10 seconds.

Thus, we have

$$\Delta F = 21 \text{ Kc/sec}$$

$$T_A = 10 \text{ seconds}$$

$$B_{no} = 150 \text{ cps}$$

---

* A.B. Glenn and G. Lieberman, "Performance of Digital Communication Systems in an Arbitrary Fading Rate and Jamming Environments," IRE Trans PGCS, March 1963.

** J.P. Frazier and J. Page, "Phase-Lock Loop Frequency Acquisition Study," IRE Trans PGSET, September 1962.

From the system parameters (Table F-6),

$$\frac{C}{N_o} = 44.3 \text{ db}$$

and for B = 150 cps,

$$\frac{C}{N} = 22.5 \text{ db}$$

Table F-6. Capsule Link Parameters

Total frequency uncertainty	=	±11 Kc/sec
Information bit rate	=	10 bits/sec
Maximum range	=	40,000 km
Transmitter power	=	20 watts
Transmitter antenna gain	=	0 db
Receiver antenna gain	=	4 db
Received Power	=	-153.7 dbw
Effective noise temperature	=	1020°K
Transmission frequency	=	136 Mc/sec
Noise power spectral density	=	-198 dbw/cps
Noise power in 44 kc bandwidth	=	-151.6 dbw

A signal margin must be allocated for the multipath fading and for the capsule antenna gain fluctuations as a function of attitude uncertainties during descent. A 6-db margin is assumed. In addition, a 6-db margin is assumed for equipment parameter uncertainties. With the total of 12-db system margin, the effective C/N is 10.5 db or a +1.5 db margin. A small fraction of the total power (less than 1/2 db) would be required for provision of a data subcarrier, thereby reducing the margin slightly.

Thus, it appears that carrier lock performance is adequate but with small margin. Of particular concern is the nature of the degradation — decreased lockup probability — if the signal margin becomes negative.

An extremely high lock up probability is required for post blackout reacquisition.

In the event that signal strength is much larger than estimated, then an additional problem of spurious lock on modulation sidebands can occur. This can be alleviated, but at the expense of added complexity, with an IQ phase lock loop.

a. Noncoherent FSK System

The system considered is shown in Figure F-11.

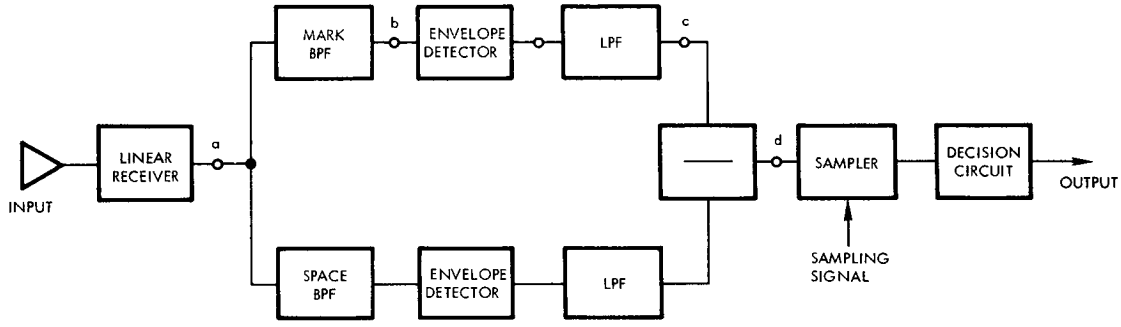


Figure F-11. Noncoherent FSK System

The analysis for the different points in Figure F-11 are:

Point A

Carrier to noise power ratio C/N = -2.1 db

$$\text{Bandwidth } B_{IF} = 2(B_1 + 2\Delta F)$$

where

B_1 = twice the information bandwidth

$= 2f_m = 20$ cps

$\Delta F = 11$ Kc/sec

$B_{IF} = 44$ Kc/sec

Point B

$$\left(\frac{S}{N}\right)_b = \left(\frac{C}{N}\right)_a \frac{2(B_1 + 2\Delta F)}{B_1 + 2\Delta F}$$

$$= 2\left(\frac{C}{N}\right)a$$

$$= +0.9 \text{ db}$$

At this point before noncoherent detection we must assume a system margin because the performance of this detector is sensitive to the input signal-to-noise ratio. We will assume a 6-db system margin for system parameter variations and a 6-db margin for fading.* This gives a total of 12-db system margin.

Therefore,

$$\left(\frac{S}{N}\right)_b = -11.1 \text{ db}$$

as measured in a bandwidth of 22 Kc/sec.

Figure F-12 shows the effect of noise on the characteristics of a linear detector.** This curve is used to determine the SNR at the audio or video output of an AM receiver. The curve is valid for sinewave modulation when the audio bandwidth is less (at least one half) than the IF bandwidth. The SNR is normalized to take into account the different IF to audio bandwidth ratio of different receivers. Each ordinate represents the calculated value of SNR at the output in db minus 10 log $IF_{BW}/2AF_{BW}$. For example, a receiver whose IF bandwidth (IF_{BW}) is 100 Kc and whose AF bandwidth (AF_{BW}) is 3 Kc, one would have to add to the value of SNR read as an

---

* A. B. Glenn and G. Lieberman, "Performance of Digital Communication Systems in an Arbitrary Fading Rate and Jamming Environments," IRE Trans PGCS, March 1963, and A. B. Glenn and G. Lieberman, "Effect of Propagation Fading and Antenna Fluctuations or Communication System Performance in a Jamming Environment," IRE Trans PGCS, March 1962.

** E. G. Fubini and D. C. Johnson, "SNR in AM Receivers" Proc. IRE, pp. 1461 to 1466, December 1948.

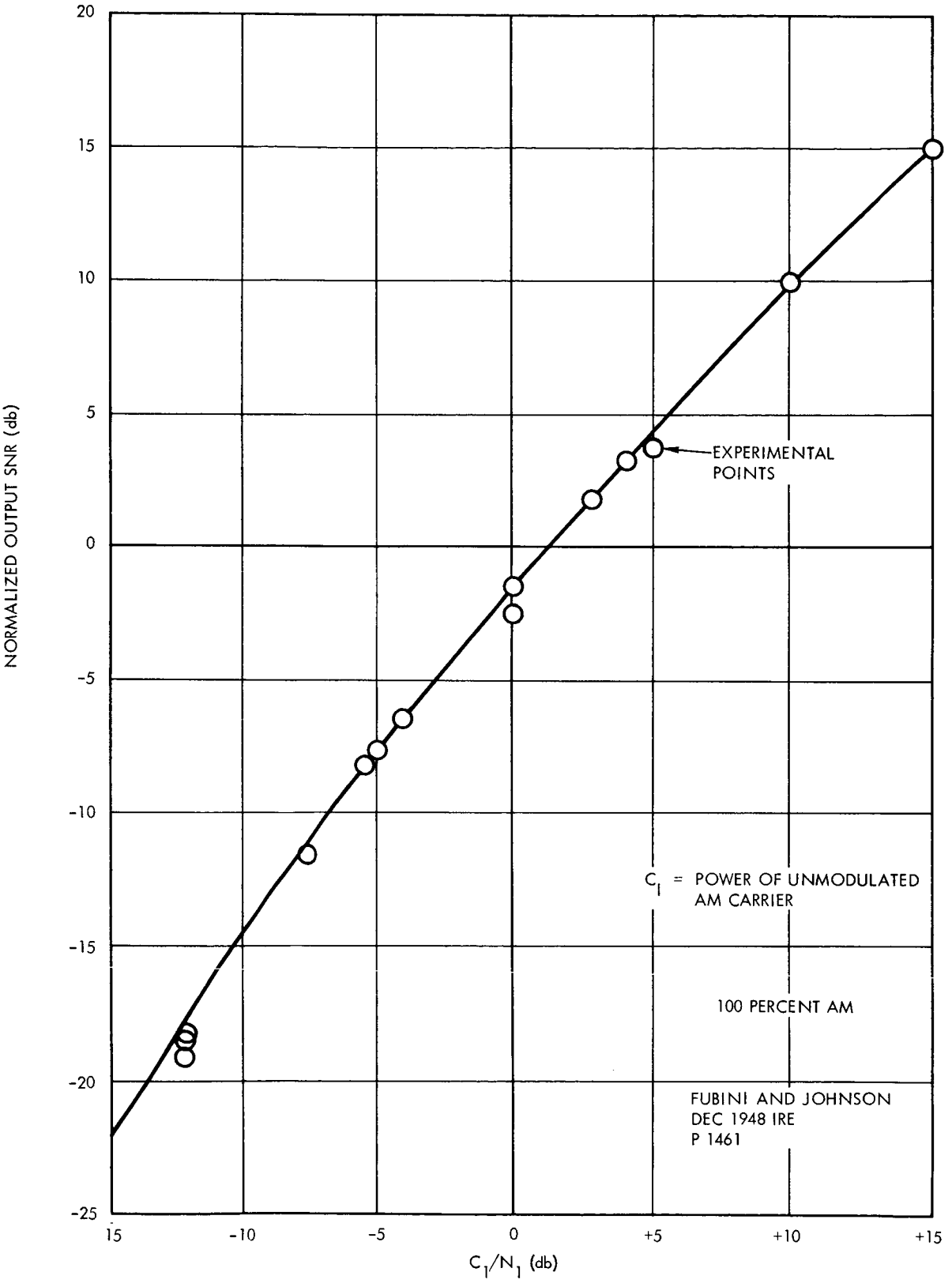


Figure F-12. Envelope Detector Characteristics

ordinate a number equal to $10 \log_{10} 100/6 = 12.2$ db. Modulation coefficients m different from 100 per cent can be taken into account with good approximation by adding $20 \log_{10} m$ to the ordinate.

From Figure F-12, the output SNR of

$$\left(\frac{S}{N}\right)_c = -17 + 10 \log_{10} \frac{(2.2)(10^4)}{(2)(10)} = +13.4 \text{ db}$$

as measured in a 10 cps bandwidth.

At point d, the noise from the channel which does not contain the signal will contribute noise to the channel which contains both signal and noise. However, the noise from the channel that contains signal and noise is the sum of the cross-product of the signal and noise plus the cross-product of the noise and noise.* Since the SNR at the input to the detector is very small, the noise from the two channels will be about equal.

Therefore, the resultant output SNR at point d is approximately

$$\left(\frac{S}{N}\right)_d \cong 13.4 - 3 \text{ db}$$

$$= 10.4$$

The energy-to-noise power spectral density is

$$\frac{E}{N_o} = \left(\frac{S}{N}\right)_d \frac{B_1}{2} \times T$$

$$= 11.0 \times 10 \times 0.1$$

$$= 10.4 \text{ db}$$

The sampling circuit will sample at the end of the data bit. If the sampled signal is greater than zero, the decision will be that the most

*M. Schwartz, Information, Transmission and Noise, McGraw Hill Book Company, 1959, Chapter 6, and W. B. Davenport and W. L. Root, Introduction to Theory or Random Signals and Noise, McGraw Hill Book Company, 1958, Chapter 12.

probable transmitted signal was a mark and vice-versa. For an error probability[3] of Pe = 10^{-3}, the required E/N_o is 10.8 db. We assume a gaussian noise distribution in the 10 cps filter.

g. FSK-AM System

The next system analyzed is the noncoherent FSK-AM system shown in Figure F-13.

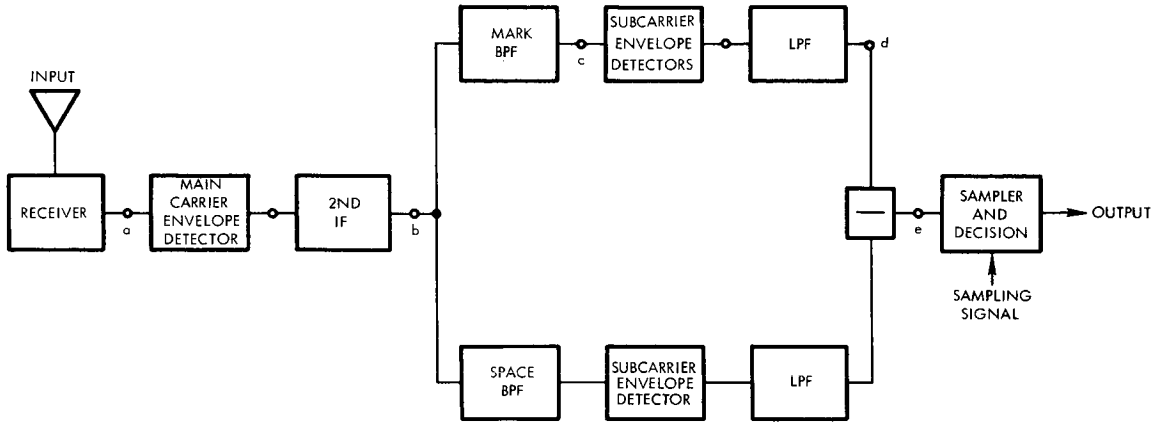


Figure F-13. Noncoherent FSK-AM System

Table F-7 shows the results of the analysis for the conditions given in Table F-6, a modulation of 100 per cent and a 12-db system margin.

Table F-7. Results of Capsule Link Parameter Analysis, FSK-AM

Point	Bandwidth (cps)	Carrier-to-Noise Power Ratio (db)
a	22,000	-11.1
b	40	-17.1 + 24.4 = 7.4 db
c	20	10.4
d	10	10.4
e	10	9.4*

*As there is approximately 1 db contribution of noise due to the space channel.

The above analysis is based on carrier power. But to obtain a more realistic comparison of FSK and FSK-AM systems the results should be based on the same prime power for both systems. For the AM system and

for 100 per cent modulation the carrier contains 67 per cent of the total power. Thus, on the basis of total power limitation, the effective signal-to-noise power ratio for the FSK-AM system is 9.4 - 1.7 or 7.7 db. There is an additional degradation of at least 1 db in the FSK-AM system because in a practical system the modulation will be less than 90 per cent instead of the 100 per cent assumed in the analysis. Thus, the FSK system requires about 3.5 db less power than the FSK-AM system.

c. Synchronization

The proper detection of the data in the spacecraft requires bit synchronization. This is necessary so the sampling is done at the maximum SNR. Thus, the error probability is minimized in the maximum likelihood decision criteria.* Many techniques may be used for bit and frame synchronization. These methods should be investigated for both performance and complexity of implementation before a technique is decided. The following is a discussion of one type of synchronization.**

In start-stop synchronization there are three required functions. These are "ready," "phasing," and "start" functions. The "ready" alerts the receiver as to when to look for the start and phasing information. The "phasing" indicates the proper orientation of the sampling while the "start" indicates the proper location of the first information bit.

Figure F-14 shows a method of combining the ready and phasing functions. At the expense of extra bandwidth, a burst of double speed reversals is used as a ready signal. Since the data signal spectrum has a null at this frequency, the ready signal may be separated by a narrow bandpass filter or equivalent. The output from this filter has a phase representing the average phase of the burst and therefore provides an accurate indication of the correct phasing for the bit sampling. This signal can also be used as a temporary receiving clock to sample for the start pattern instead of depending upon signal transitions. The start may consist of a simple isolated marking bit. After the start has been located the regular receive

* S. W. Golomb, "Digital Communications," Prentice Hall, 1964, Chapter 7.

** W. R. Bennett and J. R. Davey, Data Transmission, McGraw Hill Book Company, 1965, Chapter 14.

clock is started in the same phase as the temporary clock signal. In long messages the phase of the receiver clock may be corrected during the message by the average transition times.

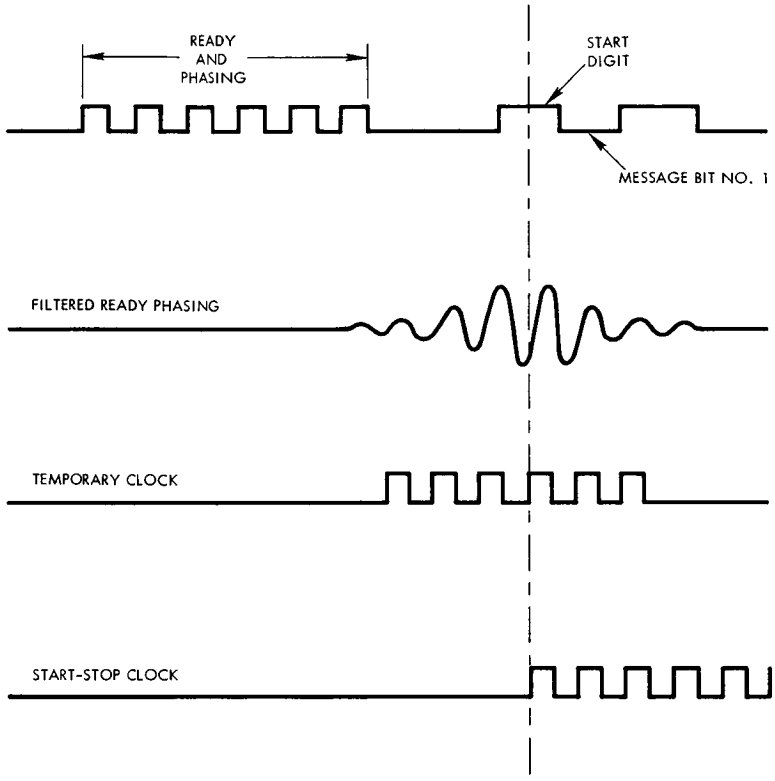


Figure F-14. Method of Combining "Ready" and "Phasing" Functions (After Bennett and Davey)

A block diagram of the FSK receiver showing the information and sync channels is shown in Figure F-15.

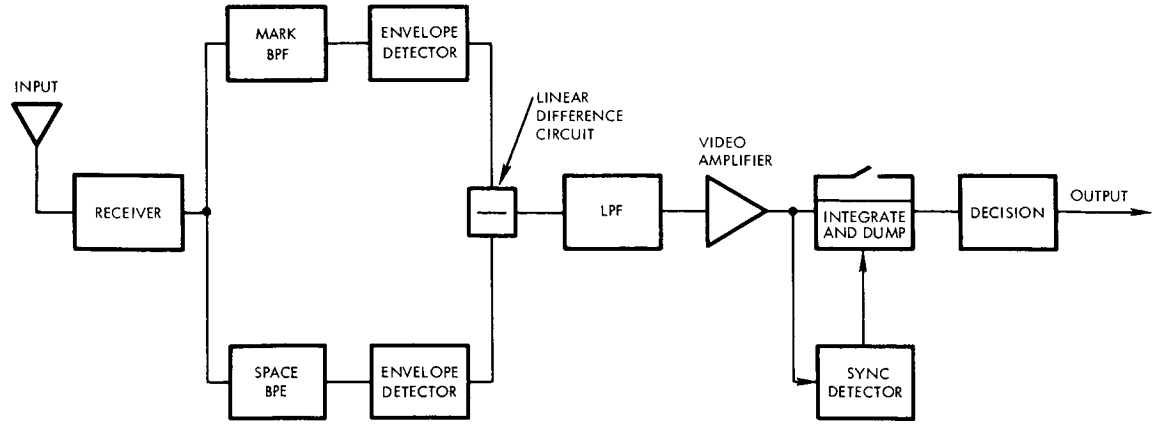


Figure F-15. Noncoherent FSK System

The output of the mark and space bandpass filters (BPF) are followed by envelope detectors. Since these detectors will be operating near the square law region, these detectors approximate energy detectors. These are more efficient than voltage detectors in a fast fading rate environment.*

The output of these detectors is applied to a linear difference circuit which is followed by a LPF and amplifier. The output of the amplifier is applied both to a detector for the synchronizing signal and to a matched filter. This filter is an integrate-and-dump type and maximizes the data SNR. The output of the sync detector provides sampling signals which will sample the output of the matched filter at the maximum SNR. A decision device which follows this match filter will decide whether a mark or space signal was transmitted. If the output of the matched filter were positive, the most probable transmitted signal was a mark and vice versa.

d. Data Rate Performance of FSK System

Since the performance of the envelope detectors in the noncoherent FSK system is sensitive to input carrier to noise ratios, it is important to determine the effect of variations in the frequency uncertainties and transmitter power. As previously discussed the assumed frequency uncertainty ΔF was on the conservative side. Also a system margin of 6 db for fading plus 6 db for other parameters was assumed necessary for 99 per cent probability of satisfactory operation. Both the frequency uncertainty and the system margin require further investigation so more precise values may be obtained on a statistical basis. The curves in Figure F-16 show the effect on noncoherent FSK for the following conditions:

Transmission range	=	40,000 km
Transmission frequency	=	136 Mc/sec
Effective receiver noise temp.	=	$1020^{\circ}K$
Transmitter antenna gain	=	0 db
Receiving antenna gain	=	4 db
Data error probability	=	10^{-3}
Total system margin	=	12 db

* A. B. Glenn and G. Lieberman, "Performance of Digital Communications Systems in an Arbitrary Fading Rate and Jamming Environments," IRE Trans PGCS, March 1963.

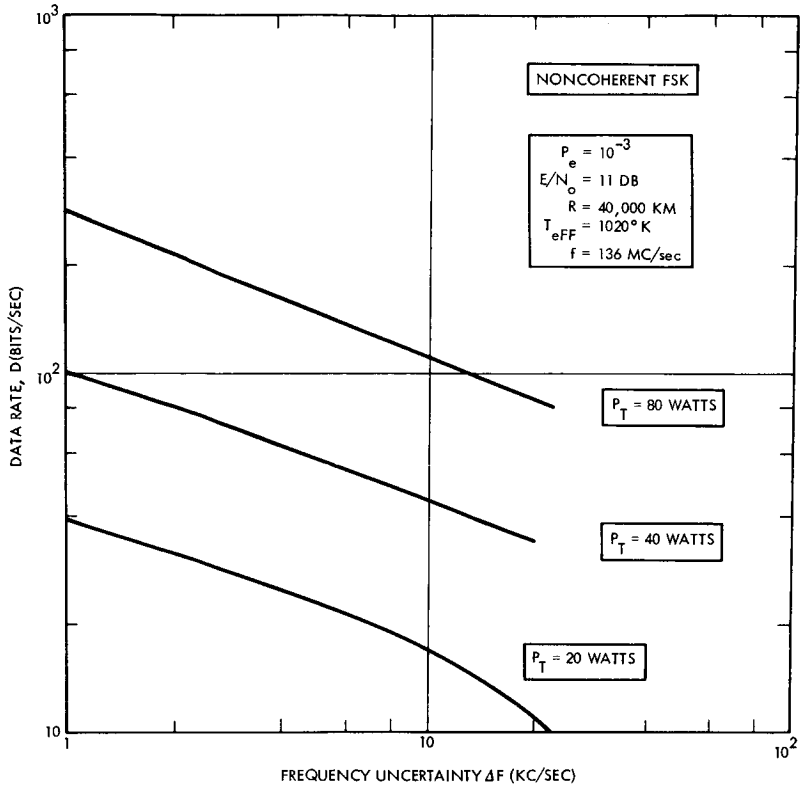


Figure F-16. Data Rate vs. Frequency Uncertainty for Noncoherent FSK

The effect of decreasing the frequency uncertainty Δ F on the data rate D shows that for a transmitter power of 20 watts a decrease in ΔF from 20 to 2 Kc/sec allows an increase of D from 10 to 32 bits/sec. A 6-db increase in transmitter power (or equivalently a 6-db decrease in system margin) from 20 to 80 watts gives about a nine-fold increase in data rate.

e. Conclusions

The FSK noncoherent system was chosen for the following reasons:

1) High probability that fading rate is comparable to information rate
2) Frequency search and acquistion required for a phase-lock loop
3) Spurious lock on modulation sideband can occur with phase-lock loop
4) S/N degradation likely to cause phase-lock dropout and complete loss of data until reacquition occurs

5) Simplest and most reliabile implementation

6) Satisfactory operation at a range of 40,000 km for an error probability of 10^{-3} and a 12 db system margin. Half of this system margin is required because of fading and antenna fluctuations for 99 percent probability of satisfactory operation.

2.3.5 Link Performance

The preceding sections have described the mission profile and have derived the characteristics of the modulation technique to be used. The appropriate parameters will be collected in this section to form a performance summary.* This is shown in Table F-8. The following comments apply to items in the table.

Item 2: It is assumed the entry VHF transmitter is mounted on the outside of the impact absorption shell of the capsule.

Item 6: Ellipticities for the spacecraft and capsule antennas are assumed to be 2 and 4 db, respectively. Each will use circular polarization.

Item 9: It is assumed that a single low noise preamplifier is used which is common to both VHF receivers in the spacecraft.

Items 10 and 11: As has been discussed in the preceding section on modulation and demodulation, the margin must be computed before detection. This is because the FSK mark and space channel detectors are operating in a negative C/N ratio region. Note that this table provides a total of 12 db of predetection margin for the sum of equipment and fading effects.

Item 16 in Table F-8 shows that the system described will provide a C/N in 44 kc of -13.9 db into the spacecraft receiver. In Section 2.3.4 it was shown that this is adequate to provide 1×10^{-3} error rate detection using the noncoherent FSK system as designed. This operation is provided at maximum range using the reasonable values of 20 watts for the capsule VHF transmitter and a 0-db gain capsule antenna.

*The official telecommunications design control table will be found in Volume 2, Section 5.3.3.

Table F-8. Performance Summary

Capsule to Spacecraft During Entry

Item	Parameter	Value
1	Total Transmitter Power	+13 dbw
2	Transmitting Circuit Losses	0.5 db
3	Transmitting Antenna Gain	0 db
4	Transmitting Antenna Pointing Loss	0 db
5	Space Loss (F = 136 Mc, D = 40,000 km)	167.2 db
6	Polarization Loss	0.5 db
7	Receiving Antenna Gain	4 db
8	Receiving Antenna Pointing Loss	1 db
9	Receiving Circuit Losses	1 db
10	Margin for Fading Effects	6 db
11	Margin for Equipment Effects	6 db
12	Total Circuit Losses	178.2 db
13	Total Received Power	-165.2
14	Receiver Noise Spectral Density (NF = 4 db, T = 420°K + 600°K = 1020°K)	-197.7 dbw/cps
15	Receiver Bandwidth (44 Kc)	46.4 db
16	Receiver C/N in 44 Kc	-13.9 db

2.3.6 Spacecraft VHF System Configuration Selection

a. Total System

As a result of the preceding analysis, a VHF link between the capsule and the spacecraft has been designed which operates in the 136 to 138 Mc space telemetry band, using circular polarization and a noncoherent FSK modulation technique. A block diagram of the spacecraft receiving system is shown in Figure F-17.

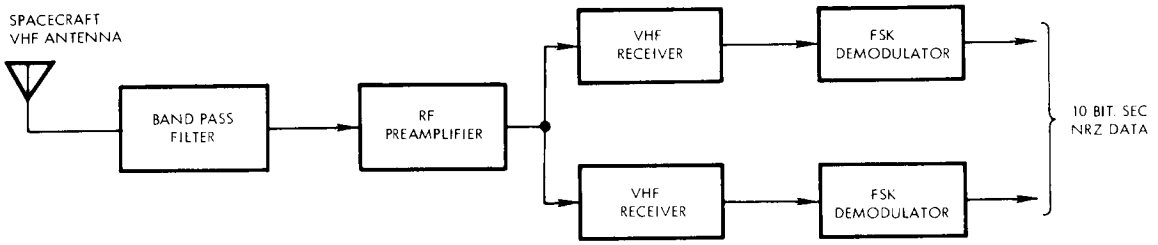


Figure F-17. Spacecraft VHF Receiving System

The spacecraft antenna receives the circularly polarized RF signals which are conducted to the RF bandpass filter. This filter prevents RF energy at other than the desired frequency from entering the RF preamplifier. It is required primarily for operation in the pad checkout and earth orbit test phase of the program. A single, simple low noise RF preamplifier is used to amplofy and supply signals to the two VHF receiver demodulator pairs. The use of one preamplifier eliminates the 3-db loss that would be present should two receiver inputs be operated in parallel. The two bit streams of demodulated data are fed to the data handling subsystem for transmission to earth via the S-band link.

b. Spacecraft VHF Antenna

The following are the basic performance specifications on the spacecraft VHF antenna:

Center frequency	136 to 138 Mc
Gain*	4 db min
Polarization	Right-hand circular
Beamwidth (3 db)	110 deg
Ellipticity (over 110 deg cone)	4 db max

c. RF Bandpass Filter

Center Frequency	136 to 138 Mc
Bandwidth (3 db)	2 Mc
Bandwidth (60 db)	To be specified
Loss	0.2 db

d. RF Preamplifier

Center Frequency	136 to 138 Mc
Bandwidth (3 db)	1 Mc
Noise Figure	4 db max
Gain	20 db min
Outputs	2

e. VHF Receiver

A block diagram of the VHF receiver is shown in Figure F-18. Its basic performance specifications are as follows:

Input Frequency	136 to 138 Mc
Output Frequency	10 Mc
Bandwidth	44 kc
Noise Figure	10 db max

*With respect to circular isotropic.

Crystal Oscillator Stability*	
Aging, power supply, center set	$\pm 3 \times 10^{-5}$
Shock offset	$\pm 2 \times 10^{-5}$

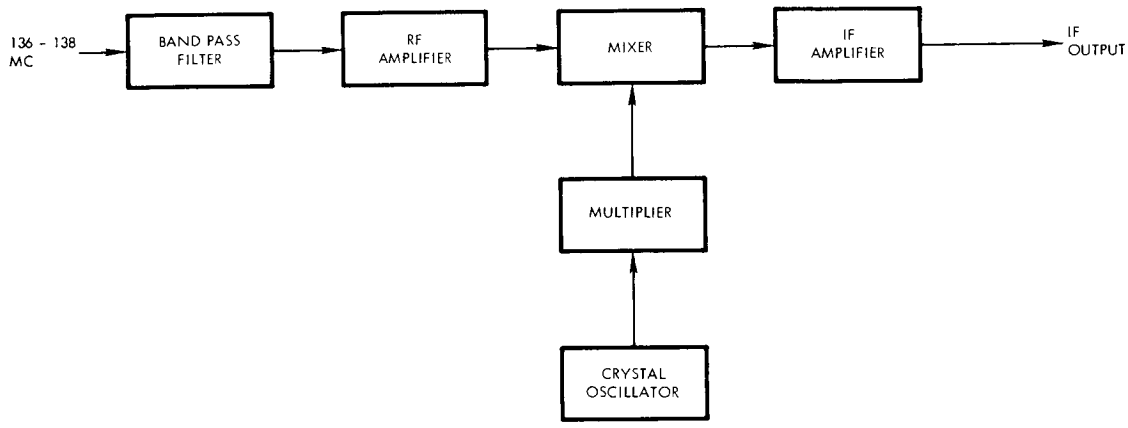


Figure F-18. VHF Receiver Block Diagram

In computing the dynamic range required in the VHF receiver in the spacecraft, assume that the start of the process of checking out the capsule takes place when the range between the spacecraft and the capsule is 100 km (approximately 10 minutes after capsule ejection). The signal in the spacecraft receiver is then 52 db above the nominal signal at maximum range (40,000 km). Adding to this the 12 db margin and a few db for positive tolerances on other parameters, it is found that a 70-db dynamic range will suffice. The absolute level of the input signal will be less than -105 dbw which is well below saturation in the RF preamplifier.

f. FSK Demodulator

A block diagram of the FSK demodulator is shown in Figure F-19. Its basic performance specifications are as follows:

Input Frequency (Nominal)	10 Mc
Input Power Level	To be specified

*To be reduced to the degree possible as a result of test data analysis.

Mark Channel Center Frequency	10.011 Mc
Space Channel Center Frequency	9.989 Mc
Mark and Space Channel Filter Bandwidths	22 kc
Output Data Rate (NRZ)	10 bits/sec
Error Rate*	10^{-3} max

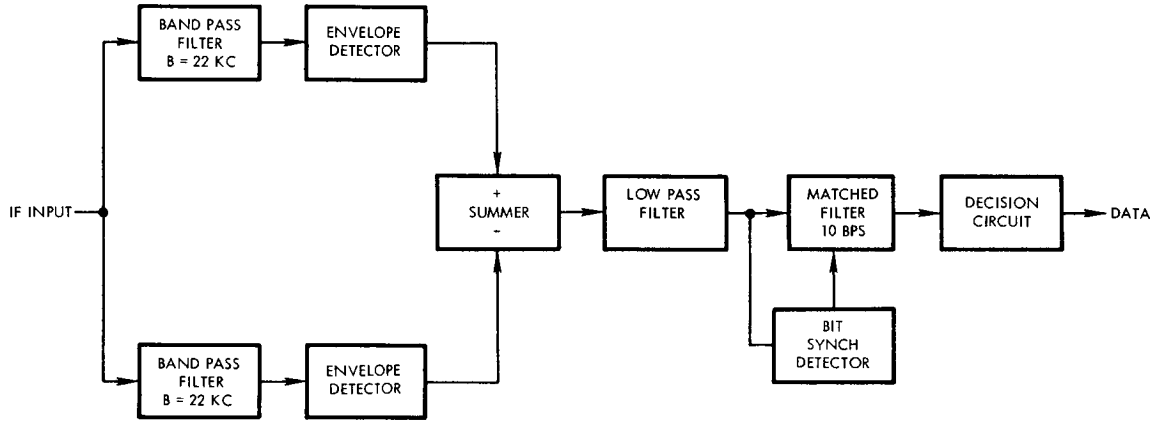


Figure F-19. FSK Demodulator Block Diagram

2.4 Constraints

2.4.1 Spacecraft

The constraints imposed upon the spacecraft by the VHF link with the capsule are the following:

a) The requirement for the 4-db gain 136 Mc antenna pointing in the direction of the lander during entry and landing.

b) No control signals are required by the VHF receiving and demodulating equipment.

c) This equipment delivers two bit streams at 10 bits per second each which are asynchronous with respect to the spacecraft. Thus, the Data Handling Subsystem must be capable of deriving word sync and processing the demodulated data.

*To be measured with an input C/N ratio of -14 db as measured in a 44 kc bandwidth.

2.4.2 Capsule

Since no spacecraft command transmitter is provided, it is assumed the capsule is either preprogrammed, hard wire programmed to its own sensors, or receives command from its own S-band command system.

It is required that the capsule possesses a VHF antenna which has zero db gain minimum and an adequate front-to-back ratio.

The required capsule 136-Mc FSK transmitter power output is 20 watts for the entry portion of the mission.

2.5 Spacecraft Nondemodulating Repeater Operation

2.5.1 General Principle

In the foregoing analyses and discussion it has been assumed that demodulation of the digital data takes place in the spacecraft. This type of system will completely satisfy the mission requirements. There is, however, an alternate approach which is worthy of investigation. In this mode the spacecraft would be used as a broadband repeater to transmit to earth the predetection IF output of the spacecraft VHF receiver. This would be done by phase modulating this IF as a subcarrier on the 2 Gc transmitter. In the DSIF this demodulated subcarrier would be recorded (following the first coherent demodulation). Then following completion of the entry portion of the mission this recording would be analyzed for its capsule signal content. A block diagram of one such system is shown in Figure F-20.

The use of this type of system would provide the following advantages:

a) More scientific data would be made available for analysis. For example, the doppler shift and doppler rate data on the tape recorder would permit making estimates of deceleration versus time profiles; signal level versus time data would provide data on blackout and postblackout signal transmission; and analysis of the doppler shifted component of the signal reflected from the planet would possibly provide data regarding the Martian terrain.

b) A redundant mode of obtaining the primary entry data is obtained. For example, failure of both the VHF data demodulator and the data handling subsystems would not prevent full data collection.

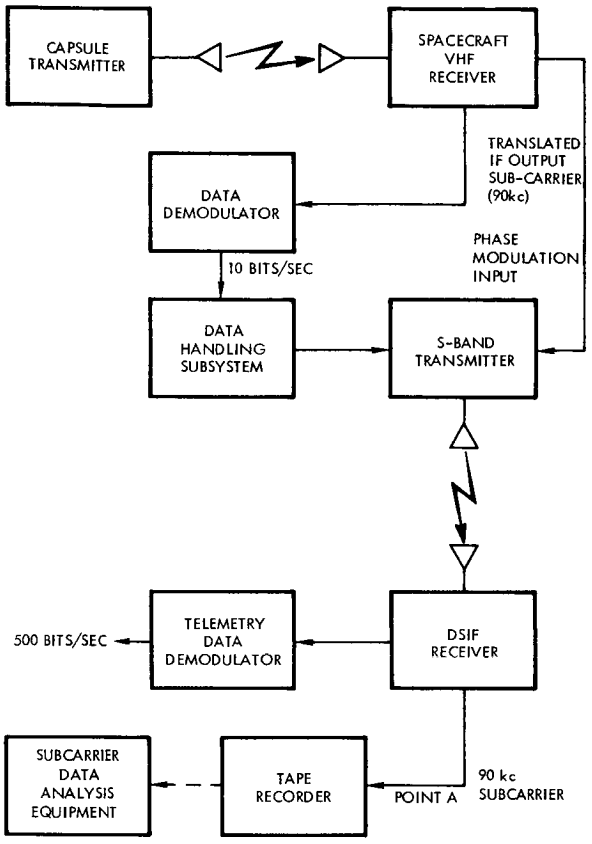


Figure F-20. Spacecraft Non-Demodulating Repeater Operation

The following section will explore the possibility of using such a system. While insufficient evidence is currently available to warrant its inclusion as a primary mode of operation at this time, the above advantages will warrant its further study in Phase IB.

It should be cautioned that in the following material, modifications will be discussed of the basic system as proposed in earlier sections of this appendix. These are to be clearly differentiated from that proposed system.

2.5.2 Operational Assumptions

Since it would be unsatisfactory for operational reasons to use the entire S-band transmitter power for the VHF receiver, IF subcarrier, it will be assumed that a 500-bit/sec telemetry channel is carried on the S-band link simultaneously with the subcarrier.

2.5.3 Revised Spacecraft Transmitter

For the purposes of this discussion it will be assumed that the VHF receiver has an additional output consisting of a translation of the main IF to a center frequency of 90 kc and that the bandwidth of this output is 44 kc. This 90-Kc subcarrier then is phase modulated on the 2 Gc carrier. The resultant single sided S-band spectrum is as shown in Figure F-21.

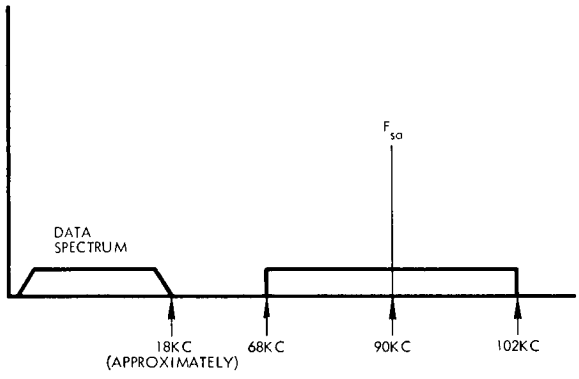


Figure F-21. S-Band Spectrum

2.5.4 Revised S-Band Down Link Computations

The following computations will give an indication of the performance achievable in the S-band down link under the following assumptions:

Maximum Spacecraft-Earth Range at Encounter	1.9×10^8 km
TWT Power Output	40 watts
Spacecraft Gain	30 db
Traffic	One 500 bit/sec channel plus the 90 Kc subcarrier

Using the Telecommunication Design Control Table found in Volume 2, Section 5.3.1, the total received nominal power under the above assumptions will be

$$-137.0 \text{ dbm} + 10 \log \frac{40}{20} + 20 \log \frac{2.5 \times 10^8}{1.9 \times 10^8} = -131.6 \text{ dbm.}$$

Allowing a 6-db margin the minimum received power is then -137.6 dbm. The noise spectral density at the DSIF is -184.8 dbm/cps.

To design a two subcarrier data link the total power is split between the carrier, 500 bits/sec telemetry subcarrier channel and the 90-Kc capsule data repeater channel. For the 500 bits/sec telemetry data channel a S/N of 7.3 db (for 5×10^{-3} bit error rate) is required in 500 cps. To satisfy this, at least -150 dbm (-184.8 + 7.3 + 27.0) must be placed in the 500 bits/sec telemetry data channel. This permits a P_{sc}/P_{tot} up to -12.9 db. The carrier tracking channel requires at least 6 db in 2 B_{LO} (12 cps) or -168.0 dbm (-184.8 + 6 + 10.8). This permits a P_c/P_{tot} up to -30.4 db.

As a first approximation it is assumed that a total rms carrier deviation of 1.1 radians is used. This gives a ratio of P_c/P_{tot} of -5.8 db for two subcarriers.* The total power in a subcarrier is given by:

$$\frac{P_{sc}^{(1)}}{P_{tot}} = 2\frac{P_c}{P_{tot}}\left[\frac{J_1(m_n)}{J_o(m_n)}\right]^2$$

for sinewave modulation. For a squarewave subcarrier $J_1(m_n)$ and $J_o(m_n)$ are replaced by $\sin(m_n)$ and $\cos(m_n)$ respectively. Substituting into the above equation on solving for m_1 (where m_1 is the deviation allotted to the 500 bits/sec telemetry data channel) gives:

$$\tan^2(m_1) = \frac{1}{2}\frac{P_{sc}}{P_{tot}}\frac{P_{tot}}{P_c}$$

$$\tan(m_1) = 0.394$$

$$m_1 = 17.8 \text{ deg } 0.310 \text{ radians (rms, peak)}$$

With the total rms deviation of 1.1 radians, the deviation (m_2) that can be allotted to capsule data sinewave subcarrier is

*JPL Technical Report 32-215 (March 15, 1962), "The Pioneer IV Lunar Probe," Benn D. Martin, pp 52, 23.

$$m_2^2 = m_{tot}^2 - m_1^2$$

$$m_2 = \sqrt{(1.1)^2 - (0.310)^2}$$

$$m_2 = 1.05 \text{ radians (rms) or } 1.49 \text{ radians (peak)}$$

If the capsule data channel is a sinewave channel, then

$$\frac{P_{sc}}{P_{tot}} = 2 \frac{P_c}{P_{tot}} \left[\frac{J_1(m_2)}{J_o(m_2)}\right]^2$$

$$= 3 - 5.8 + 0.3$$

$$= -2.5$$

Thus, for the capsule data channel the P_{sc}/N would be -137.6 - 2.5 + 184.8 or 44.7 db/cps, and the subcarrier-to-noise ratio in 44 Kc is then

$$(C/N)_{sc} = 44.7 \text{ db} - 10 \log 44,000 = -1.7 \text{ db}$$

2.5.5 Net Subcarrier-to-Noise Ratio

The above computations then show that the down link noise produces a $(C/N)_{sc}$ in 44 Kc of -1.7 db. In Section 2.3.5 it was shown that, for a 12 db system margin, the capsule carrier-to-noise ratio $(C/N)_{L1}$ as the output of the spacecraft VHF receiver in 44 Kc was $(C/N)_{L1} = -14$ db. Now the carrier-to-noise ratio $(C/N)_{LB}$ at Point A on Figure F-20 will be $(C/N)_{LB} = -14 \text{ db} - 10 \log \frac{1 + 1.48}{1} = -17.9$ db. So it can be seen that the S-band link now contributes heavily to the net $(C/N)_{LB}$ with which the earth-based subcarrier data analysis equipment must work. Thus, the price paid for being able to operate on the predetection capsule signal on earth is a decrease in its C/N by 3.9 db.

2.5.6 Earth-Based Data Analysis

Although the earth-based subcarrier data analysis equipment must now work in a noise environment 3.9 db poorer than that present in the spacecraft, this equipment has two major added degrees of freedom, namely:

a) The time to process the signal is no longer constrained to seconds or minutes.

b) The permissible equipment complexity of the demodulation equipment can be increased.

Since the data analysis can be done from the tape recorder subsequent to the mission constraints such as signal acquisition time no longer apply; also repetitive playing of the tape will allow programming out major portions of both the total frequency uncertainty and the rate of change of the capsule carrier signals.

This topic will be studied further in Phase 1B. The approach will be to work with the known signal characteristics (doppler, doppler rate, fading rate, and the likely range of characteristics of the reflected signals). Then, assuming reasonable times for post-mission data analysis, the required detector noise bandwidths will be determined. The one point of reference available in this appendix is the computation made in the section on modulation in which it was found that a noise bandwidth of 150 cps was required to acquire the signal in 10 seconds (assuming a total range of frequency uncertainty of 22 Kc). Using the value of C/N_{LB} above of -17.9 db, it is found that at the DSIF the required noise bandwidth to produce a +10 db C/N ratio is B = 44 Kc - 27.9 db = 70 cps. It would seem likely that bandwidths at least this small could be achieved using signal processing techniques operating in nonreal time.

2.5.7 Summary

As stated in the introduction, the inclusion of this mode of operation is not being recommended at this time. Further work is required on the detailed techniques to be used by the subcarrier data analysis equipment. The small C/N degradation experienced in the down link makes the approach look very promising. In addition, two added possible eventualities might make it look even more attractive:

a) Should the added scientific data provided warrant the slight added spacecraft complexity and reduction in telemetry data rate during entry; and

b) Should the very conservative estimate of the frequency uncertainty (ΔF_F = 22 Kc) be found too conservative. (As ΔF_F is reduced, the reduction in subcarrier bandwidth would reduce the contribution of the S-band down link noise.)

3. PSEUDO-NOISE SYNCHRONIZER PERFORMANCE

3.1 Introduction

Several important characteristics of PN synchronization will be derived:

- Probability density function of the loop phase error.
- Mean time to loss of lock.
- Magnitude of the false-lock lobes of the loop error function.

The first two derivations use the techniques of Tikhonov and Viterbi*. They have obtained exact solutions for some of the performance characteristics of a phaselock loop when driven by a sine wave in additive white noise. In Section 3.2 the periodic signal waveform that may take only one of two levels is considered. Two features of loop performance in additive white noise are derived: the first-order steady-state probability density function of the loop phase error, and the mean time to loss of lock. The derivation parallels that in Viterbi using Fokker-Planck equations. The solution is not exact being based on the equivalent of narrow band assumption for the usual phaselock loop. The principal results of the analysis are that the first order PN sync loop is noisier and has a shorter mean time to unlock than a phaselock loop at the same SNR. In particular, for the same asymptotic (high SNR) mean time to unlock, the PN loop requires 9 db more signal power than the PLL.**

In deriving the above results the effects of the bandpass filter and limiter in the sync loop are ignored. In Section 3.3, the narrow bandpass filter results in a loop error voltage shown as different from the ideal triangular function. The actual loop error function with the limiting case of an infinitely narrow filter is calculated. The appearance of side

---

*V. I. Tikhonov, "Phase-Lock Automatic Frequency Control Application in the Presence of Noise," Automatika i Telemekhanika, Vol. 23, No. 3, 1960, and A. J. Viterbi, "Phase-Lock Loop Dynamics in the Presence of Noise by Fokker-Planck Techniques," JPL Technical Report No. 32-427, 29 March 1963.

**The comparison of the PN sync loop with the ordinary phase lock loop does not imply any conclusions regarding the IQ phase lock loop used for NRZ sync. This comparison is treated in Section 4 of this appendix.

lobes or false-lock points is the principal feature of the practical error function. The effect of PN code length is observed: a 7-bit code has side lobes only 20 db down, whereas, for the Mariner C 63-bit code they are 40 db below the central peak. Thus, longer codes minimize the probability of false lock.

3.2 A Fokker-Planck Solution for First-Order Phase-Lock Loops With Square Inputs

3.2.1 Differential Equation and Assumptions

The circuit of concern is shown in Figure F-22. The input is $As(t) + n(t)$, where $s(t) = \pm 1$ for all t and is periodic with period $= 1/w_o$; $n(t)$ is white, i.e., $E[n(u)n(v)] = 1/2N_o\delta(u-v)$. This input is multiplied by the reference voltage, and applied to a linear filter F(s). Its output e(t) is the input to a VCO driving a code generator, which produces the reference $f(w_o t + \theta/T)$, where $f = \pm 1$. s(t) may be written in the form $s(w_o t + \xi/T)$, since it is of period $1/w_o$ (we assume from the start no frequency error exists, to simplify matters.) Hence

$$\frac{d\theta}{dt} = e(t) = F(s)\left[As\left(w_o t + \frac{\xi}{T}\right) f\left(w_o t + \frac{\theta}{T}\right) + n(t) f\left(w_o t + \frac{\theta}{T}\right)\right] \quad \text{(F. 17)}$$

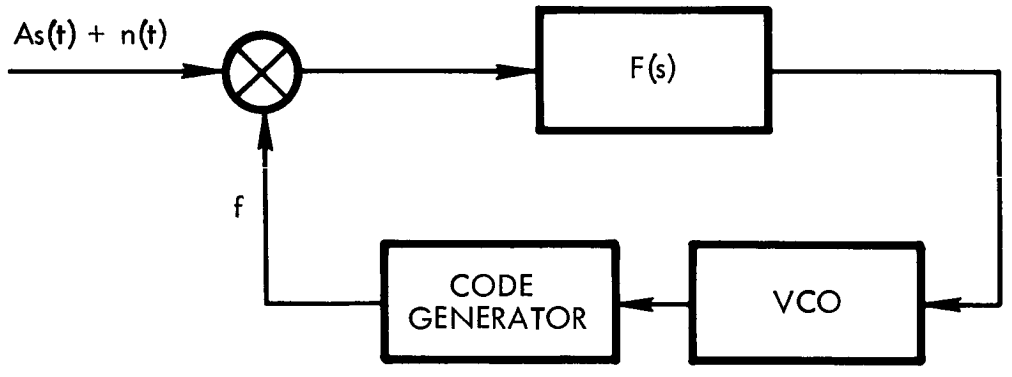


Figure F-22. Phase-Lock Loop

In Equation (F. 17), the product sf takes on only the values ± 1. It is now assumed that the period $1/w_o$ is much shorter than the phaselock

loop response time, so that the loop perceives effectively only an averaged version of this product; or that in Equation (F.42), the product sf can be replaced by

$$s\left(w_o t + \frac{\xi}{T}\ f\ w_o t + \frac{\theta}{T}\right) \rightarrow \frac{\text{Average}}{1\ \text{cycle}}\ s\left(w_o t + \frac{\xi}{T}\ f\ w_o t + \frac{\theta}{T}\right) = g(\phi) \quad \text{(F.18)}$$

with $\phi = \xi - \theta$. The function g is then the cross-correlation of the two codes s and f, and is the usual curve of loop error voltage vs. phase error. g is then an odd function of ϕ. Equation (F.17) becomes

$$\frac{d\theta}{dt} = F(s)\left[Ag(\phi) + n(t)f\left(w_o t + \frac{\theta}{T}\right)\right] \quad \text{(F.19)}$$

We treat only the first-order loop, and replace F(s) in Equation (F.19) by +K. Since ξ is a constant, (F.19) can be written as

$$\frac{d\phi}{dt} = -AKg(\phi) - K\,n(t)f\left(w_o t + \frac{\xi}{T} - \frac{\theta}{T}\right) \quad \text{(F.20)}$$

3.2.2 Steady-State Phase Error Probability Density Function

Equation (F.20) represents a Markov process, since the incremental change in position is a function only of the present position. Hence, the instantaneous probability density $p(\phi, t)$ satisfied the Fokker-Planck equation

$$\frac{\partial p(\phi, t)}{\partial t} = -\frac{\partial}{\partial \phi}\left[A(\phi)p(\phi, t)\right] + \frac{1}{2}\frac{\partial^2}{\partial \phi 2}\left[B(\phi)p(\phi, t)\right] \quad \text{(F.21)}$$

where

$$A(\phi) = \lim_{\Delta t \rightarrow 0} (1/\Delta t)\,\Delta\phi$$

$$B(\phi) = \lim_{\Delta t \rightarrow 0} (1/\Delta t)\,\sigma^2_{\Delta\phi}$$

A and B may be evaluated from Equation (F.20). Given ϕ,

$$\Delta\phi = \int_t^{t+\Delta t} \dot{\phi}(t)dt = -AKg(\phi)\Delta t - Kf\ \dot{w}_o t + \xi - \phi)\int_t^{t+\Delta t} n(t)dt \quad \text{(F.22)}$$

From Equation (F.22), then, since n(t) is assumed white with zero mean,

$$\overline{\Delta\phi} = - AKg(\phi)\Delta t$$

$$\sigma^2_{\Delta\phi} = K^2 f^2 (w_o t + \xi - \phi) \int_t^{t+\Delta t} du \int_t^{t+\Delta t} dv \, \overline{n(u)n(v)}$$

$$= \frac{1}{2} K^2 N_o \Delta t$$

since $f^2 = 1$. Thus,

$$A(\phi) = - AKg(\phi)$$

$$B(\phi) = \frac{1}{2}K^2 N_o$$

Equation (F.21) is then

$$\frac{\partial p(\phi, t)}{\partial t} = + \frac{\partial}{\partial \phi} \left[AKg(\phi)p(\phi, t) \right] + \frac{1}{2} \frac{\partial^2}{\partial \phi^2} \left[\frac{1}{2}K^2 N_o p(\phi, t) \right] \qquad \text{(F.23)}$$

We are interested in the steady-state probability density function $p(\phi, \infty)$. Equation (F.48) becomes (F.23)

$$\frac{d}{d\phi} \left[AKg(\phi)p(\phi) + \frac{1}{4}K^2 N_o \frac{dp(\phi)}{d\phi} \right] = 0 \qquad \text{(F.24)}$$

The solution to Equation (F.24) is

$$p(\phi) = \exp\left(-\alpha' \int_{-T/2}^{\phi} g(x)dx \right) \left[D + C \int_{-T/2}^{\phi} \exp\left(+\alpha' \int_{-T/2}^{x} g(y)dy \right) dx \right]$$

(F.25)

where C and D are constants to be evaluated, $\alpha' = 4A/KN_o$, and ϕ is assumed periodic over $(-T/2, T/2)$. The boundary conditions for Equation (F.25) are

$$p(T/2) = p(-T/2); \quad \int_{-T/2}^{T/2} p(\phi)d\phi = 1$$

Using these to evaluate the constants, Equation (F.25) becomes

$$p(\phi) = \frac{\exp[\alpha' h(\phi)]}{\int_{-T/2}^{T/2} \exp[\alpha' h(x)]\, dx} \tag{F.26}$$

where

$$h(\phi) = -\int_{-T/2}^{\phi} g(x)dx \tag{F.27}$$

Equation (F.26) is the expression of interest.

3.2.3 Mean Time to Loss of Lock

Suppose initially that $\phi = 0$. Due to the noise n(t), it departs from zero for $t > 0$. Whenever it exceeds some value ϕ_1 in magnitude, suppose that the circuit is removed forever from operation. How much time on the average is required before ϕ reaches ϕ_1? Before ϕ reaches ϕ_1, $p(\phi, t)$ is described by Equation (F.23). After reaches ϕ_1, $p(\phi, t) = 0$. Thus, we have the conditions

$$p(\phi, 0) = \delta(\phi); \; p(\phi_1, t) = p(-\phi_1, t) = 0; \; p(\phi, \infty) = 0. \tag{F.28}$$

Given the angle ϕ_1, it may be argued similarly to Viterbi that the mean time to lose lock is

$$\tau(\phi_1) = \int_0^{\infty} dt \int_{-\phi_1}^{\phi_1} p(\phi, t)\, d\phi \tag{F.29}$$

(F.29) may be evaluated by first integrating both sides of (F.23) with respect to t over $(0,\infty)$, obtaining

$$p(\phi,\infty) - p(\phi,0) = \frac{\partial}{\partial\phi}\left[AKg(\phi)P(\phi)\right] + \frac{1}{4}K^2N_o\frac{\partial^2P(\phi)}{\partial\phi^2} \qquad (F.30)$$

where

$$P(\phi) = \int_0^\infty p(\phi,t)dt$$

Using the first and third equations of (F.28) in (F.30),

$$-\delta(\phi) = \frac{\partial}{\partial\phi}\left[AKg(\phi)P(\phi)\right] + \frac{1}{4}K^2N_o\frac{\partial^2P(\phi)}{\partial\phi^2}$$

The solution of this equation for P is

$$P(\phi) = \exp\left(-\alpha'\int_{-\phi_1}^{\phi} g(x)dx\right)\left[D + \int_{-\phi_1}^{\phi}\frac{C - u(x)}{\gamma}\exp\left(+\alpha'\int_{-\phi_1}^{x} g(y)dy\right)dx\right] \qquad (F.31)$$

where $\gamma = 1/4K^2N_o$, u(x) is the unit step function, and C and D are again constants of integration. These may be evaluated using the second equality in (F.28), that

$$P(\phi_1) = \int_0^\infty p(\phi_1,t)dt = 0 = P(-\phi_1) = \int_0^\infty p(-\phi_1,t)dt$$

with the result that

$$P(\phi) = \frac{1}{\gamma}\exp\left[-\alpha'\int_{-\phi_1}^{\phi} g(x)dx\right]\int_{-\phi_1}^{\phi}\left[\frac{1}{2} - u(x)\right]\exp\left[+\alpha'\int_{-\phi_1}^{x} g(y)dy\right]dx \qquad (F.32)$$

(F. 32) may be substituted into (F. 29) to obtain :

$$\tau(\phi_1) = \frac{1}{\gamma}\int_{-\phi_1}^{\phi_1} d\phi \exp\left[\alpha' h'(\phi)\right]\int_{-\phi_1}^{\phi}\left[\frac{1}{2} - u(x)\right]\exp\left[-\alpha' h'(x)\right]dx$$

$$= \frac{1}{\gamma}\int_{0}^{\phi_1} d\phi \int_{\phi}^{\phi_1} dx \exp\alpha'\left|h'(\phi) - h'(x)\right| \qquad (F.33)$$

where

$$h'(\phi) = -\int_{-\phi_1}^{\phi} g(x)dx \qquad (F.34)$$

using the fact that h' is an even function, since g is an odd function.

3.2.4 PN Bit Synchronization

Similarly to Viterbi, the numbers α' and γ may be related to parameters of usual interest. Hence, it can be shown that $\alpha' = A^2\dot{g}(0)/N_o B_L$, where $B_L = Ak\dot{g}(0)/4$ is the loop bandwidth for the first-order loop, so that $\alpha = \alpha'\dot{g}(0)$ is the signal-to-noise ratio in the loop bandwidth. Similarly $\gamma = 4B_L/\alpha\dot{g}(0)$.

Suppose that s(t) is a k-bit PN code. If the block diagram of Figure F-22 is used, the function $g(\phi)$ takes the form

$$g(\phi) = \begin{cases} 0 & -\frac{T}{2} < \phi < -\frac{T}{k} \\ -(\phi + \frac{T}{k})k/T & -\frac{T}{k} < \phi < -\frac{T}{2k} \\ k\phi/T & -T/2k < \phi < T/2k \\ -(\phi - \frac{T}{k})k/T & T/2k < \phi < T/k \\ 0 & T/k < \phi < T/2 \end{cases}$$

This function is sketched in Figure F-23. From (F.27),

$$h(\phi) = \begin{cases} 0 & -T/2 < \phi > -T/k \\ +\left(\frac{1}{2}\phi^2 + T\phi/k\right) k/T + \frac{1}{2}\frac{T}{k} & -T/k < \phi > -T/2k \\ -\frac{1}{2}k\phi^2/T + \frac{1}{4}\frac{T}{k} & -T/2k < \phi > T/2k \\ \left(+\frac{1}{2}^2 - T\phi/k\right) k/T + \frac{1}{2}\frac{T}{k} & T/2k < \phi > T/k \\ 0 & T/k < \phi > T/2 \end{cases} \qquad (F.35)$$

while from (F.34), for $\phi_1 = T/2$, $h'(\phi) = h(\phi)$. The function $h(\phi)$ is sketched in Figure F-24.

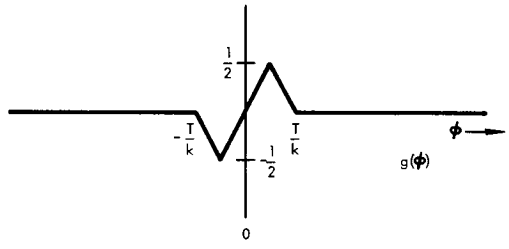


Figure F-23. Loop Error Function for PN Code

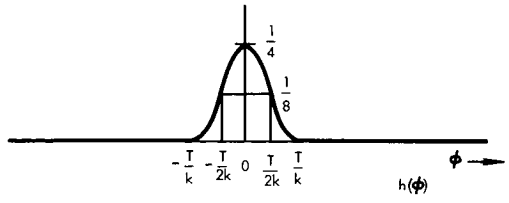


Figure F-24. Integral of Loop Error Function - PN Code

(F. 35) may then be used in (F. 26) and in (F. 33) to obtain the probability density function of the loop phase error, and the mean time to loss of lock by suitably choosing ϕ_1. ϕ_1 is chosen to be equal to a PN bit-time, T/k, rather than a PN code length T. It is felt that if the loop phase is in error by T/k, no loop correction voltage is available, and the loop is subject to a random walk. If T is used instead, the time it takes for the loop to randomly walk out of this 'dead zone' to the next PN code position is included in the mean time to loss of lock, an unrealistic situation.

Neither (F. 26) nor (F. 33) are available in closed form using (F. 35). The shape of $p(\phi)$ in (F. 26) is obtainable exactly, but the normalization integral in the denominator must be evaluated numerically. This is done, and plotted in Figure F-25 for α = 6, 20, and 60, for PN code lengths k of 7 and 63. If this is compared to similar plots in Viterbi, it is seen that for the same signal-to-noise ratio in the loop bandwidth, α, the probability density function for the PN code is somewhat wider than that for the sine wave, as a fraction of one PN bit, or of one cycle of the sine wave. This indicates that one requires a larger α to maintain the loop phase jitter at the same value.

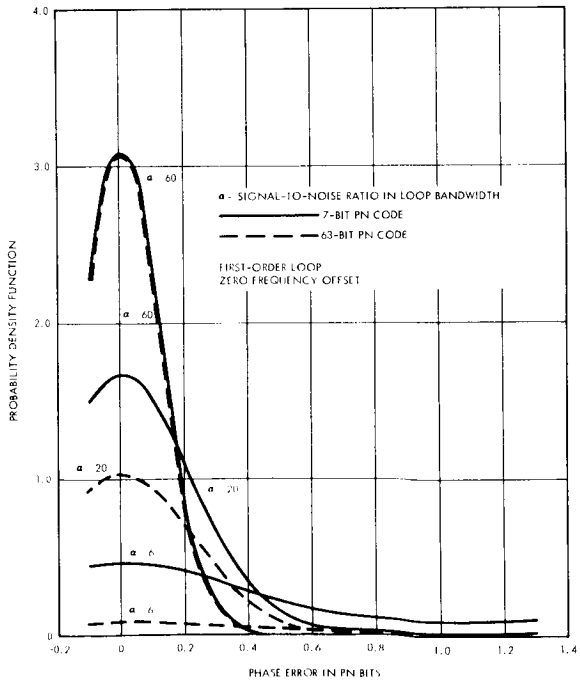


Figure F-25. Probability Density Function of Loop Phase Error

The normalized mean time to loss of lock, τB_L, is plotted in Figure F-26. (F.33) was evaluated numerically for $\alpha = 20$ and 60. In addition, an asymptotic value for large α can be derived. Writing $z = k\phi/T$, (F.33) is

$$\tau(1) = \frac{T^2}{k^2} \frac{1}{\gamma} \int_0^1 dx \int_z^1 dx \exp \alpha \, [h(z) - h(x)] \qquad (F.36)$$

The integral with respect to x in (F.36) has an integrand which is appreciable only for x close to unity, by inspection of (F.35). Hence, one may replace the lower limit by 0, and use for h(x) the expression in (F.35) near z = 1. Conversely, the integral with respect to z in (F.36) has an integrand which is appreciable only for z close to zero, hence, one may use for h(z) the expression in (F.35) near z = 0. When this is done, (F.36) becomes

$$B_L\tau \cong \frac{\alpha}{4} \int_0^1 dz \exp \frac{\alpha}{2}\left(\frac{1}{2} - z^2\right) \int_0^1 dx \exp -\frac{\alpha}{2}(x-1)^2$$

$$\rightarrow \frac{\pi}{8} e^{1/4}$$

The asymptote (F.37) is also shown on Figure F-26. This may be compared to the asymptotic expression in Viterbi for the sine wave case: $B_L\tau \rightarrow \pi/4 \, e^2\alpha$. It is seen that for the same $B_L\tau$, α must be approximately 9 db larger in the case of the PN code, in the limit of large α.

3.3 Calculation of Error Function for Mariner C Bit Synchronizer

The circuit is shown in Figure F-27. It is desired to calculate the d.c. component of the error voltage e(t), as a function of τ, the timing error between the input and the local clock. For simplicity, the local clock is taken to be at phase zero, and the input, in the absence of noise, is written as $s(t) = PN(\tau) \, \theta \, 2f_s(\tau)$. As usual, θ denotes binary addition, or normal multiplication if the codes take the values ± 1, a feature which we always assume. The approach taken here is to calculate the component of v(t) in phase with the reference, f_s, where v(t) is the input to

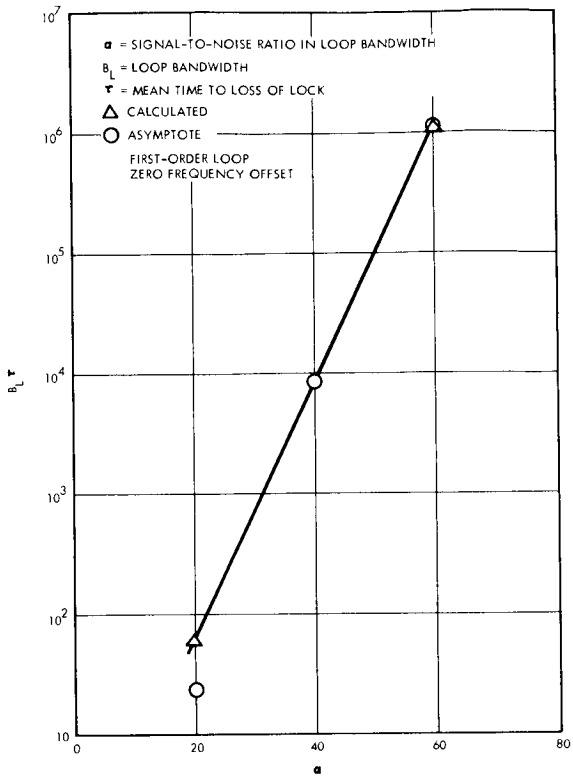


Figure F-26. Mean Time to Loss of Lock — PN Code

the bandpass filter whose effect we are trying to assess. Hence one may think of v(t) as being expanded in a Fourier series; its components at the frequency f_s are in terms of a sine and a cosine term in phase and in quadrature with the reference f_s. Neglecting the effect of the limiter, multiplying this Fourier series by f_s produces a d. c. output due only to the term at the frequency f_s and in phase with the reference f_s; all other terms are zero. This calculation then gives the d. c. component of e(t) for a fixed timing error τ, if an infinitely-narrow band filter, centered at f_s, were used in the circuit of Figure F-27.

The loop error voltage in the absence of the bandpass filter is the triangular-type function shown in Figure F-28. Since the bandpass filter rejects high-frequency components, it may be expected to modify this error function in two ways. In the region of small τ, the triangular-type error function is somewhat smoothed out, and decreased in amplitude.

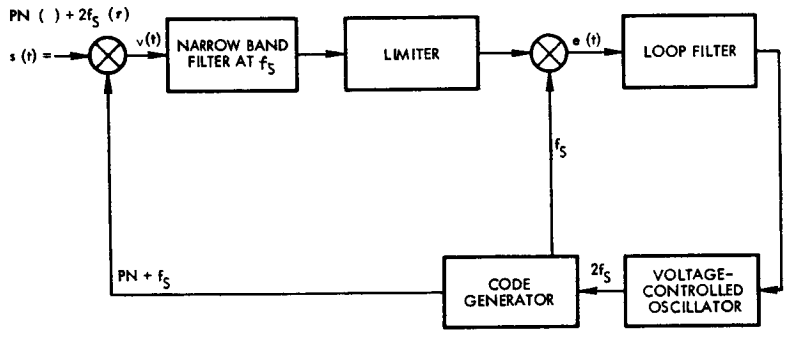


Figure F-27. Bit Synchronizer Circuit

In the region of large τ, where the nonfiltered error function is identically zero, the filter produces false-lock points. The magnitude of these false lock points is of interest, since these points affect the ease of acquisition and of reacquisition.

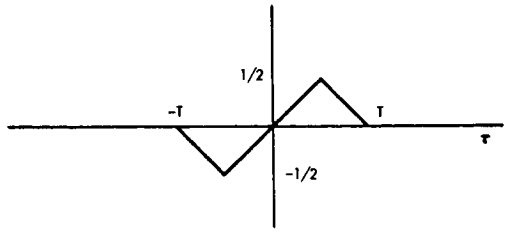


Figure F-28. Ideal Loop Error Function

3.3.1 Decomposition of v(t)

The technique used is to decompose v(t) into ordinary sums of terms. Superposition may then be used, and the effect of each term on e(t) considered separately.

$$v(t) = 2f_s(\tau) \theta PN(\tau) \theta f_s \theta PN$$

$$= 2f_s \theta f_s \theta[2f_s \theta 2f_s(\tau) \theta PN \theta PN(\tau)] \quad (F.37)$$

Let $\tau = kT + \alpha$, where T is a PN bit-time, k is an integer, and $-1/2\ T < \alpha < 1/2\ T$

Then

$$PN \theta PN(\tau) = PN \theta PN(kT) + \delta_{k\alpha} \cdot PN \quad (F.38)$$

where PN(kT) is PN shifted k units to the right, and $\cdot$ denotes ordinary multiplication since $\delta_{k\alpha}$ is no longer binary:

$$\delta_{k\alpha} = PN(kT + \alpha) - PN(kT) \quad (F.39)$$

Also, let

$$2f_s(\tau) \theta 2f_s = 2f_s(\alpha) \theta 2f_s = 1 - \Delta_\alpha \quad (F.40)$$

the last equality defining Δ_α. Using (F.38) and (F.40) in (F.37),

$$v(t) = 2f_s \theta f_s \ PN \theta PN(kT) - 2f_s \theta f_s \theta PN \cdot \left[PN(kT) \cdot \Delta_\alpha - 2f_s(\alpha) \theta 2f_s \cdot \delta_{k\alpha}\right] \quad (F.41)$$

Consider the first term in (F.41). Its component at the frequency f_s, in phase with f_s, produces a d.c. output at e(t). f_s, however, is in phase with PN and with PN(kT). Hence over any PN bit-time T, the term $f_s \theta PN \theta PN(kT)$ is a constant. On the other hand, $2f_s$ is an odd function over T. Hence multiplying the first term in (F.41) by a sine wave in phase with f_s and integrating over T yields zero. This is illustrated in Figure F-29.

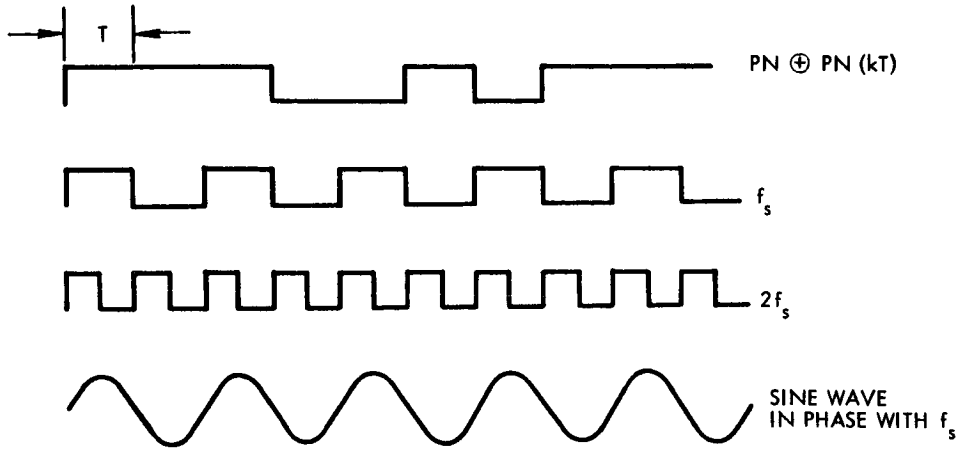


Figure F-29. Bit Synch Wave Shape

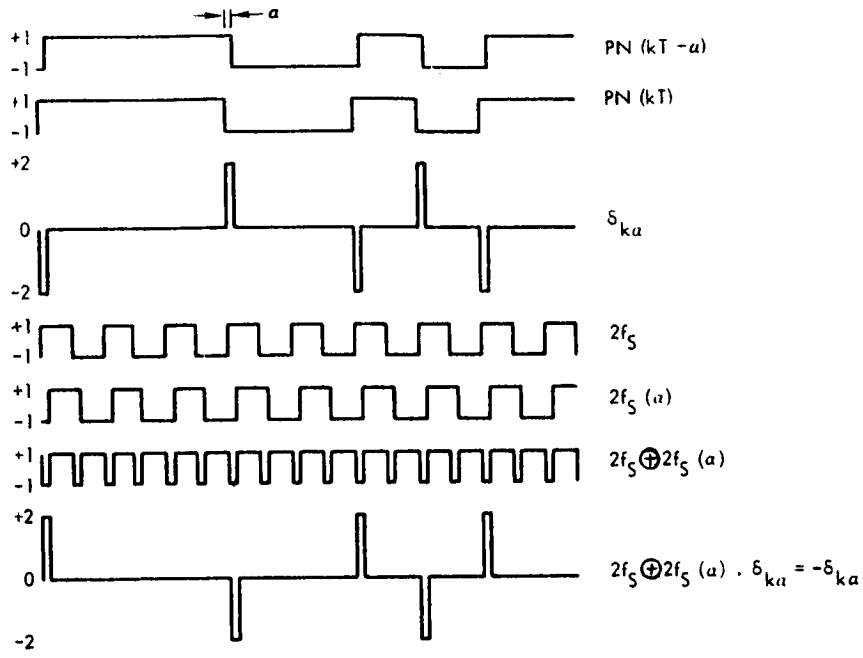
Consider the last term in the brackets in (F.41). $\delta_{k\alpha}$ is nonzero only in the intervals $(kT, kT+\alpha)$ from (F.39). On the other hand, $2f_s(\tau)\ \theta\ 2f_s$ is periodic with period T, and always negative in the intervals $(kT, kT+\alpha)$. This is illustrated in Figure F-30. Hence insofar as its effect on the d.c. output of e(t) is concerned, (F.41) may be replaced by

$$v_1(t) = -2f_s\ \theta f_s\ \theta PN \cdot \left[PN(kT) \cdot \Delta_\alpha + \delta_{k\alpha}\right] \qquad (F.42)$$

3.3.2 Decomposition of Δ_α

Next, decompose Δ_α into an arithmetic sum of two parts: $\Delta_\alpha = \Delta_\alpha' + \Delta_\alpha''$. From Figures F-30 and F-31, it is seen that Δ_α is a train of pulses of width α, occurring every T/2 seconds. The decomposition is shown in Figure F-31 so that Δ_α' and Δ_α'' are two pulse trains both with pulses of width α occurring every T seconds; however, the two pulse trains are displaced T/2 seconds apart from each other. Hence (F.42) is

$$v_1(t) = -2f_s\ \theta\ f_s\ \theta\ PN \cdot \left[\delta_{k\alpha} + PN(kT) \cdot \Delta_\alpha' + PN(kT) \cdot \Delta_\alpha''\right] \qquad (F.43)$$



Illustrating that $2f_s \oplus 2f_s(\alpha)\ \delta_{k\alpha} = -\delta_{k\alpha}$

Figure F-30. Bit Sync Wave Shapes, Δ_a

Now PN(kT)$\cdot\ \Delta_\alpha'$ is a sequence of pulses of width α, T seconds apart, with polarity dictated by the sequence PN(kT). Comparing the last illustration of Figure F-30 and the first illustration of Figure F-32, it is seen that the term $\delta_{k\alpha}$ + PN(kT)$\cdot\ \Delta_\alpha'$ is a sequence of pulses of width α, occurring only where there are no transitions in the code PN(kT), and of the same polarity as PN(kT). This is denoted $h_{k\alpha} = \delta_{k\alpha}$ + PN(kT)$\cdot\ \Delta_\alpha'$, and is illustrated in Figure F-32. (F.43) is

$$v_1(t) = -2f_s\ \theta f_s\ \theta PN \cdot h_{k\alpha} - 2f_s\ \theta f_s\ \theta PN\ \theta PN(kT) \cdot \Delta_\alpha'' \qquad (F.44)$$

Consider first the second term in (F.44). Both $2f_s$ and Δ_α'' are periodic with period T, hence as may be seen by comparing Figures F-30 and F-31

$$2f_s \cdot \Delta_\alpha'' = \pm \Delta_\alpha''$$

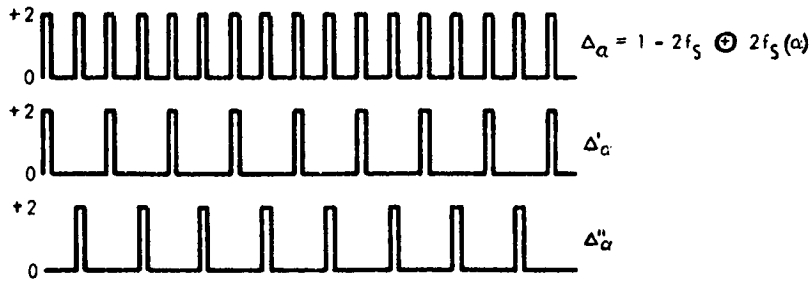


Figure F-31. Decomposition of $\Delta_\alpha = \Delta'_\alpha + \Delta''_\alpha$

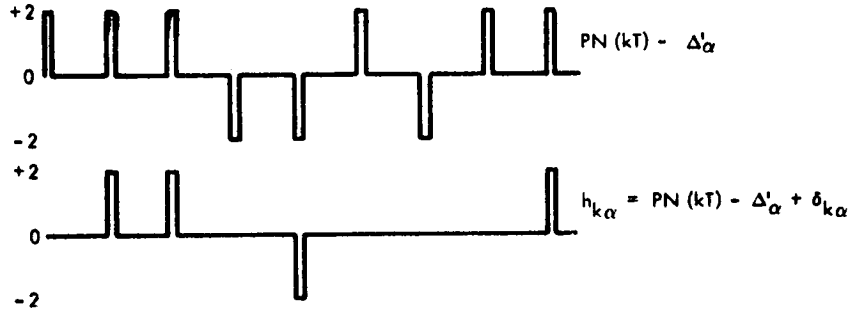


Figure F-32. Calculation of $h_{k\alpha}$

one of the signs being chosen for $\alpha > 0$, the other otherwise. Which sign is chosen is for the moment unimportant, since $2f_s$ could well be 180° out of phase to that drawn. However, we choose the + sign for $\alpha > 0$. Now, multiplying this second term by a sine wave in phase with f_s is equivalent to multiplying the term τ PN θPN(kT) Δ_α'' by a rectified sine wave in phase with f_s. This product, averaged over a PN bit-time T, varies from bit to bit, being either positive or negative depending on PN θ PN(kT). We may, however, average over the entire PN code, n bits long, to obtain the contribution of the second term of (F.44) to the d.c. component of e(t), giving

$$\mp b_2(\tau) = \frac{\mp 1}{nT} (\Sigma \text{ PN } \theta\text{PN(kT)}) \int_{-T/2}^{T/2} g_2(t, \ ) \cos \frac{\pi t}{T} \, dt$$

where

$$g_2(t,\alpha) = \begin{cases} 2 & |\alpha| < t < 0 \\ 0 & \text{otherwise} \end{cases}$$

and the symbol Σ denotes arithmetic summation over the code length.

Similarly, in the first term in (F.44), both $2f_s$ and $h_{k\alpha}$ are periodic with period T, hence as may be seen by comparing Figures F-30 and F-32,

$$2f_s \cdot h_{k\alpha} = \mp h_{k\alpha}$$

the negative sign corresponding to $\alpha > 0$, to be consistent with the previous choice. Again, multiplying this first term by a sine wave in phase with f_s is equivalent to multiplying the term $\pm h_{k\alpha} \cdot PN$ by a rectified sine wave in phase with f_s. Denote

$$PN'(kT) = \begin{cases} 1 & \text{if the present bit in PN(kT) is identical to the previous bit} \\ -1 & \text{otherwise} \end{cases}$$

it is seen that, for $\alpha > 0$, $h_{k\alpha} \cdot PN = |h_{k\alpha}| \cdot PN \theta PN'(kT)$, while for $\alpha < 0$, $h_{k\alpha} \cdot PN = |h_{k\alpha}| \cdot PN(T) \theta PN'(kT) = |h_{k\alpha}| \cdot PN \theta PN'((k-1)T)$. Hence averaging over the code length n, the first term contributes a d.c. component

$$\pm b_1(\tau) = \frac{1}{nT} (\Sigma PN \theta PN'(kT)) \int_{-T/2}^{T/2} g_1(t,\alpha) \cos \frac{\pi t}{T}, \quad \alpha > 0$$

$$\frac{-1}{nT} (\Sigma PN \theta PN'((k-1)T)) \int_{-T/2}^{T/2} g_1(t,\alpha) \cos \frac{\pi t}{T} dt, \quad \alpha < 0$$

with

$$g_1(t,\alpha) = \begin{cases} 2 & \frac{1}{2}T - |\alpha| < t < 0 \\ 0 & \text{otherwise} \end{cases}$$

3.3.3 Calculation of Error Function

Finally, the sum of these two terms is the desired error function

$$E(\tau) = \pm \left[b_1(\tau) - b_2(\tau) \right]$$

the positive sign being chosen for $\alpha > 0$. Evaluating the integrals, the entire error function is

$$E(\tau) = \begin{cases} \frac{2}{n\pi} \left[(\Sigma PN \epsilon PN'(kT)) \left(1 - \cos \frac{\pi\alpha}{T}\right) - (\Sigma PN \theta PN(kT)) \sin \frac{\pi\alpha}{T} \right], & \alpha > 0 \\ -\frac{2}{n\pi} \left[(\Sigma PN \theta PN'((k-1)T)) \left(1 - \cos \frac{\pi\alpha}{T}\right) + (\Sigma PN \theta PN(kT)) \sin \frac{\pi\alpha}{T} \right], & \alpha < 0 \end{cases} \qquad \text{(F.45)}$$

It is noted at this point that the derivation of (F.45) does not require any particular property of the code PN, but is entirely general. From (F.45), to calculate the error function, it is necessary only to evaluate the three sums $(\Sigma PN \theta PN(kT))$, $(\Sigma PN \theta PN'(kT))$, and $(\Sigma PN \theta PN'((k-1)T)0$, for $k = 0, 1.., n-1$. Since evaluating the second sum also gives the third, only two such sums need be found. In addition, if PN is a maximal length shift register code, it possesses the cycle-and-add property. In this case the first sum is known, being

$$(\Sigma PN \theta PN(kT)) = \begin{cases} n & k=0 \\ -1 & \text{otherwise} \end{cases}$$

Hence for a maximal length shift register code, given any specific PN code, the only computation to be performed is the evaluation of the second sum.

This last may be done quite easily by writing down the given PN code, and underneath it, PN'(0); i.e., copy down the PN code from above if the present bit is identical to the preceding bit, otherwise leave a blank. This is shown in Figure F-33 for the 7-bit PN code, 1110010. Next, cycle PN'(0) successively, generating PN'(T), PN'(2T), etc. The required sum for any k, say k=2, is found by subtracting the number of disagreements of PN'(2T) with PN, from the number of agreements.

In the illustration of Figure F-33, it is seen that this sum is -1 for all k except k=0 and 6 (or k= -1). In the latter two cases, this sum = +3. From (F.45), then, the error function may be plotted, and is shown in Figure F-34.

In general, for a maximal length shift register code, $(\Sigma PN \theta PN'(0)) = n-1/2 = (\Sigma PN \theta PN'((n-1)T)$, since this number is just the number of nontransitions in the code. In the region $-T < \tau < T$, we may now be more explicit:

$$E(\tau) = \begin{cases} -\frac{2}{n\pi}\left[n \sin \frac{\pi\tau}{T} - \frac{n-1}{2}\left(1 - \cos \frac{\pi\tau}{T}\right) \right] & 0 < \tau < T/2 \\ +\frac{2}{n\pi}\left[\sin \frac{\pi}{T}(T-\tau) - \frac{n-1}{2}\left\{1 - \cos \frac{\pi}{T}(T-\tau)\right\}\right] & T/2 < \tau < T \end{cases}$$

and the negative of the above in the negative region.

PN	1	1	1	0	0	1	0	$(\Sigma PN \oplus PN^1(kT))$
$PN^1(0)$		1	1		0			+3
$PN^1(T)$			1	1		0		-1
$PN^1(2T)$				1	1		0	-1
$PN^1(3T)$	0				1	1		-1
$PN^1(4T)$		0				1	1	-1
$PN^1(5T)$	1		0				1	-1
$PN^1(6T)$	1	1		0				+3

Calculation of $(\Sigma PN \oplus PN'(kT))$ For a 7-Bit Code

Figure F-33. Calculation of $(\Sigma PN \oplus PN'(kT))$ For a 7-Bit Code

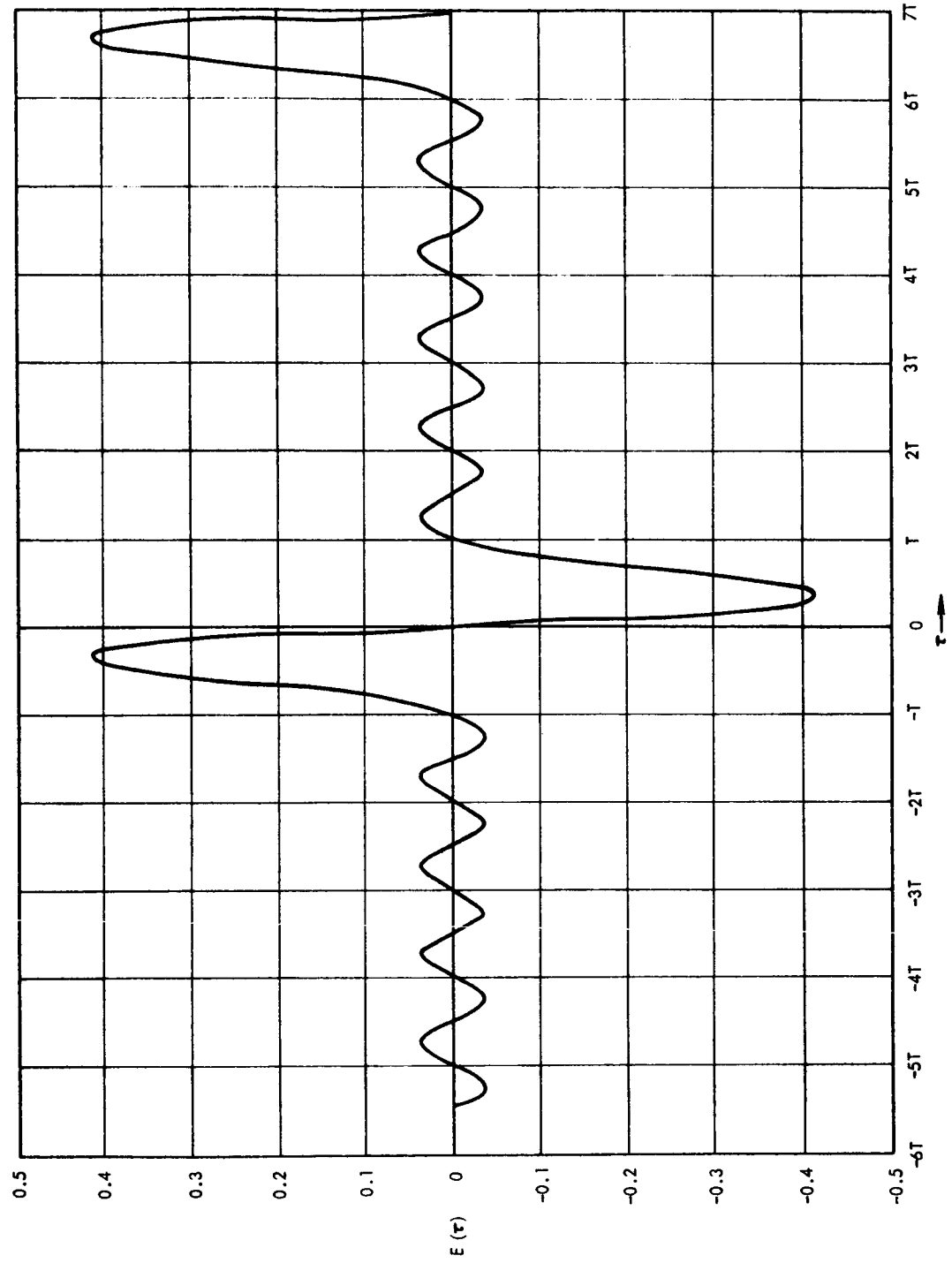


Figure F-34. Error Function for 7-Bit Code 1110010

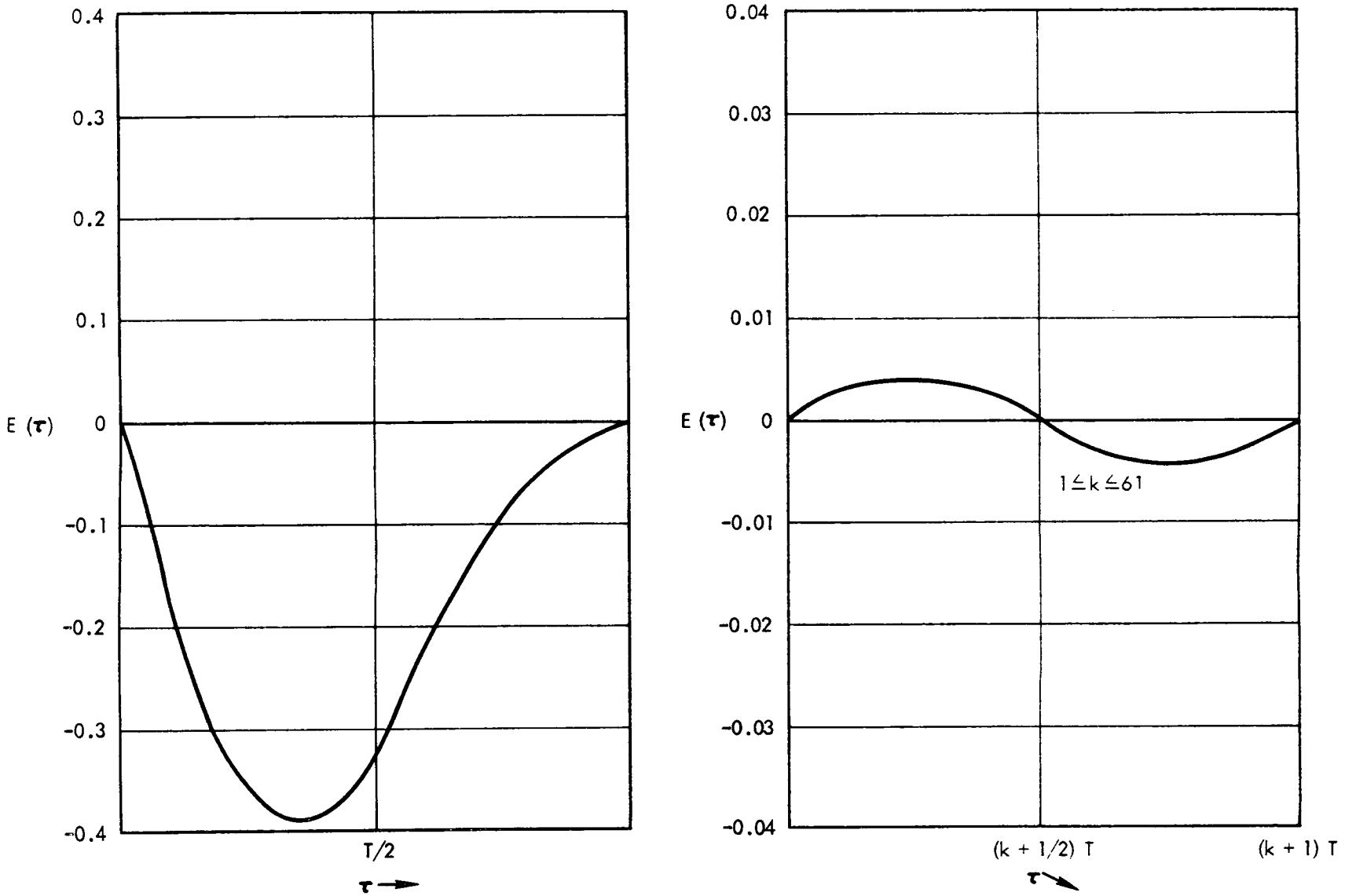


Figure F-35. Error Function for Mariner C Telemetry Code

(F. 45) was also evaluated for the 63-bit PN code used on the telemetry link of Mariner C. This code is:

100000111111010101100110111011010010011100010111100101000110000

It was found, by performing the computation illustrated in Figure F-35, that similar to the 7-bit code, $(\Sigma PN\ \theta PN'(kT)) = -1$ for all k except k=0, 62. Hence the error function is identical in any interval (kT, (k+1)T), for $1 \leq k \leq 61$. Hence we plot in Figure F-35 only the error function for small τ, $|\tau| < T$, and for large τ, $|\tau| > T$. Notice that the vertical scale differs by a factor of 10 in the two cases. Hence the 'sidelobes' of the error function are approximately 40 db below the main curve.

Comparing Figures F-34 and F-35, we note that the peak of the error function for the 7-bit code is slightly higher than that of the 63-bit code; however, its sidelobes are only about 20 db down compared to 40 db for the 63-bit code. We also note that the error function for the unfiltered loop (no narrow bandpass filter) has peaks of 0.5 compared to about 0.4 for the two cases considered here.

In summary, the error function as derived applies to an infinitely-narrowband filter centered at f_s, since what was done was to calculate the coefficient of the Fourier series term at f_s, in phase with the reference. On the other hand, we know that the error function is of the triangular type illustrated in Figure F-28 if this filter were infinitely wide. It may perhaps then be expected that for filters of intermediate bandwidth, the actual error function lies somewhere between the two extremes.

4. TELEMETRY LINK ANALYSES

This section investigates certain aspects of the Voyager telemetry link. Specifically, the topics covered include:

a) Comparison of Synchronization Methods

PN synchronication (using a separate channel) and NRZ synchronization (single channel) are compared with respect to bandwidth requirements, oscillator stability, acquisition, mean time to loss of lock, etc.

b) PN Synchronization Acquisition Performance

Acquisition time is calculated for a particular acquisition procedure.

c) Single-Versus Two-Channel System

The two basic system types are compared with respect to equipment and communication efficiency for the Voyager data rates.

d) Performance of Two-Channel System

The performance of the two-channel Voyager telemetry system is evaluated for bandwidth requirements power requirements, intermodulation and interference.

4.1 Comparison of Synchronization Methods

This section compares two basic methods of obtaining bit synchronization using Voyager parameters: the PN (pseudonoise) synchronization system of Mariner C and synchronization to an NRZ code as implemented on IQSY Pioneer. It is recognized that an integral part of the bit synchronization problem is the choice of bit-waveforms to avoid interaction with the carrier loop; hence the problem of demodulation of a subcarrier, where used, is also considered.

A simple description of the two synchronization schemes is presented.

4.1.1 PN Synchronization

The theory of PN synchronization is based on the properties of maximal length linear shift register codes, denoted PN. The number of '1's in such a code exceeds the number of '0's by one. PN also

possesses the co-called cycle-and-add property; i.e., let PN(kT) denote PN cycled k units to the right:

PN	1110010
PN(2T)	1011100

the cycle-and-add property says that for every k, there exists a j so that PN $\oplus$ PN(kT) = PN(jT), where $\oplus$ denotes binary addition.

Springett* discusses the two-channel system used on Mariner C. The transmitted code is PN $\oplus$ $2f_s$, where $2f_s$ is a squarewave of period T, the length of a PN bit (Figure F-36). At the receiver, this is

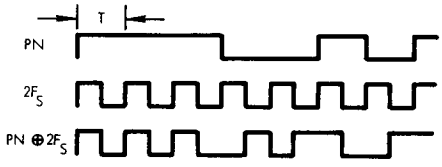


Figure F-36. Transmitted Waveform in PN Synchronization

correlated with PN. The cross correlation of PN $\oplus$ $2f_s$ with PN(τ), where τ is the timing difference between the received code and the local clock, is shown in Figure F-37 and is denoted g (τ). Hence if the receiver is of the form shown in Figure F-37, the error voltage presented to the loop, as a function of the timing error between the input and the local clock, is the cross correlation g (τ). A further property of interest is the spectrum of the transmitted waveform, PN $\oplus$ $2f_s$ shown in Figure 18 of Springett's report.

*J. C. Springett, "Telemetry and Command Techniques for Planetary Spacecraft," JPL Technical Report No. 32-495, 16 January 1965.

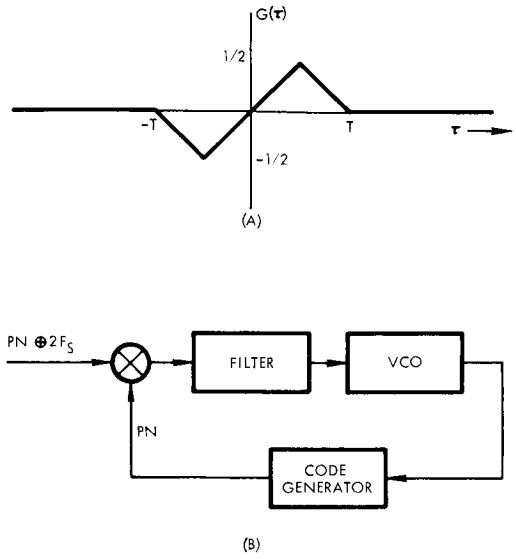


Figure F-37. Receiver for PN Synchronization

To preserve the 'squareness' of the waveshape at the input of the receiver of Figure F-37, a large bandwidth must be maintained prior to the receiver, often resulting in a small signal-to-noise ratio at its input. The limited dynamic range of the product device is then a problem. A solution is the circuit of Figure F-38. In the absence of the narrowband filter, centered at f_s, the circuit of Figure F-38 becomes that of Figure F-37. The narrowband filter, however, obtains a reasonably large SNR at its output, so that the dynamic range of the second product device need not be large. On the other hand, since the output of the first product device does not contain any DC component, DC drift due to this device may be rejected. In this case, the loop error function is no longer that shown in Figure F-37. Section 3 derives the loop error function for the circuit of Figure F-38, assuming an infinitely narrowband filter centered at f_s. This error function is sketched in Figure F-38, together with the nonfiltered version for comparison. Two features are observed: the error in the vicinity of in-lock ($\tau < T$) has a steeper slope than the nonfiltered function. In addition, the error voltage for large timing errors ($|\tau| < T$) is no longer identically zero.

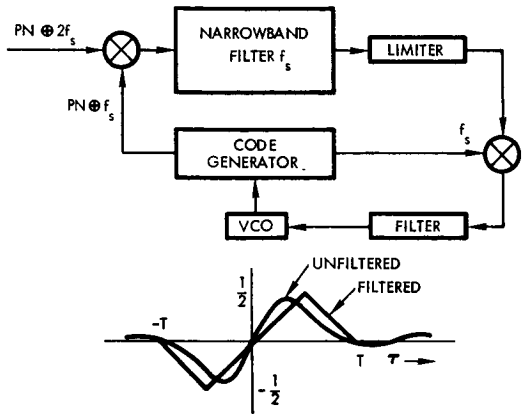


Figure F-38. Modified PN Receiver

We note some gross features of PN synchronization: when the receiver achieves lock, the timing error may be expected to be a fraction of a PN bit-time T. No error voltage, in the case of Figure F-37, is available for loop correction when the timing error exceeds one PN bit-time. In the case of Figure F-38, false lock points may exist. From the spectrum of Figure 18 of Springett's report, no energy is present at DC, with most of the energy centered at $1.5f_s$. About 86 per cent of the total power is within $4f_3$, while about 93 per cent is within $8f_s$.

4.1.4 NRZ Synchronization

The method of synchronization used on Pioneer is based on a modification of the synchrolink circuit first proposed by J. P. Costas*. Called the I-Q loop, the circuit is illustrated in Figure F-39, and is capable of achieving synchronization to a data-modulated bit stream. Let the information bit-time be T_i, and for simplicity assume that the bit-waveform over T_i be a code (i.e., it assumes only the values ± 1). For instance, an example of such a code is a squarewave over the bit-time T_i. The code generator c_i generates the information bit-waveform successively, so that the output of the integrate-and-dump at the sampling time is the best

*J. P. Costas, "Synchronous Communication," Proc. IRE, Vol. 44, pp. 1713-1718, December 1956.

estimate of the data over the preceding bit-time, in the presence of white Gaussian noise, when the loop is correctly locked. The output of the decision device in this I-, or in-phase channel, is the mitched-filter detected version of the data. The code generator c_q generates periodically a different waveform (with the period T_i), which may be thought of as being in quadrature with the data waveform. Its product with the input is also integrate-and-dumped in order to introduce the same delay as in the I-channel. The result, the output of the Q-, or quadrature channel may be thought of as furnishing a proper loop error signal in the absence of information modulation. In the presence of information modulation, multiplying the outputs of the I- and Q-channels removes this modulation, providing proper loop sense information to the filter.

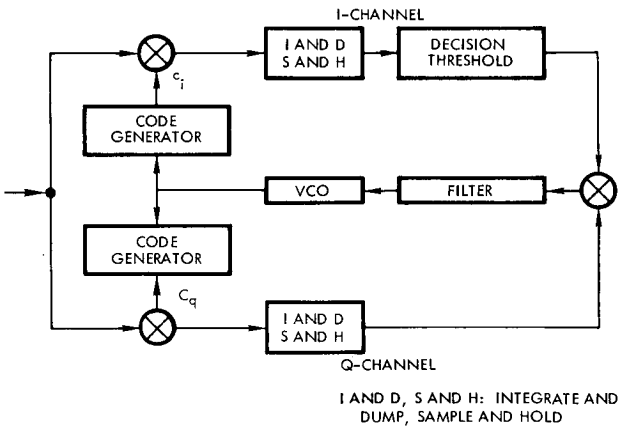


Figure F-39. I-Q Loop

For a squarewave of period T_i/n, the loop error voltage as a function of τ, the timing difference, is plotted in Figure F-40 for n = 4, and with and without an information transition. Twon false-lock points are present without an information transition, but unlike the error function of Figure F-41, the magnitude of the sidelobes are such that the circuit is as likely to lock incorrectly as correctly. In the presence of an information transition, the false-lock points shift, and the sidelobes are not as high. In usual language, the squarewave with period T_i/n is an n-cycle/bit squarewave subcarrier; the loop is then a subcarrier demodulator. A subsidiary circuit is necessary to resolve these n false-lock points. For

Pioneer, it was decided to perform this resolution independently of the subcarrier demodulator, so that what is required is a conventional NRZ bit synchronizer.

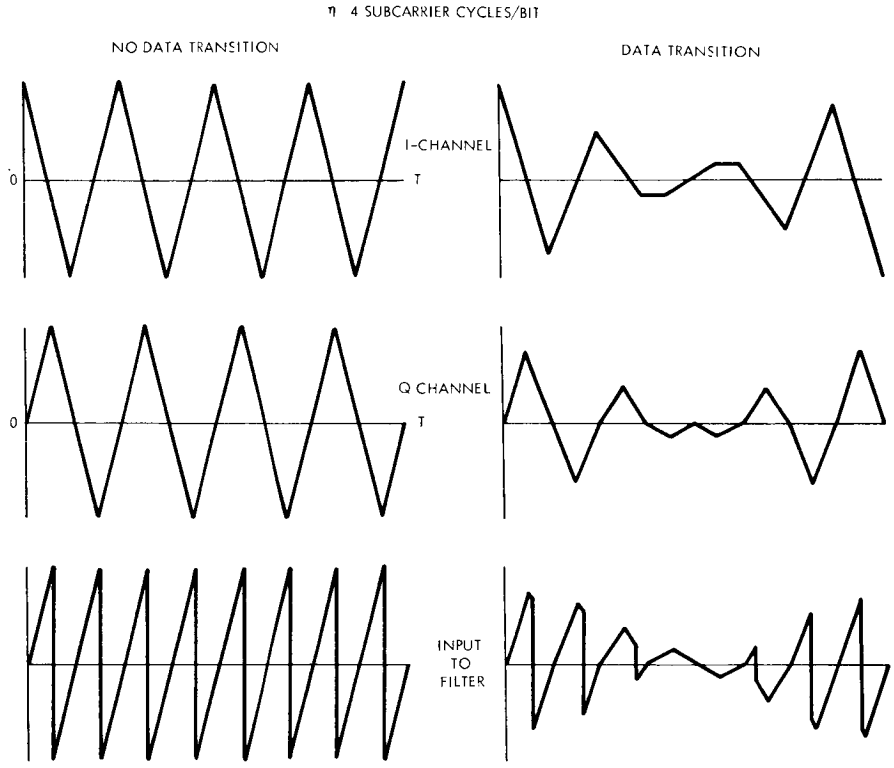


Figure F-40. Error Function for Demodulator Loop

By choosing the code generators c_i and c_q propertly, the I-Q loop may be used as such a bit synchronizer. In this case c_i is a constant over T_i, so that the inphase multiplier is unnecessary. c_q is a square-wave with period T_i. The loop error function also depends on whether or not an information transition occurs, but is identically zero in the absence of such a transition. This is shown in Figure F-42. Finally, the output of the bit synchronizer operates the integrate-and-dump, sample-and-hold circuits in both the subcarrier demodulator and the bit synchronizer.

We note some gross features of this synchronization method: timing information is directly available from the data-modulated bit stream, without the use of a separate synchronization channel.* When the loops are

*Discussion of the single-channel PN system is deferred to Section 6.

properly locked, the subcarrier demodulator provides timing information to a fraction of a subcarrier cycle, while the bit synchronizer loop provides timing information to a fraction of an information bit. Timing information is available to the subcarrier demodulator loop at all times, while the bit synchronizer loop requires the presence of information transitions. The spectrum is sketched in Figure F-43, with approximately 81 per cent of the energy below the fundamental, and none at DC.

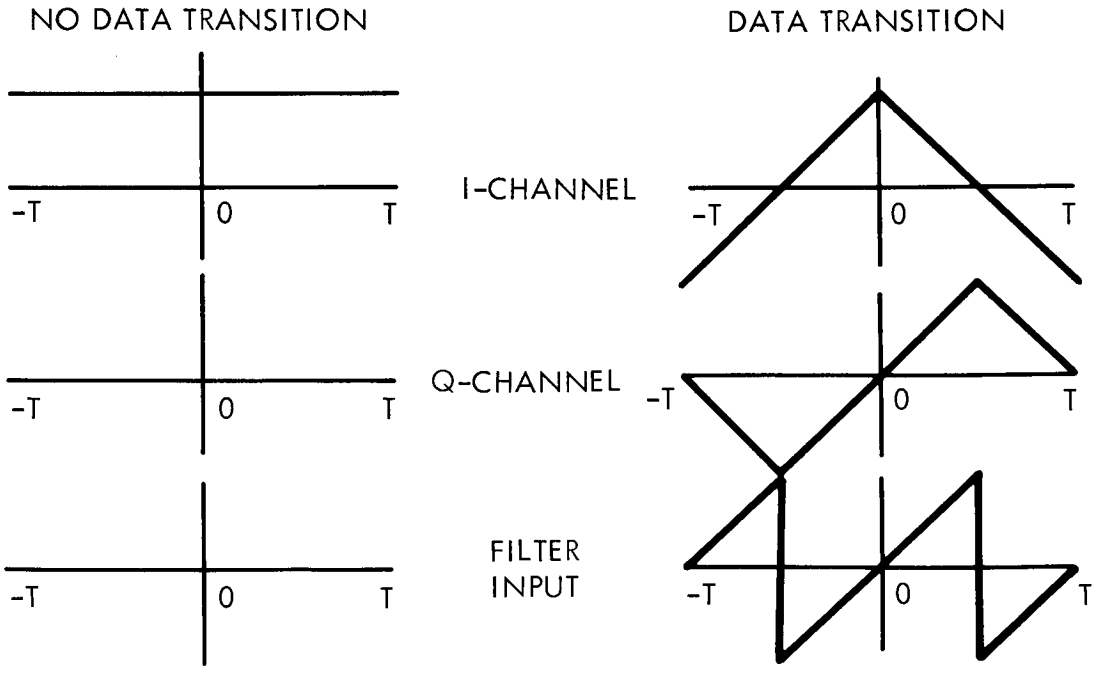


Figure F-41. Error Function for Bit Synchronizer

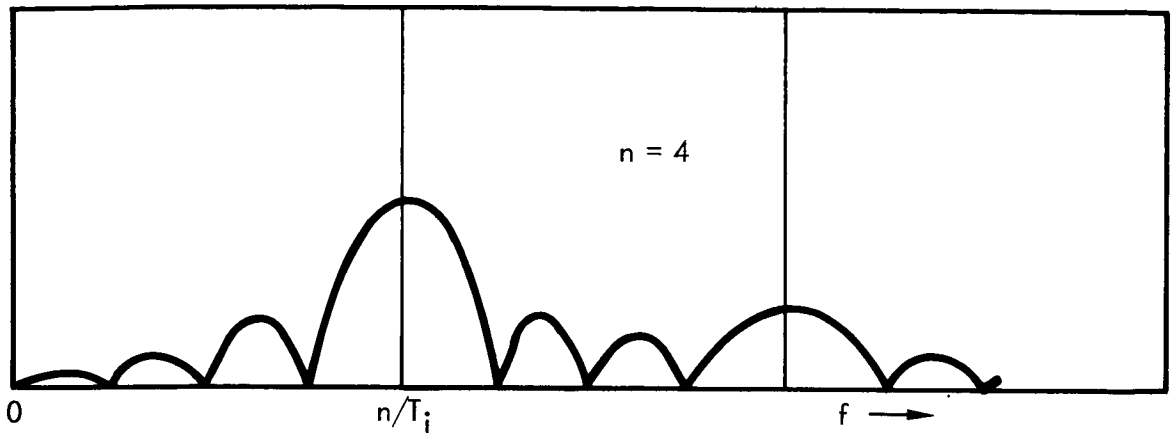


Figure F-42. NRZ Spectrum With 4 Cycles per Bit Subcarrier Random Data

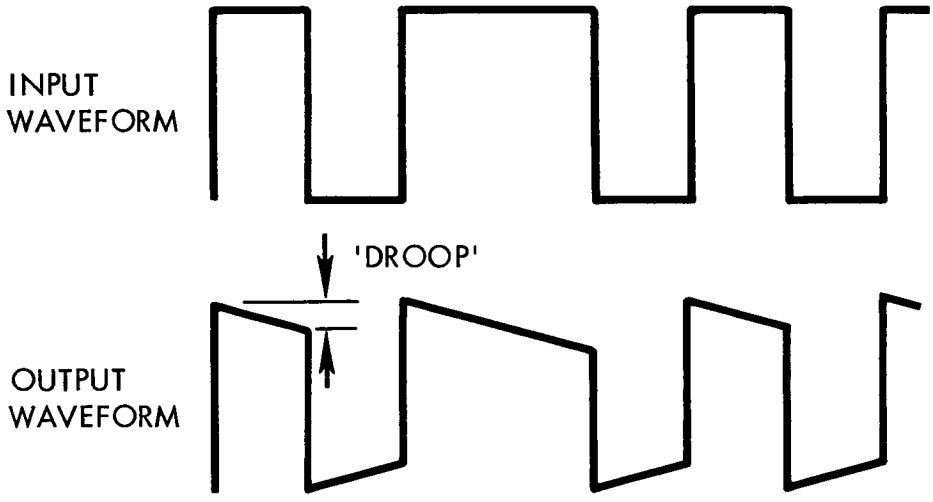


Figure F-43. Tracking Out of Subcarrier by Carrier Loop

4.1.3 Choice of PN Code Length and Subcarrier Frequency

A criterion for the choice of bit-waveform is the avoidance of interaction with the carrier tracking loop. As may be seen from Figures 8 (Springett)[1] and from Figure F-43, both synchronization methods avoid spectral components at DC. More than this is necessary, of course, since significant energy around zero frequency results in distortion of the bit-waveforms due to the carrier tracking loop. The importance of this distortion should not be judged purely on an energy basis; in the NRZ

synchronizer, a nonsymmetric bit-waveform results in a bias in the timing reference, while in the PN synchronizer, distortion may produce larger false-lock sidelobes as well. In the NRZ synchronizer, the amount of energy a fixed distance from zero frequency depends both on the information bit-time T_i and the number of subcarrier cycles per bit n. In the PN synchronizer, this depends only on the PN bit-time T (this is as yet unrelated to T_i).

For the carrier phase-lock loop in the DSIF receiver, $2B_{L0}$ is normally 12 cps, although it expands to about 120 cps for high signal-to-noise situations. The bit rates used in Voyager are 128, 1024, 2048, and 4096 bit/sec. To avoid operational difficulties of narrowing the carrier loop bandwidth for high signal-to-noise situations, we choose n and T so that for all T_i's, the effect of the carrier tracking loop may be neglected.

For a critically-damped second-order loop, the effect of carrier loop tracking is illustrated in Figure F-44. N must be chosen sufficiently large for the largest T_i in the NRZ synchronizer so that the amount of 'droop' is small, since the bias error introduced is about one-half of the fractional droop. Chose n = 8, so that for T_i = 1/128 (worst case), the 1024 cps squarewave has a droop of 10 per cent (assuming the carrier loop is critically damped at $2B_{L0}$ = 120 cps—which it isn't), corresponding to a bias in the demodulator loop of around 9 degrees. For smaller T_i's, n is maintained constant. For T_i = 1/2048, the subcarrier is a 16 kc squarewave, still far removed from the DSIF receiver high frequency bandwidth limitation.

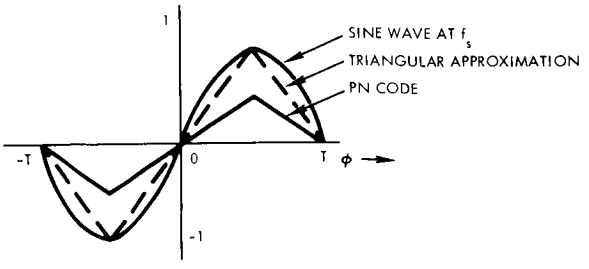


Figure F-44. Different g(Ø) Functions

For the PN synchronizer, $T_i = mT$, where m must be a divisor of n, the PN code length, if the synchronization channel is to provide bit synchronization unambiguously. m must be chosen large so that T is small, making f_s large and reducing the energy in the region 0 to 60 cps. It may be desirable to choose n larger than m, n = km, for two reasons: k may be chosen equal to the number of information bits per word, so that word synchronization is provided as well. In addition, as may be seen from Section 3 of this appendix, increasing n reduces the magnitude of the false-lock sidelobes. Similarly to Mariner C, we choose m = 9, n = 63. Hence f_s = 576 cps for T_i = 1/128, while since k = 7 and there are 7 information bits per word, word synchronization is provided. The droop in the square waveforms introduced by the carrier loop is twice as large as in the NRZ synchronizer, but, considering Figure 18 (Springett), this may be expected to be satisfactory. Again, maintaining m and n fixed for all T_i is not a problem even at the highest bit rate, from the standpoint of the DSIF receiver high-frequency cutoff.

4.1.4 Choice of Loop Bandwidths

Section 3 applies the Fokker-Planck equation to a first-order phase-lock loop with square inputs. Our design is based on this analysis, with the implicit assumption that second-order loops behave similarly.

For the PN synchronizer, the data is deposited on a squarewave subcarrier, with a frequency which may be a multiple of f_s, since the synchronizer should also provide subcarrier demodulation. Increasing the subcarrier frequency requires a quieter loop for the same jitter on the subcarrier; on the other hand, decreasing the subcarrier frequency (from $4f_s$) results in crosstalk of the subcarrier and synchronization channels, where these are linearly added as in Mariner C. If the data subcarrier and synchronization powers are about equal, then the data subcarrier should be placed at $4f_s$ to avoid interference from the synchronization signal. On the other hand, the subcarrier does not particularly bother the synchronization channel, since its spectrum is spread by the first product device in Figure F-41, and little energy is passed through the narrowband filter. For this reason, the data channel is chosen to have 10 times the power in the synchronization channel, and the data subcarrier is assumed at $2f_s$, or 1152 cps for the lowest bit rate.

From Section 3, for the PN synchronizer with n = 63, it appears that the signal-to-noise ratio in a loop bandwidth of $2B_L0$ should be in the order of 17 db for a data subcarrier at $2f_s$ to provide a reasonably clean reference.* A number of this magnitude may also be arrived at by a simpler but perhaps convincing argument. From Figure F-37, the non-filtered loop error function $g(\phi)$ extends from 0 to T in one direction with a peak of one half. A sinewave at frequency f_s has an error function also extending from 0 to T in one direction, with a peak of 1; we may approximate it by a triangular waveform and compare it with $g(\phi)$ as in Figure F-45. To make the two error functions coincide, the voltage of the input PN signal may be doubled, quadrupling the power and doubling the loop bandwidth. This doubles the signal-to-noise ratio in the loop bandwidth. Next, since the subcarrier is at $2f_s$, the loop bandwidth needs to be four times as narrow to maintain the same rms jitter at $2f_s$ as at f_s. Combining these two factors, the signal-to-noise ratio must be 8 times, or 9 db larger for the PN loop with subcarrier at $2f_s$, than for a sinewave phase-lock loop at f_s. Since a sinewave phase-lock loop at f_s provides 15 degrees of phase jitter at a SNR in $2B_{L0}$ of 9 db, the PN loop requires a SNR of 18 db.

For a loop SNR of 17 db, τB_L is greater than 10^7, where τ is the mean time to loss of lock. Since a bit error rate of 5×10^{-3} is achieved for a signal-to-noise ratio of 7db (5.2 db plus circuit losses), for T_i = 1/128 the loop bandwidth should be about $T/100T_i$ (remembering that the signal channel has ten times the power), corresponding to an f_n for the second-order loop of 0.2 cps. The mean time to loss of lock, is then greater than 200 hours.

Loop bandwidths need to be chosen for the NRZ synchronizer for both the demodulator and bit synchronizer loops. Section 3 may also be applied to the demodulator loop. However, since the $g(\phi)$ function is similar to that for a sinewave input, we choose conservatively a signal-to-noise ratio of 12 db in $2B_{L0}$. This implies an f_n for the second-order

*B_L as used in Section 3 corresponds to B_{L0}; 17 db in 2 B_{L0} corresponds to 20 db for β of Section 3.

loop of about 7 cps. However the mean time to loss of lock, using Section 3, is about 5 minutes, perhaps too small a figure (a much smaller mean time to loss of lock may be acceptable for the NRZ synchronizer compared to the PN, since reacquisition times are less). We choose f_n = 3 cps, increasing the mean time to loss of lock to over 100 hours, and the rms phase jitter to less than 10 degrees.

Design of the bit synchronizer loop depends on the frequency of data transitions. In the Pioneer telemetry link, it was decided to use 1 bit in each 7-bit word to provide error detection. This check bit was conveniently chosen to have odd parity, ensuring a minimum data transition density of one each 7 bits. To achieve the same communication efficiency as the PN system, we choose one out of every 11 bits to provide odd parity, hence a minimum transition density of 1/11. If transitions were to occur every bit, by the reasoning of the previous paragraph, a SNR of 12 db in the loop bandwidth should be sufficient, or an f_n of 7 cps is required. However, at the minimum transition density, only 1/11 of the signal energy is available, while noise continually excites the loop even in the absence of a transition. The result is that the loop is in effect $(11)^2$ = 121 times noiser.* To maintain the same loop jitter at this minimum transition density, an f_n of 7/121 = 0.05 cps is needed. Using this value, the mean time to loss of lock, using a signal-to-noise ratio of 12 db, is around 10 hours in the worst case.

4.1.5 Bandwidth Expansion for Strong Signals

For the NRZ synchronizer, since there are 8 cps per information bit, the SNR in a bandwidth equal to the subcarrier frequency is - 2 db for a 7 db SNR in T_i. The bandwidth preceding the input to the demodulator of Figure F-39 should be approximately 10 times this, to avoid distorting the square wave subcarrier (it may be noted that the effect of this distortion, together with the low-frequency distortion due to carrier tracking, results in a more symmetric waveform, thus compensating for each other to some degree). Hence the signal-to-noise ratio at the input to the demodulator, assuming a prefilter at 10 times the subcarrier frequency, is -12 db. This is sufficiently large that the dynamic range of

*R. Y. Huang, "Design of Bit Synchronizer Loop," TRW Memorandum 9330.11-22, 1 May 1964.

the product device at the input is not a hindrance. Hence if a coherent AGC is provided prior to the demodulator-bit synchronizer (which is available from the DSIF carrier demodulator), the bandwidths of the loops are essentially independent of the input SNR, and no bandwidth expansion occurs.

For the PN synchronizer, approximately the same numbers apply as above. However, since only 9 per cent of the power is in the synchronization channel, the SNR at its input is in the order of -23 db. This number is probably not so small that the dynamic range of the input product device is a limiting factor. However, if one desires to maintain synchronization for signal-to-noise ratios in T_i below 7 db, then this limited, dynamic range may be a problem. For this reason, the circuit of Figure F-38 was used on Mariner C.

The analysis of Section 3 demonstrates that the narrow bandpass filter at f_s could be made arbitrarily narrow without unacceptable distortion of the loop error function. However, to avoid loop stability problems, it is desirable to choose this filter wide compared to the highest loop bandwidth. A suitable choice is about 20 cps. This is large compared to 0.2 cps, the loop natural frequency at 128 bits/sec, yet small enough so that the SNR at its output, for a 7 db SNR at T_i, is in the order of 4 db. Hence no loop expansion occurs. For smaller T_i's, the loop natural frequency may be maintained at 0.2 cps if desired; otherwise the filter bandwidth may have to be widened correspondingly.

4.1.6 Acquisition

Since no error voltage is available if the timing error exceeds one PN bit, the PN synchronizer needs a subsidiary means of generating such an error voltage. While the frequency uncertainty in an ordinary phase lock loop may exceed its pull-in range, necessitating a frequency search, in the PN loop, the phase uncertainty may exceed the loop pull-in range, necessitating a search in phase. This may be accomplished by offsetting the received and local clocks intentionally, so that their phases drift relative to each other at a predetermined rate. Gilchriest* seems to indicate

*C. E. Gilchriest, "Pseudonoise System Lock-in," JPL Research Summary No. 36-9, pp. 51-54.

that a good value for this maximum offset is $W_n/2$. For the PN synchronizer at 128 bits/sec, then, the two clocks may be offset by 0.6 cps. Hence the maximum search time is $63/(0.6 \times 2) = 50$ seconds. Since the clockrate is $f_s = 576$ cps, an oscillator stability in the order of 0.05 per cent is required, assuming that the ground clock is perfectly stable.

Whether or not the circuit of Figure F-38 is used, it appears that false locks are not a problem, since these false lock peaks are about 40 db down, from Section 3 and no loop bandwidth occurs. Whether or not the word synchronization provided by this PN synchronizer is useful, it nevertheless appears from Section 3 that it is desirable to choose n, the PN code length, large in order to minimize these false lock peaks.

Acquisition characteristics for the NRZ synchronizer are not completely understood. With many data transitions, the demodulator loop tends to acquire after the bit synchronizer, based on TRW's experience on Pioneer. Conversely, with few data transitions, the demodulator loop acquires before the bit synchronizer. However, Pioneer parameters are different from the ones used here. For Voyager, since the square wave subcarrier is a 1 Kc for a data rate of 128 bits/sec, and since the demodulator loop bandwidth is 3 cps, an oscillator with 0.1 per cent stability ensures fast lockon without the necessity of a frequency search. For the bit synchronizer loop with a loop bandwidth of 0.05 cps at 128 bits/sec, an oscillator with 0.04 per cent stability is required without a frequency search, again assuming perfect ground clocks. It does not appear that acquisition times should exceed 10 or 20 seconds in the worst-case condition of minimum transition densities.

4.2 PN Synchronization Acquisition Performance

The computational method for acquisition of the telemetry signal is the same as the method used for the ranging signal (Section 1).

Single component maximal length codes of lengths 63, 15, and 7 will be considered. The information in each coded word is

$$n = \log_2 L$$

where L is the code length.

From Figure F-8 of Section 1, the ST_B/N_o for a word error probability $P_w(n)$ of 10^{-3}, the results are shown as follows:

L	n	$ST_B/N_o = x$
63	5.98	2.7
15	3.91	3.5
7	2.80	4.5

The time for receiving n bits of information T is nT_B. The acquisition time T_A is given by

$$T_A = nT_B L$$

$$= n \frac{x}{(S/N_o)} L$$

The total received power level S versus the transmission range R is shown in Figure F-45. The following assumptions are made:

a) The signal power in the tracking channel is 10 per cent of the total received power.

b) The signal power in the telemetry synchronizing channel is 10 per cent of the power available to the data plus synchronizing channels.

c) The telemetry PLL sync bandwidth is 2 cps. For example, at a range of 2×10^8 km

Total received power	= -173 dbw
Signal power in carrier channel	= -183 dbw
Signal power available to synchronizing and data channels	= -173.4 dbw
Signal power in the synchronizing channel	= -183.4 dbw
Signal power in the data channel	= -173.8 dbw
Noise power spectral density	= -211 dbw

The results for the three different length codes at a range of 2.5×10^8 km are as follows:

L (bits)	T_A (sec)
63	1.77
15	0.35
7	0.15

It is seen that T_A is negligible compared to the transmission delay times. Thus, the difference in T_A for the different length codes is unimportant.

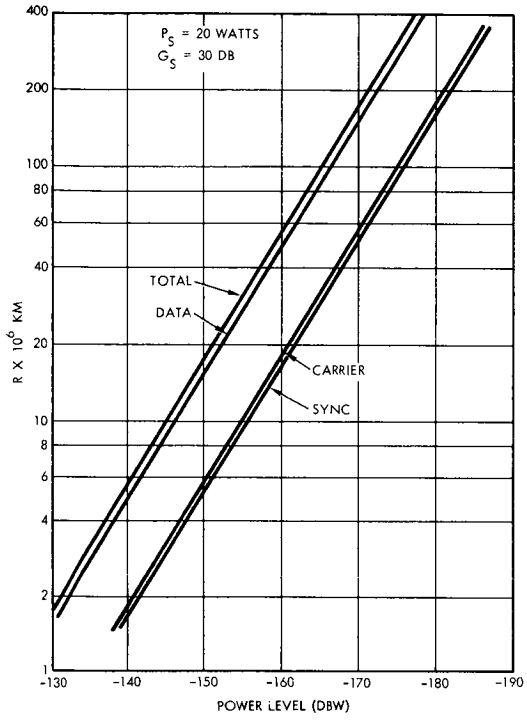


Figure F-45. Range vs. Power Levels in Carrier Data and Sync Channels

The information rate D, time pwer word T_W (there are seven information bits per word), ratio of acquisition time to word duration, and ratio of integration time T to word duration are shown below. These calculations are made for a range of 2.5×10^8 km and a code length of 63 bits.

D (bit/sec)	T_W (msec)	T/T_W	T_A/T_W
2048	3.43	8.2	516
1024	6.86	4.1	258
512	13.72	2.05	129
128	54.88	0.51	32.2

The above table shows that the integration time is about 8 times the word duration for bit rates of 2048 bits/sec while the acquisition time is about 500 times the word duration for this bit rate.

The acquisition time T_A, S/N power ratio P_S/N for a 2 cps phase-lock loop bandwidth and the power level P_S at the synchronizing circuit as a function of transmission range R for the 63-bit length code are as follows:

R 10^6 km	T_A (sec)	P_S/N (db)	P_S (dbw)
250	1.77	24.6	-183.4
100	0.28	32.6	-175.4
25	0.02	44.6	-163.4

More complete results of the analysis are shown in Figures F-46 and F-47 for a maximal length code of 63. The ratio of power level between the synchronizing channel and data channels which is assumed to be 10 per cent is conservative. This is based on the fact that the ratio of the lowest data channel bandwidth to the synchronizing channel bandwidth is greater than 60 and the required SNR in both channels are approximately the same. Under these conditions it is seen from Figure F-46 that practically all of the power is available to the data channel.

4.3 Single- Versus Two-Channel Systems

For a telemetry (or command) system employing PN synchronization techniques, two basic multiplexing or modulation formats can be devised. In the two-channel scheme, the data and sync channels are linearly summed to form a frequency division multiplexed (FDM) signal. The composite baseband then phase modulates the carrier. The PN sync waveform is essentially two-valued, i.e., "squarewave," whereas the data is modulated on either a sinewave or squarewave subcarrier. In the latter case, since each channel is binary, the composite waveform is four-level. In contracts, in the single-channel system the binary data and sync are summed modulo two producing a binary composite waveform.

4.3.1 System Descriptions

The methods of generating the baseband single- and two-channel signals are indicated in Figure F-48. The modulators are seen to be fundamentally similar, each requiring a clock, PN generator, data synchronizer, and logical (half adders) devices. The two-channel modulator

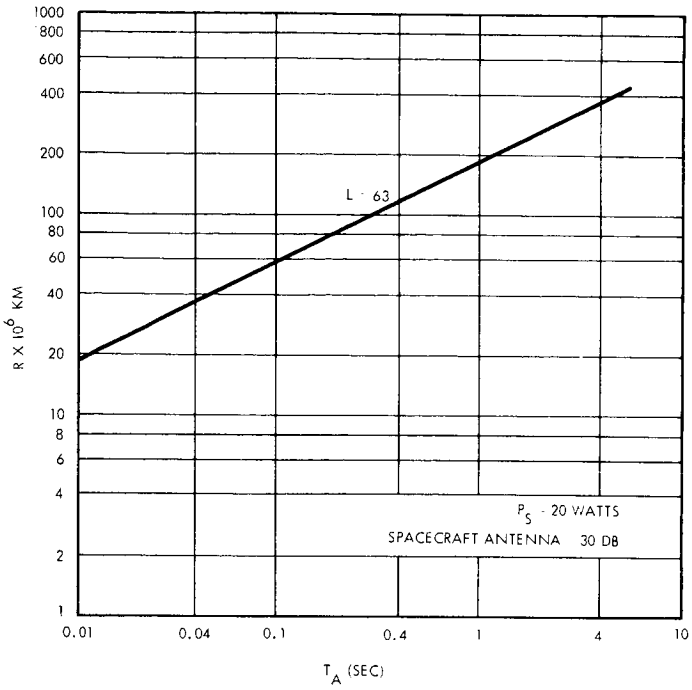


Figure F-46. Range vs. Acquisition Time for 63-Bit Code

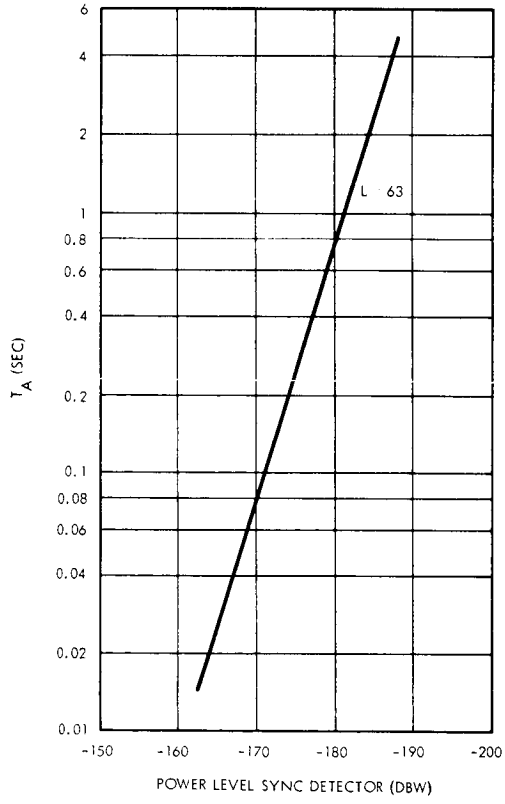


Figure F-47. Acquisition Time vs. Power Level in Sync Channel for 63-Bit Code

is conceptually and practically somewhat more complicated because it requires, in addition, a divider;(possibly) a bandpass filter, and the analog summing circuit. From the spacecraft designers' viewpoint, this is a disadvantage of the two-channel system. Symbolically the output of two-channel modulator is

$$(PN \oplus 2f_s) + (D \oplus 4f_s)$$

where PN is the sync and D is the data. The single-channel modulator forms

$$D \oplus PN \oplus 2f_s$$

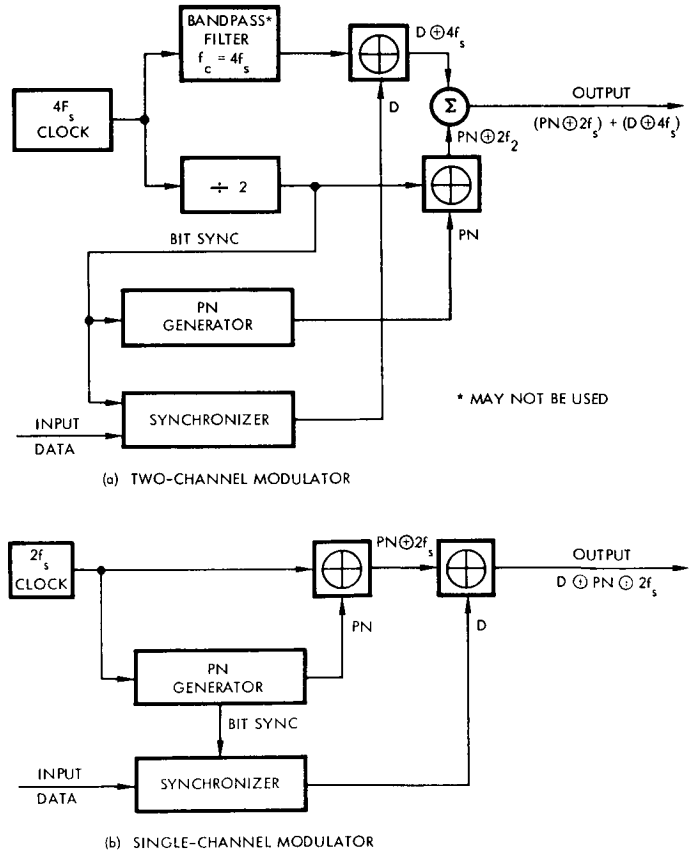


Figure F-48. Single and Two-Channel Modulators

Following reception and coherent demodulation, the baseband signals, corrupted by noise, are detected in the detectors of Figure F-49. In the two-channel detector the sync and data channels are separated by their

basic difference in frequency. However, it will be noted that the sync (lower) channel does not require a bandpass filter prior to the first multiplier. Discrimination is provided by the spreading properties of the PN* code which effectively distributes interfering data frequency components over the entire sync bandwidth. Thus, very little data energy will fall in the filter at f_s and the ultimate effect on the sync loop is negligible. In this realization the data subcarrier is at $4f_s$ in a null of the sync spectrum. However, if the sync power falling in the data channel can be made sufficiently small, other placements are possible.

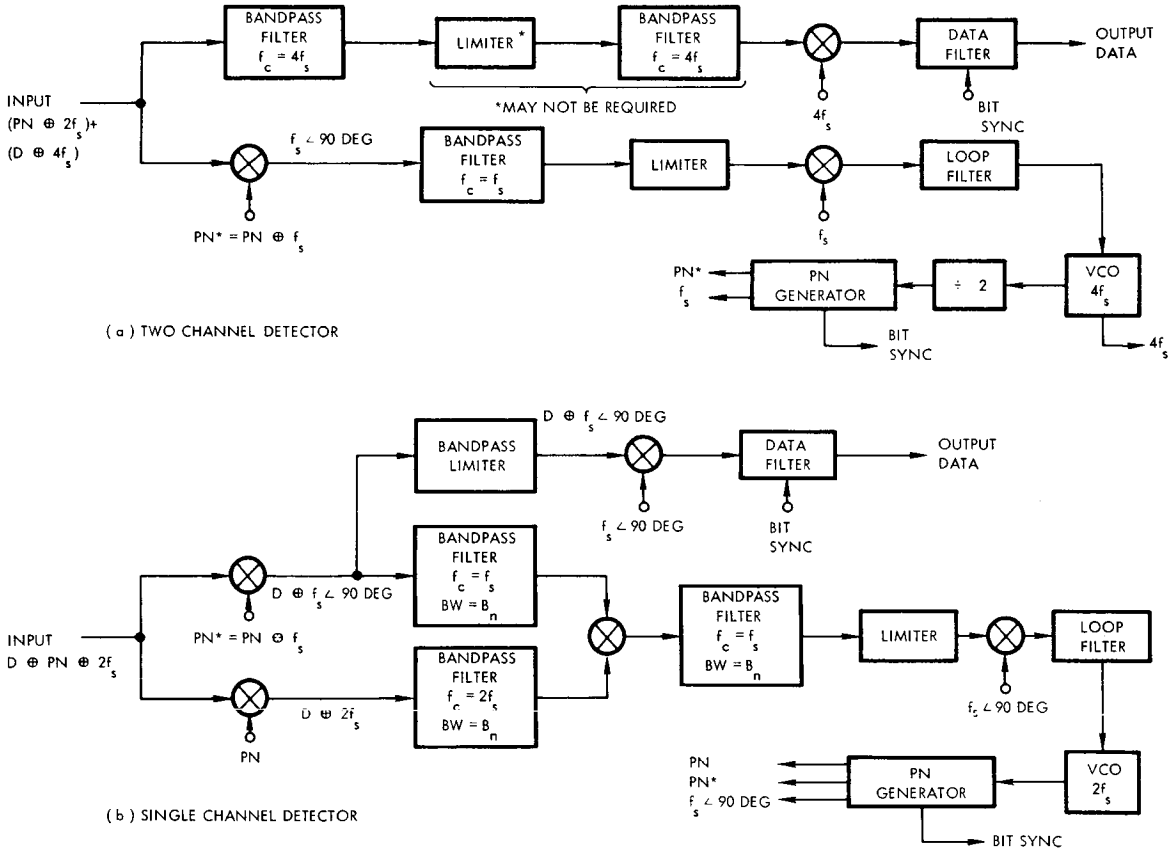


Figure F-49. Single- and Two-Channel Detectors

In the single-channel system the data and sync components are separated by the characteristics of the PN code. First, the PN sequence is removed by multiplying the input D ⊕ PN ⊕ $2f_s$ with PN and PN*. The multiplier outputs contain the data modulated on subcarriers at $f_s \angle$ 90 degrees and $2f_s$. After filtering to restrict the noise bandwidth

(B_n), the modulated subcarriers are multiplied to remove the data modulation and recover the clock at f_s. These operations depend on the fact that

$$2f_s = f_s \oplus f_s \text{ < 90 degrees (squarewave)}$$

$$2f_s = f_s \times f_s \text{ < 90 degrees (sinewave)}$$

Finally, the clock frequency f_s is filtered by a phase-lock loop. The sync channel and the basic method of data removal is seen to be quite analogous to the operation of the in phase/quadrature or I-Q demodulator used for carrier, subcarrier and bit sync reconstruction.

Comparison of the two detectors shows many common features. In the single-channel detector the upper half of the sync channel (exclusive of the extra bandpass filter and multiplier), the bandpass limiter, the phase-lock loop and the PN generator are essentially duplicates of the sync channel in two-channel detector. The single-channel detector has in addition the "quadrature" sync channel making a total of two extra bandpass filters and two more multipliers than the two-channel device. Therefore, the single-channel detector suffers from greater complexity both conceptually and practically.

On the other hand, an important advantage of the single-channel system is the use of frequency f_s as the data subcarrier reference rather than $4f_s$ as in the two-channel system. Since both sync PLL's operate, at f_s the phase jitter on the $4f_s$ reference will be four times as great as for the f_s reference. Equivalently, the sync channel PLL for the two-channel detector must have an SNR 12 db greater than for the single-channel PLL to provide the same quality of subcarrier demodulation. Offsetting this advantage to some degree is the additional degradation caused by multiplying two noisy signals in the third multiplier of the single-channel detector.

4.3.2 Communication Efficiency Comparison

To compare the communication efficiency of the two systems, we must consider the SNR requirements of both the data and sync channels.

The output of the two-channel modulator can be written as

$$k_1(D \oplus 4f_s) + k_2(PN \oplus 2f_s)$$

where k_1 and k_2 are modulation indices which determine the power split between the carrier and the data and sync channels. For the single-channel system the modulation output is

$$k(D \oplus PN \oplus 2f_s)$$

where k is a modulation index which determines only the power split between the carrier and the information sidebands. Except for incidental sources of degradation, all the sideband power is available in both the data and sync channels of the detectors. Therefore, the channel requiring the greater ratio of signal-to-noise density (usually the data) will determine the overall system threshold.

Clearly, the single-channel system is capable of greater communication efficiency because normally no extra sideband power need be allocated for sync. This is especially important when the required sync power approaches that of the data. This occurs for very low data rates such that the sync loop bandwidth is comparable with the data bandwidth. However, for high data rates the proportion of power allocated to sync can be quite small.

These relations can be readily demonstrated. The following telemetry thresholds are established

Data	ST/N/B = 7db for $P_e = 5 \times 10^{-3}$
Sync	18.4 db in $2B_{LO}$ = 0.5 and 2 cps; 15.4 db/cps and 21.4 db/cps
Carrier	6 db in $2B_{LO}$ = 12 cps; 16.8 db/cps

The data S/N/B is plotted against bit rate 1/T in Figure F-50. The sync threshold gives a 0.34 rad rms phase jitter on a reference frequency f_e. For other subcarrier frequencies, the sync threshold power increases 6 db for each doubling of the reference frequency. The carrier threshold is also shown on the figure.

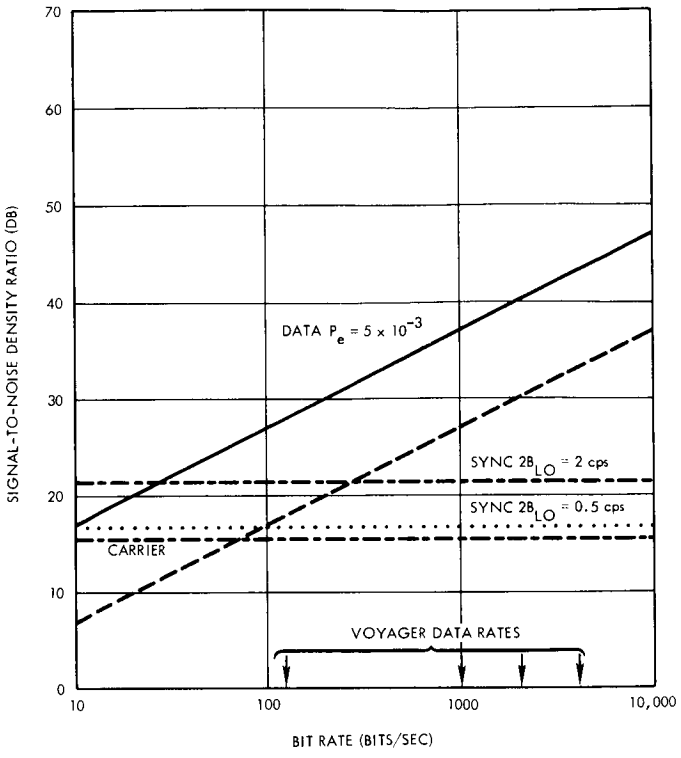


Figure F-50. Signal-to-Noise Density Ratio Versus Bit Rate

Also shown is a dashed line indicating the power available for the sync channel of a two-channel system at data threshold if 10 per cent of the sideband power is allocated to sync. This would represent a loss to the data of about 0.5 db in power if the data and sync power were simply additive. The vertical distance between this line and the sync thresholds indicates the sync performance margin at data threshold. It is seen that with this apportionment of power the sync channel with $2B_{LO} = 0.5$ cps has excess margin over the data at all Voyager bit rates. With $2B_{LO} = 2$ cps the sync margin is negative below 500 bits/sec.

Above 500 bits/sec the communication efficiency advantage of the single- over the two-channel system can be made less than 1 db as is shown in Section 4.4 below. Using a 2 f_s data subcarrier, this performance could be extended down to 128 bits/sec. Considering the small difference

in performance at the bit rates of primary interest, and the proven capabilities of the two-channel system, this is the logical choice for the Voyager telemetry system.

4.4 Performance of Two-Channel System

4.4.1 Bandwidth Requirements

The data and sync channels impose certain requirements on both the low and high frequency response of the telemetry channel. The former is determined by the highpass filtering action of the carrier phase-lock loop. Since the data subcarrier (at $2f_s$ or $4f_s$) is above the peak of the sync spectrum, the principal effect here will be on the sync channel performance. On the other hand, inadequate high frequency response in the telemetry channel will penalize the data subcarrier at $4f_s$. As observed by Springett, the phase characteristics of the filters are especially important. Constant time delay or linear phase shift with frequency should be the design objective for these filters.

The low frequency response is determined by the transfer function between the carrier PLL input and the phase detector output. Springett states (p. 30) that it has been determined experimentally that if

$$0.394\,(a_o/a)\left(f_s/B_o\right)^2 \geqq 10$$

no serious distortion of the PN $\oplus$ $2f_s$ waveform will result. The worst case occurs for high SNR in the carrier loop since a_o/a is smallest under these conditions. Also, the criterion is most likely to be violated for the lowest bit rates (smallest f_s).

Consider the following parameters:

$f_s = \frac{9 \times 128}{2} = 576$ cps for 128 bits/sec

$B_o = 12/1.06 = 11.3$ rad/sec, the minimum DSIF loop natural frequency

$$\frac{a_o}{a} = a_o \simeq \sqrt{\frac{\pi}{4}\left(\frac{S}{N}\right)_{if}} = \sqrt{\frac{\pi}{4}\frac{2B_{Lo}}{B_{if}}\frac{1}{k}}$$

$$\simeq \sqrt{\frac{\pi}{4}\frac{12}{2000}\frac{1}{0.1}} = 0.22$$

k = fraction of total power in carrier

= 0.1 from Figure F-50.

Substitution shows that the criterion is quite adequately satisfied under the worst conditions contemplated.

The high frequency response requirements are determined by considering the RF (and IF) bandwidths required to pass the data and sync sidebands. Springett (p. 17) defines $4f_s$ as the minimum bandwidth to pass the sync PN $\pm f_s$ based on 85.6 percent of the energy residing in this band. To this bandwidth must be added an allowance for the data subcarrier at $4f_s$ and its sidebands, the upper limit of the composite baseband signal will be

$$4f_s + 2 \cdot \frac{2f_s}{9} = \frac{40}{9} f_s$$

and the RF (or IF) bandwidth will be

$$2 \cdot \frac{40}{9} f_s = \frac{80}{9} f_s \simeq 9f_s$$

Table F-9 summarizes the significant rates, frequencies and bandwidths for the two-channel telemetry system. The PN bit rate or basic clock frequency $2f_s$ is none times the bit rate since there are 63 PN bits per word.

Table F-9. Basic System Rates, Frequencies and Bandwidths

Data Rate	Clock ($2f_s$)	Subcarrier ($4f_s$)	Bandwidth ($9f_s$)	DSIF Telemetry Bandwidth
128 bit/sec	1152 cps	2304 cps	5.2 Kc	20 Kc
1024	9216	18.4 Kc	41.4	420
2048	18.4 Kc	36.9	83.0	420
4096	36.9	73.8	166.0	420

The data subcarrier is placed at $4f_s$. Finally, the minimum IF bandwidths are related to the presently available DSIF telemetry predetection bandwidths (from TM 33-83).

The high frequency capabilities of the link should not limit telemetry performance. Basically, any bandwidth up to the receiver bandwidth of 3.3 Mc could be provided for the telemetry phase detector. However, excessive bandwidths result in high noise levels being applied to the phase detector which give rise to large dynamic range requirements, rectification and bias offsets, etc. For example, the nominal RF bandwidth $9f_s$ is about 40 times the data bandwidth. With a 7 db SNR in the latter bandwidth, the SNR in the predetection bandwidth is -9 db. If the bandwidth is 10 times the nominal as suggested by the 1024 bps entry in Table F-9, the predetection SNR drops to -19 db. This is probably still not excessive.

A large telemetry bandwidth is desirable in order to preserve the shape of the squarewave data subcarrier. If the fifth harmonic of the subcarrier at $20f_s$ is within the passband, it has been estimated that the data degradation will be about 0.5-0.6 db. This criterion is reasonably well satisfied with the bandwidth choices of Table F-9 except for the 4096 bit/sec rate. Either the additional data degradation (about 0.5 db) must be accepted, the DSIF bandwidth increased, or the 4096 bps subcarrier frequency changed to $2f_s$. The alternatives require further study.

4.4.2 Power Requirements

The power requirements of any synchronous, coherent PSK system depend fundamentally on the effects of thermal noise and imperfect phasing or timing of the reference waveforms. The latter effects reduce the available signal power, thus making the signal more difficult to distinguish against the thermal noise background. The sources of this multiplicative timing noise are:

- Bit sync
- Subcarrier reference
- Carrier reference.

Bit synchronization is derived from the PN generator which in turn is driven by the noisy reference $2f_s$. Since the jitter on $2f_s$ will be no greater than 15 degrees rms, the jitter in the bit sync should be no greater than

$$\frac{15^o}{360^o} \times \frac{T}{9} = \frac{T}{216} \text{ sec rms}$$

or 0.5 percent of a bit period T. This represents a loss of 0.04 db rms in signal out of the data matched filter due to sampling at the wrong time. Thus, when the PN sync loop is in lock, the data degradation caused by imperfect bit synchronization is essentially negligible.

As indicated in the previous section, the sync threshold has been defined as the point at which the phase jitter on the subcarrier reference is 0.34 rad rms. As noted by Springett, the data degradation occasioned by this jitter can be found by assuming that the phase jitter is independent of the data channel noise, and that the phase jitter has a gaussian distribution. The result is

$$\text{Subcarrier degradation} = \exp \theta^2 - 1$$

where θ is the rms phase jitter in radians on the subcarrier reference. For $\theta = 0.34$ rad, the degradation is 0.5 db. However, $\theta = 0.34$ rad at $4f_s$ corresponds to 0.08 rad at f_s or 18.4 db SNR in $2B_{LO}$, the sync PLL bandwidth. Springett (p. 19) states that 9 db in $2B_{LO}$ is the absolute sync loop threshold at the input to the double loop detector including the effects of limiter suppression. Therefore, a sync performance threshold of 18.4 db guarantees a sync loop operating well above absolute threshold.

Data degradation caused by the reconstructed carrier has been investigated at TRW and also at JPL by W. Lindsey. These investigations are summarized in Section 6. From Lindsey's basic formula

$$\text{Carrier degradation} = \frac{I_1^2(2SNR)}{I_0^2(2SNR)}$$

where SNR is the signal-to-noise ratio in the loop bandwidth, an optimum division of power between data and carrier can be found. However, it is also shown in the appendix that the "6 db in $2B_{LO}$" threshold criterion employed in JPL TM 33-83 and elsewhere provides a nearly optimum division of power. At this threshold signal level, the SNR in the actual operating bandwidth is 3.84 db and the data degradation is calculated at 1.0 db.

Thus, the total degradation of the signal by the three types of synchronization noise is bounded by about 1.6 db. This degradation is conveniently combined with the theoretical ST/N/B required for the data. For the specified telemetry bit error probability

$$\frac{ST}{N/B} = 5.2 \text{ db at } P_e = 5 \times 10^{-3}$$

using the well-known relation

$$P_e = \frac{1}{2}\left(1 - \text{erf}\ \sqrt{ST/N/B}\right)$$

The over-all SRN in a bandwidth 1/T is therefore not greater than

$$\frac{ST}{N/B} = 6.8 \text{ db}$$

including carrier, subcarrier and bit synchronization noise.

To this requirement must be added the effects of band-limiting on the squarewave subcarrier. As shown in Section 5.1 this is about 0.5 db:

$$\frac{ST}{N/B} = 7.3 \text{ db}$$

with all degradations included.

4.4.3 Intermodulation and Interference

Because it is basically an FDM system, the two-channel, system will suffer to some degree from intermodulation "noise." This phenomenon can be appreciated from the following simple arguments. The modulated carrier is

$$\cos (\omega_c t + k_1 D \oplus 4f_s \oplus k_2 PN \oplus 2f_s)$$

where the Boolean functions have been used to indicate the phase modulation rather than the actual (±1) - valued time functions. Expanding the modulated signal,

$$\cos \omega_c t \cos (k_1 D \oplus 4f_s + k_2 PN \oplus 2f_s) - \sin \omega_c t \sin (k_1 D \oplus 4f_s + k_2 PN \oplus 2f_s)$$

$$= \cos \omega_c t \cos k_1 \cos k_2 - (D \oplus 4f_s \oplus PN \oplus 2f_s) \sin k_1 \sin k_2$$

$$-\sin \omega_c t \ (D \oplus 4f_s) \sin k_1 \cos k_2 + (PN \oplus 2f_s) \sin k_2 \cos k_1$$

When the signal is coherently detected with the reference $\sin \omega_c t$, the low frequency output is

$$(D \oplus 4f_s) \sin k_1 \cos k_2 + (PN \oplus 2f_s) \sin k_2 \cos k_1$$

which are the data and sync signals, respectively. No cross terms or intermodulation between the channels is apparent in the recovered baseband signal.

The $\cos \omega_c t$ term is identified as the carrier component of the PM signal: the first term in the brackets is a constant or dc term while the second is time-varying. The time variation is embodied in

$$D \oplus 4f_s \oplus PN \oplus 2f_s = D \oplus PN \oplus 2f_s \measuredangle 90 \text{ degrees}$$

The time average of this function is clearly zero, i.e., there is no dc component, since the average over a PN bit time is zero because of the $2f_s \measuredangle 90$ degree term. Therefore, the useful carrier component supplied to the PLL is

$$\cos k_1 \cos k_2 \cos \omega_c t$$

The power contained in the RF intermodulation term is essentially wasted. However, this intermodulation power does not appear at baseband except to the extent the RF quadrature term appears because of a phase error in the $\sin \omega_c t$ reference.

The power distribution between signal components is

$$P_D = P_T \sin^2 k_1 \cos^2 k_2 \quad \text{(data)}$$

$$P_S = P_T \sin^2 k_2 \cos^2 k_1 \quad \text{(sync)}$$

$$P_C = P_T \cos^2 k_1 \cos^2 k_2 \quad \text{(carrier)}$$

$$P_{IM} = P_T \sin^2 k_1 \sin^2 k_2 \quad \text{(intermodulation)}$$

$$\text{Total power} = P_D + P_S + P_C + P_{IM} = P_T$$

Thus, in comparing a two-channel system to a single-channel system, we must account not only for the power required by the sync channel but also for the power wasted in RF intermodulation products. Basically, for the two-channel system we wish to minimize the total power P_T required to provide satisfactory operation of the carrier, data, and sync channels if this is possible.

The minimization of P_T proceeds as follows. We concentrate on the data and sync requirements and check the carrier performance after the P_T minimization.

$$P_T = \frac{P_D}{\sin^2 k_1 \cos^2 k_2}$$

$$= \frac{P_D}{\sin^2 k_1 \left[1 - \dfrac{P_S}{P_T \cos^2 k_1}\right]}$$

solving again for P_T,

$$P_T = \frac{P_D}{\sin^2 k_1} + \frac{P_S}{\cos^2 k_1}$$

and the minimum P_T occurs for

$$\frac{\partial P_T}{\partial k_1} = 0 \text{ and } \tan^4 k_1 = \frac{P_D}{P_S}$$

With $P_D/P_S = 10$ as assumed in Figure 15, the optimum data deviation $k_1 = 1.06$ rad and the sync deviation $k_2 = 0.513$ rad.

From the basic power distribution relations the modulation losses can now be found and are shown in Table F-10. It turns out that there will usually be sufficient carrier power using this procedure. The 10- to -1 power split between data and sync applies roughly for the lowest bit rate, 128 bps. At the higher bit rates the sync channel requires less than 1 percent of the power. The optimum indices for the 100:1 power split are $k_1 = 1.26$ rad and $k_2 = 0.316$ rad. The modulation losses for the 10:1 and 100:1 power splits are given in Table F-10.

Table F-10. Modulation Losses for Minimum Total Power

Power Division P_D/P_S	Optimum Deviations (rad)	Modulation Losses (db)			
		Data	Sync	Carrier	Intermodulation
10	Data: 1.06 Sync: 0.512	2.38	12.40	7.41	7.37
100	Data: 1.26 Sync: 0.308	0.84	20.84	10.84	10.84

From Table F-10 an efficiency comparison with a single-channel system can be made. Specifically, for $P_c \cong 0.1\ P_D$ the modulation index $k = 1.25$ rad and

Data and sync modulation loss = 0.45 db
Carrier loss = 10.02 db

There is no loss of power in RF intermodulation products. Thus, for the same data power requirements, the two-channel system needs 1.9 db more total power at 128 bps, and 0.4 db more power at the higher bit rates. The latter comparison assumes that the same indices are employed at the

highest bit rate since it is impractical to leave less than 10 per cent of the power in the carrier because of deviation tolerances, etc.

It is also clear that the relative inefficiency of the two-channel system is caused by the unavoidable power wasted in the RF intermodulation products and, to some extent, in the carrier component. That is, with two independent channels phase modulating the transmitter, it is not always possible to allocate precisely the required carrier power while exactly satisfying the data and sync channel requirements. In the single-channel system the power can be distributed optimally between carrier and data-plus-sync channels according to

$$P_{D+S} = P_T \sin^2 k$$

$$P_C = P_T \cos^2 k$$

without generating any IM products. Although ideally the intermodulation products do not appear at baseband to produce interference in the two-channel system, they do consume received power. In the examples in the table, the intermodulation and excess carrier power are dominant over the modest sync requirements.

Finally, two idealizations in the above analysis should be noted:

a) The sync threshold (0.34 rad rms phase jitter on the reference) is arbitrary.

b) The data subcarrier is unlikely to be strictly a squarewave.

The first point stems from the desire to keep the subcarrier synchronization degradation at 0.5 db. However, the proper criterion is to find the optimum power split between data and sync to achieve a maximum bit error rate for a minimum total power. Less power in the sync, resulting in greater subcarrier degradation, may be tolerable provided the power saved can be more effectively used in the data channel. The situation is completely analogous to the question of optimum power division between carrier and data (Section 6).

If the data subcarrier is really a sinewave rather than a squarewave, then in the power division formulas for data, sync and carrier

$$\sin^2 k_1 \rightarrow 2J_1^2(k_1)$$

$$\cos^2 k_1 \rightarrow J_o^2(k_1)$$

Intermodulation products appear at both baseband and RF and can conceivably cause interference with the data, especially. Therefore, it is preferable to use a squarewave subcarrier in a two-channel system. Unfortunately, IF and RF bandwidth limitations will restrict the higher order harmonics of the data subcarrier at $4f_s$ as discussed in Section 4.4.1.

By reversing this reasoning, one may conclude that, starting with a square subcarrier and PN sync, baseband intermodulation products will be created by inadequate predetection filter characteristics. In particular a nonlinear phase characteristic in these filters creates IM distortion. Since these products appear at baseband, they will in general interfere with the data and sync channels. Further study of this problem is required.

In addition to the interference created by IM products, there is direct interference at baseband because of the overlap of the data and sync spectra. This interference is minimized by placing the data subcarrier in the null of the sync spectrum. However, the data will interfere with the sync channel. Cross-correlation with the local PN sequence effectively spreads the data subcarrier throughout the sync band and the subsequent PLL filtering removes most of the interference. Basically, the sync detector is a matched filter for which the following relation between input and output signal-to-interference ratios applies:

$$\left(\frac{S}{I}\right)_0 = 2BT\left(\frac{S}{I}\right)_i$$

where B is the input bandwidth and T the effective integration time of the PLL. Let $B = 4f_s = 2304$ cps for 128 bps, $T = 1/BW_{3db} \cong 3/2B_{LO} = 6$ sec for $2B_{LO} = 0.5$ cps. Thus, the "procecessing gain" $2BT \rightarrow 10^4$. If the total sync power is maintained at no less than 1 percent of the data power,

then $(S/I)_i \geq 0.01$ and $(S/I)_O \geq 100$ (20 db). The performance threshold for the sync detector for 0.5 db degradation of the data subcarrier is 18.4 db in $2B_{LO}$. The above limitation on minimum sync power is therefore reasonable.

5. TELEMETRY SYNCHRONIZATION AND ACQUISITION ANALYSIS

5.1 Frame Synchronization Analysis

Proper identification at the receiving station of PCM telemetry data requires periodic transmission of a specially coded frame sync pattern. After frame sync is acquired, then word sync may be obtained by counting down from the bit rate (which is available from the bit synchronizer), if it is not independently available. However, word sync can be obtained from the PN code link.

To maximize the over-all data transmission rate, it is desirable that an optimal sync pattern by used and an optimal recognition procedure be followed by the receiving station. The performance of any synchronization scheme may be described in terms of 1) sync acquisition time T_A, 2) probability P_1 of recognition of the true sync pattern, 3) probability P_2 of recognition of a false sync pattern somewhere in frame, 4) probability P_3 of maintaining sync after acquisition, and 5) lock hold time T_H.

The factor which prevents the probability of a true sync pattern recognition from being unity is the occurrence of errors in the link. If perfect reception of a true sync pattern is arbitrarily required in order that recognition be established, then for the probability of recognition

$$P_1 = (1 - h)^n \qquad \text{(F.46)}$$

Where h is the link error rate, i.e., the probability that any transmitted binit will be received in error, and n is the number of code bits in the chosen sync pattern. If the error rate is small, P_1 will be close unity, but if H and/or n is large, P_1 may not be satisfactory. This is overcome by permitting up to a certain number ϵ_1 errors to be tolerated in the ground recognizer system for which recognition is achieved, for then P_1 can be increased to $P_1(\epsilon_1)$:

$$P_1(\epsilon_1) = \sum_{r=0}^{\epsilon_1} \binom{n}{r} h^r (1-h)^{n-r} > (1-h)^n \qquad \text{(F.47)}$$

False synchronization in a frame can occur due to n of the data bits randomly assuming the sync pattern or by a combination of n - k bits of the true sync code and k adjacent data bits randomly assuming the sync pattern. In the former case the probability of false recognition at each trial is

$$F_1 \ (\epsilon_1) = 2^{-n} \sum_{r=0}^{\epsilon_1} \binom{n}{r} \qquad \text{(F.48)}$$

However, the probability $F_2 \ (\epsilon_1, k)$ that a false sync pattern occurs in a position displaced by $k<n$ bits from true sync position is highly dependent on the actual sync code employed. The use of Barker codes or pseudo-random codes (which exhibit good autocorrelation functions) is necessary to reduce the probabilities $F_2 \ (\epsilon_1, k)$ for $k = 1, 2, \ldots, n-1$ (see Section 2 of this appendix). The total probability of one or more false synchronizations in a frame of N bits is then approximately given by

$$P_2 \ (\epsilon_1) \cong 1 - (1-F_1)^{N-2n+1} \left[\prod_{k=1}^{n-1} \left\{ 1 - F_2 \ (\epsilon_1, k) \right\} \right]^2 \qquad \text{(F.49)}$$

Now both $F_1 \ (\epsilon_1)$ and $F_2 \ (\epsilon_1, k)$ $(k = 1, 2, \ldots, n-1)$ increase as the number of allowed errors ϵ_1 is increased, so that P_2, the probability of false sync, increases with ϵ_1. On the other hand, to keep the probability P_1 of recognizing a true sync pattern close to one, ϵ_1 must be large. Therefore, ϵ_1 must be correctly chosen to yield the desired values of P_1 and P_2. Of course in any case the sync code length n must be sufficiently long. The portion of the channel capacity used for synchronization is $\frac{n}{N}$ and for a given P_1 and P_2 this quantity decreases as the frame size N is increased (at the expense of additional acquisition time of course).

For the simple case where h is very small, ϵ_1 may be chosen to be 0. Then $P_1 = 1.0$, $F_1 = 2^{-n}$, and $F_2 = 0$ for a Barker code or a

reasonably efficient pseudo-random code. From Equations (F. 48) and (F. 49) the frame length N may be solved for approximately:

$$N = -2^n \ln (1 - P_2) + 2n-1$$

This is plotted in Figure F-51.

Figure F-52 shows the variation of P_1 for an error rate of h = 0. 1. This is usually considered to be the highest link error rate for which the data return is usable.

For the Voyager mission, the maximum error rate specified is $h = 5 \times 10^{-3}$, and the frame length is N = 448 bits. Based on this and the following analysis, the frame sync code length chosen is

$$n = 21 \text{ bits}$$

which comprises three words. This 21-bit sync pattern consists of a 7-bit Barker code 1110010 followed by its complement repeated twice.

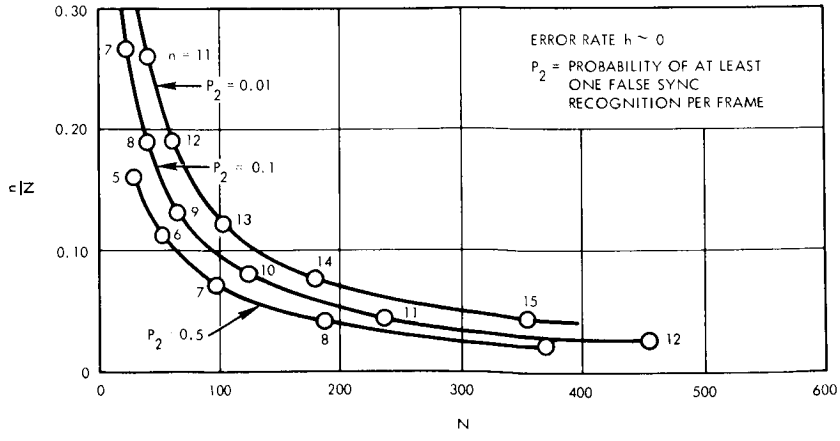


Figure F-51. Frame Length Versus n/N

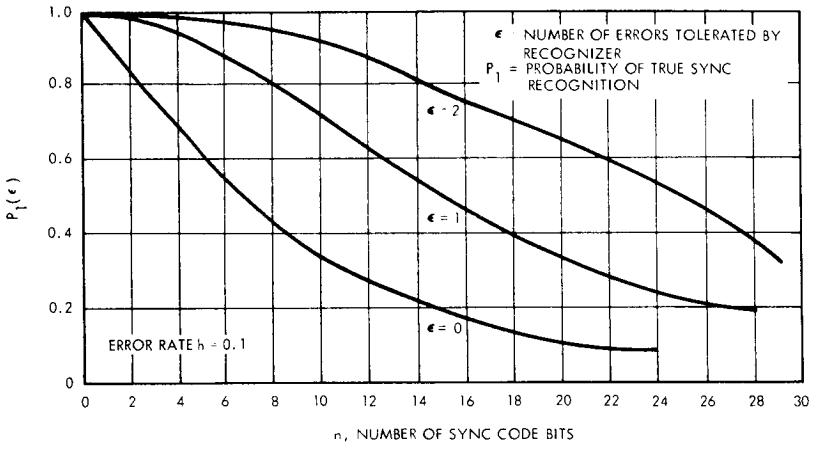


Figure F-52. P_1 Versus Number of Sync Code Bits

This sync code has the advantages of being easily generated by the DTU and of having a good autocorrelation function (yielding low values of $F_2(\epsilon_1, k)$ as shown in Section 2 of this Appendix.

The procedure used to acquire frame sync may be described as follows. Immediately after bit sync acquisition a sequence of n received binits appears in a shift register A (Figure F-53). A recognizer circuit B compares the contents of A with the stored sync code and determines whether the number of errors is less than ϵ_1, in which case a recognition pulse is generated. If there are more than ϵ_1 errors, the shift register A is allowed to shift right as the next binit is received from the bit synchronizer, and the procedure is repeated. The window is said to be open and the incoming data is examined until a recognition (true or false) occurs.

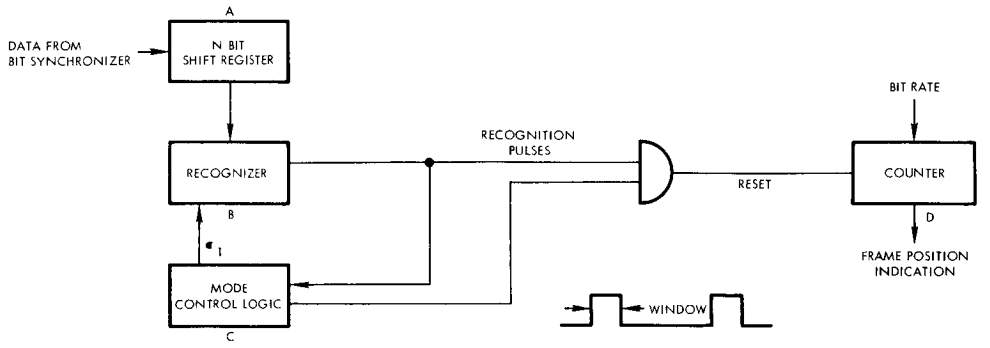


Figure F-53. Synchronization Block Diagram

The questions next arises as to the proper approach to be adopted which will verify that the recognition is not of a false sync code, and after verification, insure that the frame sync lock is retained for the longest possible time. Several investigators have suggested that the optimum approach consists of three modes of operation - acquisition, verification, and retention modes. The number of bits examined each frame time (window size) and the number of allowed errors (ϵ) are chosen differently to best match the a priori information concerning the frame sync status.

However, to prevent the procedure from becoming unduly complex, only two modes of operation are suggested for which near-optimum performance can be achieved:

- Acquisition mode - window open; ϵ_1 allowed errors; go to retention mode after first sync code recognition is achieved.
- Retention mode - 3-bit window; ϵ_2 allowed errors; go back to acquisition mode if sync recognition fails for all three tests in window.

The 3-bit window in the retention mode means that after frame sync is acquired, the recognizer examines the data at positions corresponding to one frame time later and one frame time plus or minus one bit later. As contrasted to a 1-bit window this allows for possibility of a 1-bit/frame slippage of the phase-locked oscillator in the bit synchronizer at low

signal-to-noise ratios. The criteria for the selection of $_1$ and $_2$ are the minimization of average acquisition time $\overline{T}_H$, respectively.

The average acquisition time is given (see Section 2) approximately by

$$\overline{T}_A = \frac{1 + NF_1(\epsilon_1)}{P_1(\epsilon_1)} \quad \text{frames} \qquad \text{(F. 50)}$$

The average hold time, i.e., average time in retention mode, is

$$\overline{T}_H = 1 + \frac{1}{1 - P_1(\epsilon_2)(1 - F_2)(\epsilon_2, 1)} \quad \text{frames} \qquad \text{(F. 51)}$$

A short tradeoff may be performed to determine the appropriate optimum error tolerances ϵ_1 and ϵ_2 to be used for the sync code of length n = 21 bits in a frame of length N = 448 bits. The results are shown in Table F-11 for error rates of h = 0.05 and h = 0.005.

Table F-11. Acquisition and Hold Time Optimization

Error Rate	Error Tolerances		Average Acquisition Time	Average Hold Time	Comments
h	1	2	$\overline{T}_A$	$\overline{T}_H$	
0	0	0	1 frame	∞	Ideal case under assumption of no link noise
0.05	0	0	2.94 frame	2.52	ϵ_1, ϵ_2 too small
	1	2	1.39	12.3	ϵ_1, ϵ_2 too small
	1	4	1.39	308	ϵ_1, ϵ_2 too small
	2	5	1.16	2180	optimum
0.005	0	0	1.11	11	ϵ_1, ϵ_2 too small
	1	1	1.006	201	ϵ_2 too small
	1	2	1.006	6260	ϵ_2 too small
	1	3	1.006	250,000	Optimum

At the maximum specified error rate h = 0.005 and using the optimum error tolerances, $\epsilon_1 = 1$, $\epsilon_2 = 3$, it is seen that the acquisition and hold times are very good, that is, frame sync is acquired almost with certainty at the first appearance of the sync code and the "mean time" to sync loss is 250,000 frame-times.

As a matter of fact, the proposed sync code is still satisfactory at a degraded error rate of h = 0.05 (provided ϵ_1, ϵ_2 are also changed) as the above table shows. This raises the question as to whether a n = 14 sync code (two word lengths) would be satisfactory, at an error rate of h = 0.005. However, a n = 14 sync code yields only marginal performance.

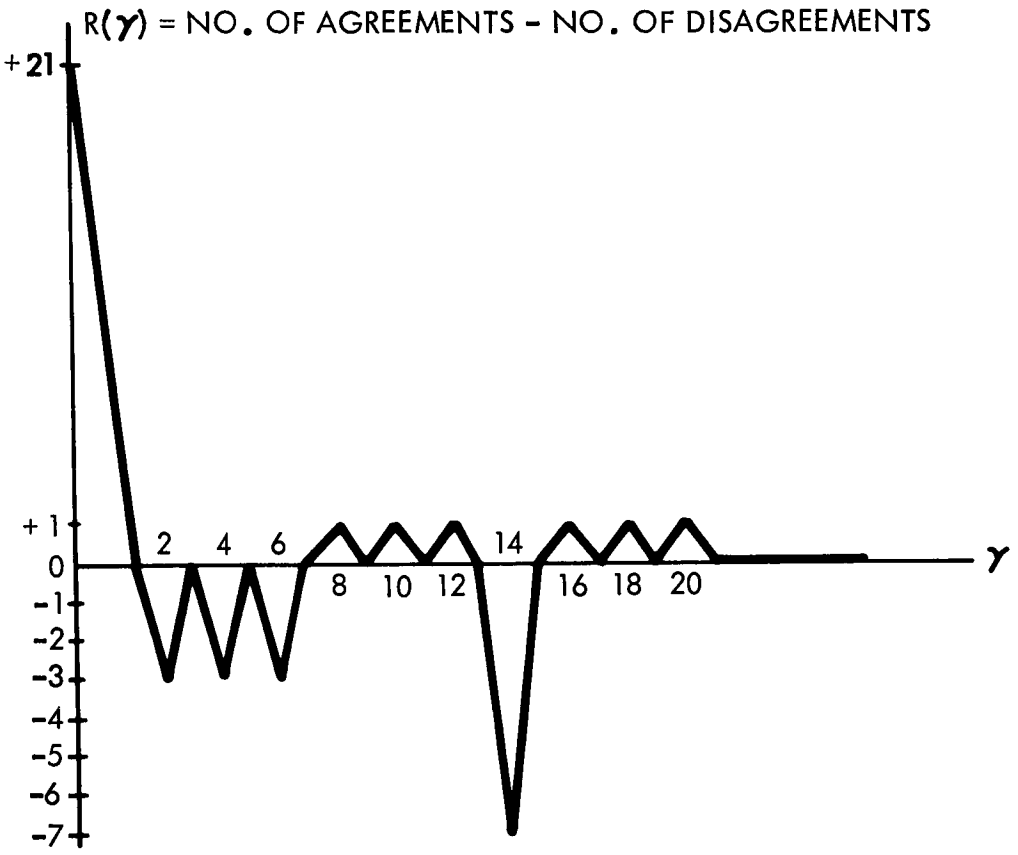
In summary, the above analysis shows that the chosen sync code and sync acquisition and retention procedure yields a performance which exceeds that which might be considered satisfactory as expressed in terms of average acquisition and hold times. Thus proper frame synchronization has been provided for all system modes of operation whether word synchronization is independently available or not.

5.2 Derivation of $F_2(\epsilon_1 k)$

The 21-bit sync code consisting of 7-bit Barker code followed twice by its complement is shown below

Bit position in frame	1 B_1	2 B_2	3 B_3	4 B_4	5 B_5	6 B_6	7 B_7	8 B_8	9 B_9	10 B_{10}	11 B_{11}	12 B_{12}	13 B_{13}	14 B_{14}	15 B_{15}	16 B_{16}	17 B_{17}	18 B_{18}	19 B_{19}	20 B_{20}	21 B_{21}	22 B_{22}
Sync code	1	1	1	0	0	1	0	0	0	0	1	1	0	1	0	0	0	1	1	0	1	
Sync code shifted one position		1	1	1	0	0	1	0	0	0	0	1	1	0	1	0	0	0	1	1	0	

For comparison to PN codes, the autocorrelation function of this sync code is plotted as follows.



As an example $F_2(\epsilon, 1)$ will be derived. A nonzero link error h rate is assumed. The sync code shifted by K=1 bit is shown in the preceding plot. B_1 consists of a data binit which is equally likely to be a 1 or a 0. If the shifted sync code were received unchanged and $B_1 = 1$, then mismatches would be present in bits B_4, B_6, B_7, B_{11}, B_{13}, B_{14}, B_{15}, B_{18}, B_{20}, B_{21}.

For a zero error tolerance, i. e. $\bar{E} = 0$, a false recognition can occur only if B_1 happens to be a 1, B_4, B_6, B_7, B_{11}, B_{13}, B_{14}, B_{15}, B_{18}, B_{20}, and B_{21} are received changed and the remaining 10 binits are received unchanged. Thus

$$F_2(0_1\ 1) = 1/2\ (1-h)^{10} h^{10}$$

If exactly one recognition error is allowed, a false recognition may occur in any one of three mutually exclusive ways: 1) the recognition error is allowed in B_1, 2) the error is allowed in any one of the 10 mismatched positions, and 3) the error is allowed in any one of the 10

matched positions. Consequently, the probability of recognition when the maximum error tolerance is = 1 is the sum of the probabilities of these three events plus the probability $F_2(0, 1)$ of a recognition with no errors:

$$F_2(1,1) = F_2(0,1) + (1-h)^{10} h^{10} + \frac{1}{2}\left(\frac{10}{1}\right)(1-h)^{11} h^{9}$$

$$+ \frac{1}{2}\left(\frac{10}{1}\right)(1-h)^{9} h^{11}$$

$$= h^{9}(1-h)^{11}\left[5 + 1.5\left(\frac{h}{1-h}\right) + 5\left(\frac{h}{1-h}\right)^{2}\right]$$

Similarly, for other error tolerances $\epsilon > 1$, the various events for which recognition occurs may be determined and their probabilities computed.

Thus

$$F_2(2,1) = F_2(1,1) + h^{8}(1-h)^{12}\left[22.5 + 10\left(\frac{h}{1-h}\right)\right.$$

$$\left. + 50\left(\frac{h}{1-h}\right)^{2} + 10\left(\frac{h}{1-h}\right)^{3} + 22.5\left(\frac{h}{1-h}\right)^{4}\right] \quad \text{etc.}$$

5.3 Derivation of Average Acquisition and Hold Times

If frame sync has been lost and a search is initiated to reacquire sync when the window is open and each time the contents of the n bit shift register is examined, the result of the trial has three possible outcomes:

N - no recognition occurs

F - a false recognition occurs

T - a true recognition occurs

If, as before, P_1 denotes the probability of a true sync recognition given that a true sync code is present (Equation (F. 46)) for each trial in a frame of N bits

$$P(T) = \frac{P_1}{N} \cong \alpha$$

Similarly, it is seen that the per trial probability of false recognition P (F) is given by (see Equation (F. 48))

$$P(F) = \frac{P_2}{N} = \beta$$

Therefore the per trial probability of no recognition is

$$P(N) = 1 - \alpha - \beta$$

As a good approximation, successive trials will be assumed to be independent. In general, the acquisition time is determined by the number m of false recognitions and the number r of no recognitions which occur (in any order since successive trials are independent) before the first true sync recognition occurs. Thus, in the process of attempting to acquire frame sync, if a sequence of events NNNNFNNF... NFT occurs haveing R occurrences of N (no recognition) and m occurrences of F before T occurs, the probability of this sequence is $\binom{m+r}{m} \beta^m (1-\alpha-\beta)^r \alpha$. Then the scheme is complete because if t = m + r then

$$\sum_{t=0}^{\infty} \sum_{m=0}^{t} \binom{t}{m} \beta^m (1-\alpha-\beta)^{t-m} = \sum_{t=0}^{\infty} \alpha (1-\alpha)^t = 1$$

The acquisition time T_A of the sequence is

$$T_A = Nm + r + 1 \text{ bit times}$$

since each false recognition causes a one frame time delay in each. No recognition event causes a one bit time delay. The expected acquisition time is therefore

$$\overline{T}_A = N\overline{m} + \overline{r} + 1 = (N - 1)\,\overline{m} + \overline{t} + 1$$

Thus, it can be shown that

$$\overline{t} = \alpha \sum_{t=0}^{\infty} t \sum_{m=0}^{t} \binom{t}{m} \beta^{m} (1 - \alpha - \beta)^{t-m} = \frac{1}{\alpha}$$

$$\overline{m} = \alpha \sum_{t=0}^{\infty} \sum_{m=0}^{t} m \binom{r}{m} \beta^{m} (1 - \alpha - \beta)^{t-m} = \frac{\beta}{\alpha} \quad (1 = \alpha)$$

A useful simplify expression can be obtained for $\overline{T}_A$ under the condition $F_2 (1, \epsilon_1) < \frac{F_1 (\epsilon_1)}{n}$ which is usually the case. Then $\beta = F_1 (\epsilon_1) = \sum_{k=0}^{\epsilon_1} \binom{n}{k} 2^{-n}$. Furthermore since $\alpha = \frac{P_1}{N}$ we obtain finally that

$$\overline{T}_A = 1 + (N-1) \frac{\beta}{\alpha} (1 + \alpha) + \frac{1}{\alpha}$$

$$= 1 + \frac{N}{P_1} \left[1 + (N-1) \left(1 + \frac{P_1}{N} \right) F_1 (\epsilon_1) \right] \text{ bit times}$$

$$\cong \frac{1 + N F_1 (\epsilon_1)}{P_1} \quad \text{frame times} \quad (N \gg 1)$$

In a similar manner, assuming a three bit window for the retention mode as previously described, it can be shown that the expected time in retention mode is

$$\overline{T}_H = 1 + \frac{1}{1 - P_1 (\epsilon_2) (1 - F_2 (1_1 \epsilon_2)} \quad \text{frames.}$$

6. THRESHOLD CRITERIA FOR PHASELOCK RECEIVERS

6.1 Tracking Loop Dynamic Errors

The carrier tracking loop in the ground receiver experiences phase errors because of doppler and doppler rate resulting from orbital motion about Mars and motion of Mars relative to earth. These errors must be evaluated to insure that the ground receiver is capable of accommodating them. The orbiter-ground station range is the sum of three components: Mars-orbit, Mars-earth center, and earth center - DSN station.

The Mars-earth center velocity component, though the largest, varies very slowly and can be programmed out by DSIF frequency selection. The remaining two velocity components produce a worst case velocity variation of 2.7 km/sec. The rate of change of velocity is primarily the orbital component, 1.53 m/sec^2.

For two-way communications, the doppler frequency is given by

$$f_d = \frac{2 f_r \dot{r}}{c} \quad , \tag{F.52}$$

and we have for $f_r = 2295$ Mc

$$\left| f_d \right| \max = 41.3 \text{ Kc}$$

$$\left| \dot{f}_d \right| \max = 23.4 \text{ cps/sec}$$

The loop error because of the doppler effect can be expressed as

$$\epsilon_1 = \frac{2\mu f_d}{K} \tag{F.53}$$

where K is the static loop gain of the loop. If we require ϵ_1 to be less than 0.1 rad then

$$K \leq \frac{2\pi (41.3) 10^3}{.1}$$

$$= 2.6 \times 10^6 \text{ sec}^{-1}$$

This requirement is very easily fulfilled by the operational amplifier in the loop filter.

The error because of tracking a doppler ramp is given by

$$\epsilon_2 = \frac{2\pi \dot{f}_d}{\omega_n^2} \qquad \text{(F.54)}$$

Because of limiter suppression, the loop natural frequency, ω_n, is a function of the received carrier level. We wish to calculate the error for a bandwidth corresponding to a threshold level of 6 db in the receiver loop. Since the DSIF receiver loop is optimized to 12 cps at 0 db in the 12 cps bandwidth, ω_n for 6 db is

$$\omega_n = \omega_{n_o} \sqrt{\frac{\alpha}{\alpha_o}}$$

$$= \frac{12}{1.06} \sqrt{2.0} \qquad \text{(F.55)}$$

$$= 16.0 \text{ rad/sec}$$

Thus

$$\epsilon_2 = \frac{2\pi (23.4)}{(16.0)^2}$$

$$= 0.57 \text{ rad peak}$$

This value is pessimistic because it assumes only 6 db SNR in the receiver loop bandwidth. If we consider the worst flight conditions with a satisfactory performance margin at encounter plus 180 days, the tracking error is reduced considerably. For the 128-bits/sec bit rate using the medium gain antenna and the 210-ft dish, the SNR in the 12 cps DSIF bandwidth

is 19.1 db (Volume 2, Section 5.3.1). This results in an ω_n of 34 r/s and a tracking error

$$\epsilon_2 = 0.13 \text{ rad peak},$$

a quite acceptable dynamic error.

Similar calculations can be performed for the transponder which, of course, encounters only one-way doppler. Thus for the transponder

$$\left| f_d \right|_{max} = 20.6 \text{ Kc}$$

$$\left| \dot{f}_d \right|_{max} = 11.7 \text{ cps/sec}$$

For a maximum static loop error less than 0.1 rad the loop gain must be

$$K = 1.3 \times 10^6 \text{ sec}^{-1}$$

The transponder loop bandwidth is 32 cps at +6 db in the loop (Volume 5, Section 1.5.4). If we consider the threshold level of 3.8 db (Volume 2, Section 5.3.1), we have

$$\omega_n = \frac{32}{1.06} \sqrt{.776}$$

$$= 26.6 \text{ rad/sec}$$

The peak error due to doppler rate is therefore,

$$\epsilon_2 = \frac{2\pi (11.7)}{(26.6)^2}$$

$$= 0.10 \text{ rad peak}$$

6.2 Carrier Loop Degradation in Two-Way Mode

When the communication link is operating in the two-way mode, the ground receiver loop receives an additional noise component because of up-link noise transmitted by the transponder. To determine the magnitude of this component consider the transponder phase noise. It can be expressed as

$$\overline{\epsilon_t^2} = \frac{\Phi_t}{2C_t} G^2 \int_{-\infty}^{\infty} \left| H_t(\omega) \right|^2 \frac{d\omega}{2\pi} \qquad \text{(F.56)}$$

where the subscript t denotes the transponder and

$\frac{C}{\Phi}$ = carrier-to-noise density ratio

G = ratio of up-link to down-link carrier frequencies

H = loop phase transfer function

The total receiver noise is the sum of thermal plus transponder noise or

$$\overline{\epsilon_r^2} = \frac{\Phi_r}{2C_r} \int_{-\infty}^{\infty} \left| H_r(\omega) \right|^2 \frac{d\omega}{2\pi}$$

$$+ \frac{\Phi_t}{2C_t} G^2 \int_{-\infty}^{\infty} \left| H_t(\omega) \right|^2 \left| H_r(\omega) \right|^2 d\omega \qquad \text{(F.57)}$$

$$= \frac{\Phi_r}{2C_r} B_{N_r} + \frac{\Phi_t}{2C_t} G^2 K(\beta) B_{N_r}$$

where

$$B_n = \text{(two-sided) noise bandwidth}$$

$$\beta = B_{N_t} \Big/ B_{N_r}$$

and $K(\beta)$ is a parameter representing the second integral above as a function of the bandwidth ratio. For the case where both loops are second-order and adjusted 0.707 damping $K(\beta)$ has been plotted,* and it can be shown that at least for $B_{N_t} \Big/ B_{N_r} \geq 1$, the factor K is not too dependent upon the damping ratio.

Since

$$\frac{S}{N} = \frac{2}{\Phi B_N} \tag{F.58}$$

is the SNR in the loop noise bandwidth, Equation (F.57) can be rewritten as

$$\overline{\epsilon_r^2} = \frac{1}{2\left(\frac{S}{N}\right)_r} + \frac{G^2 K(\beta)}{\left[\frac{S}{N}\right]_t \beta} \tag{F.59}$$

To evaluate this expression for Voyager we consider two cases. In the first case, both the receiver and the transponder loops are at their design threshold level. In the second case, the receiver is at threshold but the transponder is at its minimum operational power level taken from the system design control table (Volume 2, Section 5.3.2).

*J. K. Holmes, "A consideration of VCO and Thermal Noise in a Phase Coherent Two-Way Doppler Communication System, "IEEE Transactions PG SET, March 1965.

For the first case we have

$$B_{N_r} = 12 \text{ cps at } 0 \text{ db } (S/N)_t$$

$$B_{N_t} = 27 \text{ cps at } 3.8 \text{ db } (S/N)_t$$

(corresponding to 32 cps at 6.0 db)

$$G = \frac{2295}{2115} = 1.086$$

so that

$$= 2.26$$

$$K(\beta) = 1.1$$

With no up-link degradation the mean square error of the receiver at threshold is 0.5 $(\text{rad/sec})^2$. Hence, if we set the total mean square error at this value and calculate the resulting receiver SNR, we will have a measure of the degradation caused by the up-link. Thus

$$0.5 = \frac{1}{2\left(\frac{S}{N}\right)_r} + \frac{(1.086)^2\,(1.1)}{2(2.4)\,(2.26)}$$

so that

$$\left(\frac{S}{N}\right)_r = 1.30 \text{ db}$$

The degradation, therefore, is 1.3 db since the receiver SNR must be increased by this amount to maintain the same output phase noise as in the one-way mode. By comparison, Mariner C specifications quote 2 db for this degradation.

For the second case, we have a transponder SNR equivalent to 13.6 db in 32 cps so that due to the limiter

$$B_{N_t} = 62.5 \text{ cps at } 10.7 \text{ db}$$

$$\beta = \frac{62.5}{12} = 5.2$$

$$K(\beta) = 1.1$$

Thus

$$0.5 = \frac{1}{2\left(\frac{S}{N}\right)_r} = \frac{(1.086)^2\,(1.1)}{2\,(11.8)\,(5.2)}$$

yielding

$$\left(\frac{S}{N}\right)_r = 0.09 \text{ db},$$

as essentially negligible degradation.

6.3 Data Degradation Caused by Carrier Loop

In the past, coherent communication links have been designed by adjusting the carrier deviation so that both the carrier tracking loop and the data channel are above some arbitrary threshold. Such a design is somewhat artificial in that the actual effect of noise in the carrier loop upon the data channel SNR is not taken into account. A more realistic approach is to adjust the deviation so as to maximize the data SNR or minimize data error probability taking into account the degradation from the carrier loop. The carrier loop margin per se is of secondary interest.

A first attempt to account for carrier loop degradation of the data SNR is an analysis given in an unpublished TRW memorandum by C. M. Thomas. In this memo, the carrier loop was replaced by a VCO phase-modulated by white gaussian noise filtered by a first-order loop transfer function. The spectrum of the VCO output is obtained by assuming the modulated index is small (i.e., carrier loop SNR high) so that the

shape of the VCO noise spectrum is essentially that of the modulating noise. This VCO spectrum is convolved with that of the incoming data and noise, the resulting spectrum is then translated by the subcarrier frequency and filtered by an integrate-and-dump filter. The resulting expression for output data SNR is given by

$$SNR_o = \frac{\epsilon^{-\bar{\theta}^2}}{\left(\frac{1}{SNR}\right)_{nd} + 2(\bar{\theta}2)^2 F\left(\frac{1}{2\omega_n T}\right)}$$

where

$(SNR)_o$ = data SNR in bandwidth $1/T$

$(SNR)_{nd}$ = data SNR in $1/T$ with no carrier loop degradation

$\bar{\theta}^2$ = mean square carrier loop phase noise

$F\left(\frac{1}{2\omega_n T}\right)$ = a factor dependent upon bit time and loop natural frequency

The factor F is plotted in the memo and is near 0.15 for threshold cases of interest. The data SNR is most readily optimized with respect to index by cut-and-try calculations to maximize SNR.

Recently W. C. Lindsey of JPL* has approached the problem using an expression for the probability density of the carrier VCO phase obtained from his analysis of the second-order loop using Fokker-Planck techniques. Furthermore, his results given in JPL Space Programs Summary

*W. C. Lindsey, "Optimal Design of One-Way and Two-Way Coherent Communication Links, JPL Space Programs Summary, No. 37-33, Vol. IV, 1965.

Nos. 37-32, and 37-33, Volume IV, consider both one-way and two-way links. Lindsey's expression for data error probability from Equation (2) of SPS 37-33 is

$$P_E(n) = \frac{1}{2}\left[1 - \frac{8}{\pi}(SNR)_{nd}\sum_{k=0}^{\infty} e^{-(SNR)_{nd}}(-1)^k \epsilon_k\, b_{2k+1}(n)(1-4K^2)^{-1} I_k(1/\bar{\theta}^2\right]$$

where

$$b_k(n) = \prod_{i=i}^{n} \frac{I_1(\bar{\theta_i^2})}{I_0(\theta_i^2)}$$

$$\epsilon_k = 1,\ k = 0$$

$$\epsilon_k = 2,\ k > 0$$

and where n = 1 refers to one-way link and n = 2 to two-way. Using a computer, Lindsey plotted $P_E(n)$ for selected values of

$$\frac{P_{T2}\, T_{b2}}{N_{02}},$$

and

$$\frac{1}{T_{b2}\, B_{N2}}$$

as a function of cos θ_d. Ideally these curves permit an optimum choice of deviation to minimize P_E. However, in actual practice B_{N1} and B_{N2} are unknown because they are functions of the carrier power at the spacecraft and the ground, respectively, due to limiter suppression. Thus, Lindsey's curves are not directly applicable and further computer study is required to incorporate the effect of limiter suppression.

In addition to $P_E(n)$, Lindsey also has an expression for the data SNR given by

$$SNR_1 = \sin^2 \theta_d \frac{P_T T_b}{N_o} \left[\frac{I_1 (1/\bar{\theta}^2)}{I_0 (1/8^2)} \right]^2$$

for one-way and

$$SNR_2 = SNR_1 \left[\frac{I_1 (1/\theta^2)}{I_0 (1/8_2^2)} \right]^2$$

for two-way links. Because this expression is much simpler than that for P_E, it is possible to include the effect of limiter suppression for one-way link without recourse to a computer.

To show this we note that

$$\frac{1}{\theta^2} = 2 (SNR)_{B_N}$$

When B_N is the total loop noise bandwidth.

Furthermore, it can be shown that because of limiter suppression

$$(SNR)_{B_N} = \frac{3(SNR)B_{N_o}}{1 + 2\sqrt{(SNR)\,B_{N_o}}}$$

where B_{N_o} is the bandwidth at the design power level. Thus

$$SNR = \sin^2 \theta_d \frac{PT}{N_o} \left[\frac{I_1\left(\frac{6 \cos^2 \theta_d \left(\frac{P}{N_o B_{N_o}} \right)}{1 + 2 \cos \theta_d \, P/N_o B_{N_o}} \right)}{I_1\left(\frac{6 \cos^2 \theta_d \frac{P}{N_o B_{N_o}}}{1 + 2 \cos \theta_d \, P/N_o B_{N_o}} \right)} \right]^2$$

For a given system power budget PT/N_o and $P/_{N_o} B_{N_o}$ are given. The data SNR can then be optimized with respect to θ_d by calculating SNR for several trial values of θ_d.

An interesting comparison of the two methods for computing data SNR was performed in connection with the power budget for Pioneer. The parameters for this comparison were $B_{N_o} = 12$ cps, $P/N_o = 22.1$ db/cps, and $1/T = 8$ cps. Using the expression of Thomas, the optimum index was found to be 1.0 radian which resulted in a maximum SNR of 10.0 db. Using Lindsey's equation, the optimum index was 1.1 radian resulting in a 10.6 db SNR. With an index of 1.0, Lindsey's expression gave a SNR of 10.45 db. Thus, the two methods are in agreement with Thomas being somewhat pessimistic regarding the carrier degradation. It is interesting to note that the 1.0 radian deviation results in a loop SNR of 6.0 db within the 12 cps or 3.75 db in the 20 cps expanded bandwidth. This is well below the criteria of 9.0 db sometimes used in specifying carrier threshold, although it happens to agree exactly with the JPL criterion specified in TM33-83.

7. TELEMETRY MEASUREMENT LIST

This section contains Tables F-12 and F-13. Table F-12 is a preliminary engineering measurement list, and Table 13 is a summary of the measurement list sampling rate.

Table F-12. Preliminary Engineering Measurement List

1) ATTITUDE CONTROL SUBSYSTEM MEASUREMENT LIST

Measurement Type	Measurement Description and Location P Pitch Axis R Roll Axis Y Yaw Axis	Range			Frequency Response or Sampling Rate		Per Cent Accuracy	
		Maximum	Minimum	Nominal	Preferred	Minimum Acceptable	Preferred	Minimum Acceptable
Analog voltage	P Gyro output	3 deg	0	3 deg	1 cps	0.5 cps	2	5
Analog voltage	R Gyro output	3 deg	0	3 deg	1 cps	0.5 cps	2	5
Analog voltage	Y Gyro output	3 deg	0	3 deg	1 cps	0.5 cps	2	5
Analog voltage	P Derived rate filter output	0.1 deg	0	0.01 deg	0.01 cps	0.001 cps	2	5
Analog voltage	R Derived rate filter output	0.1 deg	0	0.01 deg	0.01 cps	0.001 cps	2	5
Analog voltage	Y Derived rate filter output	0.1 deg	0	0.01 deg	0.01 cps	0.001 cps	2	5
Discrete voltage	P Switching amplifier output	ON	OFF	OFF	Gate	Gate	NA	NA
Discrete voltage	R Switching amplifier output	ON	OFF	OFF	Gate	Gate	NA	NA
Discrete voltage	Y Switching amplifier output	ON	OFF	OFF	Gate	Gate	NA	NA
Analog voltage	Acquisition sun sensor output	4 SR	0	0	0.01 cps	0.01 cps	2	5
Analog voltage	P Fine sun sensor output	±10 deg	0	0	10/hr	1/hr	2	5
	Y Fine sun sensor output	±10 deg	0	0	10/hr	1/hr	2	5
Analog voltage	Canopus sensor output	± 4 deg	0	0	10/hr	1/hr	2	5
Analog voltage	Canopus sensor output	± 4 deg	0	0	10/hr	1/hr	2	5
Analog voltage	Earth sensor output	6 deg	0	0	10/hr	1/hr	2	5
Analog voltage	R Integrator output	0.5 deg	0	0	0.01 cps	0.001 cps	2	5
Discrete voltage	P Gyro torquer current generator outputs	0.2 deg/sec	0	0	Gate	Gate	NA	NA
Discrete voltage	R Gyro torquer current generator output	0.2 deg/sec	0	0	Gate	Gate	NA	NA

Table F-12. Preliminary Engineering Measurement List (Continued)

1) ATTITUDE CONTROL SUBSYSTEM MEASUREMENT LIST (Cont)								
	Measurement Description and Location P Pitch Axis R Roll Axis Y Yaw Axis	Range			Frequency Response or Sampling Rate		Per Cent Accuracy	
Measurement Type		Maximum	Minimum	Nominal	Preferred	Minimum Acceptable	Preferred	Minimum Acceptable
Discrete voltage	Y Gyro torquer current generator output	0.1 deg/sec	0	0	Gate	Gate	NA	NA
Analog voltage	P (2) Jet vane position (monopropellant)	±25 deg	0		1 cps	0.5 cps	2	5
Analog voltage	Y (2) Jet vane position (monopropellant)	±25 deg	0		1 cps	0.5 cps	2	5
Analog pressure	Attitude control N_2 tank pressure (2)	3500	0	3000 psi	1/hr	0.1/hr	2	5
Analog voltage	P Solid engine actuator TVC valve position	±2 in.	0		1 cps	0.5 cps	2	5
Analog voltage	Y Solid engine actuator TVC valve position	±2 in.	0		1 cps	0.5 cps	2	5
Analog pressure (2)	Regulated pressure	75 psi	0	50 psi	1/hr	0.1/hr	2	5
Analog pressure	Freon pressure	500 psi	0	400 psi	1/sec	1/10 sec	2	5
Discrete voltages (6)	Control electronics				Gate	Gate	NA	NA
Discrete voltage	Sun gate detector	ON	OFF	ON	Gate	Gate	NA	NA
Discrete voltage	Acquisition gate	ON	OFF	ON	Gate	Gate	NA	NA
Analog voltage	Earth pointing antenna hinge act position	+140 deg	0	±90	Gate	Gate	2	5
Analog voltage	Earth pointing antenna scan act position	±180 deg	0	±90	Gate	Gate	2	5
Discrete voltage	P Gyro spin motor output	ON	OFF	OFF	Gate	Gate	NA	NA
Discrete voltage	R Gyro spin motor output	ON	OFF	OFF	Gate	Gate	NA	NA
Discrete voltage	Y Gyro spin motor output	ON	OFF	OFF	Gate	Gate	NA	NA

Table F-12. Preliminary Engineering Measurement List (Continued)

1) ATTITUDE CONTROL SUBSYSTEM MEASUREMENT LIST (Cont)								
		Range			Frequency Response or Sampling Rate		Per Cent Accuracy	
Measurement Type	Measurement Description and Location	Maximum	Minimum	Nominal	Preferred	Minimum Acceptable	Preferred	Minimum Acceptable
Analog Temperature	Earth pointing actuator temp				1/hr	0.1/hr	2	5
Analog voltage	AGC fine sun sensor signal				10/hr	1/hr	2	5
Discrete voltage	Canopus tracker-acquisition tracking mode indicator	ON	OFF		Gate	Gate	NA	NA
2) SCIENCE PAYLOAD AND POP MEASUREMENT LIST								
Digital voltage	POP shaft position	±180 deg	0	±180 deg	0.5 cps	0.2 cps		11 bits
Digital voltage	POP gimbal position	±130 deg	0	±130 deg	0.5 cps	0.2 cps		11 bits
Digital voltage	POP shaft command	±180 deg	0	±180 deg	0.5 cps	0.2 cps		11 bits
Digital voltage	POP gimbal command	±130 deg	0	±130 deg	0.5 cps	0.2 cps		11 bits
Analog voltage (2)	Horizon scanner outputs	± 30 deg	0	± 30 deg	0.5 cps	0.2 cps	1	3
Analog voltage	Gimbal drive temp	130°F	0		1/hr	0.1/hr	2	5
Analog voltage	POP package temp	130°F	0		1/hr	0.1/hr	2	5
Analog voltage (11)	Science inst temp	130°F	0		1/hr	0.1/hr	2	5
Analog voltage (22)	Science inst voltages				2/hr	1/hr	2	5
3) CENTRAL SEQUENCING AND COMMAND (CS&C) SUBSYSTEM MEASUREMENT LIST								
Voltage analog	28 vdc, power			28	1/day		3	5
Voltage analog	12 vdc, power			12	1/day		3	5
Voltage analog	4 vdc, power			4	1/day		3	5
Frequency	Oscillator pickoff after divide					1/2 sec		26 bits
Digital voltage	Selected word (18 bits)				1/10 min	1/hr*		

*1 per 10 seconds during maneuvers.

Table F-12. Preliminary Engineering Measurement List (Continued)

Type Measurement	Measurement Description and Location	Range			Frequency Response or Sampling Rate		Per Cent Accuracy	
		Maximum	Minimum	Nominal	Preferred	Minimum Acceptable	Preferred	Minimum Acceptable
3) CENTRAL SEQUENCING AND COMMAND (CS&C) SUBSYSTEM MEASUREMENT LIST (Cont)								
Event-discrete	Voltage signal for output occurrence	4V	0	0	1/32 sec max		10	20
Accept-reject	Voltage signal indicating data input acceptance	4V	0	0	1/32 sec max		10	20
Analog voltage (2)	Sequence on-line	ON	OFF		Gate	Gate	NA	NA
Digital voltage	Sequence mode code				1/10 min	1/hr	NA	4 bits
4) COMMUNICATION SUBSYSTEM MEASUREMENT LIST (INCLUDES DATA HANDLING SUBSYSTEM)								
Voltage analog	S-band Rcvr #1 - Static Phase Error	$\pm 10^{o}$	0	0	1/sec	1/sec	1	3
Voltage analog	S-band Rcvr #1 - Signal Strength	-10	0	-5	1/min	1/hr	1	3
Temperature analog	S-band Rcvr #1 - VCO Temp (Freq)	$+70^{o}C$	$-10^{o}C$	$+25^{o}C$	1/10 min	1/hr	3	5
Voltage discrete	S-band Rcvr #1 - In-lock	ON	OFF	ON	1/sec	1/min	NA	NA
Voltage analog	S-band Rcvr #2 - Static Phase Error	$\pm 10^{o}$	0	0	1/sec	1/sec	1	3
Voltage analog	S-band Rcvr #2 - Signal Strength	-10	0	-5	1/min	1/hr	1	3
Temperature analog	S-band Rcvr #2 - VCO Temp (Freq)	$+70^{o}C$	$-10^{o}C$	$+25^{o}C$	1/10 min	1/hr	3	5
Voltage discrete	S-band Rcvr #2 - In-lock	ON	OFF	ON	1/sec	1/min	NA	NA
Voltage analog	S-band Rcvr #3 - Static Phase Error	$\pm 10^{o}$	0	0	1/sec	1/sec	1	3
Voltage analog	S-band Rcvr #3 - Signal Strength	-10	0	-5	1/min	1/hr	1	3

Table F-12. Preliminary Engineering Measurement List (Continued)

4) COMMUNICATION SUBSYSTEM MEASUREMENT LIST (INCLUDES DATA HANDLING SUBSYSTEM) (Cont)								
		Range			Frequency Response or Sampling Rate		Per Cent Accuracy	
Type Measurement	Measurement Description and Location	Maximum	Minimum	Nominal	Preferred	Minimum Acceptable	Preferred	Minimum Acceptable
Temperature analog	S-band Rcvr #3 - VCO Temp (Freq)	+70°C	-10°C	+25°C	1/10 min	1/hr	3	5
Voltage discrete	S-band Rcvr #3 - In-lock	ON	OFF	ON	1/sec	1/min	NA	NA
Current analog	Power Amp #1 Helix Current	20	0	2	1/min	1/10 min	1	3
Power analog	Power Amp #1 Power Output	30	0	20	1/min	1/10 min	3	5
Temperature analog	Power Amp #1 Baseplate Temp	+100°C	-10°C	+50°C	1/min	1/10 min	3	5
Current analog	Power Amp #2 Helix current	20	0	2	1/min	1/10 min	1	3
Power analog	Power Amp #2 Power output	30	0	20	1/min	1/10 min	3	5
Temperature analog	Power Amp #2 Baseplate Temp	+100°C	-10°C	+50°C	1/min	1/10 min	3	5
Voltage analog	VHF Rcvr #1 Regulated Voltage	-24	0	-20	1/min	1/10 min	1	3
Voltage analog	VHF Rcvr #1 Signal Strength	-10	0	-5	1/min	1/10 min	1	3
Voltage analog	VHF Rcvr #2 Regulated Voltage	-24	0	-20	1/min	1/10 min	1	3
Voltage analog	VHF Rcvr #2 Signal Strength	-10	0	-5	1/min	1/10 min	1	3
Voltage discrete	Capsule Demod #1 In-lock	ON	OFF	OFF	1/min	1/10 min	NA	NA
Voltage discrete	Capsule Demod #2 In-lock	ON	OFF	OFF	1/min	1/10 min	NA	NA
Voltage analog	Modulator-Exciter #1 Regulated Voltage	-24	0	-20	1/min	1/hr	1	3

Table F-12. Preliminary Engineering Measurement List (Continued)

4) COMMUNICATION SUBSYSTEM MEASUREMENT LIST (INCLUDES DATA HANDLING SUBSYSTEM) (Cont)									
Type Measurement	Measurement Description and Location		Range			Frequency Response or Sampling Rate		Per Cent Accuracy	
			Maximum	Minimum	Nominal	Preferred	Minimum Acceptable	Preferred	Minimum Acceptable
Voltage analog	Modulator-Exciter #1	Regulated Voltage	+15	0	+10	1/min	1/hr	1	3
Power analog	Modulator-Exciter #1	Power Output	150	0	100	1/min	1/10 min	3	5
Voltage analog	Modulator-Exciter #2	Regulated Voltage	-24	0	-20	1/min	1/hr	1	3
Voltage analog	Modulator-Exciter #2	Regulated Voltage	+15	0	+10	1/min	1/hr	1	3
Power analog	Modulator-Exciter #2	Power Output	150	0	+10	1/min	1/10 min	3	5
Voltage analog	Low Power Trans	Regulated Voltage	-24	0	-20	1/min	1/hr	1	3
Voltage analog	Low Power Trans	Regulated Voltage	+40	0	+35	1/min	1/hr	1	3
Power analog	Low Power Trans	Power Output	1.5	0	1.0	1/min	1/10 min	3	5
Voltage discrete	Command Demod #1	In-lock	ON	OFF	OFF	1/sec	1/sec	NA	NA
Voltage discrete	Command Demod #2	In-lock	ON	OFF	OFF	1/sec	1/sec	NA	NA
Position 12 bit binary	High Gain Antenna	Shaft Angle	$\pm 180^{\circ}$	0	Any	1/min	1/min	NA	NA
Position 12 bit binary	High Gain Antenna	Hinge Angle	$\pm 90^{\circ}$	0	Any	1/min	1/min	NA	NA
Temperature analog	High Gain Antenna	Shaft Axis Temp	$+70^{\circ}C$	$-10^{\circ}C$	$+25^{\circ}C$	1/10 min	1/hr	3	5
Temperature analog	High Gain Antenna	Hinge Axis Temp	$+70^{\circ}C$	$-10^{\circ}C$	$+25^{\circ}C$	1/10 min	1/hr	3	5

Table F-12. Preliminary Engineering Measurement List (Continued)

4) COMMUNICATION SUBSYSTEM MEASUREMENT LIST (INCLUDES DATA HANDLING SUBSYSTEM) (Cont)									
Measurement Type	Measurement Description and Location		Range			Frequency Response or Sampling Rate		Per Cent Accuracy	
			Maximum	Minimum	Nominal	Preferred	Minimum Acceptable	Preferred	Minimum Acceptable
Power analog	High Gain Antenna	Radiated Power	30	0	20	1/min	1/10 min	3	5
Position 12 bit binary	Medium Gain Antenna	Shaft Angle	$\pm 180^{\circ}$	0	Any	1/min	1/min	3	5
Temperature analog	Medium Gain Antenna	Shaft Axis Temp	$+70^{\circ}$	-10°C	$+25^{\circ}$C	1/10 min	1/hr	3	5
Power analog	Medium Gain Antenna	Radiated Power	30	0	20	1/10 min	1/hr	3	5
Power analog	Low Gain Antenna	Radiated Power	30	0	20	1/10 min	1/hr	3	5
Temperature analog	Tape Recorder	Temperature	$+50^{\circ}$C	$+10^{\circ}$C	$+25^{\circ}$C	1/10 min	1/hr	3	5
Pressure analog	Tape Recorder	Pressure	20	0	15	1/10 min	1/hr	3	5
Speed analog	Tape Recorder	Motor Rotation Speed	125	0	100	1/min	1/10 min	1	3
Voltage discrete	Tape Recorder	Read Mode	ON	OFF	OFF	1/10 min	1/hr	NA	NA
Voltage discrete	Tape Recorder	Write Mode	ON	OFF	OFF	1/10 min	1/hr	NA	NA
Voltage discrete	Tape Recorder	End of Tape, Read	ON	OFF	OFF	1/10 min	1/hr	NA	NA
Voltage discrete	Tape Recorder	End of Tape, Write	ON	OFF	OFF	1/10 min	1/hr	NA	NA

Table F-12. Preliminary Engineering Measurement List (Continued)

Measurement Type	Measurement Description and Location	Range			Frequency Response or Sampling Rate		Per Cent Accuracy	
		Maximum	Minimum	Nominal	Preferred	Minimum Acceptable	Preferred	Minimum Acceptable
5) MECHANICAL SUBSYSTEM MEASUREMENTS LIST								
Pos. Desc.	S and A (Arm or Disarm)	ON	OFF	OFF	8 cps	2 cps	NA	NA
Pos. Desc.	Booster to Spacecraft Sep.	ON	OFF	OFF	8 cps	1 cps	NA	NA
Pos. Desc.	Separation Verification - Lander Cover from Bus	ON	OFF	OFF	8 cps	1 cps	NA	NA
Pos. Desc.	Thermal Louvers Position 0° to 90° Position	90°	0°	45°	1/5 min	1/30 min	1	3
6) POWER SUBSYSTEM MEASUREMENTS LIST								
Voltage analog	Regulated Bus Voltage (1)	55V	45V	50V	1/min	1/hr	2	5
Voltage analog	Shunt Bus Voltages (4)	30V	20V	25V	1/min	1/hr	2	5
Voltage analog	Battery Voltage (1)	50V	30V	50V	1/min	1/hr	2	5
Voltage analog	4 KC Inverter Output (1)	60V	40V	50V	1/min	1/hr	2	5
Voltage analog	400 cps 1 Ø Inverter Output (2)	35V	25V	30V	1/min	1/hr	2	5
Voltage analog	800 cps 2 Ø Inverter Output (2)	30V	24V	27V	1/min	1/hr	2	5
Current analog	Solar Array Current (1)	10 amp	0	5a	1/min	1/hr	2	5
Current analog	Solar Array Shunt Currents (4)	3 amp	0	1a	1/min	1/hr	2	5
Current analog	Battery Current (1)	10 amp	0	5a	1/min	1/hr	2	5
Current analog	Charge Regulator Input (1)	2 amp	0	1a	1/min	1/hr	2	5
Current analog	Boost Regulator Output (1)	6 amp	0	3a	1/min	1/hr	2	5
Current analog	4 KC Inverter Input (2)	7 amp	0	3a	1/min	1/hr	2	5
Current analog	4 KC Inverter Output (2)	6 amp	0	3a	1/min	1/hr	2	5
Current analog	400 cps, 1 Ø Inverter Input (2)	1 amp	0	1a	1/min	1/hr	2	5
Current analog	800 cps, 2 Ø Inverter Input (2)	1 amp	0	1a	1/min	1/hr	2	5

Table F-12. Preliminary Engineering Measurement List (Continued)

6) POWER SUBSYSTEM MEASUREMENTS LIST (Cont)								
		Range			Frequency Response or Sampling Rate		Per Cent Accuracy	
Measurement Type	Measurement Description and Location	Maximum	Minimum	Nominal	Preferred	Minimum Acceptable	Preferred	Minimum Acceptable
Temperature analog	Battery (2)	150°F	25°F	70°F	1/min	1/hr	1	3
Temperature analog	Shunt Elements (4)	200°F	-220°F	0°F	1/min	1/hr	1	3
Temperature analog	Battery Regulator (1)	175°F	25°F	70°F	1/min	1/hr	1	3
Temperature analog	5 KC Inverter (1)	175°F	25°F	70°F	1/min	1/hr	1	3
Temperature analog	400 cps, 1 Ø Inverter (1)	175°F	25°F	70°F	1/min	1/hr	1	3
Temperature analog	400 cps, 3 Ø Inverter (1)	175°F	25°F	70°F	1/min	1/hr	1	3
Temperature analog	Solar Array (6)	200°F	-220°F	0°F	1/min	1/hr	1	3
Relay - discrete	Solar Array Switching (5)	ON	OFF	OFF	9334.17-407 Attachment 1/hr	(VM-100) 1/day	NA	NA
7) PROPULSION SUBSYSTEM MEASUREMENTS LIST								
Pressure analog	Propellant Tank Pressure	500	0	250	1 cps	(not critical)	2	5
Pressure analog	Combustion Chamber Pressure	300	0	150	25/sec	5/sec	2	5
Temperature analog	Propellant Temperature	125°F	25°F	70°F	1 min	1/hr	2	5
Position discrete	Up to 20 position Discretes may be required to monitor press. system and engine control valves.	Fired	Non	Fired	5/sec	1/sec	NA	NA
Position discrete	Solid retro Elect. Fire Signal	ON	OFF		5/sec	1/sec	NA	NA
8) THERMAL CONTROL SUBSYSTEM INSTRUMENTATION LIST								
Analog	Structural Temp. (Main Bus)	190°F	-30°F	70°F	1/5 min	1/30 min	2	5
Analog	Structural Temp. (External Comp.)	250°F	-250°F	0°F	1/5 min	1/30 min	5	10
Analog	Engine Temperature	800°F	-100°F	60°F	1/5 min	1/30 min	5	10

Table F-13. Summary of Measurement List Sampling Rate

Subsystem	Sampling Preferred						Rate Minimum						Per Cent Accuracy	
	5/s	2/s	1/s	1/m	1/10 m	1/hr	2/s	1/s	1/10 s	1/m	1/10 m	1/hr	Pre-ferred	Mini-mum
Communications														
(Analog)			3	26	10			3			15	19	1	3
(Discrete)			5	38	4			2		39	2	4		
Attitude Control														
(Analog)	9		2	8	6	3	9		1	5		9	2	5
(Discrete)				30						30				
Thermal Control														
(Analog)					110							110	2	5
CS&C														
(Analog)						10							3	5
(Discrete)	4			6	20					2		20		
Mechanical														
(Analog)					2							2	1	3
(Discrete)	24						9							
Power														
(Analog)				39								39	1	3
(Discrete)						5						5		
Propulsion														
(Analog)	6			1			1		2			1	2	5
(Discrete)	21							21						
Science														
(Discrete)		55						55						
(Analog)						5						4		
Totals - Analog	15		5	74	128	18	10	3	3	5	15	184		
Discrete	49	55	5	74	24	5	9	78		71	2	29		
	-8	+51	+12	+227	-382									

Integrated Data Bit Rates

1) Preferred - 949 bits/sec
2) Minimum - 263 bits/sec

When formatted as permitted by 2 level commutation plus cross strapping and adding synchronization and identification allowance, these values become:

1) Preferred - 1295 bits/sec
2) Minimum - 389 bits/sec

APPENDIX G
SOLAR ARRAY DESIGN

1. SOLAR CELL TRADEOFF ANALYSIS

The tradeoff study to select the optimum base-resistivity solar cell and cover glass thickness indicates that, in general, the nominal 10-ohm-cm cell and a 6 mil cover glass yield a higher watt per pound solar array than thicker cover glass.

The basis for a tradeoff study of base resistivity is that higher base resistivity solar cells provide more power at a higher radiation flux levels than low base resistivity cells for the identical initial efficiency. The curves in Figure G-1 show that a cross-over exists at an equivalent flux of 9×10^{14} 1-Mev electrons/cm^2 total dose. Since the curve is constructed for solar cells at $+27^{\circ}C$, the results are subject to a small error at higher and lower operating temperatures (discussed below). Nevertheless, the curves show that above 9×10^{14} electrons/cm^2 the higher base resistivity cell produces more power and requires less area for a fixed power requirement.

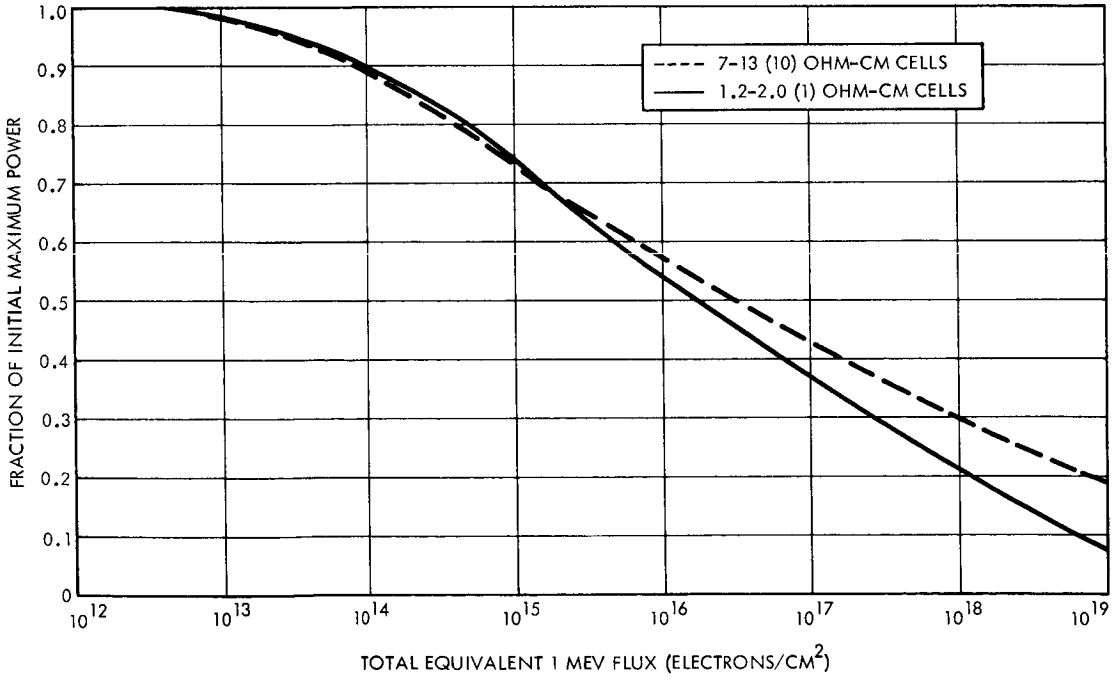


Figure G-1. Fraction of Initial Power Remaining versus Total 1 Mev Equivalent Electron Flux

In general, as the cover glass thickness is increased, more charged particles are prevented from reaching the solar cell surface; but at the same time, the array weight per unit of area is increased as the result of the extra glass. Whether or not an optimum glass thickness exists and if so, what that exact value is depends upon the make-up of the particle spectrum, i.e., the relative quantities and spectral distributions of protons and electrons.

The damage factors which have been used to convert the raw flux spectrum into damage-equivalent 1-Mev electrons were obtained from the Figures 32 and 33 in "Results of the Telstar Radiation Experiments," by W. L. Brown, et al, in the July 1963 issue of the Bell System Technical Journal.

In general, the damage factor increases with electron energy for a given glass thickness, and reduces with increasing glass thickness. For protons, increasing the glass thickness tends to increase the required minimum proton energy for glass penetration. At higher proton energies, however, increased glass thickness is not significantly effective in reducing the damage factors.

1.1 Details of Analysis

The analysis was based upon the assumptions discussed in the following paragraphs.

1.1.1 Flux

The raw flux spectrum is presented in Table G-1 (also see Appendix B). The analysis was performed for Mars radiation environments ranging from 10^{-1} to 10^{4} of the earth's radiation referred to as $E_m = 10^{-1}E_o$ to $10^{4}E_o$.

Table G-1. Voyager Flux Spectrum

A. Near Earth

Electrons

E > 0.5 Mev	=	4×10^{10} e/cm^2

Protons*

4-15 Mev	=	10^9 P/cm^2
15-30 Mev	=	10^8 P/cm^2
> 30 Mev	=	10^7 P/cm^2

B. Cruise

Solar flares - 1/2 yearly rate for 177 day Type 1 Class 1 Mission

Protons

>30 Mev	=	5×10^9 P/cm^2
>100 Mev	=	4.8×10^8 P/cm^2

Solar wind = no damaging particles.

C. Mars Orbit

Nominal Orbit:

$2,000^{km} = h_p$

$20,000^{km} = h_a$

Inclination = 45 deg

Period = 14.5 hr

Eccentricity = 0.628

Based on Mars Equal to One Earth Model

Electrons

E > 0.5 = 1.6×10^{13} e/cm^2 for 6 months in orbit.

*Derived from Flux Map AE 1 Velte, - Aerospace Corporation, January 1965.

Table G-1. Voyager Flux Spectrum (Continued)

Protons

4-15 Mev	=	2.2×10^{9} P/cm^2/orbit
15-30 Mev	=	3.9×10^{7} P/cm^2/orbit
34-50 Mev	=	8.6×10^{6} P/cm^2/orbit
> 50 Mev	=	1.1×10^{6} P/cm^2/orbit

For 6 months, multiply per orbit values by

$$\frac{24 \text{ Hr/Day}}{14.5 \text{ Hr/Orbit}} \times 183 \text{ days} = 303 \text{ orbits}$$

For a 1/10 earth model, multiply above values by 10^{-1}.

For earth models of 10 through 10^{4}, multiply flux values for the E_o case by the approximate scaling factor 10^{N}.

Electrons and Protons in 6 Month Mission

Protons	1 Earth Model (E_o)	1/10 Earth Model ($10^{-1}E_o$)
E > 4 - 15	6.7×10^{11} P/cm^2	6.7×10^{10} P/cm^2
E = 15 - 30	1.3×10^{10} P/cm^2	1.3×10^{9} P/cm^2
E = 34 - 50	2.6×10^{9} P/cm^2	2.6×10^{8} P/cm^2
E > 50	3.3×10^{8} P/cm^2	3.3×10^{7} P/cm^2
Electrons		
> 0.5 Mev =	1.6×10^{13} P/cm^2	1.6×10^{12} P/cm^2

Solar Flares - Protons

> 30 Mev 5×10^{9} P/cm^2

> 100 Mev 4.8×10^{8} P/cm^2

Solar Wind

No damage.

Except as noted, all values of per cent power remaining, areas and weights required are based on the total flux received by the solar array throughout the 12-month mission life. This includes the near earth flux, cruise flux, and flux encountered during 6 months of Mars orbiting. Except for the flux received from solar flares, all flux incurred at Mars is directly scaled when considering Mars environments ranging from 10^{-1} to 10^{4} of the earth radiation flux environments.

1.1.2 Damage Factor

This is described in the array electrical design section (Volume 5, Section IV - 3.3.3).

1.2 Array Characteristics

These consist of the following:

a) Backshielding, including two layers of 5-mil thick aluminum skins, primer, bonding, adhesive, and paint equivalent to 0.11 gm/cm^2 or about 20 mils of fused silica cover glass.

b) Array weight exclusive of cover glass = 0.816 lb/ft^2.

1.3 Solar Cell Damage Curve

The curve in Figure G-1 is a plot of the relative maximum power remaining versus equivalent 1-Mev electron flux. It assumes the same efficiency for the two resistivity types at +27°C. The 1-Mev flux obtained with the data in (a) and (b) for each of several glass thicknesses is used to enter this curve to establish the remaining power at the respective flux levels. The total flux incident upon a solar cell includes that impinging on the front for glass thicknesses of 6 mils, 18, 36, and 54 mils and on the cell rear surface through an equivalent 20 mil coverglass. To extend the analysis to flux corresponding to E_o of 10^2 and above required extrapolation of the solar cell radiation damage curves to flux levels much higher than that for which damage data is available. Thus, although general conclusions are valid, care must be taken when using any data for $E_o \geq 10^2$.

1.4 Results

Table G-2, shows the per cent of initial power remaining for each glass thickness, from $E_M = 10^1 E_o$ to $10^4 E_o$ for 1 and 10 ohm-cm solar cells. The table accounts only for radiation damage to the solar cells; other degradation mechanisms are not included in the analysis.

Table G-2. Relative Power Remaining at End of Life

E_M	$10^{-1}E_o$	10^0E_o	10^1E_o	10^2E_o	10^3E_o	10^4E_o
Glass Thickness (mils)			1 Ohm-Centimeter Cells			
6	0.815	0.623	0.445	0.284	0.137	0.014
18	0.827	0.640	0.460	0.298	0.150	0.025
36	0.842	0.653	0.472	0.307	0.160	0.033
54	0.858	0.680	0.493	0.327	0.177	0.048
			10 Ohm-Centimeter Cells			
6	0.800	0.640	0.490	0.354	0.234	0.130
18	0.814	0.655	0.504	0.366	0.244	0.139
36	0.827	0.666	0.513	0.375	0.250	0.145
54	0.844	0.690	0.532	0.392	0.265	0.158

Table G-3 shows the relative solar array area required for a fixed end of life power. The results are all normalized for 6 mil glass over the range of E_M values. Note that the 1 and 10 ohm-centimeter cells are normalized separately. The results are consistent with that of Table G-2: the higher the percentage of remaining power (Table G-2), the lower is the relative area.

Table G-3. Relative Areas Required

E_M	$10^{-1}E_o$	10^0E_o	10^1E_o	10^2E_o	10^3E_o	10^4E_o
Glass Thickness (mils)			1 Ohm - Centimeter			
6	1.00	1.00	1.00	1.00	1.00	1.00
18	0.99	0.97	0.96	0.95	0.91	0.56
36	0.97	0.95	0.94	0.93	0.86	0.42
54	0.95	0.92	0.90	0.87	0.77	0.29
			10 Ohm-Centimeter			
6	1.00	1.00	1.00	1.00	1.00	1.00
18	0.98	0.98	0.97	0.97	0.96	0.94
36	0.97	0.96	0.96	0.94	0.97	0.90
54	0.95	0.93	0.92	0.90	0.88	0.82

All numbers rounded off to two significant figures.

Note: All relative areas are with respect to the 6-mil glass for each flux case. Different flux levels cannot be compared in this table.

Table G-3 shows only the relative areas and thus that the thicker glass requires less total area is as expected. However, the weight increases with glass thickness, and if the values in Table G-3 are multiplied by the respective lb/ft^2 values for the specific glass thickness, it is found also that the total array net weight increases with increasing glass thickness. Thus, the reduction in flux reaching the cell with increasing glass thickness, is offset by the increased unit area weight with the single exception at $E_M = 10^4E_o$ for 1 ohm-centimeter.

The results in Table G-4 have again been normalized for a 6-mil glass thickness. At each flux level, the values represent the total array weight required to supply the same end of life power. In general, a lower array weight is achieved by using the thinner glass and providing

the additional area required. The most significant effect of increasing the array area is the increased solar cell cost, which is a first order approximation is inversely proportional to the relative areas in Table G-3.

Table G-4. Relative Solar Array Weight

E_M	$10^{-1}E_o$	10^0E_o	10^1E_o	10^2E_o	10^3E_o	10^4E_o
Glass Thickness (mils)			1 Ohm - Centimeter			
6	1.00	1.00	1.00	1.00	1.00	1.00
18	1.09	1.08	1.07	1.06	1.01	0.62
36	1.24	1.22	1.20	1.18	1.09	0.54
54	1.37	1.32	1.30	1.25	1.11	0.42
			10 Ohm - Centimeter			
6	1.00	1.00	1.00	1.00	1.00	1.00
18	1.09	1.08+	1.08-	1.07	1.06	1.04
36	1.23	1.22+	1.22-	1.20	1.19	1.14
54	1.36	1.33	1.32	1.30	1.27	1.18

The results of Table G-4 are plotted in Figure G-2 for the 1 ohm-cm cells.

The results for $E_M = 10^4E_o$ for the 1 ohm-centimeter cell are different from the other cases because the relative power remaining is extremely small* (less than 5 per cent) and undergoes a wide variation between 6 and 54 mils (about 3.5 to 1). Thus, the relative area required (Table G-3) is a factor of 3 smaller for 54 mils (relative to 6 mils), and the increased unit area weight cannot offset the larger area as for the remaining cases in Table G-4.

*In fact, the remaining power is probably within the uncertainty level of any system of measurements used to determine flux magnitudes and power levels.

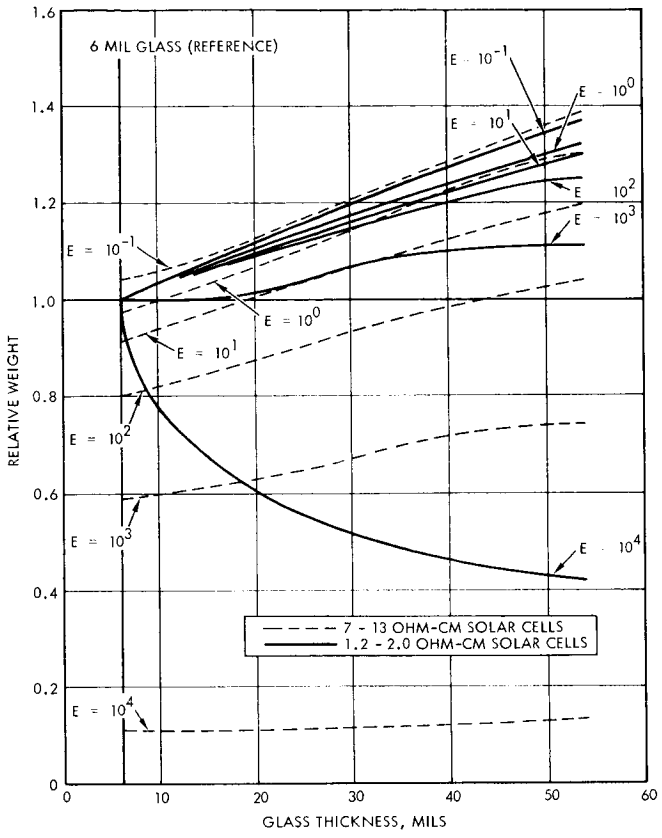


Figure G-2. Relative Weight Versus Glass Thickness

A direct comparison of 1 and 10 ohm-centimeter cells is obtained by normalizing the data for the latter cells with respect to the former in Table G-3 (again each flux level is maintained separately). Table G-3 shows a greater relative power remaining for the 1 ohm-cm cells for $E_M = 10^{-1}E_o$, but the 10 ohm-cm cell is superior for all remaining cases of E_M. Maintaining the normalization would alter Table G-4 to that shown in Table G-5. The results are again with respect to relative weight to yield a specific end of life power, but the normalization of the 10 ohm-cm to the 1 ohm-cm data permits a direct comparison of the two cell types. The results show the clear superiority of the higher base resistivity cells for $E_M \geqq 3E_o$.

Table G-5. 10 Ohm - Centimeter Cell Data for Relative Array Weight Normalized to 1 Ohm-Centimeter Cell Data in Table G-4

E_M	$10^{-1}E_o$	10^0E_o	10^1E_o	10^2E_o	10^3E_o	10^4E_o
Glass Thickness (mils)	10 Ohm - Centimeter					
6	1.02	0.97	0.91	0.80	0.50	0.11-
18	1.10	1.05	0.98	0.86	0.62	0.11+
36	1.26	1.19	1.11	0.97	0.70	0.12
54	1.39	1.30	1.20	1.04	0.74	0.13

In general, minimum system weight is achieved with the 6 mil glass and the 10 ohm-cm solar cell.

One more comparison is significant, the determination of the array weight required to supply a constant end of life power as a function of the total radiation flux. Figure G-3 shows a plot of the required array weight (normalized to $E_M = 10^{-1}E_o$) for 6 mil glass covered solar cells versus the total close-in equivalent 1-Mev electrons. Note, however, that the total equivalent 1-Mev flux for two successive E_o cases do not ratio by 10:1 because the total flux includes fixed components not affected by scaling the earth flux from one level to another.

One and 10-ohm-cm cells are also compared (based on 27°C data) to show the importance of the higher base resistivity cell. At $E_M = 10^{-1}E_o$, the 1 ohm-cm cell is superior (see Table G-4) by about 2 per cent, but this is more than offset with increasing flux (see Figure G-1). At the extremely high flux levels, represented by $E_M > 10^2E_o$, the poorer radiation resistance of the lower base resistivity cell is clearly demonstrated by the sharp separation of the two curves. Thus as a protection against higher unexpected flux, the 10-ohm-cm cell should be selected.

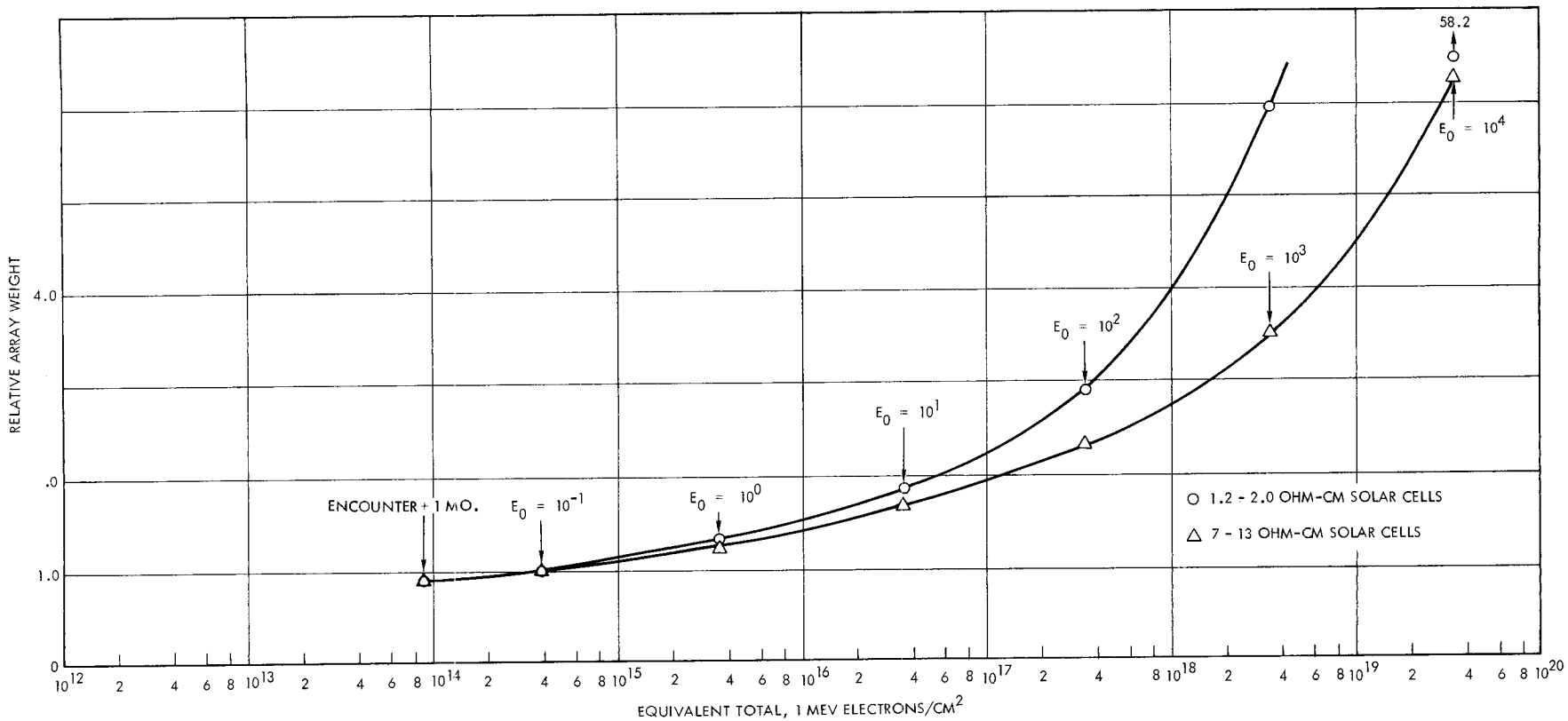


Figure G-3 Relative Array Area (Weight) versus Integrated 1-Mev Electron Flux for Encounter + 6 Months (6 Mil Glass)

Figure G-3 also shows the relative weight at Mars encounter plus one month, based on a total six-month flux accumulated for $E_M = 10^{-1} E_o$. Here the two cell types are nearly identical as a result of the low flux and relatively small damage incurred.

The superiority of the 10 ohm-cm cell is accentuated at temperatures below 27°C (which occur in the last six months of life) because the increase of voltage with decreasing temperatures is higher for the 10 ohm-cm solar cell. Specifically, $\frac{dV_{MP}}{dt}$ = 2.7 mv/°C for the 10 ohm-cm cell and only 2.2 mv/°C for the 1 ohm-cm cell. Inclusion of the low temperature characteristics in Figure G-3 would show still lower relative weights for the 10 ohm-cm cell, compared to the 1 ohm-cm cell.

2. ARRAY MECHANICAL DESIGN

2.1 Summary

Structural design of the solar array is discussed in Section V-1. Factors governing the design of the solar array for Voyager included:

- Over-all specific weight, including solar cells and cover glass with an assumed packing factor of 0.88, not to exceed 1 lb/ft^2.
- Structural deflection because of vibration, steady state and impulsive accelerations not to exceeds 1 inch.
- Mechanical properties of the substrate should not be changed by repeated temperature cycling.
- The solar array should be sectioned to facilitate fabrication, handling, and testing, and all sections should be identical.

During the Phase IA study, three substrate materials were considered:

- A 0.10-inch single flat aluminum skin bonded to a corrugated sheet of 0.0008-inch aluminum, reinforced by four aluminum hat-shaped stiffeners bonded to the panel.
- A 3/8-inch thick aluminum honeycomb panel with 0.005-inch aluminum facing skins reinforced by four aluminum hat-shaped stiffeners boned to the panel.

- o A 1-inch honeycomb panel with 0.010-inch facing on a hexagon cell core with no reinforcement.

Because of the possibility of having to implement a development program in the field of thin gauge corrugated structures, study effort was concentrated on the honeycomb structures. Stress analysis indicated very minor differences between the deflection characteristics of the 3/8 inch reinforced and the 1-inch plain honeycomb panels when supported on three sides. Thermal considerations favored the use of the plain honeycomb panel with 7075-T6 aluminum alloy facing skins to minimize thermal gradients over the panel surface during eclipse.

The selected material for the substrate has the following characteristics:

Core	
Material	5056-H39 aluminum
Density	1.6 lb/ft^3
Cell Size	Either 1/4 inch (0.007 inch thickness) or 3/8 inch (0.001 inch thickness)
Facing Sheets	
Material	7075-T6 aluminum
Thickness	0.010 inch
Adhesive	
Material	FM 1000 Epoxy Film
Density	0.040 lb/ft^2

The array includes six identical fixed panels, each as shown in Figure G-4. Each panel will carry 6,496 2 x 2 cm cells, arranged in 4 series strings of 116 10-cell modules and 2 series strings of 116 8-cell modules. The dielectric material separating the cells from the substrate, chosen primarily because of its resistance to thermal cycling, is SMP 62/63 impregnated No. 108 glass cloth. A blend of RTV 580/560 is used for bonding of the solar cells to the dielectric.

The rim of the panel is a thin channel. The substrate contains threaded inserts for mounting protective covers on both sides of each panel. The covers will be installed during all handling, storage, and shipping, removed only for testing when the presence of the covers would alter mechanical characteristics or interfere with illumination.

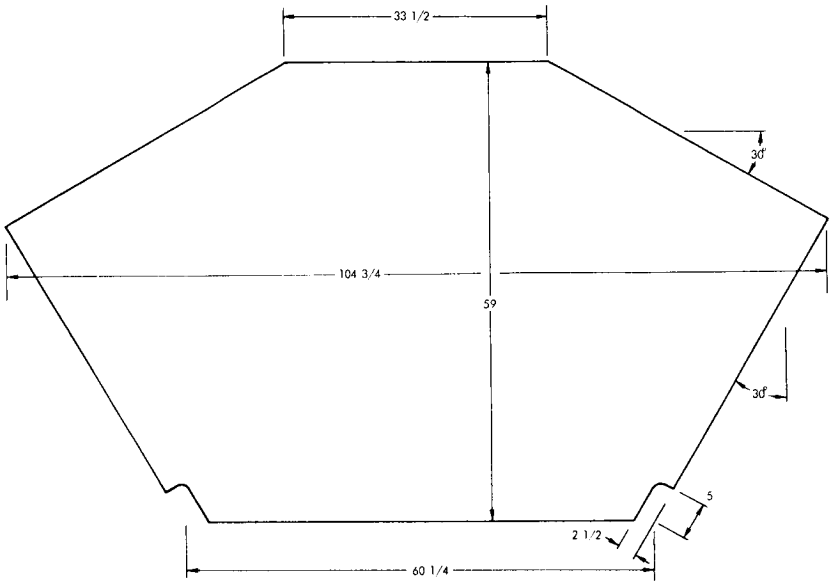


Figure G-4. Solar Panel Outlines

2.2 Substrate

Initially, the array design was based on fixed annular panels with an inside diameter of 120 inches and an outside diameter of 234 inches, having a total area of 247 square feet. The panels were to be supported along their radial edges and stiffened on the inner edge. The outer edge was to be used for attachment of certain scientific instruments and sensors. For this approach a reinforced 3/8 inch honeycomb substrate was proposed, in order to minimize deflection of the unsupported edge. The results of the stress analysis of this design of the panel are given in Appendix C.

It was concluded from the preliminary analysis that the outer edge of the array should be supported to minimize deflection under vibration and to provide support for instruments and sensors. This approach has the further advantage that the six panels can be made interchangeable.

The additional supporting structure enables a plain honeycomb substrate to be used. The panel design was further modified to the shape shown in Figure G-4 to increase the field of view for the POP, with a resultant reduction of area to 191 square feet.

The selected material for the honeycomb skin is 7056-T6 aluminum alloy, a high strength alloy with good thermal properties at the low temperatures encountered during eclipse. To minimize the rate of change of temperature during eclipses, it is desirable to have a material with a specific heat which remains high as its temperature decreases. The specific heat of aluminum plotted in Figure G-5 as a function of temperature is typical for most aluminum alloys. An exception is 7075-T6, which because of its zinc content, maintains an almost constant value of specific heat as the temperature decreases (Figure G-6). Hence, for missions which may have extended eclipse times and resultant low temperatures ($<0^{\circ}C$), 7075-T6 is the preferred material.

The honeycomb is standard 5056-H39 aluminum hexagon cell, with a density of 1.6 lb/ft^3.

During the study a tapered panel design was considered in an effort to reduce substrate weight. This approach was rejected, however, because it would unnecessarily complicate fabrication. Thermal design would also be complicated because an isothermal heat sink is desirable for the solar cells. The practicality of using beryllium was also examined, since it has high strength (4.27 times that of aluminum) and light weight (0.69 times that of aluminum). A stiffened flat plate design was evaluated, but resulted in approximately 3 per cent increase in weight as shown below:

Solar cell weight	12.55 lb/panel
Beryllium sheets	13.90 lb/panel
Stiffeners	6.55 lb/panel
Total	33.00 lb/panel

This compares with 31.71 lb for the selected design. It was also considered that cost and unavilability of large sheets would prohibit the use of beryllium.

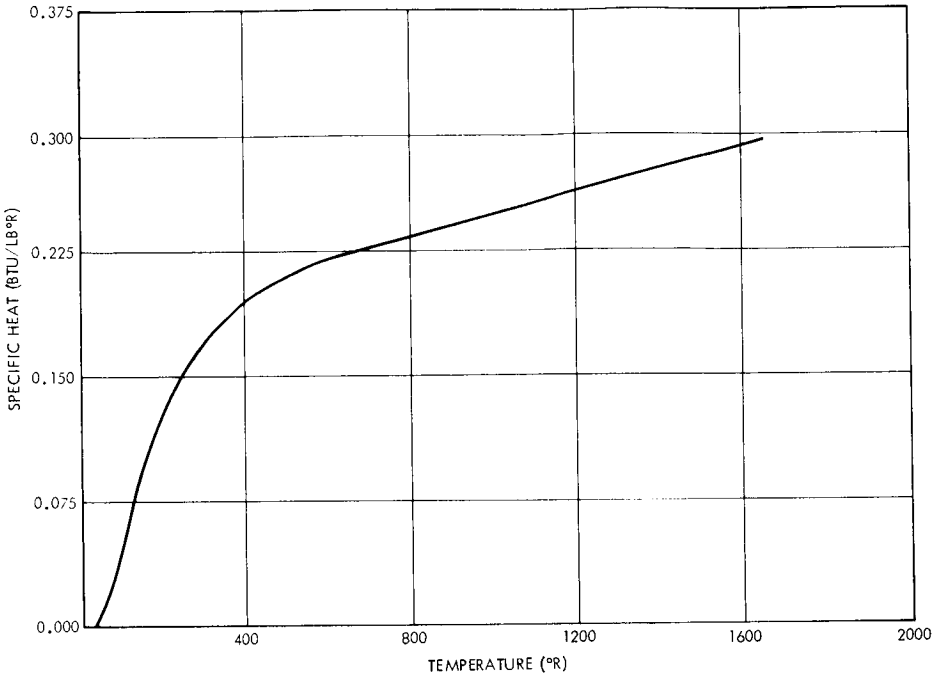


Figure G-5. Aluminum Specific Heat

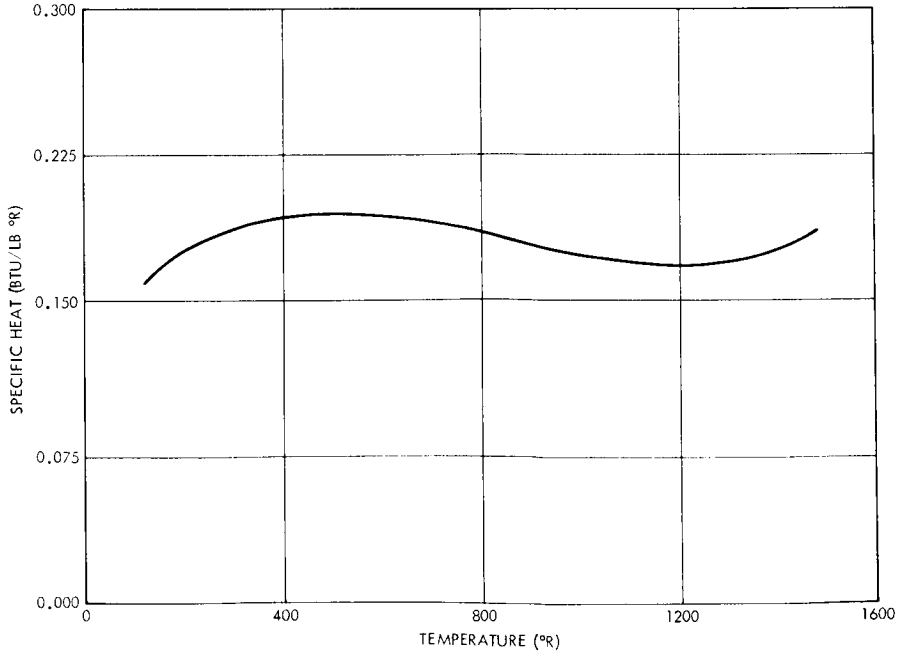


Figure G-6. Aluminum + Zinc + X Specific Heat

2.3 Panel Weight

The weight per panel for the selected design is:

Solar Cells	12.55
Honeycomb Adhesive (.04 lb/ft)	2.53
Facing Sheets	8.61
Core	4.32
Closing Channels	2.30
Attach. and Misc. (5 per cent)	1.50
Total	31.71

2.4 Adhesive Materials

A materials testing program was conducted to evaluate plastic adhesives effect bonding between the aluminum honeycomb core and its aluminum foil skins and the honeycomb panel and its internal, local structural inserts. The program was divided into two parts: 1) tests to obtain basic physical and mechanical properties of various adhesives such as outgas characteristics, lap shear, peel and flexural strengths under static loading conditions, 2) structural tests that would provide information related to the actual solar panel designs to permit correlation between analytical and test results. The tests were conducted at room temperature, atmospheric pressure conditions, and in an environment simulating the actual anticipated exposures to which the solar panel structural subtrate will be subjected.

2.4.1 FM-1000 Film

On the basis of the tests FM-1000 film was recommended as the adhesive to bond the skins to the core of the honeycomb panel. The 0.04 lb/ft^2 film weight was found to be the optimum from the standpoint of peel strength, for skins of 0.010-inch thick. With this film weight, and a core ribbon thickness of 0.001 inch the peeling of the honeycomb panel skin was realized through 40 per cent core tear and 60 per cent adhesive failure. The peel strength was 10.8 lb/in average, which is considered to be adequate. For a film weight of 0.025 lb/ft^2 the peeling was found to be attributed to 100 per cent adhesive failure of the bond. A 0.06 lb/ft^2 film weight would result in such a strong

bond that 100 per cent core tear occurred in the peel tests. The flexural strength of the FM-1000 bonded honeycomb panels was found to be exceeding that determined theoretically. The criterion for determining the flexural strength of the particular honeycomb panel was the inter-cell buckling of the panel skins because of bending compressive stress.

For skin thickness of 0.010 inches or more, a film weight of 0.08 lb/ft^2 may be required. This will be evaluated during the Phase IB study. Alternative adhesive films based on nylon epoxy (3M Co. AF-300 or AF-302) will also be evaluated for bonding the honeycomb, since they have good low temperature properties.

2.4.2 Outgassing

Outgassing tests were carried out on pure adhesives, plain honeycomb specimens, and specimens of hat section stiffener bonded to honeycomb panel, exposed to a pressure of 5×10^{-6} torr at 120°C for 7 days. Two areas were investigated, effects of outgassing on strengths of adhesives and the amount of condensation of outgassed particles on camera lenses. The test results indicated that no degradation of strength was evident. In fact a slight increase in flexural strength and adhesive modulus was noted in most tests. In the pure adhesive outgas test, the weight loss of the fully exposed adhesives in 3 days constituted approximately 80 to 95 per cent of that in 7 days. Therefore, additional weight loss beyond 7 days could be assumed to be negligible in this test. A study on the paths of the outgassed particles of the adhesives in the solar panel structural subtrate indicated a condensation film of less than 10^3 Å on adjacent glass surfaces for 30 days. Outgassing tests will be repeated for nylon epoxides during Phase IB.

2.4.3 Thermal Cycling

Plain honeycomb panel and hat panel specimens were cycled between -120 and 120°C for 50 cycles. The specimens were subsequently subjected to peel and flexural tests. As in the case of thermal vacuum exposure, no decrease of strength was noted. It was also observed that the flexural strengths were 20 to 40 per cent greater than those obtained with no prior exposure.

2.4.4 Tensile and Flexural Tests on Bonded Inserts

Tensile and flexural tests conducted on specimens with internally bonded aluminum inserts indicated that the presence of such inserts did not create local high stress concentration to the extent that the tensile and flexural strengths of the honeycomb panel are reduced. The average compressive force on the insert surface required to shear out the insert from the honeycomb panel was found to exceed the design requirement by a large margin. The adequacy of the inserts has been demonstrated in single-panel vibration tests. Inserts will be bonded into the honeycomb section using HT-424 foam.

2.4.5 Finishes

The finish on the back face of the honeycomb skin will be determined by a thermal analysis of the required $\alpha/_{\epsilon}$. A chromic acid etch will be used to treat the skin prior to bonding.

2.5 Substrate to Module Interface

For the resin to be used for bonding the solar cell modules to the substrate high level performance is needed by polymeric materials during prolonged exposure to the space environment. The worst case environmental conditions include thermal cycling with simultaneous exposure to 10^{-9} torr, corresponding to the vehicle environment during the last month of the 6-month orbiting phase. Another restrictive condition, inherent in the design, is the vibration experienced by the bonding agents during powered flight. This requirement demands adequate static performance by the bonding system and a high degree of dynamic capability. Still another important consideration is the effect of the linear coefficients of thermal expansion over the relatively wide temperature extremes involved. Although the bonding system may have the ability of accommodating the shear forces caused by a differential coefficient of expansion, the solar cell interface with the adhesive (e.g., silver titanium solar cell backing) must be considered since it may be weaker than the bonding system.

The materials and their application are considered from a systems viewpoint rather than individually. For example, the bonding of the solar array involves the pretreatment of the aluminum honeycomb

subtrate, the application of a dielectric film or coating, the bonding of primed solar cell modules, and the bonding of cover glasses onto the solar cells. The failure of any component of this system may result in system electrical degradation or even catastrophic failure.

2.5.1 Dielectric Materials

Four types of dielectric materials were considered as films capable of providing electrical insulation of the solar cell modules from the aluminum honeycomb skin. These materials included:

a) SMP 62/63 Epoxy Polyamide (0.004 thick dry film sprayed)

b) Glass cloth impregnated with SMP 62/63

c) Mica ply epoxy glass laminate

d) Doryl LD 3055 Polyester glass laminate

The four dielectric materials were evaluated in an earlier test program. Application of Alodine 600 and chromic acid etching were evaluated as pretreatments for enhancing the adhesion of the dielectric film to the aluminum substrate. SMP 62/63 and the SMP 62/63 impregnated glass cloth utilize the epoxy polyamide as the adhesive. The mica ply film was bonded with RTV silicones. Doryl LD 3055 was bonded to pretreated substrate at elevated temperatures and under pressure. As a result of the testing program outlined below, the following materials and finishes were chosen.

Application	Materials
Sun side surface pre-treatment	No. 631 aluminum cleaner Deoxidine No. 170 Alodine 600
Dielectric film	SMP 62/63 Impregnated No. 108 glass cloth

A room temperature vulcanizing (RTV) adhesive was considered most applicable for bonding solar cell modules to the substrate. The use of a silicone adhesive generally requires the application of a silicone primer to the bonding surface of the substrate. RTV-615, RTV-60, RTV-560, RTV-580 and silastic 881 filled with alumina were evaluated with silicone primers SS-4004 and A-4094 on a 5052-H39 aluminum honeycomb skin.

The results of a comprehensive series of tests outlined below led to the choice of blend of RTV 580/560 for the solar cell module adhesive and SS-4004 as the silicone primer coating.

Tests conducted to select adhesive and silicone primers for the solar cell module bonding system were the following:

Butt-tensile tests:	utilizing scrap solar cells.
Lap shear tests:	an evaluation of curing of RTV-560.
Lap shear tests:	an evaluation of the primer variable with RTV-60 and RTV-560.
Lap shear tests of Silastic 881.	
Lap shear tests of spot bonding with RTV-580/560.	
Lap shear tests:	an evaluation of silicone primer application by spray and brush.
Outgassing tests:	vacuum test of RTV-60, RTV-560 and RTV-615 in vacuum of less than 5×10^{-6} torr, for a periof of 2 weeks.
Outgassing tests:	thermal tests of above materials and RTV 580/560 at room temperature through 125°C.

The physical properties of five silicone rubber blends were determined to obtain information for design criteria. Physical properties determined were:

Density and hardness
Gel time
Application time
Thermal conductivity
Thermal coefficient of linear expansion
Volume resistivity
Dielectric constant and dissipation factor
Flow test

2.6 Wiring and Layouts

Figure 4-75 (Volume 5, Section IV) is a sun side panel of six paralleled circuits of modules composed of 116 series-connected modules in each circuit. The entire available area of the panel, 31.7 square feet, was utilized to package required number of 6496 cells. The remaining

area could be utilized for additional modules if there is a requirement for additional power.

The salient features of this layout ar as follows: to minimize magnetic dipole moments, current carrying paths for each circuit were laid out symetrically about the panel center line. Each current path has a return wire directly beneath it on the dark side of the panel in which current flows in an opposite direction.

The effective packing factor achieved (ratio of active silicon to total array area) is 0.84*. Figure 4-76 (Volume 5, Section IV) shows the wiring layout of the dark side of the panel. The wires (AWG No. 22) carrying the output of each circuit are run in twisted pairs to reduce the dipole moment magnetic effects. Two diodes per circuit serve as protection against open circuits. All wires will be fastened to the panel using a Thixotropic RTV-560 as a staking compound.

3. ARRAY THERMAL DESIGN

The destailed thermal analysis data for the solar array is presented in Appendix D. The analysis has shown that the sun oriented body-fixed array temperature can be maintained within temperature limits of -35 to 65°C, from launch to encounter + 6 months if there is no eclipse of the sun by Mars. This temperature range applies for the normal range of α, ϵ_F, and ϵ_B satisfying the constraint that $\alpha/\epsilon \leq 0.5$. Values used were:

$$\alpha = 0.76 \text{ to } 0.72$$
$$\epsilon_F = 0.78 \text{ to } 0.82$$
$$\epsilon_B = 0.68 \text{ to } 0.88$$

Eclipses will take place, however, during the later phases of the mission and may occur early in the orbiting mission for certain orbits. This section is concerned with examining some of the problems associated with eclipse of the solar array, leading to the choice of materials best suited to survival at extremely low temperatures.

---

*This number is determined by dividing the total number of cells per panel times 3.8 cm^2, by the per-panel area.

3.1 Thermal Cycling

The assumed nominal orbit is partially described as follows:

Periapsis	2,000 km
Apoapsis	20,000 km
Orbit inclination to Mars equator	45 degrees
Orbital period	14.5 hours
Eccentricity	0.628

The eclipse time for this orbit may vary from 0 to 2.3 hours per orbit. Approximately 150 to 200 orbits with eclipse periods may occur. The thermal analyses show that low temperature of the order of -160°C can occur assuming array weight density of 1 lb/ft^2. On the other hand, the maximum array temperatures anticipated are within the approximate range of 0 to -35°C for high back emissivity panels during the latter part of orbiting about Mars. The Voyager specifications require qualification testing at temperature limits 40°C above the highest temperature predicted and 30°C below the minimum predicted temperature. Qualification tests may thus involve low temperature cycling between the temperature limits of 40C to -190°C, as a worst case.

The ability of solar cell assemblies to successfully survive thermal cycling has been demonstrated for several temperature regimes by different spacecraft designers. An industry-wide survey has yielded the information listed on the following page as representing the most extensive thermal cycling data available.

The results demonstrated that solar array assemblies have been qualified over the temperature range of -120 to 115°C for up to 600 cycles (a sweep from −120 to + 115°C and back to -120°C is one complete cycle). A cycle-limited qualification has been achieved at a low temperature of -140°C, but insufficient data is available at this time to establish performance for hundreds of cycles at that temperature. At temperatures in these regions some problems have occurred with adhesives and cover glasses. The module design which successfully survived testing on Nimbus for 1000 cycles from -80 to 60°C failed to

Tester and Program	Temperature Extreme (°C)	No. of Cycles	Solar Cell Configuration Tested	Results
RCA Nimbus	-80 to + 60	1,000	Modules bonded to substrate	2 per cent degradation in current at maximum power voltage
RCA Lunar Orbiter	-120 to + 115	600	Modules bonded to substrate	2 per cent degradation in voltage at maximum power point
TRW; OGO	-140 to +98	3	Modules bonded to substrate	Negligible degradation
JPL; Mariner C	-80 to + 60	Soak Test	Modules bonded to substrate	
Hughes; Surveyor	-170 to +115	Soak Test	Shingles bonded to substrate	Adhesive embrittlement and glass cracking at low temperatures. At high temperature, 3 per cent power loss due to adhesive discoloration.

qualify to the 600 cycle -120 to 115°C requirement on Lunar Orbiter. Thus, it does not necessarily follow that a specific design which qualifies at -120°C will qualify below this temperature. The lack of test data for temperatures below -120°C means that a phase IB program should include a thermal cycling program designed to:

1) Establish a low temperature limit and a corresponding number of cycles to which a high probability of success can be assigned.

2) Establish by test the low temperature limit(s) beyond the qualification limits at which a specific array assembly design will fail and the corresponding number of cycles at which failure occurs.

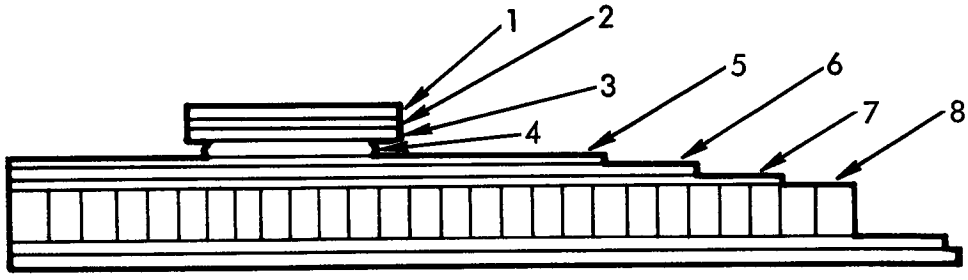
3) Identify failure and degradation mechanisms and the cause of failure, i.e., the number of accumulated cycles or the test temperature limits.

The starting point of such a thermal cycling program should be designs which successfully qualified in the aforementioned test programs.

3.2 Thermal Characteristics of the Module-to-Substrate Interface

Discussion in this section has been limited to consideration of the materials and attachment methods successfully utilized for Tiros, Relay, Nimbus, and Lunar Orbiter solar arrays and their applicability to the expected Voyager thermal environment (< -150 to $+ 60^{\circ}C$).

To date, adhesives have been successfully employed for attachment of both modules and shingles to substrates. A typical cross-section is shown in Figure G-7.



(1) Cover slip

(2) Cover clip/silicon cell adhesive. Epocast 15E, RTV-602, or Sylgard 182; 0.0005 to 0.0025 in. thick

(3) Solar cell

(4) Module/substrate adhesive, FM-97, RTV-60, or a blend of RTV-560 and RTV-580; 0.009 to 0.015 in. thick

(5) Dielectric coating, SMP 62/63 or glass cloth impregnated with SMP 62/63; 0.003 in thick

(6) Aluminum alloy skins, 0.003 to 0.005 in

(7) Skins/core film adhesive, FM-1000; 0.025, 0.040, or 0.060 lb/ft^2

(8) Aluminum alloy honeycomb, 0.001 in. web thickness.

Figure G-7. Cross-Section of the Module-to-Substrate Interface

Unlike the arrays built in the past, the Voyager must survive eclipse temperatures which will cause even the best qualified cover slip and module adhesives to undergo a transition to a hardened glassy) state.

Arrays which have been required to survive temperatures below -70°C have generally employed either a methyl (RTV-60) or methyl-phenyl siloxane (RTV-560 made thixotropic with the addition of RTV-580) for attachment of solar cell modules to substrates; the former was used for the Nimbus platforms and the latter to meet the lower temperature requirement of the Lunar Orbiter platforms (-120°C).

Undesirably large coefficients of expansion are associated with the silicone rubber family of adhesives (Figure G-8); however, their excellent retention of flexibility over an extremely wide temperature range, low modulus of elasticity, and room tempetature curing capability make them highly desirable. A multilayered, experimental thermal stress analysis* has shown almost complete isolation between the module and substrate at temperatures ranging from 90 through -60°C.

The more recently developed methyl-phenyl group extends the glassy transition point to approximately -120°C. Figures G-9 through G-13 illustrate this transition for RTV-560. Below -140°C, the adhesive lacks flexibility and has a hardness comparable to a rigid epoxy system. Operation in this low temperature regime will probably require extensive testing, and possibly modification or redesign of the basic cross-section. For example, one of the alternate methods would be to reduce the adhesive area in contact with the substrate and cell by using small multipad adhesive attachments, rather than a large single pad. To predict what temperature failures in either the solar module or adhesive occur is an extremely complicated problem. Not only must a five-layer model be analyzed, but two adhesive layers have visco-elastic properties which are not defined.

*RCA Comsat Phase I Final Report, M. E. No. 81, AED C-2276, Section II, Thermal Stress Analysis of Solar Cell/Adhesive/Quartz Composite, March 1965

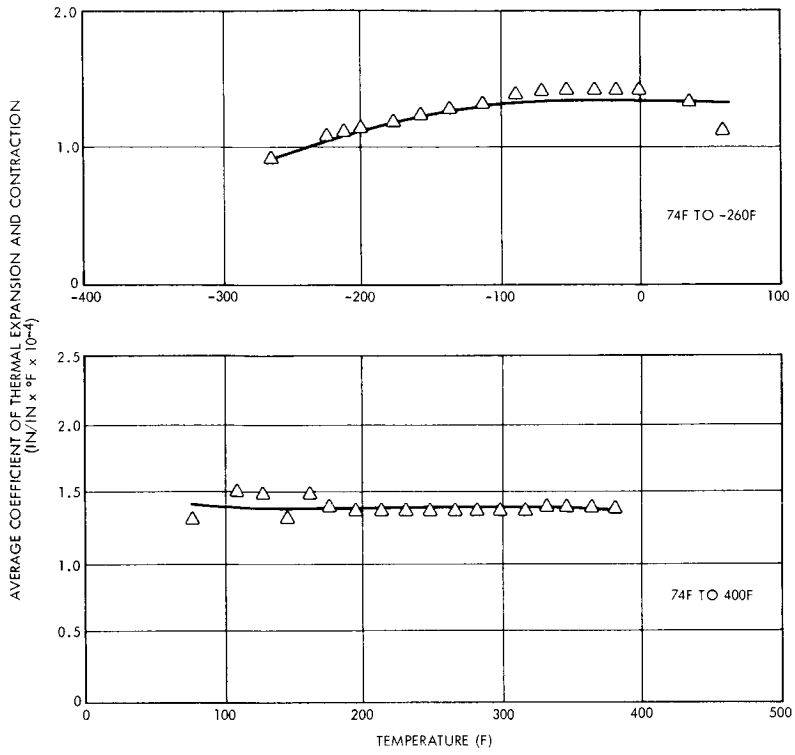


Figure G-8. Average Coefficients of Linear Thermal Expansion and Contraction for RTV Compounds

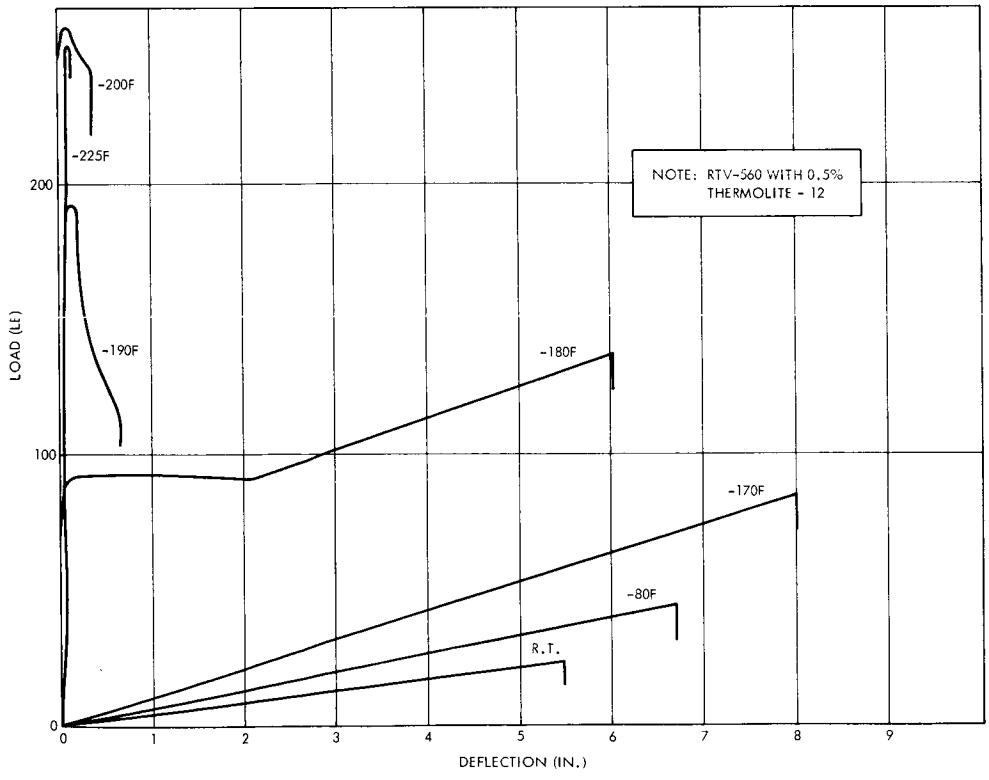


Figure G-9 Typical Load-Deflection Recorded by Deflectometer

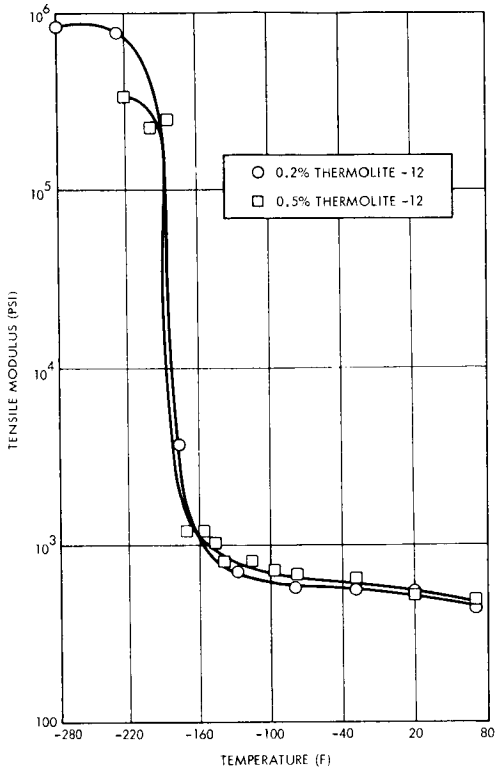


Figure G-10. Tensile Modulus versus Temperatures

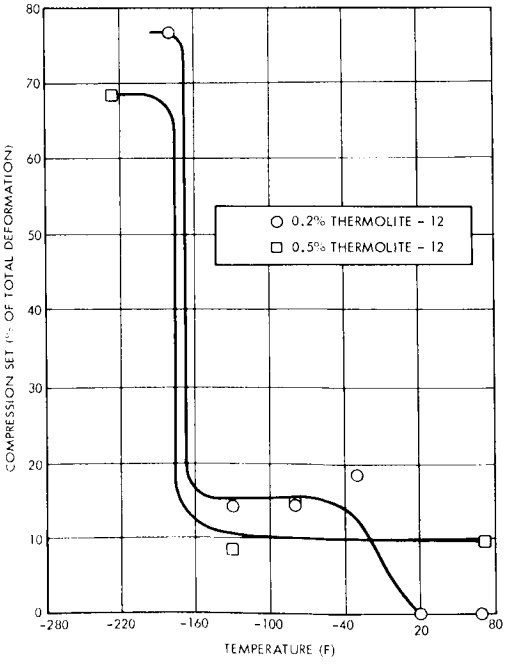


Figure G-11. Compression Set (Per Cent of Deformation versus Temperature

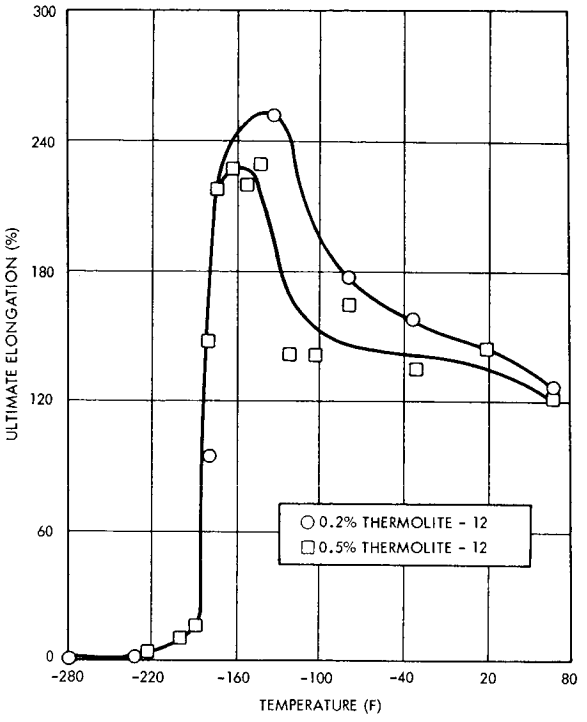


Figure G-12. Ultimate Elongation versus Temperature

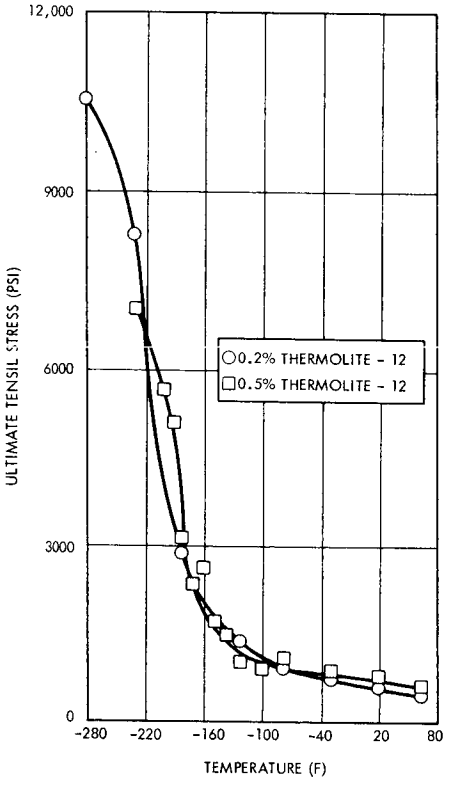


Figure G-13. Ultimate Tensile Stress versus Temperature

It has been reported* that RTV-731 has been utilized for the bonding of solar shingles to substrates and tested at -187°C; however, the array was required to survive only a few cycles. RTV-731 may have to be vacuum cleaned for several days at relatively high temperatures to remove sublimable products. Based on only limited test data, it may not possess the low temperature capability of the methyl-phenyl family.

3.3 Diode Packaging

The blocking diode selected for the solar cell panels is a silicon power rectifier, 12A - Type JAN IN1202. It is a rugged stud mounted semiconductor qualified for space application. Two diodes will be used for each 116 series string of cell modules, mounted on a dielectric angle support to which a parallel electrical connection using copper foil has been bonded to the dielectric. Although the military specification rating indicates a minimum operating temperature of -65°C, tests at -120°C have not uncovered any failures.

3.4 Honeycomb Substrate Adhesive

There is general agreement** that the nylon filled, epoxy-polyamine and polyurethane adhesives are the best for cryogenic temperatures; however, both show gross deterioration of mechanical strength (e.g. tensile shear strengths < 1000 psi) at temperatures above 125°F. FM-1000 has superior room temperature properties and a tensile shear strength in excess of 2,000 psi even after long term aging and testing at 250°F. FM-1000 is a well known thermosetting, nylon-epoxy adhesive manufactured by the Bloomingdale Rubber Company. It has been successfully used for Relay and Nimbus, and has been chosen for Lunar

---

*Surveyor Progress Report issued by the Jet Propulsion Laboratory for the period April 1, 1963 through May 31, 1963.

**"Evaluation of Structural Adhesives for Potential Cryogenic Usage," Paper presented by Luther Roseland Douglas Aircraft Company, May 1964,

"Adhesives for Cryogenic Application," Paper presented by B Smith and E. Susman, Narmco Research and Development Division.

Orbiter after an extensive materials evaluation program. The latter test program has shown no deterioration of the bond after 50 thermal cycles between 120 and -120°C.

Honeycomb samples constructed of 0.010 inch titanium facings, aluminum core with 0.004 inch web, and adhesive HT-424 (a phenolic epoxy on a glass cloth carrier), have been successfully fabricated and tested at extremely low temperatures. There was no deterioration of the substrates following 25 thermal cycles from liquid argon at -185 to + 40°C.

A back-up material proposed is AF-300, a nitrile rubber-phenolic epoxy manufactured by Minnesota Mining and Manufacturing Company. This adhesive is reported superior to the FM-1000 at cryogenic temperatures as an adhesive but its mechanical properties are inferior to FM-1000 in the range of 120 through -120°C.

3.5 Cover Glass Adhesive

Sylgard 182, RTV-602, and Furane Epocast 253 (formerly 15E) were used to bond covers on solar cell modules mounted on qualification boards. The boards were subjected to 600 thermal vacuum cycles between +120 and -120°C.

The tests showed that the Furane 15E is more likely to cause cracked cover glass than RTV 602. The Sylgard 182 produced no cracked cover glass, but the smaller sample size precluded an exact comparison to the other adhesives. The performance of the Sylgard 182 and RTV 602 should be similar, however, because both belong to the same family of methyl siloxanes, have practically the same coefficient of expansion, and the same crystallization temperatures (-90°C) (See Figure G-14).

The occurance of failures using Sylgard 182 will be largely dependent on the cover glass thickness and the extent of the low temperature requirement because at -126°C Sylgard becomes a glass (Figure G-14). This is an area which is likely to require extensive developmental testing.

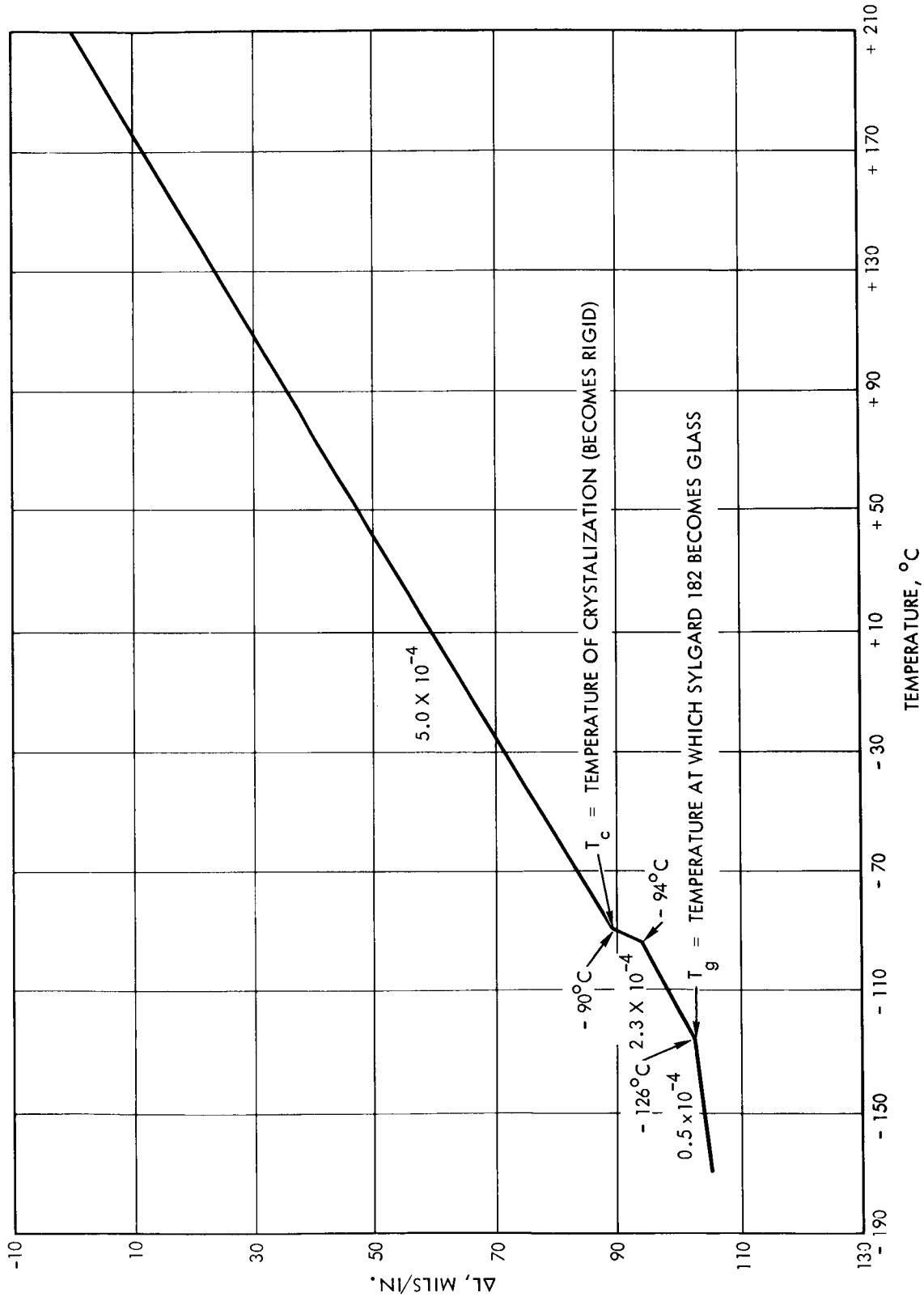


Figure G-14. Coefficient of Linear Expansion, Sylgard 182

APPENDIX J

BIPROPELLANT AND MONOPROPELLANT FEED SYSTEM CONFIGURATION STUDIES

1. BIPROPELLANT FEED SUBSYSTEM

1.1 Summary

In the study of the bipropellant supply for the Voyager spacecraft, as used in Configuration B, the supply system was subdivided, by function, into five sections: 1) pressurant supply (for pressurization of the propellant tanks), 2) pressurant control (for shutoff of the pressurization between engine firings), 3) pressure regulation, 4) pressurant distribution, and 5) propellant tankage/expulsion. Each of these subdivisions was then studied to determine the possible design alternatives, considering interactions with the other elements. These alternatives were then analyzed to determine their application to the Voyager requirements. Several design alternatives were thus eliminated from detailed consideration. From the alternatives a simplified baseline configuration was selected, and the other design approaches in each of the five functional sections were traded with the baseline on the basis of weight, reliability, and development status (for Voyager conditions). The resulting augmented configuration was then studied to assure that possible interactions between the selected functional-section designs did not adversely influence the result. The reliability studies indicate small differences between the various supply system combinations with reliability figures generally exceeding 0.99. This, in combination with small corresponding weight differences, resulted in a configuration selection based primarily on component development and experience status for Voyager conditions.

The selected bipropellant supply system utilizes ambient temperature, helium gas as the pressurant, parallel-series quadruple solenoid valves as the pressurant control, a regulator backed up by a pressure-switch-controlled normally open solenoid valve for pressure regulation, rubber bladder expulsion for the fuel, and a start-tank type of bellows expulsion for the oxidizer.

1.2 Alternate Designs, Description, and Tradeoffs

Several design approaches to pressurization supply and control and to propellant expulsion and feed were studied. A schematic diagram of the baseline design is shown in Figure J-1. As indicated in the figure, the design was divided, by function, into four sections: (F) pressurant supply, (G) pressurant control, (H) pressure regulation, and (J) pressurant distribution. The alternate approaches for each section are shown in Figures J-2 through J-10.

1.2.1 Gross Tradeoffs and Configuration Selection

Several approaches were eliminated prior to selection of a baseline configuration and are not shown in the Figures. Each had at least one inherent disqualifying limitation.

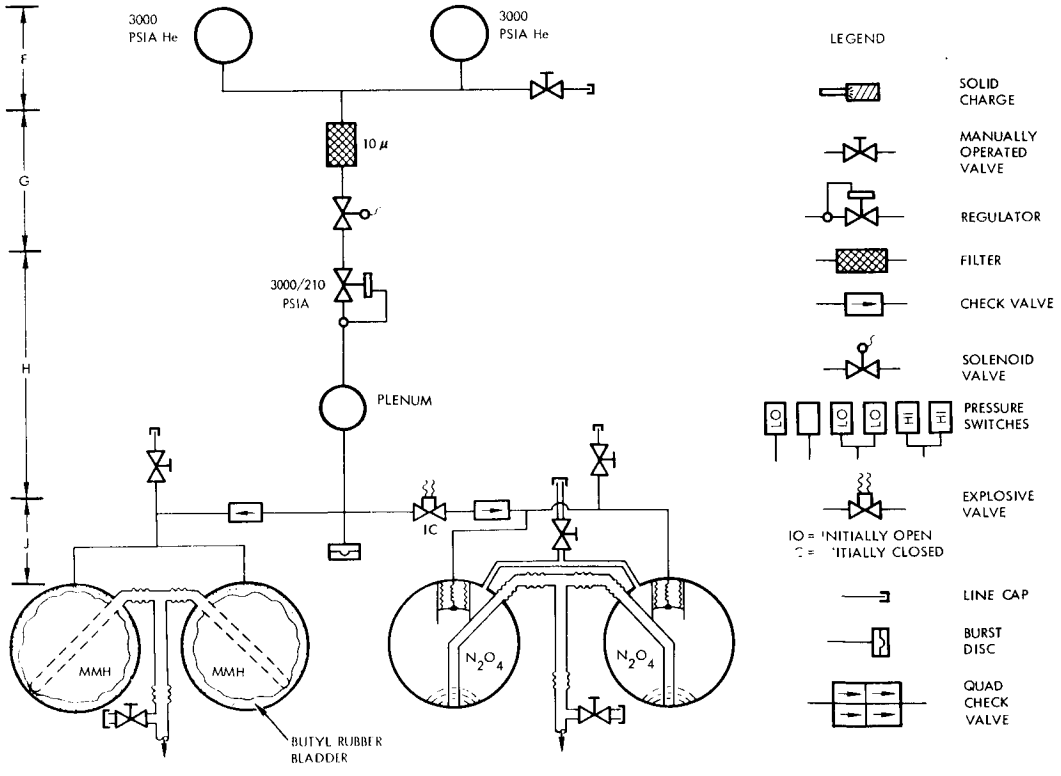


Figure J-1. Propellant Baseline Configuration

a. Pressurant Supply

Helium and nitrogen ambient temperature gases were studied as a pressurant supply. Helium gas was selected over nitrogen due to a weight saving of 24 pounds. Although the helium is more difficult to contain (to prevent leakage), investigation showed (see Section 1.2.1a) that the total helium leakage would be negligible. Independent fuel and oxidizer pressurization method was not selected for several reasons. Weight and space requirements would increase considerably. Regulator operating-pressure tolerances would cause a variation in engine-mixture ratio and thus increase the unusable propellants. The reliability would decrease unless the two pressurant sources had an interconnect which could be opened in the event of a failure on either side. If the interconnect were used, then the only advantage obtained from complete separation of the fuel and oxidizer pressurization source, elimination of any possibility of the two propellant vapors mixing, would be violated.

One possible weight saving (approximately 10.5 pounds) investigated was the use of an umbilical and a quick disconnect to pressurize the pressurant bottle immediately prior to launch. This would remove the hazard-to-personnel restriction placed on the pressure containers. This approach was rejected because the use of a quick disconnect is less desirable than hand-closed valves, from a reliability aspect. Hand valves can also be leak checked after pressurization.

b. Oxidizer Tankage/Expulsion

The candidate expulsion techniques for the oxidizer include: collapsing teflon bladders, reversing metal diaphragms, complete expulsion by collapsing metal bellows, and partial start-tank type expulsion by small expanding metal bellows inside spherical tanks. Orientation of both propellants using ullage rockets or surface tension devices was also considered.

Spherical tankage with teflon bladder expulsion saves 22 pounds over the selected tankage configuration, yielding the lowest weight of any tankage system considered. Teflon is compatible with

N_2O_4, but it is permeable to N_2O_4 vapors. This adverse characteristic must be overcome with upstream shutoff valving which adds to the complexity of the over-all system and eliminates a small part (about 2 pounds) of the weight saving. In addition, the teflon is permeable to the helium used as a pressurant. This could result in helium gas becoming mixed with the propellant. Attempts are being made to construct bladders made with metal teflon laminates, but these attempts are in an early stage of development. The confidence that such a method would be ready in time for Voyager is low, especially if recycling capability is desired. Therefore, the teflon bladder is considered unsatisfactory for long term storage of N_2O_4.

Spherical tankage without expulsion, utilizing small solid-rocket motors for ullaging thrust is also lighter than the selected design. However, to give confidence in propellant settling, the firing duration and thrust required from the ullage rockets yields a total impulse representing several feet per second. This total impulse, in combination with the minimum impulse bit from the bipropellant engine, exceeds the minimum commandable velocity set forth in the Mission Specification.

Cylindrical tankage with stainless steel bellows positive expulsion gives the highest confidence level of any tankage system considered. This approach will be used on the Saturn S-IVB/1B auxiliary propulsion system (APS) and has been successful in operational testing. However, it weighs 120 pounds more than the selected bipropellant design. This weight increase is sufficient to render the performance of this design alternate inferior to any other considered.

The conclusion reached after investigation into compatible bladder materials (teflon compounds) was that only all-metal tankage would meet the operational requirements for the Voyager mission. Reversing metal diaphragms were therefore considered for expulsion. As with the teflon-metal laminates, metal diaphragms are at a comparatively early stage in their development and are not recycleable. It is desirable that the design be recycleable, both for checkout and for ground tests. The confidence that reliable recycleable reversing metal diaphragms will be available for Voyager is low. The metal diaphragm

would save little if any weight over the selected partial bellows expulsion. Finally, the possibility that the positive-expulsion bellows could be manufactured of titanium was considered. Investigation showed that the basic advantage of titanium over stainless steel, namely lower density, is more than offset by its drawbacks, which are the reduced modulus of elasticity, lower experience level, and possible impact sensitivity with N_2O_4. Present experience indicates that a titanium bellows has less than 10 per cent of the cycle life of an equivalent stainless steel bellows.

c. Pressurant Control and Regulation

A pressurant control and regulation method that is simpler than the baseline system was considered. This method utilizes a pressure regulator to perform both shutoff and pressure regulation functions, however, and it was eliminated because of lack of confidence that a gas-pressure regulator could reliably meet shutoff sealing requirements with helium gas after intermittent operation over a period of 9 months. Also, the propellant tanks become pressurized whenever there is pressurant gas on board. Thus, the propellant tanks would have to meet the hazard-to-personnel requirements for pressure vessels, with a resultant increase in subsystem dry weight.

In performing the tradeoffs leading to selection of an augmented configuration, careful consideration was given to the prevention of catastrophic malfunction of the bipropellant engine due to propellant supply subsystem malfunction. One method of increasing reliability through redundancy of the pressurant control squib valve arrangement is to add an extra bank of squib valves. Then if one of the banks fails to operate, the required number of starts would still be available. However, this method cannot be used with a bipropellant engine. After the first start, the propellant tanks are pressurized and any initially closed valve failure could result in catastrophic failure to the engine as it would be difficult to detect the control valve failure in time to shut off the engine. If the control valve failed to open, the propellant supply would operate in a blowdown mode off the ullage volume, and with a

small ullage volume the pressure would drop rapidly. A bipropellant engine could go unstable to the point of destruction. Backup ground control signals cannot be employed with the bipropellant system to correct for failures to provide the propellants at safe operating pressures.

1.2.2 Evaluation and Tradeoff

a. Pressurant Supply

The alternate shown in Figure J-2 utilizes the heat generated by the firing of a small solid charge within each pressurant bottle to achieve significantly more complete use of the gas in the pressurant storage spheres. When the bottle pressure decays to some predetermined level at a time well into the retrofire sequence, the solid charge would be fired by a signal from the pressure switches to raise the gas remaining in the sphere back to the initial pressure of 3000 psi. Thus, a greater percentage of the mass of the gas can be blown down from the sphere. This allows use of less total gas than the ambient baseline configuration, resulting in a weight decrease of 62.6 pounds. This decrease in weight must be purchased at the cost of decreased system reliability, higher development risk, longer development time, and increased system complexity. The proper operation of the pressure switches, correct sizing of the charge, detailed analysis of heat transfer and expansion characteristics of gas and storage sphere, protection against inadvertent ignition of the charge, all become critical determinants for the achievement of mission success. If propulsion system performance without the alternate of J-2 were marginal due to excess weight, it would be a good approach. None of the aforementioned problems is prohibitively difficult. However, since propulsion system performance is not marginal, these impediments to the development of a reliable propulsion subsystem were not considered justified.

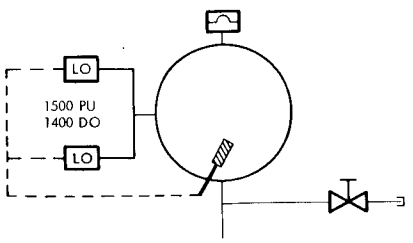


Figure J-2

Solid Gas Generator
Pressurization Alternate

b. Pressurant Control

The alternate shown in Figure J-3 replaces the single solenoid valve used in the baseline with individual banks of explosive squib valves for each start. Flow is initiated by opening the initially closed valve and stopped by firing the initially open valve. This agrees with the Mariner 4 approach, except that a five-start capability has replaced the two-start Mariner 4 system (four starts for midcourse correction and one for orbit injection). The squib valves possess superior sealing qualities because of their intimate metal contact. This makes them immune to common valve problems such as seat erosion, seal cold flow or deformation, wear, and contamination. The squib valves do not require onboard filtration of their working media. Final shutoff of the pressure sphere by a squib valve is positive and complete for practically an unlimited time. This feature is desirable from the standpoint of orbit duration without planet contamination. Gas would not bleed down from the pressurant tank, over-pressurize the propellant tank, and burst it. The weight penalty for this change (0.5 pound) is minimal. However, the reliability and flexibility, are considerably less than the selected configuration.

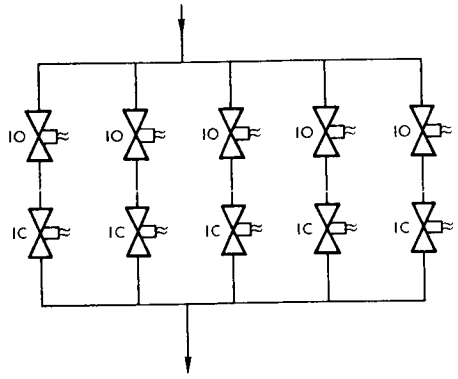


Figure J-3

Conventional Explosive Pressurant Control Alternate

Alternate of Figure J-4 represents a variation of alternate J-3 and adds complete redundancy to the squib valve banks for the fail-to-fire mode of failure only. This scheme does not offer protection against the premature-firing mode of failure. Based on the assumption that a stray signal powerful enough to fire any of the squib valves could fire others in the immediate vicinity, there is no point in achieving

theoretical redundancy in order to protect against the premature firing-mode of failure. For this reason, and because the valves are shielded against radio frequency interference, no design schemes for this type of redundancy are presented. The increase in reliability associated with alternate J-4 over the J-3 is probably not justified when the added complexity is taken into account the weight penalty for this change is 2.5 pounds.

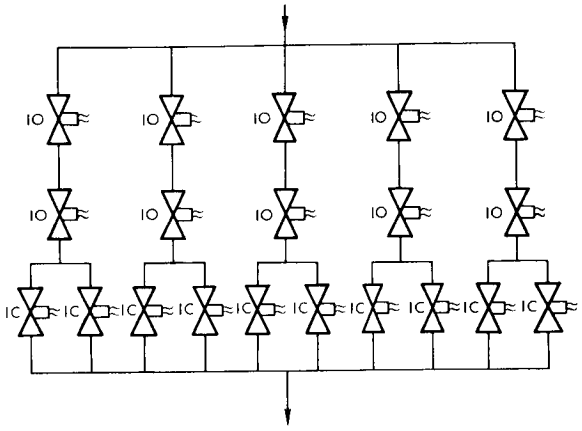


Figure J-4

Redundant Explosive Valve Pressurant Control Alternate

The alternate shown in Figure J-5 adds three normally closed solenoid valves to the baseline valve to achieve redundancy by a series-parallel quad valve arrangement. This method is attractive because of its high reliability and flexibility. It offers the capability for multiple orbit trims until propellant is exhausted. The ready availability and long experience record of 1/4-inch helium solenoid valves implies low development risk. These advantages (reliability, complete redundancy, and flexibility) were considered to justify the increased complexity and added weight (3.3 pounds). Therefore, this design was selected for the augmented configuration.

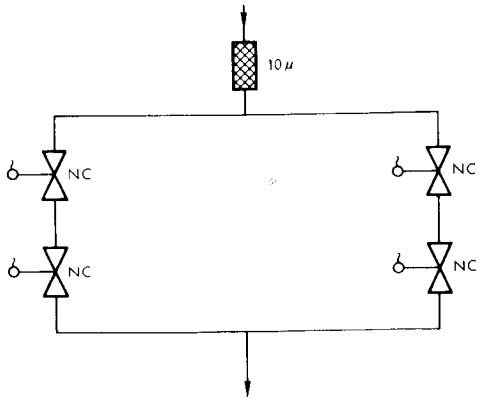


Figure J-5

Quadrant Solenoid Valve Pressurant Control Alternate

c. Pressure Regulation

The alternate shown in Figure J-6 replaces the single pressure regulator with a quadredundant parallel-series arrangement of the four regulators. This arrangement gives protection against fail-open, fail-closed, or excessive-leakage modes of failure for any single regulator. In addition, this arrangement protects against two failures caused by excessive leakage or fail-open for any combination except two regulators in the same bank. The number beside each regulator indicates its nominal outlet pressure. Each regulator is assumed to have an operating tolerance of ± 10 psi, which results in a regulator group operating band of ± 30 psi. The narrow tolerance of ± 10 psi is somewhat optimistic. A more conservative estimate of ± 15 psi would raise the possible operating band of the regulator group from ± 30 psi to a less desirable ± 45 psi.

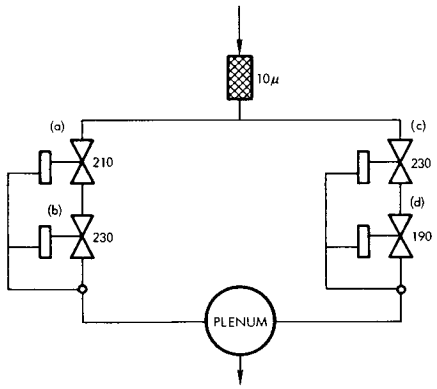


Figure J-6

Quadrant Pressure Regulator Alternate

Under normal operating conditions of 210 psia, unit (a) provides the pressure regulation. Unit (b) remains open, unit (d) closes as the tank pressure reaches 190 psia. Failure of unit (a) to open shifts the regulation to unit (d) which maintains tank pressure at 190 psia. Failure of (a) to close activates unit (b), which maintains tank pressure at 230 psia. This method has been developed for Apollo but not flight proven, or tested for Voyager conditions which require intermittent operation over a several-month period. This arrangement is the most complex and heaviest of any configuration studied. Although the calculated reliability is high, the above drawbacks caused its elimination in favor of the selected design. The weight penalty for this system is 7.9 pounds.

The alternate of Figure J-7 adds a normally open, pressure-switch-actuated, solenoid valve to the baseline single regulator. If the regulator outlet pressure exceeds the upper tolerance, a pressure switch picks up and initiates closure of the solenoid valve. As the pressure then drops below the drop-out setting of the switch, the valve closure circuit is opened, causing it to reopen. A signal initiated through both switches is required to close the solenoid valve; either switch dropping out will allow the valve to open. Existing Mariner technology has proven the reliability of the single regulator system of pressure control. However, the single regulator provides no safe-guard against possible excessive seat leakage, which industry experience has shown to be the most likely mode of failure.

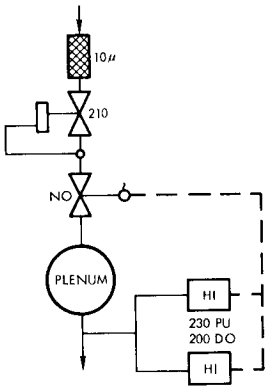


Figure J-7

Series Pneumatic Pressure

Addition of the normally-open solenoid valve protects against this failure mode, and also against the fail-open mode. The low probability that the normally open solenoid valve would fail in the closed position imposes little degradation of system reliability for this mode of failure. The fail-closed mode is considered least likely of all failure modes of the regulator. The pressure switches which actuate the valve are protected against their most likely mode of failure, that is, failure to drop out. Either switch dropping out interrupts the signal, allowing the solenoid valve to open. Both must pick up to close the valve, thereby protecting against inadvertent closure. This technique proved successful on the Saturn S-IV vehicle, and is being utilized on the Saturn S-IVB vehicle and auxiliary propulsion system.

The alternate of J-7 was selected because it is a proven technique for increasing reliability with minimal penalty in weight and complexity. The weight increase over the baseline configuration is 1.9 pounds. The small calculated reliability increase is felt to be conservative as a result of inadequate data. The data is historical and is not divided according to regulator design type. The alternate of J-7 was designed to take advantage of a specific regulator type whose prime mode of failure is in the open position. Also, the reliability calculations did not differentiate between failure in the "pick up" versus the "drop out" positions of the pressure switches. Experience indicates that failure to "drop out" is the prime failure mode for the specific pressure switch design.

The alternate of Figure J-8 adds a second bank, incorporating a regulator and a normally-closed solenoid valve, to alternate of J-7. This system gives complete redundancy for any mode of failure of a single component. Should the primary regulator, in the right bank, fail to open, the plenum pressure would decay until the low-pressure switch is actuated. The switch signals the normally closed solenoid valve to open and the backup regulator goes into operation. In the event of a primary regulator failure-to-close, the resultant pressure rise in the plenum would activate the high-pressure switch which signals the normally open solenoid valve to close. The subsequent decay in plenum pressure activates the backup system as previously described. Thus, a failure of the primary regulator in either open or closed mode causes the flow to shift to the parallel backup system. A similar system is used on the auxiliary propulsion system of the S-IVB vehicle. The increase in calculated reliability it provides over the selected configuration cannot be justified by its increased complexity. The weight increase of this system over the baseline is 5.5 pounds.

Possible combinations of control valve and pressure regulation alternates were compared. None of the combinations resulted in a more nearly optimum system than the alternates already selected on an individual basis.

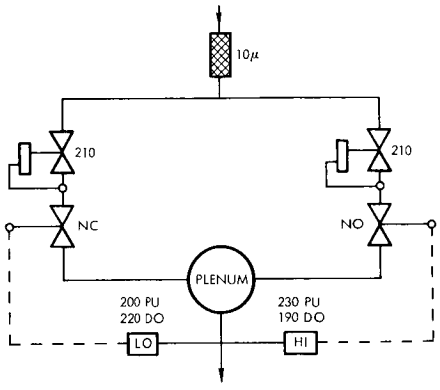


Figure J-8

Parallel Redundant Series Pneumatic Pressure Regulator

d. Pressurant Distribution

The alternate shown in Figure J-9 replaces the baseline check valves with quadredundant check valves. Thus, in the event of a failure of the initially-open explosive-squib valve, a backup seal is provided to prevent N_2O_4 entry into the pressurization system after retrofire. However, no existing check valve will prevent leakage of N_2O_4 vapors past its seal indefinitely. Thus, the best that can be expected of a quad-check valve is a time delay as far as the eventual passage of N_2O_4 vapors. Once past the check valves, and assuming a squib valve malfunction (which is improbable), the N_2O_4 vapors have an open path to the butyl-rubber bladder and the MMH residual. Also, the inherent reliability of the explosive-squib valve is higher than the quad-check valve from a leakage standpoint and this alternate does not appear worthwhile. The weight increase over baseline is 3.2 pounds.

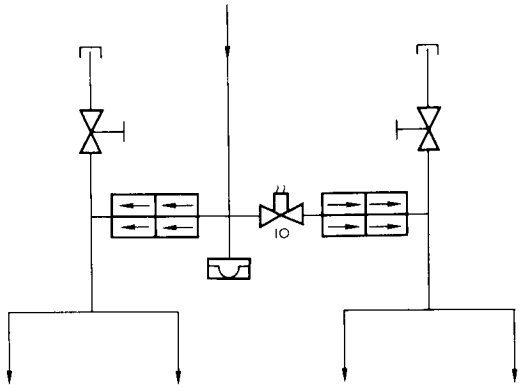


Figure J-9

Quadredundant Check Valve Propulsion Task Isolation Alternate

The alternate of Figure J-10 adds a second initially-open explosive-squib valve in series with the baseline-squib valve. This

gives protection against a fail-to-fire failure mode. However, the reliability of the single valve is high enough so that this addition is not required. The weight increase of this change is 0.5 pound.

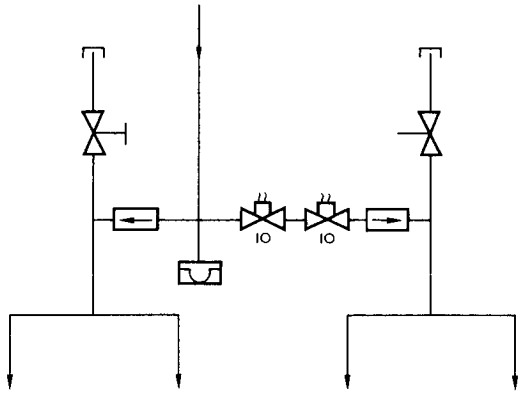


Figure J-10

Series Explosive Valve
Propulsion Tank Isolation Alternate

1.2.3 Reliability and Weight Summary

Table J-1 presents the detailed weight increments for the various alternates that were considered. These figures are plotted in Figure J-11 to show the reliability improvements as a function of weight.

Table J-1. Changes in Weight and Reliability Resulting From Alterations of Baseline Configuration (B-2)

Figure J-11 Reference Numbers	Alternate	Bipropellant Feed System Weight Change (lb)
	Figure J-2	-62.6
	Figure J-3	+1.0
	Figure J-4	+3.5
	Figure J-5	+3.3
	Figure J-6	+7.9
	Figure J-7	+1.9
	Figure J-8	+5.5
	Figure J-9	+3.2
	Figure J-10	+0.2
1	Figures J-3 and J-6	+8.9
2	Figures J-3 and J-7	+2.9
3	Figures J-3 and J-8	+6.5
4	Figures J-4 and J-6	+11.4
5	Figures J-4 and J-7	+5.4
6	Figures J-4 and J-8	+9.0
7	Figures J-5 and J-6	+11.2
8	Figures J-5 and J-7	+5.2
9	Figures J-5 and J-8	+8.8

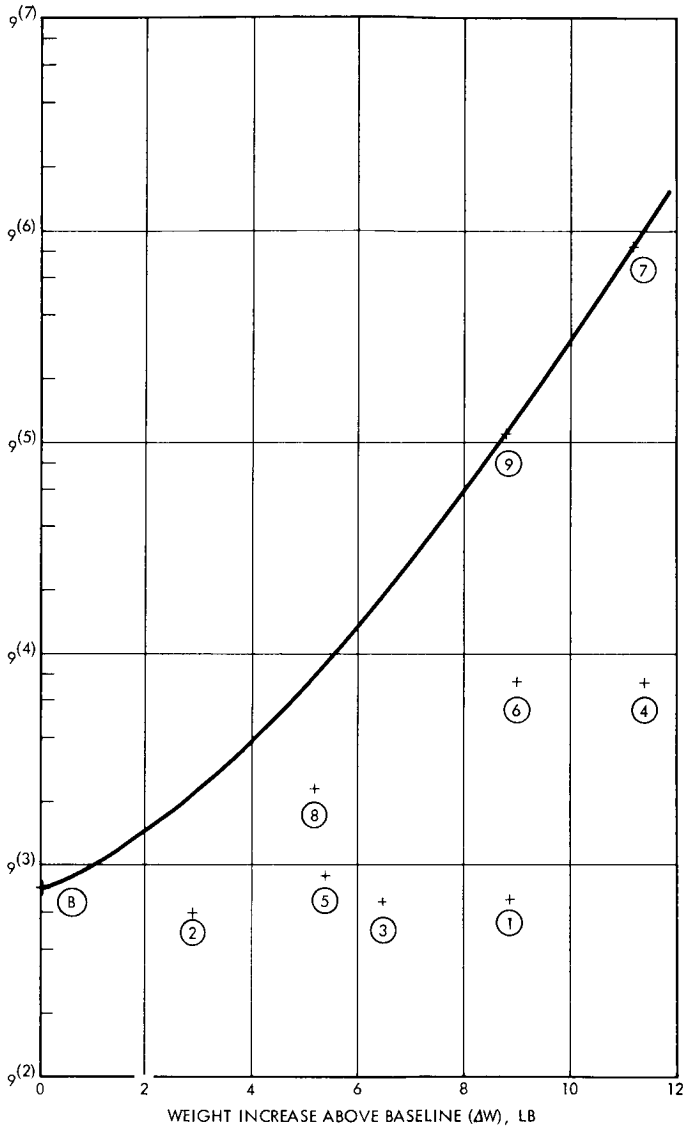


Figure J-11. Reliability Improvement as a Function of Weight

1.3 Bipropellant Feed System Design

The selected bipropellant feed system for vehicle Configuration B is shown in Figure J-12. The weight associated with this system is itemized in Section VII of Volume 5. The performance and design of the system is described below.

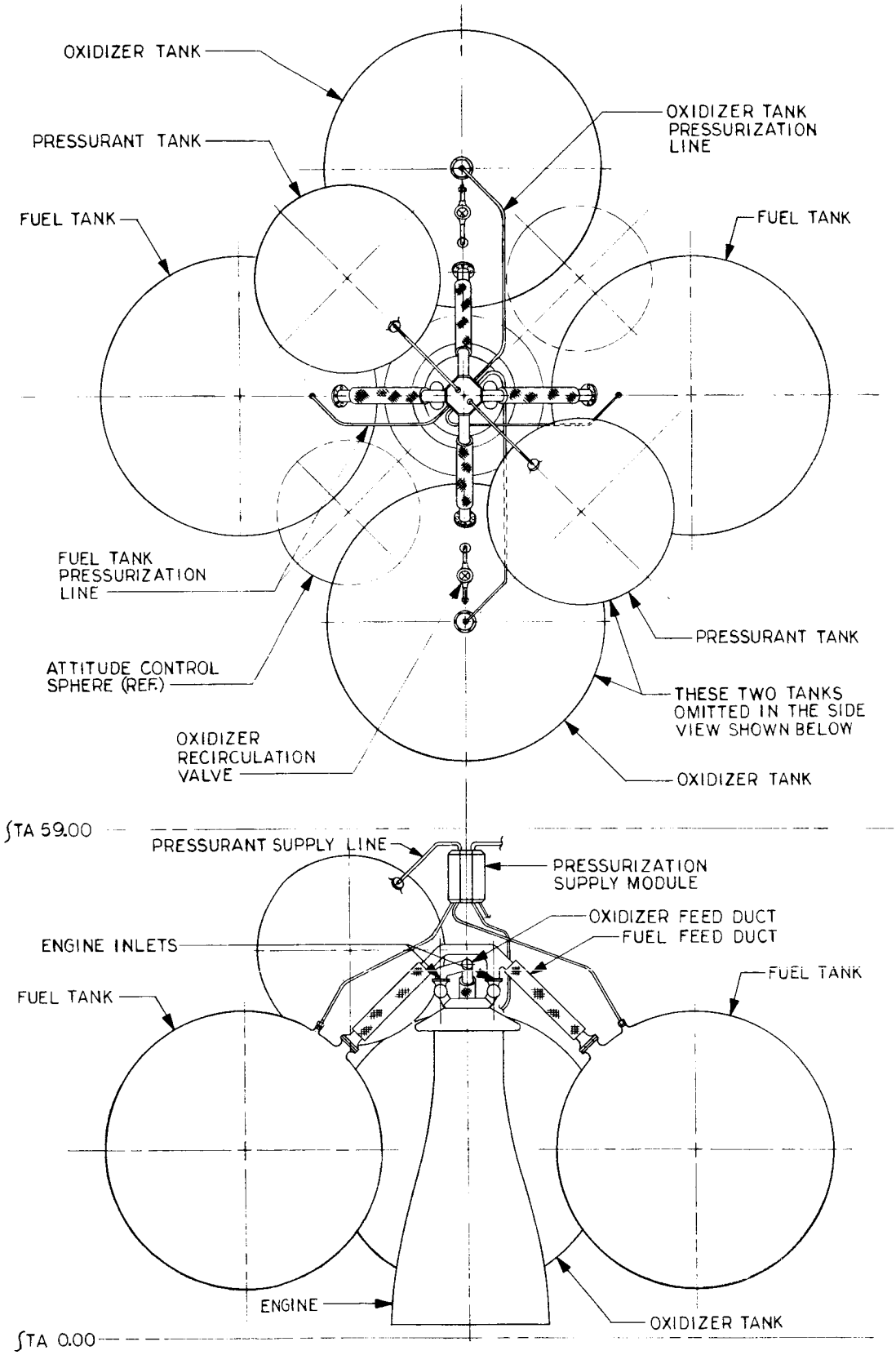


Figure J-12. Bipropellant Fuel System Layout

1.3.1 Sizing Analysis

a. Pressurant Supply

Helium stored at 3000 psia was selected to pressurize the fuel and oxidizer tanks. The amount of helium required to complete propellant expulsion was determined from an equation relating tank volume and pressure with pressurant properties and storage conditions (see Appendix C). A gas expansion process midway between adiabatic and isothermal was assumed based on the transfer of sensible heat from the storage bottles, lines and components, and propellant tanks. The spacecraft thermal control subsystem will restore the system to nominal operating temperature between midcourse maneuvers and the relatively low pressurant flow rate during operation aids in the efficient extraction of this heat. Conversion of thermal energy to perform expulsion work and pressurant residuals were accounted for in the calculations. A propellant tank pressure of 210 psia was assumed, allowing 10 psi for flow losses and pressure drop across the positive displacement device.

Based on a propellant loading of 2900 pounds at an oxidizer/fuel ratio of 1.65 (equal volume), a required helium weight of 9.3 pounds was determined. A helium leakage rate analysis was conducted to determine the required pressurant reserve. To establish a worst-case model, a leakage rate of 1×10^{-4} standard cubic cm, (scc)/min was assumed for each of 33 possible leak points at operating pressure. This rate corresponds to the maximum capability of the simplest leak detection technique, bubble fluid. The analysis revealed a leakage rate on the order of 6×10^{-4} lb/year. A 0.7 pound weight allocation for leakage increases the total helium weight to 10 pounds and provides more than adequate reserve for leakage. Eight of the joints in the pressurization system are separable and use the NASA developed MC-type flared-tube fittings. These fittings are capable of holding leakage to 5×10^{-5} scc/min. The remainder of the joints will be sealed by in-place welding. Further reduction of helium leakage could be accomplished through inspection of the welded joints by mass spectrometer. Leakage from a properly welded joint can be held to less than 1×10^{-8} scc/min.

Two helium spheres, 20.50 inches in diameter, will contain the 10 pounds of helium at 3000 psia and 70°F. The bottle wall thickness was designed for 3300 psia in conjunction with the appropriate safety factors to allow for pressurant temperature rise to 110°F.

b. Pressurization Control

The helium flow rate requirements are relatively low and analysis shows that 1/4-inch pressure lines may be used without inducing excessive pressure loss. A system pressure drop of 28.3 psi between supply and tankage was calculated. Calculations are given in the Appendix C. The major advantage in using 1/4-inch line is the high development level of components of this size. Many fully qualified valves, filters, regulators, etc., are available as off-the-shelf items. The small weight advantage which could be obtained by going to a smaller diameter would be more than offset by the increased fabrication and development difficulties. The application of in-place welding techniques to the smaller lines would be more difficult and the possibility of crimping, kinking, and other types of handling damage would be increased. Based upon these considerations, the pressurization control system design was based on a nominal 1/4-inch line size.

A plenum chamber is placed downstream of the pressure regulator. Under normal operating conditions the plenum serves to damp out pressure surges which otherwise would cause the regulator to close immediately after opening. Rapid cycling of this nature, known as chatter, can damage the regulator. A plenum volume of 200 $in.^3$ was selected as sufficient volume to perform the damping function. More accurate analysis requires knowledge of the characteristics of the specific regulator chosen. The final volume will be selected after breadboard testing of the pressurization subsystem.

c. Propellant Tankage/Expulsion

The propellant mixture ratio of 1.65 to 1 was selected on the basis of equal volume tankage. The tank volumes were determined by the propellant volume at the maximum spacecraft temperature. A

temperature range of 40° to 90°F is to be maintained by the thermal control subsystem. Four spherical tanks, two oxidizer and two fuel, will contain the propellants. A sphere volume of 10.5 ft^3 (32.6-inch diameter) will provide an ullage volume of about 0.5 ft^3 per tank, which will serve as a pressurant plenum and will allow for additional propellant expansion should the temperature exceed 90°F.

Positive displacement of the oxidizer (N_2O_4) is provided throughout the midcourse maneuver operations and for sufficient duration at the beginning of orbit injection tc achieve full thrust, thus ensuring orientation of the propellants at the tank outlet. Oxidizer displacement is provided by an expanding-metal bellows mounted at the top of each oxidizer tank. The bellows are initially in a partially extended condition, to allow for propellant expansion due to temperature changes, and are internally pressurized for propellant expulsion. The total internal volume of the bellows in its fully expanded position is adequate to compensate for changes in oxidizer volume due to temperature changes, to provide positive expulsion for all midcourse maneuvers, for engine start, during retrofire sequence, and to provide for an ullage space.

Positive displacement expulsion of the oxidizer is terminated just prior to full bellows extension, at which time the pressurant force is applied directly to the propellant surface.

Positive displacement of the fuel (MMH) is provided for the entire mission duration by a butyl-rubber bladder which contains the fuel. The 0.5 ft^3 of ullage volume, in each tank, at 90°F, will be provided for by a clearance between tank wall and bladder. Elasticity of the rubber bladders allows for expansion and contraction of the fuel.

d. Propellant Feed Lines

Both fuel and oxidizer feed lines were established at a nominal 1.0 inch diameter. Calculations were made to determine the pressure loss due to line length, flow restrictions, such as bends and bellows joints, and start loss due to acceleration of the propellants.

Because of the juxtaposition of the engine and propellant tanks, the elevation of the engine inlet is approximately 3 feet above the tank outlet. The maximum resultant pressure loss, occurring at the end of retrothrust, is less than 1.0 psi due to the relatively low thrust-to-weight ratio. Maximum total pressure losses were determined to be 2.4 and 3.95 psi for the fuel and oxidizer feed lines, respectively.

1.3.2 Material Selection

a. Pressurant Supply

Annealed Ti-6Al-4V is used for the helium pressurant storage spheres, which will be pressurized in the presence of personnel. Tubing used in the pressurization subsystem is fabricated entirely from 6061-T6 aluminum to facilitate in-place welding techniques.

b. Pressurant Control and Regulation

All pressurization subsystem components, including the plenum chamber, are manufactured using 6061-T6 aluminum. Alloys other than 6061-T6 might be utilized for certain internal portions of the component wherever warranted by the specific design. Seals and seats would be teflon compounds throughout.

c. Propellant Tankage/Expulsion

Heat-treated Ti-6Al-4V is used for the four equal-volume propellant tanks. Pressurization of these tanks in the presence of personnel will not be allowed. The fuel tanks employ butyl-rubber expulsion bladders and 300-series stainless-steel internal fill-feed lines. The oxidizer tanks employ 321-series stainless-steel positive expulsion bellows and Ti-6Al-4V internal fill-feed lines.

d. Propellant Feed Lines

The propellant feed lines are fabricated from 300-series stainless steels. The convoluted flexible portion is 321 series, while the wire braid, flanges, elbows, etc., are made from stainless alloys within the 300 series. The seals utilized at the inlet and outlet of both the propellant feed ducts are manufactured from 1100-series aluminum alloy.

1.3.3 Components

In-place welding techniques are utilized for joining all pressurization components into a single module. The propulsion module is installed, and if required, removed or replaced as a unit.

The teflon compounds used for component seals and seats are contained entirely within the pressurization subsystem. No portion of any teflon seal or seat is subject to outgassing due to exposure to the hard vacuum of space. The elimination of relief valves from the flight pressurization subsystem removed the last component which might experience this difficulty. It is possible to design around this difficulty, but it is not required and would only reduce the confidence level in satisfactory operation of the first flight.

The system is designed to operate and perform all intended functions over a temperature range of 40° to 90°F. The pressurant spheres are designed to take the overpressure resulting from reduced gas density due to a temperature increase to 110°F subsequent to loading. Thus, the nominal working pressure is 3000 psi and the maximum 3300 psi.

Preliminary tank diameters selected for weight and strength calculations were 34 inches maximum, including ullage volume. Detailed propulsion tank volume requirements resulted in tank diameters less than 33 inches. Since the monopropellant-solid engine combination was selected as the favored approach, the weight and strength calculations were not repeated for the smaller diameter. A reduction of approximately 3 per cent in wall thickness and tank weight would result from the use of the smaller diameter.

a. Pressurization Supply

The pressurant gas is stored in two spherical high-pressure vessels. Loading with helium gas is accomplished through a manually operated fill valve of the type used on Mariner 4. Immediately upstream of this valve is the OSE-spacecraft interface, consisting of a simple pneumatic tubing connection which is separated, capped, and sealed subsequent to loading and closing of the manual fill valve.

The remainder of the pressurization supply subsystem consists of a 10μ filter and four solenoid valves. The filter prevents impingement and subsequent imbedding on the solenoid valve seats of particles large enough to cause seat damage. The solenoid valves are of the normally-closed type arranged in series-parallel combination.

b. Pressurization Control

The pressurization control subsystem consists of a preset pressure regulator, a solenoid valve, two pressure switches, and a plenum chamber. The choice of regulator design is based on selection of the failed-closed condition as the least likely mode of failure. The upstream quad-solenoid valves provide a backup for an excessive seat-leakage mode of failure in the regulator. This is the most likely mode of regulator failure. Unless combined with the complete failure of at least one more pressurization system component, this mode of failure does not affect system performance. The solenoid valve, located downstream of the regulator, is of the normally open type. Thus, the least likely mode of failure of the solenoid valve will be failed-closed. The solenoid valve is controlled by the two pressure switches located at the outlet of the plenum chamber. Settings of the switches are the same for both: 5 psi above the maximum normal regulator outlet pressure. Both switches are required to pickup in order to actuate the solenoid valve closed. Either switch dropping-out would interrupt the signal, allowing the valve to open. This arrangement protects against the failure of a pressure switch to dropout. Although failure to dropout is an infrequent, random type of failure, it is the most likely mode of failure. In the case of a failed-open regulator, the solenoid-plenum chamber-pressure switch combination operates in a cycling or bang-bang mode, thus performing as a backup regulator. The plenum chamber and ullage volume is large enough to minimize the number of close-open-close cycles experience by the valve. The plenum chamber also prevents regulator chatter and the possible premature blowout of the burst disc due to pressure surges.

c. Pressurization Distribution

The pressurization distribution subsystem consists of a flow divider and burst disc immediately downstream of the plenum chamber, an explosive squib valve, check valve, and a manually operated valve in the line leading to the N_2O_4 tanks. It also includes a check valve and manually operated valve in the line leading to the MMH tanks. Pressurization gas flow is divided once more immediately downstream of each check valve to pressurize each of the four tanks. The explosive squib valve is of the initially-open type. It is actuated to the closed position at the completion of system operational requirements to ensure isolation of the residual N_2O_4 vapors and liquid. The squibs used to fire the explosive valves are of the dual-bridgewire design. The check valves serve to prevent propellant mixing in the event of bladder leak in the fuel tanks or a bellows leak in the oxidizer tanks.

With the bipropellant system, orbit trim capability, as discussed in Section d, exists only for a fixed relatively short period of time after the conclusion of the retrofire sequence. At this time the expulsion bellows no longer separates the ullage gas from the remaining propellants. This is because the check valve in the N_2O_4 pressurization system can only delay, but cannot prevent, passage of dangerous amounts of N_2O_4 vapor. Hence, the orbit trim must be performed prior to the time the explosive squib valve (which isolates the N_2O_4 residual) must be fired to ensure the safety of the orbiting spacecraft.

The gas side of the positive-expulsion unit must be pressure controlled during loading. The manually operated valves, located downstream of the check valves, lead to vent and relief valves supplied as part of the OSE. The lines leading to the OSE are capped and sealed subsequent to loading of the tanks and closing the manually operated valves. The burst disc installed directly downstream of the plenum chamber serves to prevent destruction of the entire spacecraft in the event of catastrophic propulsion system overpressurization.

d. Propellant Tankage/Expulsion

The two titanium fuel tanks provide complete positive expulsion for the MMH using a butyl-rubber bladder located in each tank. A perforated tube extends from the outlet and up the centerline of each tank. These tubes ensure that unsymmetrical collapse of the bladder will not result in interrupted propellant flow. This expulsion technique is well developed and entirely within the state of the art. The tanks are spherical in shape, with bosses for pressurization-line and feed-line connection. The two titanium oxidizer tanks include provision for partial positive expulsion for the N_2O_4. Expulsion is accomplished by the expansion of a cylindrical stainless steel positive expulsion bellows within the tank. The expansion is produced by helium gas furnished to the internal volume of the bellows by the pressurization system. A layout of the tank and expulsion is shown in Figure J-13. During the retrofire sequence, after the engine builds up to full thrust, the bellows reaches its full extension. As the full extension position is reached, a plug in the movable dome snaps out, thereby allowing the helium gas to pressurize the N_2O_4 directly. Plug removal is accomplished by a stainless-steel wire, attached to the tank dome, which stretches tight as the bellows approaches its fully extended position. The positive expulsion will be recycleable in that the plug could be reinserted upon removal of the tank. For the remainder of the retrofire sequence the oxidizer feed system is converted to straight pressure-fed with ullaging thrust provided by the main engine. The positive expulsion bellows, contained completely within the spherical tank, will be sealed against the tank wall with the nickel-gold-palladium braze found to be successful joining material for titanium-to-stainless-steel joints. The braze would be subjected to minimal stress levels, being a nonstructural joint. Oxidizer required for a possible orbit trim maneuver will be trapped by surface tension effects between a series of 5μ, dutch twilled weave, wire screens located at the inlet of the internal feed line. Bosses for connection to the engine feed line, pressurization line, and recirculation-propellant-loading valve are provided on the tank.

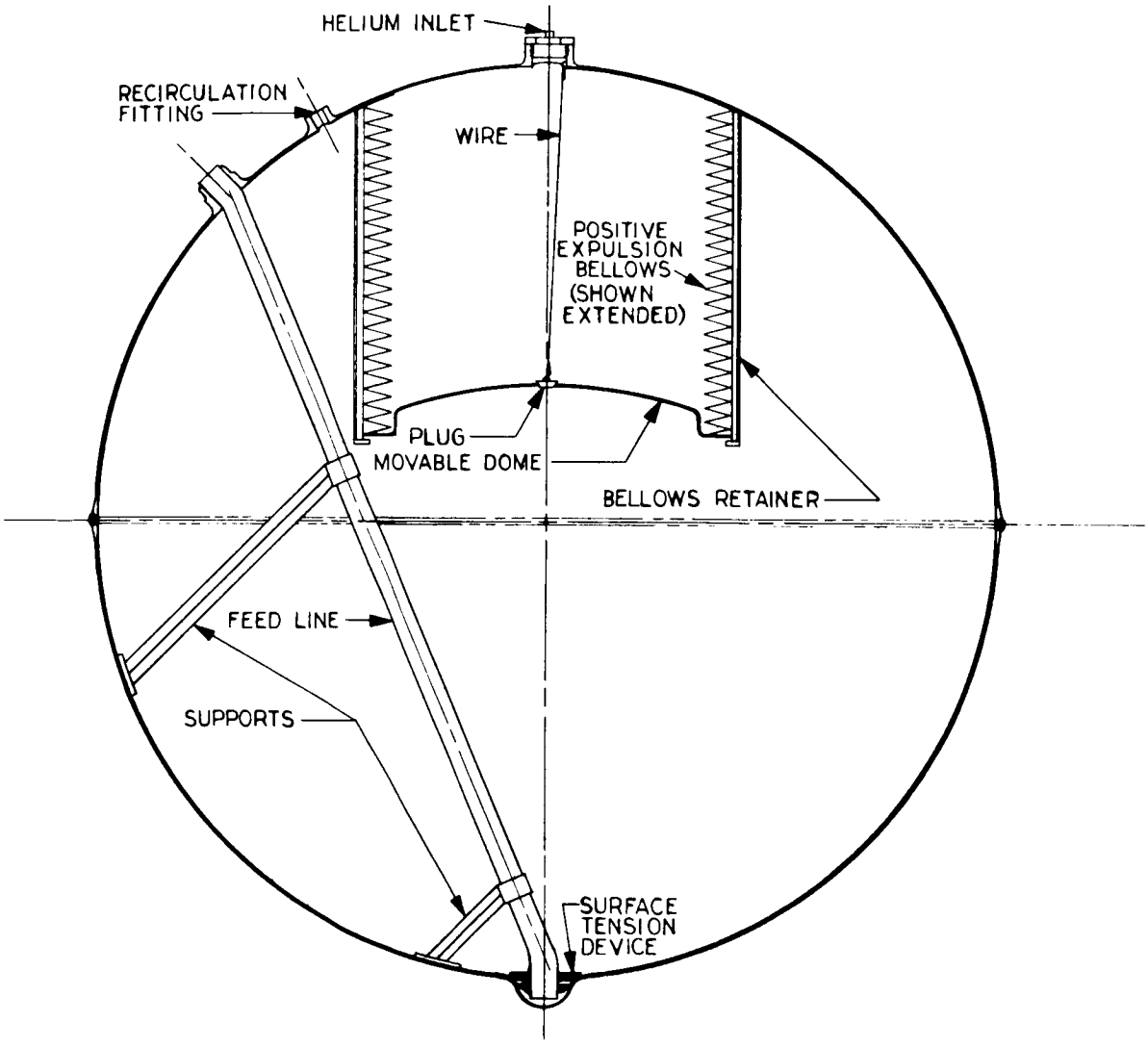


Figure J-13. N_2O_4 Tank Cross Section

e. Propellant Feed Lines

The propellant feed ducts have motion capability requirements arising from the movement capability of the engine. These motion capability requirements are satisfied by convoluted segments of wire-braided flexible metal hose. Each propellant feed line is comprised of two inlet flanges, one to connect to each of the two propellant tank outlets; two flex hose segments; a common line between the flex sections with a single line leading to the engine; and the single flange which connects to the engine.

The mechanical joints in the N_2O_4 feed line are sealed with the Titan II-type bolted-flange connection which uses the 1100-series aluminum seal.

Immediately upstream of the engine oxidizer inlet flange in the propellant feed line lies the port leading into the feed line from the oxidizer fill valve. It is positioned as close as possible to the engine flange and engine valves to minimize possibility of gas entrapment during filling. Manually operated fill and recirculation valves of the ball-seal-lapped-seat type are utilized in the fill system. The loading procedure requires use of a recirculation valve to preclude gas entrapment. The technique of loading involves a thorough purge with helium and then with N_2O_4 vapors. At the conclusion of the N_2O_4 vapor purge, N_2O_4 liquid flow is introduced and recirculated. Finally, the recirculation valve and the fill valve are closed, the OSE lines and connections removed, and the spacecraft fill and recirculation lines capped.

This loading technique minimizes the possibility of gas entrapment. The helium purge enters the N_2O_4 tanks at the bottom and escapes through the recirculation valve, which is located at the high point of the tank. This purge removes any gases which might contaminate or react with the N_2O_4 when it is loaded. The N_2O_4 purge removes the helium gas to ensure no helium will be trapped in the loaded propellant. When N_2O_4 liquid flow is introduced, it drives out any remaining helium during the recirculation cycle. The N_2O_4 vapors are either driven out ahead of the liquid, or condensed. Thus, at the completion of the filling procedure, only liquid N_2O_4 remains in the tank.

A fuel-fill valve is located immediately upstream of the engine fuel inlet flange in the propellant feed line. A manually operated fill valve of the ball-seal-lapped-seat type is utilized. The loading procedure employs a vacuum pump in the OSE connected to the fill line. Thus, when the fill valve on the spacecraft is open, it enables the evacuation of the complete fill line and both fuel bladders. Small

amounts of MMH vapors are introduced during the evacuation to ensure presence of MMH vapors exclusively at the conclusion of the evacuation procedure. Liquid MMH flow is then introduced, filling the bladders and condensing the remaining MMH vapors. When the 100 per cent full condition is reached, the manually operated fill valve is closed, the OSE-spacecraft connection broken, and the spacecraft fill line sealed and capped.

2. MONOPROPELLANT ENGINE PROPELLANT SUPPLY

2.1 Summary

The selection of the monopropellant supply system follows the same approach used for selecting the bipropellant supply. In each case, the component development status and experience status were the dominant factors in selection. However, after selection of vehicle Configuration A and selection of the monopropellant over the bipropellant engine, further study of the monopropellant supply was conducted to determine if improvements could be made. The initial studies resulted in the selection of a feed system very similar to that used on Mariner as shown in Figure J-14. It was later determined that further simplification could be made by eliminating the pressure regulator and using a blowdown system. This system is shown schematically in Figure J-15. This approach eliminates the separate pressurant supply bottle, the pressurant control valves, and the pressure regulation and distribution. The propellant supply decays from an initial pressure of 350 psia to a final pressure of 170 psia during the nominal engine operational duration.

2.2 Separately Pressurized Monopropellant Feed

2.2.1 Sizing Analysis

a. Pressurant Supply

Ambient stored nitrogen at 3000 psia was selected to pressurize the monopropellant hydrazine tanks. The amount of nitrogen required to deliver the propellant to the engine inlet at the required pressure was determined from an equation relating tank volume and pressure with pressurant properties and storage conditions (see

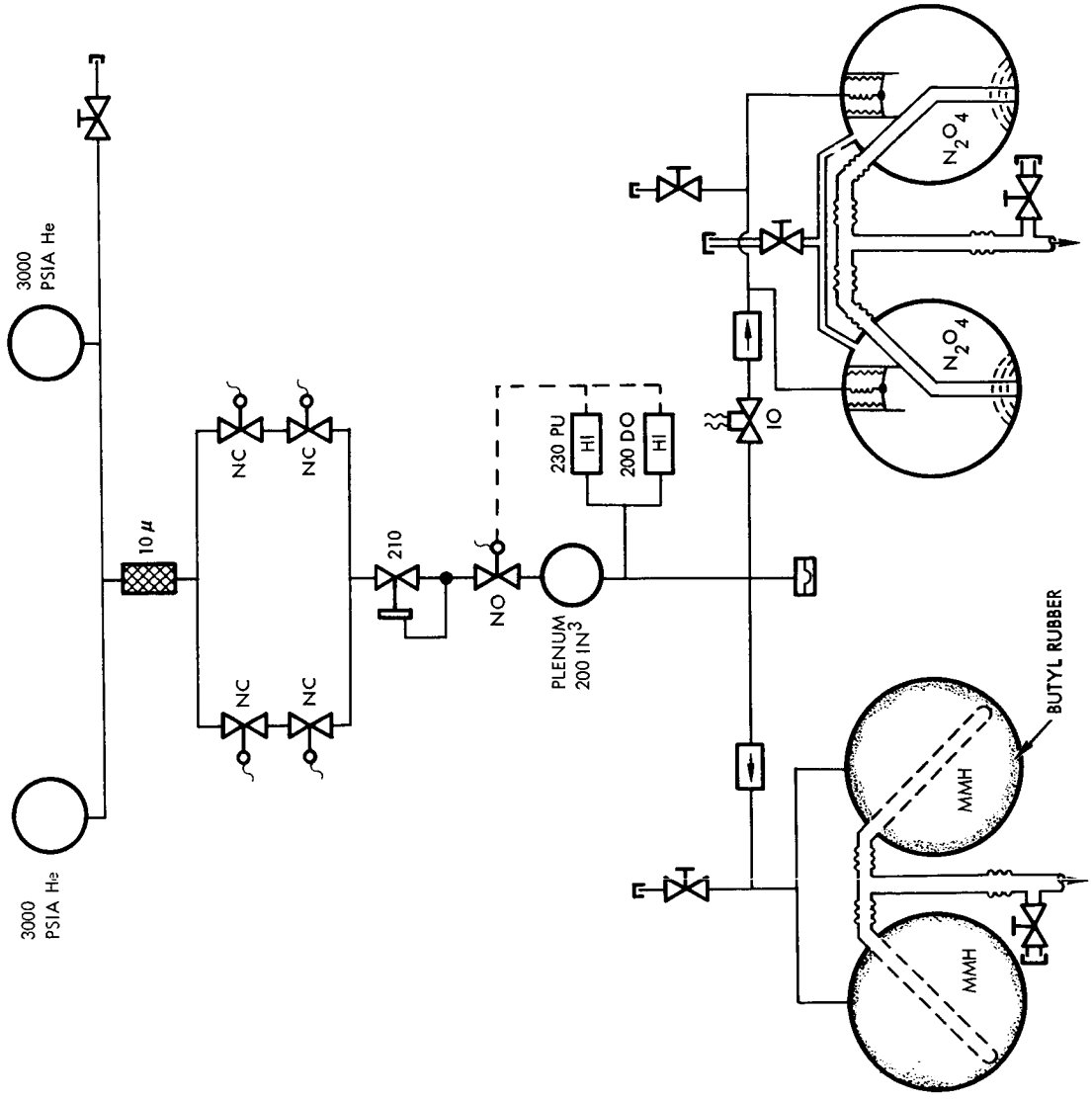


Figure J-14. Augmented A2 and C2 Configuration

Appendix C). A gas expansion process midway between adiabatic and isothermal was assumed based on the transfer of sensible heat from the pressurant bottles, lines, and components, and the propellant tanks. The active thermal control subsystem will restore the N_2 subsystem to nominal operating temperature between midcourse maneuvers and the relatively low-pressurant-flow rate during operation aids in the efficient extraction of this heat. Conversion of thermal energy to perform expulsion work and pressurant residuals were accounted for in the calculations. A propellant tank pressure of 310 psia was assumed, allowing 10 psi for flow losses and pressure drop across the positive expulsion bladders.

Based on a 246-pound propellant loading, a required nitrogen weight of 8.5 pounds was determined. A single pressurant sphere 12.4 inches in diameter will contain the nitrogen at 70°F and 3000 psia. The bottle wall thickness was designed for 3300 psi in conjunction with the appropriate safety factors to allow for pressurant temperature rise to 110°F.

b. Pressurization Control

The nitrogen flow rate required to expel the hydrazine at the desired pressure is approximately 0.006 lb/sec. A system pressure drop of 25.5 psi between pressurant supply and propellant tankage was calculated based on 1/4-inch pressurant line and controls. Smaller line could be used without inducing excessive pressure losses, but the small weight saving would be more than offset by the increased fabrication and development difficulties. In-place welding of many of the joints between line and components is proposed to minimize leakage. The application of this technique to lines smaller than 1/4 inch becomes quite difficult. Probably the major consideration, however, is the high level of industry experience with 1/4-inch components. Many fully developed valves, filters, and regulators are available as off-the-shelf items. Based on these considerations, the pressurization control system will use 1/4-inch nominal diameter line and associated components.

c. Propellant Tankage and Expulsion

Two sperical tanks 18.9 inches in diameter will contain the 246 pounds of hydrazine. The tank volumes (2.05 ft^3 per tank) were determined by the propellant volume at 70°F and a 5 per cent ullage volume. Hydrazine has a relatively low coefficient of thermal expansion thus the ullage volume is reduced by only 1 per cent at 110°F. The propellant tank environment is to be held within a temperature range of 40 to 90°F by the thermal control subsystem. Should the propellant temperature reach 110°F, the combination of tank ullage and plenum volume is more than adequate to safely accommodate the compressed pressurant.

Positive displacement of the hydrazine is provided for the full duration of each midcourse maneuver, through collapse of the butyl-rubber bladder which separates the propellant from the pressurant. A nominal clearance between the bladder and the tank will provide the ullage volume. Calculations are given in the Appendix C.

d. Propellant Feed Lines

The hydrazine feed line size was established at a nominal 1/2-inch diameter. Calculations were made to determine the pressure loss due to line length, flow restrictions, and start loss due to acceleration of the propellant. The propellant flow is divided between two lines for all but the last few inches feeding the engine. Flow restrictions have been minimized and start acceleration losses are negligible due to the low thrust to weight ratio. The resultant maximum pressure drop between propellant tanks and engine inlet was calculated to be 0.22 psi. A slightly smaller line size could have been chosen with a correspondingly small weight saving. The choice of 1/2-inch lines may be justified, however, based on the universality of this size with respect to forming techniques and component availability.

2.2.2 Components

Components utilized in the pressurization equipment are 1/4-inch nominal diameter. In-place welding techniques are utilized for the

joining of all pressurization components into a single module. This module is installed, removed, or replaced, as a unit.

The teflon compounds used for component seals and seats are contained entirely within the pressurization subsystem. The design eliminates exposure of any teflon seal or seat to the hard vacuum of space. This circumvents possible problems due to the outgassing of the seals. The removal of relief valves from the flight pressurization subsystem eliminated the components most likely to be subject to this difficulty.

The subsystem is designed to operate and perform all intended functions over a temperature range from 40 to 110°F. The pressurant sphere is designed to take the overpressure resulting from reduced gas density due to temperature increases which may occur subsequent to loading. Thus, the nominal working pressure is 3000 psi, the maximum working pressure 3300 psi.

The subsystem does not require any electrical power during the coast periods between midcourse corrections or orbit trims.

a. Pressurization Supply

The pressurant gas is stored in a single spherical high-pressure vessel. Nitrogen loading is accomplished through a manually operated fill valve of the type used on Mariner 4. Immediately upstream of this valve is the OSE-spacecraft interface. The interface consists of a simple pneumatic tubing connection which is separated, capped, and sealed subsequent to loading of the sphere and closing of the manual fill valve.

Fittings utilized in the pressurization system are generally of the NASA-developed MC-type. Joints which necessitate contact of dissimilar metals will be designed so that resultant corrosion is kept to a minimum. Surface coatings are utilized in such joints. Anhydrous propellant and dry pressurant are used, and the environment controlled, to minimize the possibility of corrosion.

The remainder of the pressurization supply equipment consists of four banks of explosive-squib-actuated valves and one hybrid bank consisting of one solenoid and one explosive-squib valve. Each bank of explosive valves is comprised of one normally-closed valve in series with one normally-open. The hybrid bank utilizes a normally-closed solenoid valve in series with an initially-closed explosive valve. This hybrid bank serves to provide capability for a number of engine starts for orbit trim purposes. In addition, it serves as a backup supply-shutoff in the event of a failure of one or more of the explosive valve banks. The number of orbit trim firings possible with the hybrid bank is limited only by the amount of propellant available after the midcourse correction firings.

The squibs used to fire the explosive valves would be of the dual-bridge-wire design. The squibs are discussed in more detail in Pyrotechnics, Section V-4, Volume 5.

b. Pressurization Control

The pressurization control equipment consists of a filter, a preset-pressure regulator, a solenoid valve, two pressure switches, and a plenum chamber. The regulator is of the type used for the Mariner 4 pressurization control subsystem. The explosive valve banks upstream provide positive and complete shutoff of the gas supply to the regulator. Thus, excessive leakage in the regulator between midcourse correction firings can add only the small quantity of gas trapped between the downstream side of the explosive valves and the upstream side of the regulator. The over-all pressure rise caused by this gas bleeding down into the tanks would be negligible.

The two pressure switches control the normally-open-configuration solenoid valve. Both switches are designed to actuate at 5 psi above the maximum normal regulator outlet pressure. Both switches must pickup to send the signal actuating the valve closed. If either switch drops out, the signal is interrupted and the valve reopens. This arrangement protects against the failure of a pressure switch to

drop out. Failure-to-drop-out is the most likely mode of failure of the pressure switches. By signalling the solenoid valve to close in the event of excessive downstream pressure, the switches enable it to perform as a backup regulator.

The failure of the regulator in an excessive-leakage mode of a failed-partially or completely-open mode results in the solenoid valve-plenum chamber-pressure switch combination taking over the regulation function. Regulator design is selected based on ensuring one of these three modes in the event of a malfunction. The plenum chamber is sized to minimize regulator chatter and line pressure surges. It must protect against premature signals to the solenoid valve from the pressure switches. For this reason, the switches are installed immediately downstream of the plenum chamber. Sensing an overpressure indicates definite regulator malfunction, rather than slow response or overshoot. The pressure switches will then pickup, sending a signal which closes the solenoid valve located upstream of the plenum chamber. Pressure in the plenum chamber then decays until one or both pressure switches drop out, allowing the solenoid valve to return to its normally-open position. Drop-out pressure is set equal to the normal minimum regulator outlet pressure. If the regulator has not recovered, a rapid pressure rise ensues, the pressure switches pickup again, sending a signal which closes the solenoid valve, and the cycle repeats. The subsystem continues in this cyclic, or bang-bang mode of operation for the duration of the midcourse correction, or orbit trim, engine firing. Due to the presence of the plenum chamber, pressurization control subsystem outlet pressure is controlled within a narrow band only 5 psi wider than the normal regulator outlet pressure variations. This technique of backup regulation was successfully utilized on the Saturn S-IV and is being used on the Saturn S-IVB and the S-IVB auxiliary propulsion system. Because the pressurant gas supply is shut off immediately downstream of the pressurant supply sphere during the coast periods between engine firings, it is not necessary to supply electrical power to the pressure switches during these periods to protect the system from overpressurization.

c. Pressurization Distribution

The pressurization distribution equipment consists of a manually operated valve, flow divider, and burst disc immediately downstream of the plenum chamber. From each of the twin outlets of the flow divider, one line leads to each propellant tank. The burst disc serves to prevent destruction of the entire spacecraft in the event of catastrophic propulsion system overpressurization. The burst disc is protected from premature rupture by the plenum chamber. Rupture pressure of the burst disc would be set at the proof pressure of the plenum chamber. The manually operated valve provides a vent capability for the gas trapped between bladder and tank which must be expelled during loading of the bladders. It would be connected to a vent and relief valve supplied as part of the OSE. This connection would be closed, capped, and sealed subsequent to loading.

d. Propellant Tankage Expulsion

The two titanium propellant tanks provide complete positive expulsion for the N_2H_4. A butyl-rubber bladder located in each tank contains the propellant. A perforated tube extends from the outlet and up the centerline of each tank. These tubes ensure that unsymmetrical collapse of the bladder will not result in interrupted propellant flow. Evidence exists indicating difficulties with storing N_2H_4 in butyl rubber at temperatures above 125°F. At and above this temperature, the decomposition rate of the N_2H_4, due to impurities present in the rubber increases. Increasing temperature accelerates this decomposition rate further. However, 125°F is considerably above the 90°F maximum temperature limit set for the spacecraft.

The butyl-rubber bladder positive expulsion technique is well developed from Ranger and Mariner experience. It is entirely within present technology. Some further testing must be done to determine the effects on propellant quality of 12-month storage in butyl rubber at slightly elevated temperatures (110 to 120°F) when intermittent demand for propellant is experienced.

The tanks are spherical in shape, with bosses for connecting the pressurization lines and the engine feed line. The collapse of the bladders results from the nitrogen gas pressure between the tanks and the bladders. Data describing the tank materials and sizes is provided in Table J-2.

Table J-2. Monopropellant System Midcourse Correction

Vessel	Contents	Total Number	Type	D_i	t wall min.	t weld min.	Material	Burst Pressure	Operating Stress Level
Propellant	Hydrazine N_2H_4	2	Sphere	18.9 in.	.0202 in.	.0303 in.	6AL-4V Ti Heat treated	682 psia	72,600 psi
Pressurization	Nitrogen N_2	1	Sphere	12.4 in.	.176 in.	.264 in.	6AL-4V Ti Annealed	7260 psia	58,900 psi

2.3 Blowdown Monopropellant Feed System Design

In addition to the conventional regulated systems discussed previously, a blowdown system which eliminates all of the functional components was analyzed. Analysis of optimum gas pressure to achieve minimum system weight resulted in a ratio of initial to final gas pressure of slightly over two to one. It was then determined that the proposed monopropellant engine could operate with this variation in supply pressure. Therefore, the pressure regulator was eliminated to achieve further simplification. A schematic and a layout of the resulting design are shown in Figures J-15 and J-16. This approach was selected over the separately pressurized approach on the basis of simplicity. A weight penalty of 18.5 pounds is involved in using the blowdown system.

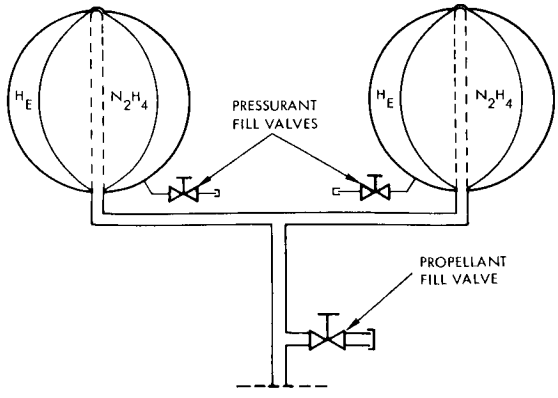


Figure J-15. Monopropellant System

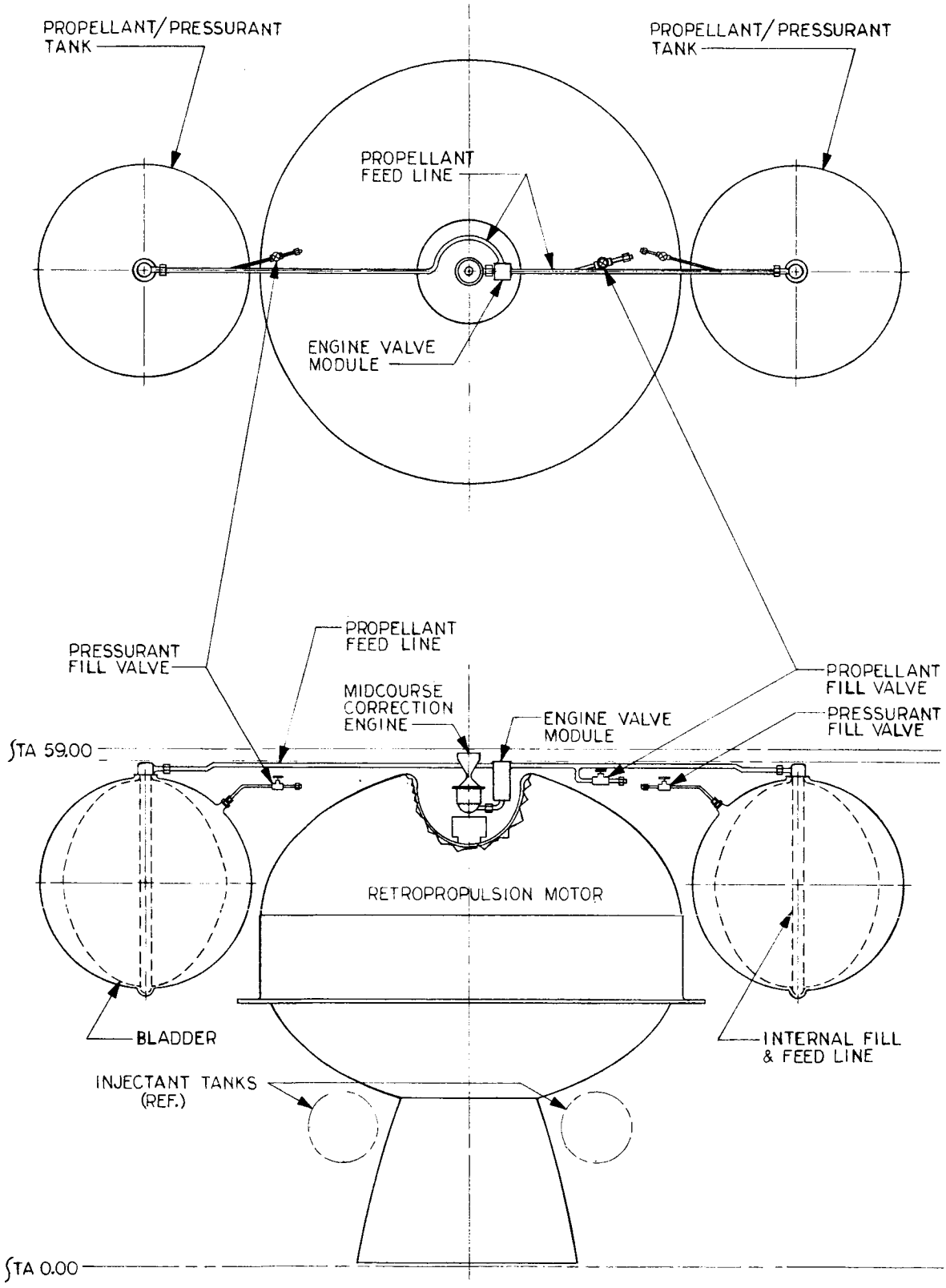


Figure J-16. Augmented Monopropellant System

2.3.1 Analysis

a. Pressurant Supply

Ambient stored helium at 350 psia will be used to pressurize the propellant tanks. Helium was selected in preference to nitrogen because of a weight savings of 7.4 pounds. Based on a propellant weight of 246 pounds and a minimum tank pressure of 170 psia, the required helium weight is 1.23 pounds, the tank volume is 4.5 ft^3, and its diameter is 24.6 inches. The sizing calculations assumed that the active thermal control subsystem will restore the propellant supply subsystem to above 50°F between midcourse maneuvers, and that about 20 per cent of the propellant (maximum) would be used in any given midcourse maneuver. The tank wall thickness is designed for 380 psia operating pressure to allow for a pressurant temperature rise to 110°F after loading. Hydrazine has a relatively low coefficient of thermal expansion and would affect the tank pressure very little if heated to 110°F after loading. Positive expulsion is provided by collapsing a butyl-rubber bladder, which separates the propellant from the pressurant. Since the rubber is permeable by helium, some helium will go into solution in the hydrazine but should have little effect on engine operation.

b. Propellant Feed Lines

As in the A2 configuration, the feed line size was established at a nominal diameter of 1/2-inch. Calculations show a resultant maximum pressure drop between propellant tanks and engine inlet of 0.22 psi. A slightly smaller line size could have been chosen, with a corresponding small weight saving. However the 1/2-inch size was chosen on the basis of universality of this size with respect to forming and fittings.

2.3.2 Design

The A3 design eliminates most of the complexity associated with propellant supply systems. The design does not require any electrical power and has only one moving part which is the rubber bladder. Though the exact design of the bladder-tank internal fill-feed line has not been determined, this does not appear to be a particular problem The tanks are loaded with propellant in the same manner as the A2 configuration. Helium is loaded simultaneously into both tanks from a single pressure source. The helium will be loaded to a specific mass as determined by gas temperature and pressure (nominal is 77°F and 350 psia). The system is designed to be stored and to operate in the range of 40 to 110°F. After helium loading, the fill hand valves will be closed, leak checked, and capped. As a result, the helium in one tank is separated from the other tank. Assuming the tanks will receive the same thermal inputs and will arrive at the same steady-state temperature during coast, this will result in close control of the effective propellant center of gravity by tending to equalize the propellant volumes remaining in the tanks. If one tank drains faster than the other, the gas in the other tank will remain at a higher pressure and thus reverse the flow differential. If the maximum temperature variation in the thermal control were to exist between the tanks (approximately 50°F) then a maximum net unbalance of approximately 13 pounds would result between the tanks prior to the first engine operation. This would result in only a small, easily controlled, disturbing torque during engine operation. Present calculations indicate that the probable maximum net unbalance would be about 7 pounds. This will be checked more closely in future analyses. The design will require less total development than the separately pressurized configuration but will require more testing of the tanks. In particular, the exact characteristics of the blowdown will need to be determined during testing so that flight performance can be accurately

predicted. The ability to use the exact tank-expulsion system in a 1969 flight will allow the design to be proven under essentially mission conditions prior to the 1971 Mission. Tank parameters for the selected design are shown in Table J-3.

Table J-3. Propulsion System Configuration A-3 Monopropellant System

Vessel	Contents	Total Number	Type	D_i	t wal' min.	t weld min.	Material	Burst Pressure	Operating Stress Level
Propellant and Pressurization	Hydrazine (N_2H_4) Helium (He)	2	Spherical	24.6 in.	0.0397	0.0595	6AL-4V Ti Annealed	836 psia	58,900 psi

APPENDIX K

PRELIMINARY CALCULATIONS FOR LANDER COVER BASE SEPARATION SPRINGS

The following calculations were made to determine the feasibility of using springs to jettison the lander cover base.

Tipoff angle rate possibilities have been examined, and no problem exists in this area. The springs are short and will be arranged so that their negligible side loads counteract one another.

Conclusion is that the spring separation method is practical in every respect.

1. ASSUMPTIONS

- o Weight of lander cover base, 150 pounds
- o Separation velocity, 2 ft/sec
- o Three springs used
- o Springs compressed must be less than 3 inches long
- o Inside diameter of coils must be more than 2 inches in diameter
- o Weight of spacecraft, 5500 pounds

2. EQUATIONS

$$V^2 = X_o^2 \, kg \left(\frac{W_1 + W_2}{W_1 \quad W_2}\right) \quad \text{(conservation of energy and linear momentum)}$$

$$WK = 1/2 \; k \, X_o^2 = \frac{V^2}{2g} \quad \left(\frac{W_1 \quad W_2}{W_1 + W_2}\right) \quad \text{(energy balance)}$$

Assume no thrust during separation.

$$V^2 = X_b{}^2 kg \left(\frac{W_1 + W_2}{W_1 W_2}\right) \text{ for relative separation velocity.}$$

$$WK = \frac{1}{2} kX_o{}^2 = \frac{V^2}{2g} \frac{W_1 W_2}{(W_1 + W_2)}.$$

Assume:

$V = 2$ ft/sec

$W_1 = 150$ lb for cover

$W_2 = 5500$ lb for spacecraft

$$WK = \frac{4 \times 150 \times 5500}{2 \times 32.2 \times 5650} = 9.07 \text{ ft/lb} = 109 \text{ in./lb}$$

Three springs needed.

$WK = 37$ in./lb per spring

Also assume:

$d = 0.100$ in. (wire diameter)

$D = 2.375 + 0.100 = 2.475$ in.

$P = 14$ lb for $S = 55,000$ psi

$$\frac{D}{d} = \frac{2.475}{.10} = 24.75$$

$N = 2$ (turns)

$k = 4.8$ lb/in.

$$WK = \frac{1}{2} K X_o^2$$

$$Xo = \sqrt{\frac{2\,WK}{k}} = \sqrt{\frac{2 \times 40}{4.8}} = 4.08 \text{ in.}$$

$$\frac{L}{D} = \frac{1 + 4.25}{2.475} = 2.12, \text{ stable}$$

at $x = 4.25$, $F = 20.2$

$S_s = 130,000$ psi - too high

Assume: QQ-W-470 spring steel wire

$d = 0.125$ in.

$D = 2.375 + 0.125 = 2.5$

$$\frac{D}{d} = \frac{2.5}{\frac{1}{8}} = 20$$

$P_s = 27.5$ lb

$P_w = 25$ lb

$N = 3$

$k = 7.5$ lb/in.

$Xo = \sqrt{\frac{2 + 40}{7.5}} = 3.26$ in.

$F = 7.5 \times 3.26 = 24.5$ lb

$X_s = \frac{27.5}{7.5} = 3.67$ in.

$h_s = (3 + 2)\frac{1}{8} = 0.625$ in.

Installed height:

$h = 0.625 + (3.67 - 3.26) = 1.035$ in.

Solid stress:

$S_s = 99,000$ psi

Free length:

$L = 0.625 + 3.67 = 4.295$ in.

Typical spring (three required)

Material: QQ-W-470 spring steel wire

$d = 0.125$ in. wire diameter

ID = 2.375 in.

$D = 2.375 + 0.125 = 2.5$

$P_s = 27.5$ lb solid compressed load

$P_w = 25$ lb installed load

N = three active coils

k = 7.5 lb/in.

$X_o = \frac{2\ WK}{k} = \frac{2 + 40}{7.5}$ = 3.26 in. working stroke

$X_s = \frac{27.5}{7.5}$ = 3.67 in. stroke to solid height

$h_s = (3 + 2)\frac{1}{8}$ = 0.625 in. solid height

h = 0.625 + (3.67 - 3.26) = 1.035 in. installed height

L = 0.625 + 3.67 = 4.295 in. free length

S_s = 99,000 psi solid stress

$\frac{L}{D} = \frac{4.295}{2.5}$ = 1.72 stable in buckling (See Wahl's "Mechanical Springs")

$$V = Xo\ k_t g \sqrt{\frac{(W_1 + W_2)}{W_1 W_2}} = (\frac{3.26}{12}) \sqrt{\frac{7.5X386X3}{150x5500}} \quad (5650)$$

$$= \frac{3.26}{12} \sqrt{59.5}$$

V = 2.1 ft/sec relative separation velocity from three parallel springs

$k_t = 3\ k$

3. SYMBOLS

V	Relative separation velocity	ft/sec
X_o	Compression of spring	in (feet)
k	Spring constant	in-lb
g	Gravational constant	32.2
W_1	Cover weight	150 lb
W_2	Spacecraft weight	5500 lb
WK	Energy	in-lb
d	Wire diameter	in.
D	Coil diameter (mean)	in.

P	Force	lb
N	Number of turns in coil	
L	Free length	in.
S	Stress	PSI
S_s	Solid height stress	PSI
X_s	Stroke of spring	in.
F	Force	lb
P_s	Force (solid height)	lb
P_w	Force (working)	lb
h_s	Solid height	in.
h	Installed height	in.
k_t	Total spring rate	

APPENDIX L
RADIOMETRIC MODEL OF MARS

The purpose of this study is to provide a basis for choosing a spectral interval to be used for attitude sensing devices employed in a space vehicle in Mars orbit.

Because the orientation needs to be controlled on both the day and night side portions of the orbit the use of scattered radiation from the sun is excluded and some sort of emitted radiation is indicated. Thermal radiation from the planet or its surrounding atmosphere best fits the need. The wavelengths can be selected such that very little interference from direct solar radiation is encountered; the day-night variation in energy received is not nearly as extreme as for visible radiation.

The visible spectrum offers much more available energy during the day, and detectors of great sensitivity compared to those used in the IR range are available. Some visible emissions are known to occur in the night atmosphere of earth, and these are detectible using photomultiplier detectors. However, the large dynamic range between day and night signals, the more delicate nature of the detectors, and the effects of scattered visible radiation weigh against the use of visible radiation.

1. INFRARED OPTICAL REFERENCES

Two choices of IR optical reference are available:

- The disk of the planet itself.
- Some atmospheric component of strong IR absorption and emission.

Using the planetary disk as a reference in the case of earth sensors is complicated by the presence of clouds and by the variable nature of the IR window resulting from changes in atmospheric water vapor concentrations. For these reasons the possibility of using strongly absorbing atmospheric components to define a disk which is above most of the clouds and outside of the window range of spectra has been examined. Hanel, Bandeen, and Conrath (Reference L-1) in 1962 and Wark, Alighouse, and Yamamoto (Reference L-2) in 1963 have considered the

problem in some detail for a wide range of model terrestrial atmospheres and have concluded that CO_2 band centered around 15 microns and the water vapor absorption in the vicinity of 33 microns are most suitable for use. Haynie, Collinge, and Erstgard (Reference L-3) report a measurement of the 15 micron CO_2 band by a satellite radiometer. They report "reasonable" agreement with theoretical predictions. For example, with a 2-micron pass band the theoretically predicted average emittance was 1.88 mw/cm^2 while the observed value was 1.45 mw/cm^2. The observed gradient width was 1.75 ± 0.55 degrees at an orbital altitude of 160 km. The emittance showed a small but real latitude variation, the value of emittance ranging from 1.30 mw/cm^2 at closest approach to one pole to 1.65 mw/cm^2 near the opposite pole.

A similar choice of optical reference disks must be made with respect to Mars before a sensor can be designed for that mission.

1.1 The Planetary Surface as an Optical Reference

In the case of earth the principal difficulties associated with using infrared radiation from the surface for attitude reference are anomolies such as variable absorption by water vapor and the presence of clouds. The skies of Mars are much clearer than those of earth and the amount of water vapor is known to be very small. Astronomical observations over many years indicate that the frequency of occurrence of highly mobile clouds is very small compared to earth.

The clouds of concern are the so-called white clouds, identified as composed of ice crystals, and the yellow clouds, usually identified as dust clouds. The yellow clouds are described as of fairly rare occurrence and are usually quite limited in area, though occasionally great planet-wide storms have been observed. The white clouds of largest area and persistence occur above the polar caps, and are presumably at fairly low altitudes. W. A. Wright (Reference L-4) of Lick Observatory found these clouds to be transparent in the photographic IR, while E. Slipher (Reference L-5) and others have found them transparent in the visible red. If these clouds are tiny ice crystals as the polarization measurements of Dolfus indicate, one would expect that in the far IR they will be opaque and radiate much like a black body of the temperature of the clouds.

The white clouds which overlie the polar caps are a persistent seasonal phenomenon and their outlines do not change greatly from day to day. For this reason they are not regarded as seriously affecting the television mapping mission even though they do contribute to an absolute error in locating the center of the planetary disk.

Yellow clouds are more variable. There is no general agreement about the altitude of such clouds, but Slipher (Reference L-5) reports that altitudes up to 30 km are considered probable on the basis of photographic evidence and visual observation. The yellow clouds are thus capable of causing a short-lived change in pointing and constitute one of the more serious sources of potential error, since they are not persistent or predictable.

Morning hazes have been observed quite consistently on the sunrise limb of the planet, but these dissipate rather quickly and probably occur near the surface where they will not contribute a large error.

Temperature variations across the disk may be as large as 100°C. This is a fairly large variation and must be accounted for in instrument design. Coblenz and Lampland at Lowell Observatory measured surface temperatures by radiometric means over a period of years (Reference L-6). The polar cap showed a fairly constant -70°C, while the bright areas in the center of the disk indicated -10° to +5°C. Adjacent dark areas gave temperatures of +10° to +20°C. Sunrise and sunset limbs of the planet in one measurement showed -45 and 0°C, respectively, to give some idea of the diurnal variation. The winter polar temperatures are probably representative of the temperature of the white clouds (or the surface beneath them, if they are transparent in the infrared). The temperature of one yellow cloud has been observed by Sinton and Strong (Reference L-6) by radiometric means. The temperature was somewhat below that of the surroundings, but not really cold.

Studies of the shape of Mars in the visible and near infrared show that the planet is flattened at the poles. The results of various observers differ, but the value of ellipticity recommended by de Vaucouleurs is 0.013 ± 0.001, which corresponds to a total polar diameter difference of about 85 km or a flattening of approximately 42 km at each pole. Although

this error is of importance in exact mapping operations it is a persistent feature and will not, therefore, prevent accurate aiming toward a selected area.

One would expect the atmosphere also to show a similar flattening except perhaps at very high altitudes. The blue haze has not been observed to show measurable flattening near the poles and for this reason it is thought to extend to high altitudes. Supporting evidence is given by the fact that the apparent diameter of Mars is greater in the ultraviolet than in the visible by 3 to 6 per cent.

Thus it would appear fairly well established that in using the planetary disk as an IR optical reference one would see a temperature range of about 200 to 300°K, and, rather infrequently, yellow cloud anomolies at altitudes up to 30 km, corresponding to an angular error of approximately 0.4 at peria psis. The point is that such occurrences are infrequent enough so that they would not be expected to ruin a great deal of data.

1.2 The 15 μ Band as an Optical Reference

The atmospheric constitution of Mars is poorly known. The best accepted modern data indicates a total pressure at the surface of the planet of about 10 millibars, with about 33 per cent of the gas being carbon dioxide (Reference L-7). The CO_2 is fairly well identified (Reference L-8), the total amount estimated at about 60 atmosphere meters or 25 times as much as in the terrestrial atmosphere.

The remaining principal constituents are assumed to be nitrogen and/or argon. Oxygen has not been detected; the upper limit of oxygen content has been put at less than 0.8 atmosphere meters. Water vapor at $(1.4 \pm 0.7) \times 10^{-3}$ gm/cm^2 has been determined spectroscopically. Traces of various other gases have been reported by some workers but denied by others, but it is certain that small amounts of such compounds as carbon monoxide, ozone, oxides of nitrogen, and the like are generated photochemically in the upper atmosphere.

Thus, it seems that the atmosphere of Mars should be quite transparent in the IR, with the exception of carbon dioxide absorption bands. The only atmospheric absorption which might reasonably be used to define a disk is the 15-micron CO_2 band.

A number of model atmospheres for Mars have been analyzed and extreme temperature profiles predicted by Schilling (Reference L-9), while more detailed profiles have been predicted by Chamberlin (Reference L-10). Unfortunately, this work was based on a surface pressure of 85 mb and has not been extended to the 10-20 mb region, which is now believed to be most probable. In particular, the height of the tropopause is uncertain, and this affects the temperature of the atmosphere at the altitudes where the absorption and reradiation by CO_2 is important. Because of the lower gravitation on Mars the atmosphere will extend to greater heights, so that the gradient angle will tend to be larger. However, this may be compensated by the higher concentration of CO_2. The precise height above the surface at which the extinction of the 15-micron band occurs will depend upon the temperature profile of the atmosphere. Two extreme cases will be examined to try to make an order of magnitude estimate for the range of variation possible within the compass of available data. Isothermal atmospheres at temperatures equal to the extremes of observed surface temperatures will be assumed.

2. THE 10-MB, 60 METER ATMOSPHERE

The Mars atmosphere is assumed to be governed by the hydrostatic equations and the perfect gas laws. The resulting equations are worked out in detail in the TRW Mars Environmental Handbook, Volume II, and the derivation will not be repeated here. The net result, assuming a linear temperature change with altitude is

$$p(z) = p(o) \left(\frac{1 - \gamma z}{T(o)}\right)^{mg/\gamma R}$$

where p (z) is the pressure at an altitude z above the surface, T (o) is the surface temperature, γ is the rate of change of temperature with altitude, m is the average molecular weight, and R is the universal gas constant. If $\gamma = 0$ i.e. if the temperature is assumed constant with altitude,

$$p(z) = p(o)\, e^{-z}/H \text{ where } H = \frac{RT(o)}{mg}$$

is called the scale height. Since the temperature normally decreases with altitude, if a constant temperature is assumed we will have a worst

case, as far as the gradient angle is concerned; i.e., the mass of CO_2 required for extinction of 15-micron radiation from an external source will be spread over the greatest altitude range for this sort of temperature distribution. This neglects the possibility of absorption which reverse the profile, as happens in the ozone band in earth, for example.

It is assumed that a thickness of gas which will cause extinction of 15 μ radiation will give a reasonable approximation to the altitude of the apparent disk for 15μ radiation. The amount of gas necessary to absorb the 15-micron radiation above Mars will differ from that above earth because pressure and temperature differences will affect line width. It is assumed that the 15-micron horizon of Mars occurs at an altitude z_o such that the mass of gas per cm^2 lying on a chord through the atmosphere at this altitude is sufficient to give nearly total absorption of radiation in the spectral range of interest. Under these conditions the mass of gas radiates like a black body over the spectral range of strong absorption.

Figure L-1 shows the coordinates to be used in the analysis which follows:

z_o = Minimum altitude of the chord

r = Planetary radius

x = Distance from the point of minimum altitude to any point on the chord

z = The altitude at x

R = $z_o + r$

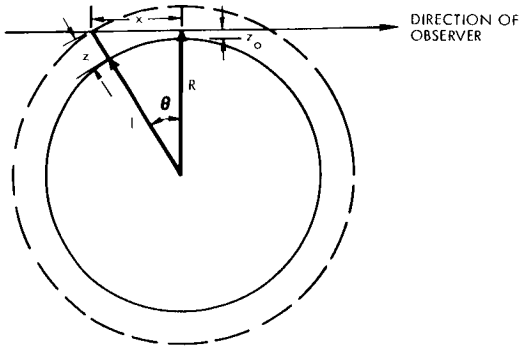


Figure L-1. Analysis of Coordinates of 10-mb 60 Meter Atmosphere Case

The absorption of IR radiation by a particular gas depends upon the total amount of absorbing gas and the pressure and temperature of the gas. The mechanism of absorption involves excitation of vibrational and rotational energy states of the gas molecules. The width of the resulting absorption lines is affected by the collision rates between molecules and by the molecular velocities, hence the pressure and temperature dependence. In general the pressure dependence is the more important effect, and the only one which will be considered in what follows.

The exact solution to the radiative transfer problem involves so much computation that it is not practical, even with the use of high speed digital computers. Plass (Reference L-11) says "....more than a million evaluations of Equation 24 $\bar{T}_\nu = \exp\left[-u \sum_{i=1} Si\, b\,(\nu - \nu_i)\right]$ would be required for a given temperature, pressure and amount of gas (and) a useful calculation ... amounts to several hundred different sets of these quantities."

For calculation to be feasible at all, a model is evaluated, rather than directly calculated. Plass et al (Reference L-12) have made these theoretical evaluations for a variety of conditions, which do not, however, permit application to our problem without further modification, because these tables do not cover the pressure and path length range expected on Mars.

Plass (Reference L-11) has shown that for conditions of long path length and low density the absorption is dependent upon the product of optical path length and pressure. The experimental results (References L-11 and L-12) can be plotted on a universal absorption curve.

In evaluating the Mars case the optical path and pressure will be calculated for isothermal atmospheres representing the extremes of observed surface temperature. Numbers from the universal absorption curve will then be used to calculate the altitude at which the 15-micron horizon will occur.

For the isothermal case

$$p(z) = p(o)\, e^{-z/H}$$

where p is the pressure at altitude z, and the density is $\rho(z) = \rho(o)e^{-z/H}$

$p(z)$ refers to the total pressure, while $\rho(z)$ refers to the density of absorber only.

The optical path is given by $du = \rho dx$. For the isothermal case $\rho(z) = \rho(o)\, e^{-z/H}$.

The product for a chord through the atmosphere is

$$F = \int_{-\infty}^{\infty} p(z)\, \rho(z)\, dx = \int_{-\infty}^{\infty} p(o)\, e^{-2z/H} dx$$

Upon transferring to angular coordinates this becomes

$$F = 2p(o)\, \rho(o) R \int_{o}^{\pi/2} e^{-2(R \sec\theta - r)/H} \sec^2\theta\, d\theta$$

$$= 2p(o)\, \rho(o) \times R e^{+2r/H} \int_{o}^{\pi/2} e^{-2\frac{R}{H}\sec\theta} \sec^2\theta\, d\theta$$

The exponential factor in the integrand decreases rather rapidly with angle. For example, the scale height of Mars is between about 10 and 20 km for the observed surface temperature extremes, while $R \simeq r = 3375$ km. The ratio of the exponential for $\theta = o$ and $\theta = \theta_1$ is, for the less rapidly converging case,

$$\frac{e^{-2 \times 168}}{e^{-2 \times 168 \sec\theta_1}} = e^{-2 \times 168 (1 - \sec\theta_1)}$$

For this ratio to be equal to 0.01 (i.e. the integrand is approximately 1 per cent of the initial value), the exponent must be about -4.6 or $(1 - \sec\theta_1) = 0.0137$ and $\sec\theta_1 = 1.0137$. This corresponds to $\theta \simeq 9\ 1/2$ degrees.

In this region $\sec^2\theta$ is very close to unity, and can be neglected.

If we restrict the integration to $\theta < 1/4$ radian we will have a good approximation to the total integrand. In this case the approximation $\sec\theta \simeq 1 + \frac{\theta^2}{2}$ is good to about 1 per cent and we have:

$$F \simeq 2p\,(o)\ \rho(o)\ R\ e^{+2\,r/H} \int_0^{1/4} e^{-2\,R/H\,(1\,+\,\theta^2/2)}\,d\theta$$

$$= 2p(o)\,\rho\,(o)\,Re^{\frac{2(r-R)}{H}} \int_0^{1/4} e^{-R/H\,\theta^2}\,d\theta$$

$$= 2p\,(o)\ \rho\,(o)\,Re^{-2\,z_o/H} \int_0^{1/4} e^{-R/H\,\theta^2}\,d\theta$$

The remaining integral can be evaluated from tables of gaussian error integrals.

$$\int_0^x e^{-t^2/2}\,dt = \sqrt{2\pi}\ \{P(x) - 1/2$$

To convert our integral to this form

Set $\frac{t^2}{2} = \frac{R}{H}\ \theta^2$

$$\int_0^{1/4} e^{-(R/H)\theta^2}\ d\theta \rightarrow \int_0^{1/4\sqrt{2R/H}} \frac{e^{-t^2/2}\,dt}{\sqrt{2R/H}}$$

$$= \sqrt{\frac{H}{2R}} \int_0^{1/4\sqrt{2R/H}} e^{-t^2/2}\,dt$$

R/H is a number of the order of hundreds. For such large arguments P(x) is for all practical purposes unity, and:

$$F = 2p(o)\ \rho\,(o)\ Re^{2\,z_o/H} \sqrt{\frac{H}{2R}}\ \sqrt{2\pi} \times 1/2$$

$$= p\,(o)\ \rho(o)\,\sqrt{\pi}\sqrt{HR}\ e^{-2\,z_o/H}$$

$R = z_o + r.$

For the atmosphere in the vicinity of the surface $z_o << r$ and we can treat R as a constant and approximately equal to r. Using the

TRW Mars Handbook figures we calculate for the scale heights at various temperatures:

$T = 176^{\circ}K$	$H = 11.6$ km
$T = 234^{\circ}K$	$H = 15.2$ km
$T = 300^{\circ}K$	$H = 19.9$ km

For comparison with the universal curve the units of F need to be cm of mercury x atmosphere cm

$$p(o) = 10 \text{ mb} \simeq 0.75 \text{ cm Hg}$$

Also from the Mars Handbook the mass of CO_2 accounts for 44 per cent of the surface pressure of a 10-mb atmosphere:

$$\rho_{176}(o) = \frac{0.44 \times p(o)}{gH}$$

$$= \frac{0.44 \times 10^4}{376 \times 11.6\ 10^5} = 1.0 \times 10^{-5} \text{ gm/cm}^3$$

$$\rho_{300}(o) = \frac{0.44 \times 10^4}{376 \times 19.9 \times 10^5} = 5.8 \times 10^{-6} \text{ gm/cm}^3$$

1 CC of CO_2 at STP is approximately $\frac{44}{22.4} \times 10^{-3}$ grams

$\simeq 2 \times 10^{-3}$ grams/cm^3

This is the factor needed to convert to atmosphere - cm

$$F_{176} = \frac{0.75 \times \sqrt{\pi} \times 10^{-5} \sqrt{11.6 \times 10^5 \times 3375 \times 10^5}}{2 \times 10^{-3}} e^{-2 z_o/H}$$

$$= 1.32 \times 10^5 e^{-2 z_o/H}$$

$$F_{300} = \frac{0.75 \sqrt{\pi} \times 10^{-5} \sqrt{19.9 \times 10^5 \times 3375 \times 10^5}}{2 \times 10^{-3}} e^{-2z_o/H}$$

$$= 1.72 \times 10^5 e^{-2 z_o/H}$$

If we assume that F = 3800 approximately defines the horizon*, we find the following values (for T = 176°K):

$$3800 = 1.32 \times 10^5 \, e^{-2z_o/H}$$

$$e^{-2z_oH} = 2.88 \times 10^{-2}$$

$$\frac{zo}{H} = \frac{1.540}{2 \times 435} = 1.77$$

Since $H_{176} \simeq 11.6$ km the horizon would appear at $1.7 \times 11.6 = 19.76$ km above the surface.

For T = 300°K

$$e^{-2z_o/4} = 2.21 \times 10^{-2}$$

$$\frac{z_o}{H} = \frac{1.656}{2 \times .435} = 1.90$$

And the horizon is at $19.9 \times 1.9 = 37.8$ km above the surface.

The transmission is approximately 10 per cent for F = 15. If we take this as the beginning of the atmosphere we can calculate the gradient angle for 10 to 90 per cent as follows:

$$15 = 1.32 \times 10^5 \, e^{-2z_o/H}$$

$$e^{-2z_o/H} = 1.14 \times 10^{-4}$$

$$z_o/H = \frac{3.944}{2 \times .435} - 4.56 \text{ for } T = 176°K$$

and for T = 300°K

$$15 = \frac{4.06}{0.87} = 4.65$$

*Plass' tables give about 92 per cent absorption over the 14-16 μ band for this F value. The number is for T = 300°C, but temperature corrections do not cause large changes, according to Plass.

Thus we see that the gradient takes place over approximately 2-3/4 scale heights, a distance ranging from 32 to 55 km for the temperature extremes assumed.

For an observer 2000 km above the surface the gradient angle in degrees is approximately this distance divided by 4180 km

$$\theta_{176} = \frac{32}{4180} \times 57.2 = 0.43 \text{ degrees}$$

$$\theta_{300} = \frac{55}{4180} \times 57.2 = 0.75 \text{ degrees}$$

The amount of energy radiated in the 15-micron band from the CO_2 layer will be taken as the black-body radiation in a 2-micron spectral band centered around 15 microns for a black-body at the temperature of the gas. For the temperatures previously used, these energies are:

λ Range	T	Black-Body Energy Emitted in 14-16 Microns Region
14-16 μ	176°K	4.4×10^{-4} watts/cm^2
14-16 μ	234°K	1.7×10^{-3} watts/cm^2
14-16 μ	300°K	4.1×10^{-3} watts/cm^2

For the planetary disk, the possible spectral regions of interest are the water vapor window between about 8 and 12 microns and the region at wavelengths longer than about 20 microns,

λ Range	T°K	Black-Body Energy Emitted
8-12 μ	176	4.1×10^{-4}
8-12 μ	234	3.0×10^{-3}
8-12 μ	300	12×10^{-3}
~20 μ	176	3.3×10^{-3} watts/cm^2
~20 μ	234	7×10^{-3} watts/cm^2
~20 μ	300	12×10^{-3} watts/cm^2

The variation in emitted energy (assuming black-body radiation) over the disk for the assumed temperature extremes is about 30 to 1 for the 8-12 micron band, 10 to 1 for the 14-16 micron band and 4 to 1 for the region about 20 microns. In addition for any given temperature in this range the available energy from the 20 micron region is as great or greater than that available from the other two spectral regions.

3. THE ALTERNATIVES

The composition and temperature distributions of the Martian atmosphere are very uncertain and no reliable theory for their prediction exists at this time. Levin, Evans and Stevens (Reference L-13) list 12 different model atmospheres which have been proposed (and this is not an exhaustive listing). For a surface temperature of about 270°K one model would predict a temperature at 40 km altitude of about 270°K while another would predict 170°K at the same altitude. The NASA models, which were selected to cover as broad a range of the 12 models as possible, would include a maximum temperature at 40 km of around 260°K and a minimum of 100°K, for a surface temperature of 300 and 200°K respectively. These results assume a lapse rate and tropopause altitude for each of the models.

These numbers are quoted only to illustrate the depth of our ignorance, and not for use. If such extremes of temperature do exist, however, the radiance variation for the CO_2 band could be even greater than those given in the previous section. If temperatures as low as 100°K really exist at these altitudes the CO_2 radiance would be small enough to strain the limits of the detectivity of available infrared detectors.

If we consider the radiation from the surface, on the other hand, it is seen that the planetary atmosphere is transparent in the 8 to 12 micron region and in the region above 20 microns. The temperature variations across the disk have been observed radiometrically and their range is reasonably well established. The anomolies which can be expected to occur are clouds, and their frequency of occurrence is much smaller than on earth. The yellow clouds appear to be at the highest altitudes and might give the largest errors. However, they are usually not of large extent nor do they occur frequently.

4. CONCLUSION

The maximum uncertainties in the position of the horizon as defined by the planetary surface anomolies and by the variation in the carbon dioxide horizon of the atmosphere in the light of present knowledge are of the same order, namely of the order of tens of kilometers.

The uncertainty in the radiance values are much greater for the atmospheric bands than for the surface, and the values may drop to unpleasantly low levels.

The frequency of variations in the CO_2 horizon are completely unknown, although clouds are known to occur above the surface, their frequency is known from many years of visual observation and has been found to be low compared to earth.

The definition of the edge is much sharper for the surface than for the atmosphere. Although far from ideal, the planetary surface of Mars appears to provide a much better optical reference than that of earth. In view of this and because of the great uncertainty concerning important details about the Martian atmosphere, radiation from the planetary surface should be used to provide attitude signals for a vehicle in Mars orbit.

5. REFERENCES

L-1 R. A. Hanel, W. R. Bandeen, and B. J. Conrath, Journal of the Atmospheric Sciences 20, 73-86 1963.

L-2 D. Q. Wark, J. Alishouse, and G. Yamamoto in "Torques and Attitudes Sensing in Earth Satellites" ed. S. Fred Singer Academic Press, 1964.

L-3 Haynie, Collinge, and Erstgard, Proceedings of Iris, Vol. 8, No. 3, August 1963.

L-4 F. Whipple, Earth, Moon and Planets, Harvard University Press, 1961.

L-5 Earl C. Slipher, "Mars," p. 24, Sky Publishing Company 1962.

L-6 Sinton and Strong, "Astrophysical Journal," 131, 459-469, 1956.

L-7 Mars Environmental Handbook 9990-6856-TU-000, Vol. II, prepared by Staff, Physical Research Division, TRW December, 1964.

L-8 L. Kaplan, A. Munch and H. Spinard, Astrophysical Journal, 139, 1 1964.

L-9 G. F. Schilling, "Limiting Model Atmospheres of Mars," Report No. R-402-JPL Rand Corporation, Santa Monica, California, pp 5-10, 1962.

L-10 J. W. Chamberlin, "Upper Atmospheres of the Planet," Astrophysical Journal.

L-11 G. N. Plass, Infrared Radiation in the Atomsphere, Americal Journal of Physics 24, 303, 1956.

L-12 V. Stuff, P. Wyatt and G. Plass, Final Report on Theoretical Study of the Infrared Radiative Behavior of Flames, Vol. II, The Infrared Absorption of Carbon Dioxide Aeronutronic Division, Ford Motor Company Report No. U-1505.

L-13 "NASA Engineering Models of the Mars Atmosphere for Entry Vehicle Design," ed. G. M. Levin, D. E. Evans and V. Stevens, 1964.

AUG 12 1965

SIGNIFICANT ERRATA. TRW Systems, Phase 1A
Study Report, Voyager Spacecraft
August 11, 1965

Volume 1. Summary

Substitute new p. 79 attached.

Volume 2. 1971 Voyager Spacecraft

p. 18. Item h) "necessary landed operations" should read "necessary lander operations."

p. 143. Section 3.4.1.a. second line should read "threshold of 0.25 gamma"

p. 282. Lines 3 and 4. Delete "or incorrect spacecraft address"

p. 284. Figure 5. Change "128 Word DRO Core Memory" to "256 Word DRO Core Memory"

p. 327. Denominator of second term on right hand side of equation should read

$$\left(\frac{1}{\epsilon_1} + \frac{1}{\epsilon_2} - 1\right)\left(N - 1\right)$$

p. 351. Figure 1, Section F-F. "separation nut" should read "bolt catcher"

Volume 3. Voyager Program Plan

Substitute new p. 12 attached.

p. 13. Figure 2-3. PTM Assemblies in item 7 move 1.5 months to right

p. 16. Figure 2-6. First milestone date should be September 1, 1969, instead of mid-January 1970, and all subsequent dates should be correspondingly adjusted 4.5 months earlier.

p. 20. Table 2-2. Third item in 1969 column should read "coincident with completion of proof test model assemblies. Fifth item in this column change "2 weeks" to "3.5 months." Fourth item in 1971 column, change "4 months" to "5 months."

p. 67. Figure 5-2. Under Intersystem Interface Specification add a block entitled "Spacecraft to OSE Interface Specification"

p. 120. Last line of paragraph c should read "shown in Table 5-2."

p. 126. Figure 5-13. Year should be 1966 instead of 1965.

p. 153. Figure 5-18. Ignore all numbers associated with lines in figure.

p. 167. Figure 5-21. In line 20 change "design revisions" to "design reviews"

p. 254. Second paragraph, third line, "The capability of the transmitter to select" should read "The capability of the transmitter selector to select."

p. 258. Section heading n should read Experiment Data Handling

p. 604. Section 3.2.1 beginning of second paragraph should read "The hydrazine fuel . . . "

Volume 4. Alternate Designs: Systems Considerations

p. 103. Figure 3-19. Caption should read "Radial Center of Mass. . . "

p. 151. Last paragraph, second line, "For the baseline, the reliability. . ." should read "The reliability . . . "

p. 158. 8th line, replace "0.06 pound/watt" by "0.6 pound/watt"

p. 215. Figure 3-50. Dot in ellipse at right should be 0.

p. 230. Section 5.3.2, second paragraph, 7th line, should read "Figure 3-52."

p. 239. Second line, "with a variable V" should read "with a variable ΔV"

p. 247. First line, "3250 km/sec" should read "3.250 km/sec"

p. 261. Figure 3-64. Interchange coordinates, clock angle and cone angle

p. 293. Figure 3-81. An arrow should connect "Low-gain spacecraft antenna" and the dashed line at 73×10^6 km

Volume 4. Alternate Designs: Systems Considerations Appendix

p. 6. Figure A-2. The shaded portion under the lower curve should extend to the right only as far as 325 lb.

p. 9. Table A-1, part (1). In last column heading change "W_3" to "W_1". In part (4) last column heading change "W_3" to "W_4"

p. 22. Second line below tabulation, replace "575 × 35" by "570 × 35"

p. 29. Tabulation at bottom of page, change "18" to "30" and "400" to "240"

p. 207. Numerator of equation for λ best at bottom of page should read "0.0201," and numerator of equation for λ worst should read "9.21"

p. 209. Table 5B, fifth line. Delete "$\times 10^{-}$." Also p. 213, Table 7A, seventh line, and p. 232, Table 3B, fifth line.

p. 217. Top portion of Table 9B should be labeled "primary mode" instead of "other modes"

p. 326. In equations following words "clearly" and "thus" insert "$>$" before second summation.

Volume 5. Alternate Designs: Subsystem Considerations

p. 3-15 Fifth line, "... is extended, spacecraft" should read "... is extended, two spacecraft"

p. 3-38 Last line, change "$= \frac{32}{4500} = M$" to "$\left(\frac{32}{4500}\right)\left(M\right)$"

p. 3-51 Two equations at bottom of page should read

$$D = 4\pi A/\lambda^2$$

$$A = \frac{D\lambda^2}{4\pi} = \frac{1000\lambda^2}{4\pi}$$

p. 3-67 Third line, last parenthesis "$\left(\frac{\pi}{2} + \phi\right) -$"

p. 3-82 6th line should read "50 degrees" instead of "50-140 degrees," and seventh line should read "140 degrees" instead of "50-140 degrees"

p. 3-111 Last line, change "50 Mc" to "1 Mc"

p. 3-137 Item g) for "... followed by 5 frames of real time" substitute "... followed by 11 frames of low rate science data and 5 frames of real time"

pp. 3-150 and 3-151 are interchanged.

p. 3-156 Last line, should read "gates, a 7 bit"

p. 5-21 Second paragraph, third line, for "others since they are" substitute "others which are"

p. 5-33 Bjork equations should identify 0.18 as an exponent, and the exponent for (ρ_p/ρ_t) in the Hermann and Jones equation should be 2/3 in both cases.

p. 5-33 Figure 5-12 should be replaced with Figure C-7 of Appendix C.

p. 5-40 Three lines above Table 5-10 substitute "permanent set" for "experiment"

Volume 5. Alternate Designs: Subsystem Considerations. Appendix I

p. B-11 Bottom of page, for "$r^{2/3}$" substitute "$(V/C)^{2/3}\ r$"

p. C-4 The title of Figure C-2 should read "Figure C-2. Meteoroid Influx Rate Circular Orbit Mars", and the title of Figure C-3 should read "Figure C-3. Meteoroid Influx Rate Cruise"

p. C-5 At bottom of page, add the following: "*Within 50,000 km of Mars"

p. C-6 Line 13 should read: "... of low density ($\rho_p < 2.4$ gm/cm^3..."

p. C-6 Figure C-4. The ordinate "2" should read "100"

pp. C-17 C-21 The figures C-6 and C-7 on pages C-17 and C-21 should be reversed.

p. C-28 The title of Figure C-8 should read "Meteoroid Shield Test Specimen"

p. C-29 The title of Figure C-9 should read "Cutaway of Meteoroid Shield Test Specimen

p. C-34 In Section 1.8 the first sentence should be replaced by the following two sentences: "Preceding sections of this appendix contain derivations of the probability of penetrations of the spacecraft outer skin by meteoroids. It is clear that to design an outer skin of sufficient thickness to reduce the probability of no penetrations to a low level, such as 0.05 to 0.01, would be prohibitive in terms of the weight required."

p. C-35 In the first equation, the expression "(t in m^2)" in two places should read "(t in cm)" and "A" in two places should read "(A in m^2)"

p. C-38 In Table C-2, all values in inches should be in centimeters. A zero should be inserted immediately following the decimal point, for example: (0.020-inch) = 0.05080, (0.020-inch) = 0.06096, (0.020-inch) = 0.04064, etc.

p. C-40 In Section 1.8.7 Computation of R_i's, the sixth line should read "... than 10^6 are neglected"

p. C-45 In listing under "Values of t Used for Extreme Environment Analysis," under Inch, the first number should read 0.020 instead of 0.202

p. C-52 In 1.10 NOMENCLATURE, "K_2" should be defined as "$K^{-2/3}$ (4 ±2)" and "B" should be

$$\frac{1000\ \rho_t\ V^2}{9.806\ H_t}$$

pp. C-150 and C-151 should be reversed.

p. C-208 Along the ordinate in the graph, "Stress $\times 10^{-3}$" should read "Stress $\times 10^{-2}$"

Volume 5. Alternate Designs: Subsystem Considerations. Appendix II

p. F-23 Lines 7 and 10 change all subscript τ to T

p. F-24 Line 14, change "$M\Xi_i$" to "$m\Xi_i$"

p. F-29 Figure F-9 title should be "Reflection Phase Angle ϕ (deg)" and Figure F-10 title should be "Reflection Magnitude R"

p. F-30 Last line, change "0.27" to "0.175"

p. F-31 Lines 14 and 15, change "14,700 ft/sec to 460 ft/sec" to 14,700 ft/sec minus 460 ft/sec" and "14,700 ft/sec to 10,000 ft/sec" to "14,700 ft/sec minus 10,000 ft/sec"

p. F-32 Last line in item 4), change "27 per cent" to "17.5 per cent"

p. F-35 Table F-4, under Assumed Parameter for item 2 insert "$\pm 2 \times 10^{-5}$", for item 3 insert "$\pm 3 \times 10^{-5}$", and for item 4 insert "$\pm 2 \times 10^{-5}$"

p. F-53 Item d. Noise Figure, change "4 db" to "3.5 db"; Gain, change "20 db" to "10 db", last line change "10 db" to "4 db"

p. F-58 Figure F-21. Change 102 kc to 112 kc.

p. F-59 Line 22, change to "M_1 = 21.5 deg or 0.375 radians (rms, peak)"

p. F-60 Line 2, change to

$$"M_2 = \sqrt{(1.1)^2 - (0.375)^2}\ "$$

p. F-60 Line 3, change to "M_2 = 1.03 radians (rms) or 1.46 radians (peak)"

p. G-6 Paragraph 1.4, second line, change "from $E_M = 10^1 E_o$ to $10^4 E_o$ ..." to read "from $E_M = 10^{-1} E_o$ to $10^4 E_o$ ..."

Volume 6. Operational Support Equipment

p. 25 Figure 6. Caption should be "Typical Grounding Scheme"

p. 39 Section 1.3.3, change opening of first sentence to read "Launch pad equipment consists of the ground power and RF consoles and the test flight program power and control equipment ..."

p. G-31 Figure 1. Lines enclosing Data Format Generator should be solid.

p. G-102 Last line substitute "4500" for "45"

p. G-113 In Section 4.4.2, change "25 per cent" to "250 per cent"

p. G-184 Section 4.5, substitute "6.5 feet" for "six feet"

p. G-311 Fifth line, change "30 per cent" to "20 per cent"

p. G-398 Section 4.2 should begin with "The hoist beam is ..."

p. G-419 Second line "4 optical alignment targets" instead of 8. Same correction top of p. G-421.

p. G-423 Section 4.9.2, substitute "20 per cent" for "50 per cent"

Volume 7. 1969 Flight Test Spacecraft and OSE

p. 90 First line should read "Launch pad equipment consists of the ground power and RF consoles and . . ."

p. 107 Last line, change Volume 5 to Volume 6.